ABSTRACT

Title of dissertation: Large-eddy simulation of variable density flows
Tingguang Ma, Doctor of Philosophy, 2006

Dissertation directed by: Professor Arnaud Trouvé
Department of Fire Protection Engineering/
Department of Mechanical Engineering

A fully compressible direct numerical simulation flow and combustion solver (S3D) is modified and turned into a Large-eddy simulation (LES) solver. In this study, Favre-averaged governing equations are formulated first, supplemented with the classical Smagorinsky model and the dynamic procedure. To simulate low-Mach number flows, the speed of sound is artificially reduced while preserving the zero-Mach number physics. This pseudo-compressibility method is called Acoustic Speed Reduction (ASR). With ASR, the code has the capability to compute low-Mach number flows in an efficient way.

The boundary conditions in S3DLES are based on a one-dimensional characteristic analysis. To stabilize the solution, a buffer layer treatment is introduced at outflow boundaries to reduce acoustic reflections. The resulting flow is stable and produces results that compare well with a reference study. The implementation of the Smagorinsky model and other sub-models are validated using published plane jet simulation results with well-defined flow and perturbation conditions.

A second test case is the simulation of a round thermal plume. The ASR method is adopted to increase the computational efficiency by a factor of at least 10, thus making the computation of a 3-D round plume feasible on a small-scale cluster.

A third configuration is the simulation of a saltwater plume that was studied experimentally at UMD and is analog to a gaseous thermal plume. A comparison methodology between saltwater and gaseous plumes is developed. It is found that the computational requirement of a configuration that includes both the near- and far-field remains large and grid-resolution in our simulations remains marginal.

The fourth and last simulation takes advantages of the compressible flow formulation and considers flow-acoustic-interactions as a part of a thermoacoustic study. Three streams of different densities and momentums are introduced into a wall-confined domain. The flow is acoustically excited by an acoustic driver. The amplitude and phase of the driver are controlled. The high frequency modal response of the chamber compares well with experimental results. A variety of numerical tests in 1D, 2D and 3D configurations reveal the mechanism of transverse resonance and the resulting flow-acoustic interactions. This suggests that S3DLES will be a good prediction tool for future combustion noise and combustion instability studies.

Overall, the series of tests presented in this work serve to document the strengths and weaknesses of the current version of S3DLES.

LARGE-EDDY SIMULATION OF VARIABLE DENSITY FLOWS

By

Tingguang Ma

Dissertation submitted to the Faculty of the Graduate School of the
University of Maryland, College Park in partial fulfillment
of the requirements for the degree of
Doctor of Philosophy
2006

Advisory Committee:
Professor Arnaud Trouvé, Advisor and Chair
Professor James Quintiere
Professor André Marshall
Professor Kenneth Yu
Professor James Baeder

…

ACKNOWLEDGEMENTS

First and foremost, I would like to offer my deepest gratitude to my committee chair, Dr. Arnaud Trouvé. Throughout my years of study at University of Maryland, he provided encouragement and valuable technical knowledge and helped me maintain my focus on the research. I appreciate the technical suggestions he has constantly offered and thank him for being patient with me during my stay at University of Maryland. I have come to appreciate the emphasis he places on the understanding of fundamental aspects of flow and acoustic research while applying them to numerical simulations of complex flow systems.

I would like to thank Dr. Ken Yu for helping me understand the basics of thermoacoustics and for the numerous occasions he spent helping me understand the acoustic phenomena. In particular, I would like to acknowledge his support for my presentation at Reno conference. I am grateful to Dr. Ken Yu, who corrected my ideas easily by a fundamental analysis of a simple behavior. Without his help I would not have been able to make some progress in numerical acoustic studies.

I would also like to thank Dr. Jim Quintiere for leading me into the world of numerical plume studies. I would like to acknowledge his strong analytical capability on plume dynamics. Though I could not follow him for Ph.D. studies, I will benefit from his kind guidance on fire studies for all my life.

I am also thankful to Dr. Andre Marshall and Dr. James Baeder for serving in my thesis committee.

There are several students who have been extremely helpful to me during my stay at University of Maryland. Amardip Ghosh deserves a generous thank for always

supporting me with experimental results. Most of the time our results are produced at weekends. Usually after that, he will give me a ride home, so his help covers from the lab to my home. I am very relaxed before him, since he can tolerate any mistakes from my side. It is really lucky to find a friend like him.

Thanks are due to Dr. Xiaobo Yao for his help in providing me with saltwater experimental results which produced valuable data for plume structure studies. Though I could not reproduce his result with current computing resources, his patience with my understanding on saltwater plume is deeply appreciated.

I owe my thanks to all faculty members in Fire Protection Engineering department. In particular, thanks are due to Dr. Mowrer, Dr. Milke from helping me from beginning to end, from my daughter born to now first grade. Special thanks are also due to Cindy Gilbert, Pat Baker, Sylvia Keane and Alison Spurrier, for their kind works in supporting my study here.

My parents have given me infinite support and have kept their faith in me during these grueling graduate school years. I thank them for always being there to listen, for all the advice they gave me from time to time and for praying for me constantly. Last but not the least, I am indebted to my wife Qiqi Yao for her continuous support. She gets my gratitude for her never-ending patience and for believing in me. Though my daughter still could not understand what I am doing, I hope to share with her my experience later.

Table of contents

List of Tables

List of figures

Nomenclature

c_p	Specific heat at constant pressure
$c_{p,k}$	Specific heat of species k
c_v	Specific heat at constant volume
C_I	Yoshizawa constant
C_S	Smagorinsky constant
D	Diameter for round plume, jet slot width for plane jet
D_k	Mass diffusivity at molecular level
e	Internal energy, $e = c_v T$
E	Total energy, including chemical, thermal and kinetic energies
E_t	Total energy, including thermal and kinetic energy
f	Frequency
Gr	Grashof number
h_k	Enthalpy of Species k
h_k^0	Enthalpy of formation
L_{ij}	Leonard Stress tensor
L_M	Morton length scales
M_k	Molecular weight of species k
M	Molecular weight of mixture
p	Pressure
Pr	Prandtl number
Pr_t	Turbulent Prandtl number

q	Any variable for Favre filtering
$\dot{q}$	Heat release rate per unit volume
q	Any variable for Favre filtering
$\dot{q}$	Heat release rate per unit volume
r	Radius
Q	Volume flux
R	Universal gas constant
Ra	Rayleigh's number
Re	Reynolds number
Sc	Schmidt number
Sc_t	Turbulent Schmidt number
S_{ij}	Strain rate
S_{kk}	Dilation of velocity field
St	Strouhal number
T	Temperature
T_{ij}	SGS turbulent stress tensor at grid filter level
u_i	Velocity in direction i
$V_{k,j}$	Diffusion velocity of species k
Y_k	Mass fraction of species k
Z	Mixture fraction

Greek letters

α	ASR factor for scaling the acoustic dilation term
γ	Specific heat ratio, $\gamma = c_p / c_v$
τ_{ij}	Viscous stress tensor
δ_{ij}	Kronecker delta, =1 if i=j

	SGS dissipation rate
ε_{SGS}	
	Ratio of test filter to grid filter
κ	
λ	Thermal conductivity
μ_t	Turbulent viscosity
μ	Molecular viscosity
ρ	Density
σ	Relaxation factor for soft-inflow, outflow pressure corrections
	SGS turbulent stress tensor at test filter level
t_{ij}	

Symbols

$\widetilde{q}$	Favre filtered variable (grid filter)
q^a	An-isotropic part of tensor q
q^i	Isotropic part of tensor q
$\dot{q}$	Rate of change
$\tilde{\bar{q}}$ *or* $\hat{q}$	Favre filtering operation by test filter
$\overline{q}$	Ensemble averaging

Chapter 1. Introduction to buoyant flows

1.1. Classical work on buoyant plumes

Fire induced flows are mainly buoyancy-dominated flows, since the fire source provides the energy to raise the temperature, and the temperature variations correspond to density variations, which in the gravitational field, generate a buoyancy force that drives the fluid motion. Buoyancy dominated flows are widely encountered in the fire configurations, such as the fire plume (with reaction), the buoyant plume (without reaction), and the ceiling jet. The buoyant plume is a fundamental (canonical) form of fluid flow, and is described in many textbooks on turbulent flows (for example, see Tennekes and Lumley, 1972, Pope, 2000). It will transport smoke to locations far from the fire, so it is very important for fire hazard calculations. The flame is the flow region with strong chemical reactions and thermal radiation effects (Zukoski, 1995). Understanding of the buoyant nature of the fire will help the understanding of the mechanisms of flame spread and smoke movement. The interaction of a buoyant plume with a horizontal wall leads to the formation of a ceiling jet (Alpert, 1972). The structure of the ceiling jet will affect the response of heat and smoke detectors, so it has many implications for fire detection and activation of suppression systems.

Many flows in environmental applications are also influenced by the buoyancy forces arising from density difference. Because of the great practical significance of buoyancy-influenced or -dominated flow phenomena, engineers, meteorologists, and also oceanographers need to be able to calculate these phenomena in order to predict and possibly control them.

The classical theoretical work on buoyant flow is carried out on boundary-layer type inviscid flows. Integral methods suitable for shear-layer flows were developed in which the partial differential equations are reduced to ordinary ones by introducing empirical similarity profiles for velocity, temperature, or concentration in the horizontal direction. The resulting ordinary differential equations describe the axial variation of the velocity, temperature or concentration scales and the characteristic shear-layer width. Further empirical input is necessary which describes the global effect of turbulence, in the case of turbulent buoyant jets and plumes, via an entrainment law relating the horizontal entrainment velocity at the jet edge to the local vertical velocity on the jet axis. The governing equations are thus simplified by dimensional analysis and problem-specific simplifications. Also, the Boussinesq assumption is adopted to limit the treatment of variable density to the buoyant term only, so the flow can be described similarly to an incompressible flow.

Zeldovich (1937) first described thermally buoyant plumes arising from a point source and from a horizontal line source of heat. His treatment does not permit a velocity component normal to the plane of symmetry of the plume. Schmidt (1941) investigated the behavior of natural convection in a turbulent plume above a line and point source of heat. A similarity technique was used. The governing flow equations were solved by assuming a series solution in terms of the similarity variable. Rouse et al. (1952) found a transformation that results in closed-form solutions for the temperature and velocity distribution. The monumental work by Morton, Turner and Taylor (1956) was concerned

with describing isolated convection in a meteorological context. Three important assumptions were made for the weak point source plume: Boussinesq approximation, self-similarity and linear local entrainment assumption (for shear-layer flows). The entrainment assumption provides the entrainment velocity by integrating the simplified Navier-Stokes governing equations in terms of top-hat variables. The similarity assumption assumes that a plume spreads linearly with height and that the mean horizontal flux across the edge of the plume is proportional to the local vertical velocity. They formed the classical plume theory and are widely used in similar plume works of a point-source type.

The general form of classical plume theory is described in the following, which can be found in any textbook on turbulence (Pope, 2000). In a neutral environment (no change in ambient density with height), the mean vertical velocity and buoyancy acceleration are given respectively as

$$W = B^{1/3} z^{-1/3} A_W e^{-B_W \eta^2} \tag{1}$$

$$g\frac{\Delta\rho}{\rho_\infty} = B^{2/3} z^{-5/3} A_T e^{-B_T \eta^2} \tag{2}$$

Where W is the mean vertical velocity along the axis of the plume, B is the rate of addition of buoyancy, z is the height (distance from the buoyancy source), A_W, B_W are the parameters which quantify the Gaussian fit to the mean velocity profile, while A_T, B_T are the corresponding ones for the density profile; η represents the similarity variable, $\eta = r/z$, where r is the radial distance at any z.

The primary disagreements among the various experimental results are regarding the centerline values of mean velocity and buoyancy profiles as well as the plume-spreading rate. According to Shabbir and George (1994), various parameters of Gaussian fit of profiles can be found in the literature: $A_W = (3.4 \sim 4.7)$, $B_W = (55 \sim 96)$, $A_T = (9.1 \sim 14.28)$, $B_T = (48 \sim 71)$. The scattering is significant. The discrepancies between different experimental data are likely to be due to various factors: 1. Boundary effects of the solid wall lateral boundaries and presence of reverse or co-flow can influence the entrainment process, 2) measurements may not have been carried out in the fully developed turbulent region in some cases; 3) hot-wire anemometer measurements are known to be insensitive to direction, and therefore the measurements made outside the half-width of the plume may not be reliable in such cases. Since B is used in the scaling for self-similarity, much depends on an accurate determination of the buoyancy flux B, the measurement of which, unfortunately, can be influenced by experimental errors.

The early work on jets and plumes with special emphasis on environmental flows is summarized in the book chapter by Fischer et al. (1979) and reviews by Chen and Rodi (1980), List (1982), List and Rodi (1982). Further work on large-scale structure can be found by Papanicolaou and List (1988, 1989), Dahm and Dimotakis (1990). To overcome the difficulties due to Schmidt number effects in water, the velocity statistics are measured for gaseous plumes by Dai, Tseng, and Faeth (1994). Measurements in buoyant flows can be found also in George, Alpert, and Tamanini (1977), Shabbir and George (1994). Most of the fundamental progress before 1994 is summarized in the book by

Davies and Neves (1994). In that book, the phenominogical plume behavior is summarized by List and Dugan (1994), and an interesting theory is proposed using a Lagrangian vortex method to simulate the plume structure (Chu, 1994). The result from this assumption is surprisingly close to those of the results of classical integral methods. Zukoski (1995) summarized the classical plume theory with special application on fires, and the book by Gebhardt et al. (1996) summarized the buoyant flow dynamics with a wide range of engineering applications.

Thus most of the classical results for buoyant plumes are based on integral models and the similarity assumption. Integral methods are suitable mainly when the flow retains its jet-type character; they are difficult to extend to more complex flow situations. For example, the interaction of the discharged jet/plumes with neighboring walls, with nearby plumes, and with layers of strong stable stratification (inversion) are difficult to describe with integral methods; the same can be said for complex geometries and boundary conditions. The reason is that in such cases the profile shapes are not similar and self-preserving, so they are difficult to describe empirically, and it is also difficult to relate the entrainment rate to all local parameters that influence this rate. So with the advances in computer technology and numerical methods for solving partial differential equations, the so-called field methods have become increasingly popular.

1.2. Numerical simulation of buoyant flows

As described by Sagaut (2002), the numerical simulations are used for two types of purposes. The first is to accompany research of a fundamental kind. By describing the

basic physical mechanisms governing fluid dynamics, numerical simulation helps us understand, model, and later control these mechanisms. The quality of the data generated by the numerical simulation also depends on the level of resolution chosen. For the best possible precision, the simulation has to take into account all the space-time scales affecting the flow dynamics. When the range of scales is very large, as it is in turbulent flows, for example, the problem becomes stiff, in the sense that the ratio between the largest and smallest scales becomes very large. Direct numerical simulation and well-resolved large-eddy simulation fall into the first category.

The second kind of purpose is engineering analysis, for instance when flow characteristics need to be predicted during a design phase. Here, the goal is no longer to produce basic data for analyzing the flow dynamics itself, but rather to predict some of the flow characteristics or, more precisely, the values of physical parameters that depend on the flow, such as the stresses exerted on an immersed body, the production and propagation of acoustic waves, or the mixing and reaction of chemical species. The purpose is to reduce the cost and time needed to develop a prototype. The simulations may be aimed at predicting either the mean values of these parameters or the amplitude of their variations.

Considered as canonical flow configurations, jets and buoyant plumes have attracted attention from the numerical researchers for a long time. The various models used in past computations belong to one of the following groups: direction numerical simulations

(DNS), Reynolds-averaged Navier-Stokes simulations (RANS) or large-eddy simulations (LES).

1.2.1. DNS

The most fundamental way to study flows is to work with the complete set of equations without turbulence modeling. This requires that the grid resolution cover the smallest scales down to the Kolmogorov scales. This kind of study requires that the physical model chosen to represent the behavior of the fluid must be pertinent and that the algorithms used, and the way they are used by the computer system, must introduce no more than a low level of error. For instance, a sixth-order compact finite difference scheme for spatial discretization, and 3rd order Runge-Kutta method for time advancement are adopted in many DNS studies (Rajandram et al. 2002).

Basu and Narasimha (1999) studied the effects of off-source volumetric heating (similar to that due to latent heat release in a cloud) using direct numerical simulation of a circular jet-like flow and found that the large-scale structures break down and entrainment is inhibited. Rajandram and Luo (2002) described the instantaneous unsteady behavior of the buoyant fire plume with a 2-D compressible reacting flow formulation. The presence of buoyancy causes the formation of large vortical structures in the plume. Decreasing the Froude number ($Fr = u_\infty^2 / gl$, the ratio of inertia forces to gravity forces) causes higher vorticity levels. The simulations successfully capture the instantaneous unsteady behavior of the buoyant fire plume. The inclusion of chemical reaction alone stabilizes the flow while the presence of buoyancy causes the formations of large vortical structures in the

fire plume. The overall integrated mean reaction rate is found to increase with buoyancy. Jiang and Luo (2001) simulated transitional noncircular buoyant reactive jets with a focus on the mechanism of vortex dynamics caused by buoyancy and chemical reaction. The interaction between density gradients and gravity produces flow vorticity and the rectangular jet has a stronger tendency of transition to turbulence due to the aspect ratio effect. Katta et al. (2000) have conducted detailed 2-D DNS of low-speed buoyancy-driven premixed, partially premixed, diffusion and triple jet flames using detailed chemical mechanisms to address the vortex-flame interactions and two phase, swirling, and extinction effects.

Currently, DNS is only used for some fundamental studies, such as the study of the role of buoyancy on turbulence, the role of coflow on entrainment, the effect of the presence of a wall etc. As the name implies, DNS directly simulates the Navier-Stokes equations without recourse to subgrid modeling, so for flows with a broad spectrum of motions (at high value of Reynolds number *Re*), the cost can be prohibitive - the number of required grid points scales like $\mathrm{Re}^{9/4}$ and the number of time steps like $\mathrm{Re}^{3/4}$ (Piomelli et al. 1996).

1.2.2. RANS methods

A cost-effective numerical simulation of a fire plume may be accomplished using Reynolds-averaged governing equations, either for a Boussinesq flow or weakly compressible flow. RANS equations require turbulence modeling. A review of turbulence models has been given by Rodi (1984) who concluded that models of an intermediate

level of complexity employing transport equations only for the *rms* velocity and integral length scale of the turbulent motions are most suitable for practical purposes. Of these so-called two-equations models, the $k-\varepsilon$ model is the most widely tested and used.

The $k-\varepsilon$ model was introduced by Launder and Spalding (1972). Patankar (1980) introduced the famous SIMPLE algorithm to compute the pressure field. Launder et al. (1972) also proposed the buoyancy correction to the $k-\varepsilon$ model, which is known as the $k-\varepsilon-g$ model. Subsequent turbulence models introduce more partial differential equations, these models are rather complex and hence, for reasons of economy, their practical application should be restricted to situations where simpler models fail, for instance, situations featuring counter-gradient diffusion. For example, in free convection situations in the atmosphere, the heat may be transported by the turbulence against the temperature gradient. Dewan et al. (2003) compared 3 buoyancy extended versions of the $k-\varepsilon-\overline{t'^2}$ model in predicting turbulent plane plume and found that the mean flow quantities predicted by all the models agree well with the experimental observations.

To name a few applications of the $k-\varepsilon-g$ model, Tamanini (1977) simulated axisymmetric forced and buoyant jets; You and Faeth (1982) simulated buoyant axisymmetric turbulent diffusion flames. Cox and coworkers developed the code SOFIE, which was successfully used to simulate the King's Cross fire. Most commercial CFD codes currently available are based on the $k-\varepsilon$ model and claim to have the ability to simulate fire-induced flows, such as PHOENICS, FLUENT, STAR-CD, SMARTFIRE,

KAMELON, SOFIE, etc. These solvers are based on similar numerical algorithms (for example, variations of the SIMPLE algorithm).

Hossain and Rodi (1980) simulated the vertical buoyant jets. Nam and Bill (1993) dealing with free plumes concluded that using the standard $k-\varepsilon$ model result in an over-prediction of velocities and temperature on the central axis of a plume, leading to an underestimation of the width of the plume. Corrections were made by tuning the turbulent viscosity coefficient and the effective Prandtl number, thereby achieving agreement with experimental data within 2% error. Hara and Kato (2004) simulated a thermal plume with a standard $k-\varepsilon$ model, and found that the cell Reynolds number is an important measure of the performance of the numerical set-up. However, this kind of traditional method cannot give a detailed picture of the fluctuating flow.

Besides the work above, the simulation of plumes with RANS approaches is still limited, partly due to the unsteady nature of the plume, and partly due to the many empirically determined constants in RANS approaches. As Baum and Rehm (1978) point out, most turbulence models in use are of the gradient diffusion type. Thus, they implicitly assume that a small-scale, locally homogeneous turbulent field underlies the organized macroscopic mean motion whose solution is sought. Various models are proposed for predicting the turbulent flows, with little success to find a general all-purpose formulation.

Another comment made by McGrattan (2004) is also important. One of the difficult problems in using a $k-\varepsilon$ model is found in introducing the turbulence at the inlet. The transport equations of k and ε need initial values at the inlet and these values are not always available. In addition, the diffusion terms in the mass, energy and momentum equations are so large that they suppress any vorticity generation, or even any fluctuation. So the plume in a RANS approach has a smoothed appearance. There is always a need to modify the standard $k-\varepsilon$ model coefficients for a fire plume, since more turbulent energy is needed at the burner to account for all the buoyancy-induced vorticity that was being suppressed. This problem is not only coming from the $k-\varepsilon$ modeling, but also from the approaches/strategies adopted in the framework of RANS methods. There is a need to overcome such problems; the LES technique provides such a solution.

1.2.3 Large Eddy Simulation

Large-eddy simulation of the buoyant flow is an intermediate approach between DNS and RANS. As it can capture the large turbulent eddies, it will produce better mixing predictions than RANS, so the flow structure will be better represented. Also the cost of simulation is relatively reasonable for engineering calculations, so it can be used as an engineering tool. LES has the advantage that its solution is less model-dependent and that it can show instantaneous large-scale structures as well as providing statistics. In LES, the large eddies are resolved numerically while the fine-scale eddies are modeled by a subgrid scale (SGS) model. The feature of capturing large-scale motions in LES is of great value to practical applications such as thermal plumes.

An interesting observation made by Chu (1994) is here quoted,

> *Turbulent flows such as jets and plumes are collections of eddies in motion. Large eddies and small eddies circulate around each other by mutually induced motions. Adjacent eddies of comparable size and strength compete for dominance. Ultimately, the largest eddy extending across the full width of the shear layer takes control over the process and, therefore, is responsible for the transfer of mass and momentum across and along the shear flow. The smaller eddies engulfed in the midst of the dominant eddy have relatively small effects on the transport processes.*

This view has been directly applied to the formulation of a Lagrangian method following the motion of the dominant eddies. The result based on such dominant-eddy hypothesis is surprisingly consistent with the classical Eularian work based on the relevant laboratory experimental results from the literature. The experimental work by List and Dugan (1994) supports the assumption that the averaging process used in integral models disguises the fact that measured instantaneous concentration levels may exceed the average concentration by as much as a factor of 6. Also regions of fluid high in tracer concentration can still remain coherent within the flow field at distances far removed from the source of the discharge. The experimental work by Shabbir and George (1994) concludes that in a buoyant plume the primary effect of buoyancy on turbulence is indirect, and enters through the mean velocity field (producing large shear production). These studies provide the theoretical basis that the large-eddy simulation will perform better than RANS approaches, since it can capture the eddies above grid level which are dominant in the plumes.

For this reason and others, Baum and Rehm (1978) borrowed the ideas from LES to capture the large scales down to the grid size. Since the turbulent kinetic energy cascades down from large to small eddies, it would accumulate (un-physically) at the grid scale, rather than diffusing into heat. Therefore, the Lanczos smoothing (which is equivalent to putting in an artificial viscosity term) was used at that time. This is equivalent to the Smagorinsky model, which is used in later versions of Fire Dynamics Simulator (FDS). Baum and Rehm (1978) also derived a new formulation for thermally driven flow (low Mach number flow). McGrattan et al. (1998) extended their pioneering work into a user-friendly robust CFD tool. To date, FDS has been widely applied in different fields of thermally driven flows, including fire problems.

Well-resolved LES simulations of a force turbulent buoyant plume have been performed by Basu and Mansour (1999). The simulations are based on an incompressible flow solver and the Boussinesq approximation. The weakly compressible formulation for plume simulations without the Boussinesq assumption is adopted by Zhou et al. (2001). The low Mach number formulation is adopted to filter-out the acoustic waves. While this treatment allows for significant gains in computational efficiency, the computational cost is still expensive and relies on parallel running on multi-processors.

A summary of LES and numerical choice is provided in the following table.

A study of LES stress and flux models applied to a buoyant jet is performed by Worthy et al. (2005). The choice of LES model can have a significant impact in a buoyant transitional flow. The stability consideration for upwind or TVD schemes sometimes

	Author(s)	Grid system	Discretization	Time-integration	Poisson equation	Boundary treatment
Boussinesq Flow	McGrattan et al. (1998)	Orthogonal	2^{nd} order central difference scheme	Explicit 2^{nd} order Predictor-corrector Scheme	FFT solver	
	Basu et al. (1999), Webb et al. (2000)	Spherical polar coordinate system	2^{nd} order finite volume method	2^{nd} order Adams-Bashforth scheme	FFT solver	Traction-free boundary conditions Buffer zone to target values
	Worthy et al. (2001)	Orthogonal	2^{nd} order central+TVD+3^{rd} upwind	2^{nd} order fractional step method	Fast multigrid	
Weakly compressible flow	Zhou et al. (2001)	Uniform Cartesian grids	2^{nd} order central difference scheme	2^{nd} order Adams-Bashforth scheme	Multigrid method	Constant pressure BC Zero-velocity gradient Non-negative velocity forcing
Fully compressible flow with pseudo-compressibility methods	DesJardin et al. (2004)	Non-uniform Cartesian grids	Finite volume method based on AUSM+ flux vector splitting 9^{th} order upwind-biased scheme+5^{th} order ENO method +4^{th} order central scheme	4^{th} order Runge-Kutta method + Pressure Gradient Scaling	N/A	Navier-Stokes Characteristic Boundary Condition
	This study	Non-uniform Cartesian grids	6^{th} order Finite Difference Scheme with 6^{th} order filtering	3^{rd} /4^{th} order Runge-Kutta method + Acoustic-speed Reduction	N/A	Navier-Stokes Characteristic Boundary Condition

Table 1. Current numerical methods for buoyancy-induced flow simulations.

overweighs the LES model constants difference. Reviews on the numerical simulation of buoyancy-induced flows can be found in Mitler (1990), Larsen (1994), Cox (1995) and Novozhilov (2001), though their reviews are predominantly focused on RANS approaches. Large eddy simulation of buoyant plumes is still primitive, primarily due to the computation cost associated with well-resolved LES and the limitations of hardware.

1.3. Outline of current work

The current LES capability corresponds to high-order numerical methods and is intended as a basic science-learning tool and a natural companion to detailed studies of laboratory-scale experimental configurations. The choice of high-fidelity numerical methods is made in order to separate issues of numerical resolution from errors associated with subgrid-scale physical modeling.

This document is organized as follows. The LES formulation and numerical solver S3DLES are presented in Chapter 2. A validation test of S3DLES corresponding to a momentum-driven high-speed jet is presented in Chapter 3. Another validation test corresponding to multiple jets mixing in a wall-confined environment is presented in Chapter 4. This study also includes a test of the ability of S3DLES to simulate the acoustic response of a chamber. The third validation test corresponding to a strong plume is presented in Chapter 5. Finally, S3DLES is used for detailed comparisons with an experimental study of buoyant plumes performed with saltwater. The Chapter 7 presents a summary of our research and discusses future developments. Some numerical development and discussions are supplied in Appendix.

Chapter 2: Development of S3DLES

2.1. Introduction

The objective of this work is to adapt an existing CFD capability, named S3D, to the large-eddy simulation technique. S3D is a direct numerical simulation code developed in a DOE-sponsored collaborative effort between the Universities of Maryland (Prof. A. Trouvé), Michigan (Prof. H. G. Im), Wisconsin (Prof. C. J. Rutland), Sandia National Laboratories (Dr. J. H. Chen) and the Pittsburgh Supercomputing Center (R. Reddy). This collaborative effort is aimed at adapting and enhancing the S3D solver for efficient implementation on massively parallel processors (MPP) platforms. S3D couples an advanced fully compressible Navier-Stokes solver (high-order finite difference discretization, high-order Runge-Kutta explicit time integration, characteristic-based boundary conditions treatment, pseudo-compressibility treatment of acoustic waves, conventional structured uniform/non-uniform computational mesh) with a solver for gas-phase exothermic chemical reaction. It is based on standard message passing interface (MPI) protocols and is both MPP-scalable (with tests performed up to 1,000 processors) and portable (IBM/Cray/SGI/Compaq/CPLANT).

The present work is based on the numerical framework developed for S3D; it also uses a large eddy simulation approach and subgrid-scale physical modeling in order to widen the domain of application of the reacting flow solver. The new code is called S3DLES. The unchanged numerical features of S3D are: a fully compressible flow formulation; a sixth/eighth-order finite difference discretization; a third/fourth-order Runge-Kutta explicit time integration; a characteristic-based boundary conditions treatment enhanced with an inflow forcing treatment for turbulent inflow; a pseudo-compressibility treatment

of acoustic waves; a conventional structured uniform/non-uniform computational mesh. These features are described in more detail by Im (1999), Kennedy et al. (2001), Wang and Trouvé (2004). These choices are based on in-depth comparisons of several numerical methods (Kennedy et al., 1997) and lengthy tests on low storage, explicit Runge-Kutta schemes (Kennedy et al. 1999). The numerical methods have been shown to be of high quality and are characterized by very low levels of numerical dissipation.

Similar to DNS, the objective of LES is to compute unsteady turbulence motions and the method must handle unsteady flow fields (at the resolved scales with adequate boundary and initial conditions). The numerical precision of the algorithm becomes a key point: subgrid scale models should not be offset by numerical errors. Although the compact schemes have a reputation for better performance over conventional higher-order schemes (Lele, 1992), the later is adopted here, due to a better parallelization performance. To damp high wave-number, non-physical perturbations, explicit high order spatial filters are also adopted. It is found by Kennedy et al. (1997) that the effect of changing the temporal or spatial scheme is less important than the filtering effects. To capture the correct physics within the compressible flow while letting spurious perturbations leave the computational domain smoothly, the characteristic-wave based boundary treatment is adopted and enhanced with several artificial relaxation terms. Since the flow speeds for fire problems are generally on the order of a few meters per second, the conventional fully compressible flow formulation leads to a problem because it is inefficient when treating low-Mach number problems (due to the convection-limited time step). The Acoustic Speed Reduction method, originally proposed by Wang and

Trouvé (2004) is adopted to increase the solver efficiency and is adapted to buoyancy-driven flows. With ASR, the time step is typically increased by a factor of 10 to 50.

The new physical modeling features of S3DLES are: a Smagorinsky model to describe subgrid-scale turbulent stresses; a dynamic implementation of the Smagorinsky model using explicit top-hat filtering; a presumed probability density function (Pdf) model to describe subgrid-scale turbulent mixing. Along with the development and validation of the code, the problems in boundary treatment, initial conditions and in pseudo-compressibility method are overcome. This chapter reviews the physical models adopted in S3DLES and presents the numerical developments that have proven necessary for a successful simulations of jets or plumes configurations.

2.2. Governing equations for fully compressible reactive flows

Fire is an unwanted combustion phenomenon characterized by exothermic chemical reactions and thermal radiation. The temperature in a combusting region can be as high as 2000K in the thin flame sheet, or 1300K on average for unconfined fires. Thus the numerical simulation of spatially evolving turbulent flows has become popular to study the chemical, buoyancy and turbulence effects on combusting processes.

The fully compressible Navier-Stokes equations for reactive flow are listed below.

Conservation of total mass:

$$\frac{\partial \rho}{\partial t} + \frac{\partial \rho u_j}{\partial x_j} = 0 \tag{1}$$

This is simply a statement that the rate of mass storage within a control volume, as measured by changes in density, is balanced by the net rate of inflow of mass by convection across the control volume boundaries.

Conservation of species mass:

$$\frac{\partial \rho Y_k}{\partial t} + \frac{\partial \rho Y_k u_j}{\partial x_j} = -\frac{\partial \left(\rho Y_k V_{k,j}\right)}{\partial x_j} + \dot{\omega}_k \tag{2}$$

Where the diffusion of species is governed by Fick's law: $\rho Y_k V_{k,j} = -\rho D_k \frac{\partial Y_k}{\partial x_j}$. Here the species diffusivity D_k is related to the momentum diffusivity (μ/ρ) via the Schmidt number: $D_k = \frac{\mu/\rho}{Sc_k} = f(p,T)$, where Sc_k (assumed constant) is the Schmidt number of species *k*. For most combustion-related problems, D_k is a function of pressure and temperature.

The equations describing the *conservation of momentum* are derived by applying Newton's second law of motion (the sum of forces acting on a fluid element is equal to the rate of change of momentum). These are known as the Navier-Stokes equations and can be written as

$$\frac{\partial \rho u_i}{\partial t} + \frac{\partial \rho u_i u_j}{\partial x_j} = -\frac{\partial p}{\partial x_i} + \frac{\partial \tau_{ij}}{\partial x_j} + \rho g_j \tag{3}$$

The left-hand side of the equation simply represents the local rate of change of momentum of a small volume element traveling with the fluid. The right-hand side comprises the forces acting upon it. The first two terms are associated with surface forces acting on the fluid within the control volume and the third, the volumetric body force

term, is associated with influences on the fluid from external forces such as a gravitational field.

For a Newtonian fluid obeying Stokes's law (where shear stress is assumed to be linearly proportional to the rate of deformation, the coefficient of proportionality being the molecular viscosity), the viscous stress tensor is given by

$$\tau_{ij} = \mu\left[\frac{\partial u_i}{\partial x_j} + \frac{\partial u_j}{\partial x_i} - \frac{2\mu}{3}\frac{\partial u_k}{\partial x_k}\delta_{ij}\right] \tag{4}$$

The viscosity for gaseous species is computed using Sutherland's Law: $\mu = \mu_0 (T/T_0)^b$, where b=0.76 in S3DLES. It is usually adopted for combustion problems in air under normal atmospheric pressure.

The equation describing the principle of conservation of energy for a multi-component, reacting system of gases is extremely complex involving both thermal and mechanical energy and the inter-diffusion of chemical species. It describes a balance between the rate of accumulation of both internal and kinetic energies within the control volume, and energy influx due to convection, conduction, thermal radiation, the inter-diffusion of species, together with the net rate of work done on the gases by pressure forces, viscous stresses and body forces. It may be written in a variety of ways depending upon whether temperature, enthalpy or internal energy is chosen as the principal variable.

Here the conservation of total energy is the starting point:

$$\frac{\partial \rho E}{\partial t} + \frac{\partial \rho E u_j}{\partial x_j} + \frac{\partial p u_j}{\partial x_j} = \rho g_j u_j - \frac{\partial q_j}{\partial x_j} + \frac{\partial \tau_{ij} u_i}{\partial x_j} \tag{5}$$

Where E is the total energy (per unit mass):

$$E = \left(\sum_{k=1}^{N} h_k Y_k - \frac{p}{\rho}\right) + \frac{u_i u_i}{2} = \text{ internal energy + kinetic energy}$$

In a more detailed form, the total energy can be expressed as:

$$E = \left(\sum_{k=1}^{N} h_k^0 Y_k + \int_{T_0}^{T} c_p dT - \frac{p}{\rho} \right) + \frac{u_i u_i}{2} = \left(\sum_{k=1}^{N} h_k^0 Y_k + \int_{T_0}^{T} c_v dT - \frac{R}{M} T_0 \right) + \frac{u_i u_i}{2} \qquad (5a)$$

where $c_p = \sum_{k=1}^{N} Y_k c_{p,k} = c_v + \frac{R}{M}$, and

$h_k = h_k^0 + \int_{T_0}^{T} c_{p,k} dT =$ Enthalpy of formation + thermal enthalpy (of species k)

The expression above is the total energy in a detailed chemistry framework as commonly adopted in Direct Numerical Simulation (DNS) of reactive flows. For LES, the reaction is not based on a detailed chemistry scheme, and the reaction is usually modeled with simple chemistry. So the species chemical energy can be lumped into the reaction term and not computed inside the energy term.

For simple chemistry, we can rewrite the total energy as:

$$E = \sum_{k=1}^{N} h_k^0 Y_k + \left(\int_{T_0}^{T} c_v dT - \frac{R}{M} T_0 \right) + \frac{u_i u_i}{2} = \sum_{k=1}^{N} h_k^0 Y_k + E_t \qquad (5b)$$

Here $E = chemical + thermal + kinetic$ energy, and $E_t = thermal + kinetic$ energy

The new energy equation for E_t is:

$$\begin{aligned} \frac{\partial \rho E_t}{\partial t} + \frac{\partial \rho E_t u_j}{\partial x_j} + \frac{\partial p u_j}{\partial x_j} = \rho g_j u_j + \frac{\partial \tau_{ij} u_i}{\partial x_j} + \frac{\partial}{\partial x_i}\left(\lambda \frac{\partial T}{\partial x_i} \right) \\ - \frac{\partial}{\partial x_i}\left(\rho \sum_{k=1}^{N} h_k Y_k V_{k,j} \right) - \sum_{k=1}^{N} h_k^0 \left(\dot{\omega}_k - \frac{\partial}{\partial x_j}\left(\rho Y_k V_{k,j} \right) \right) \end{aligned} \qquad (6)$$

The term before last on the RHS of Equation (6) is the heat release rate due to combustion. We write:

$$\frac{\partial \rho E_t}{\partial t} + \frac{\partial \rho E_t u_j}{\partial x_j} + \frac{\partial p u_j}{\partial x_j} = \rho g_j u_j + \frac{\partial \tau_{ij} u_i}{\partial x_j} + \frac{\partial}{\partial x_i}\left(\lambda \frac{\partial T}{\partial x_i} \right) - \sum_{k=1}^{N} h_k^0 \dot{\omega}_k + \sum_{k}^{N} c_p T \left[- \frac{\partial \left(\rho Y_k V_{k,j} \right)}{\partial x} \right] + Extra \text{ Terms} \qquad (7)$$

The right side has the gravity term, stress term, conduction term, reaction term, heat transfer due to mass diffusion, and extra terms due to the molecular mass diffusion terms. Extra terms vanish if the specific heat is the same for the different gases in the mixture, *i.e.* $c_{p,k} = c_p$. So the final form of *the conservation of total energy* is:

$$\frac{\partial \rho E_t}{\partial t} + \frac{\partial \rho E_t u_j}{\partial x_j} + \frac{\partial p u_j}{\partial x_j} = \rho g_j u_j + \frac{\partial \tau_{ij} u_i}{\partial x_j} + \frac{\partial}{\partial x_i}\left(\lambda \frac{\partial T}{\partial x_i}\right) - \sum_{k=1}^{N} h_k^0 \dot{\omega}_k \tag{8}$$

In the following, we also assume that c_p and c_v are constant. We then have $E_t = c_v T + \frac{u_i u_i}{2}$, $\lambda = \frac{\mu c_p}{\mathrm{Pr}}$, where Pr is the Prandtl number which is also assumed constant. The total energy equation may be modified using the conservation of kinetic energy:

$$\frac{\partial}{\partial t}\rho\left(\frac{u_i u_i}{2}\right) + \frac{\partial}{\partial x_j}\rho\left(\frac{u_i u_i}{2}\right)u_j = \rho g_i u_i - u_i \frac{\partial p}{\partial x_i} + u_i \frac{\partial \tau_{ij}}{\partial x_j} \tag{9}$$

And the conservation equation for internal energy becomes:

$$\frac{\partial \rho e}{\partial t} + \frac{\partial \rho e u_j}{\partial x_j} = -p\frac{\partial u_i}{\partial x_i} + \tau_{ij}\frac{\partial u_i}{\partial x_j} + \frac{\partial}{\partial x_i}\left(\lambda \frac{\partial T}{\partial x_i}\right) - \sum_{k=1}^{N} h_k^0 \dot{\omega}_k \tag{10}$$

where $e \equiv E_t - \frac{u_i u_i}{2} = c_v T$.

This corresponds to a generalized form of the temperature equation, including compressibility and combustion effects.

The equations (1), (2), (3), (8) constitute the governing equations in a description of a reactive flow with simple chemistry. To close the system of equations, an additional constitutive relationship is required, we use *the ideal gas law*:

$$p = \rho \frac{R}{M} T = \rho R T \sum_{k=1}^{N} \frac{Y_k}{M_k} \tag{11}$$

Where M is the molecular weight of the mixture, and M_k that of the species k.

2.3. LES filtering and filtered equations

The direct numerical simulation of turbulent flow for engineering problems is all but impossible as a result of the wide range of scales that are present. Consequently, the solution to such problem must invariably be based on some form of turbulence modeling. Traditional turbulence models based on Reynolds averaging had only limited success since the large scales of the turbulence – which contain most of the energy - are highly dependent on the geometry of the flow being considered. The small scales are more universal in character and serve mainly as a source for dissipation. Hence, it can be argued that a better representation of turbulent flows could be achieved if just the small scales are modeled while the large scales are calculated (Deardorff, 1970). This is the basic idea behind large-eddy simulations.

Generally, it is agreed that Smagorinsky first proposed the idea of an eddy-viscosity concept used for large-scale atmospheric flows. It is Lilly (1967) who utilized the famous assumption that if the subgrid kinetic energy is assumed to be in equilibrium and the filter is in the inertial range, this dissipation term is equivalent to the total dissipation. This paved the way for the application of LES technology. Deardorff (1970) and later Schumann (1975) modeled the flow near a wall successfully with LES. Rogallo and Moin (1984) wrote a good review summarizing the basic ideas and achievements in the field before the beginning of the cheap computing resource era. Their paper is a landmark work for the development of the LES technology. After that, Germano et al. (1991) proposed the dynamic procedure based on the assumption of scale similarity at different

levels. Later on, Lilly (1992), Ghosal et al. (1995) and Meneveau et al. (1996) made significant improvements on the averaging used in the dynamic procedure. Now, the LES technology has grown into maturity, and has been widely applied to different types of flow simulations.

Along with the mainstream of LES technology development are some turbulence model development and sub-models for reactive flows. To name a few, Bardina et al. (1980) proposed the similarity model based on the scale similarity and Zang et al. (1993) applied a dynamic procedure to the mixed model. A comparative study of LES using different subgrid models is performed by Vreman et al. (1997). It was found that the eddy viscosity term models distant interactions, that is, among scales below filter-size and much larger than filter-size, whereas the similarity term models the local interactions, that is, among the scales below filter-size and marginally larger than filter-size. So they behave differently for low Re and high Re flows (Meneveau et al. 2000). Erlebacher et al. (1992) extended the LES methodology to the case of compressible turbulent flows. Moin et al. (1991) proposed the dynamic procedure for parameters used in reactive flow simulations. Cook and Riley (1994) extended the mixture fraction-based theory and the subgrid-scale PDF theory to modeling the reaction at the subgrid scale. Their assumed PDF model for turbulent reaction is combined with a dynamic procedure by Pierce and Moin (1998). Their pioneering work laid the foundations of the formulation used in the present work.

The equations discussed in the previous section are directly solved in a DNS treatment, but in a LES approach these equations are filtered in order to reduce the range of scales to be solved. After filtering, the resulting equations for the large-scale component of the

flow contain terms representing the effect of the unresolved small scales. These subgrid-scale (SGS) effects must be modeled.

Here a spatial low-pass filter is applied to the DNS equations and the fundamental LES decomposition is introduced as:

$$q = \overline{q} + q' \text{ =LES grid resolved component + subgrid scale component} \tag{12}$$

where $\overline{q}(\vec{x},t) = \iiint_{\Omega} G_{\Delta}(\vec{x}-\vec{\zeta})q(\vec{\zeta},t)d\vec{\zeta}$ is the volume integral of q convoluted with the LES filter G_{Δ}. By construction, the filter G_{Δ} satisfies $\iiint_{\Omega} G_{\Delta}(\vec{x}-\vec{\zeta})d\vec{\zeta} = 1$. Δ is called the filter width, which is usually related to the fact that G_{Δ} is of compact support and takes non-zero values in a finite sub-domain of Ω.

In the following, a top-hat filter is adopted because it is consistent with the choice of a rectangular Cartesian grid.

$$G_{\Delta} = G_{\Delta,1}(x_1)\cdot G_{\Delta,2}(x_2)\cdot G_{\Delta,3}(x_3), \text{ where } G_{\Delta,i}(x) = \begin{cases} 1/\Delta, & -\Delta/2 \le x \le \Delta/2 \\ 0, & x \le -\Delta/2 \text{ or } x \ge \Delta/2 \end{cases} \tag{13}$$

We then have

$$\overline{q}(x_1,x_2,x_3,t) = \int_{x_1-\Delta/2}^{x_1+\Delta/2}\int_{x_2-\Delta/2}^{x_2+\Delta/2}\int_{x_3-\Delta/2}^{x_3+\Delta/2} q(\zeta_1,\zeta_2,\zeta_3,t)d\zeta_1 d\zeta_2 d\zeta_3 \tag{14}$$

The filter function has the property that the amplitudes of the high-frequency spatial Fourier components of any flow variable are substantially reduced. Thus the filtered variables represent the large-scale dynamics. If the size Δ of the LES filter is uniform and constant, the filtering operator commutes with the differentiation operator:

$$\overline{\left(\frac{\partial q}{\partial t}\right)} = \frac{\partial \overline{q}}{\partial t}; \quad \overline{\left(\frac{\partial q}{\partial x_i}\right)} = \frac{\partial \overline{q}}{\partial x_i} \tag{16}$$

Note that, multiple filtering operations are not in general equivalent to a single filter operation: $\bar{\bar{q}} \neq \bar{q}$.

All the filtering is performed at the grid level. A thorough discussion on the commutation properties for LES is provided by Vasilyev et al. (1998). It is found that non-uniform grids will introduce commutative errors. These commutative errors are different from the discretization errors that characterize how grid resolution will be degraded by non-uniform stretching. So for the most part of this work, uniform grids are used in the area of main flow activity, whereas the use of grid stretching is limited to near the computational domain boundaries. The stretched grids also introduce numerical damping that may help in stabilizing the numerical boundary scheme.

For a variable density flow, the Favre-averaged filtering operation is adopted (Favre 1965). Favre averaging simplifies (reduces the number of new terms) the filtered compressible equations significantly.

$$\tilde{q} = \frac{\overline{\rho q}}{\bar{\rho}} = \frac{\iiint_{\Omega} G_{\Delta}(\vec{x}-\vec{\zeta})\rho(\vec{\zeta},t)q(\vec{\zeta},t)d\vec{\zeta}}{\iiint_{\Omega} G_{\Delta}(\vec{x}-\vec{\zeta})\rho(\vec{\zeta},t)d\vec{\zeta}} \tag{17}$$

The filtered ideal gas law becomes

$$\boxed{\bar{p} = \bar{\rho}\left(\frac{R}{M}\right)\tilde{T}} \tag{18}$$

Where M is assumed constant.

The filtered continuity equation is

$$\boxed{\frac{\partial \overline{\rho}}{\partial t}+\frac{\partial \overline{\rho}\widetilde{u}_j}{\partial x_j}=0} \tag{19}$$

Applying the LES filter to the conservation of species mass, we have:

$$\frac{\partial \overline{\rho}\widetilde{Y}_k}{\partial t}+\frac{\partial \overline{\rho Y_k u_j}}{\partial x_i}=\frac{\partial \overline{\rho Y_k V_{k,i}}}{\partial x_i}+\overline{\dot{\omega}}_k \tag{20}$$

Furthermore, we write: $\overline{\rho Y_k u_j}=\overline{\rho}\widetilde{Y}_k\widetilde{u}_j+(\overline{\rho Y_k u_j}-\overline{\rho}\widetilde{Y}_k\widetilde{u}_j)$, where the first term is the LES grid-resolved convective flux of species mass and the second term the subgrid scale (SGS) convective flux. We then adopt the approximation $\overline{\rho D_k\frac{\partial Y_k}{\partial x_j}}\approx\overline{\rho}\widetilde{D}_k\frac{\partial \widetilde{Y}_k}{\partial x_j}$, where $\widetilde{D}_k=D_k(\widetilde{T},\overline{\rho})=\frac{\mu(\widetilde{T})}{\overline{\rho}Sc_k}$. Finally, the filtered species equation is

$$\boxed{\frac{\partial \overline{\rho}\widetilde{Y}_k}{\partial t}+\frac{\partial \overline{\rho}\widetilde{Y}_k\widetilde{u}_j}{\partial x_j}=-\frac{\partial \lambda_{k,i}}{\partial x_j}+\frac{\partial}{\partial x_j}\left(\overline{\rho}\widetilde{D}_k\frac{\partial \widetilde{Y}_k}{\partial x_j}\right)+\overline{\dot{\omega}}_k} \tag{21}$$

where $\lambda_{k,j}=\overline{\rho Y_k u_j}-\overline{\rho}\widetilde{Y}_k\widetilde{u}_j$. In equation (21), closure models are needed for $\lambda_{k,j}$ and $\overline{\dot{\omega}}_k$.

Applying Favre averaging to the momentum equations, we get:

$$\frac{\partial \overline{\rho}\widetilde{u}_i}{\partial t}+\frac{\partial \overline{\rho u_i u_j}}{\partial x_j}+\frac{\partial \overline{p}}{\partial x_i}=\overline{\rho}g_i+\frac{\partial \overline{\tau}_{ij}}{\partial x_j} \tag{22}$$

We also use the decomposition $\overline{\rho u_i u_j}=\overline{\rho}\widetilde{u}_i\widetilde{u}_j+(\overline{\rho u_i u_j}-\overline{\rho}\widetilde{u}_i\widetilde{u}_j)$, where the first term is the LES grid-resolved convective flux of x_i-momentum and the second term the corresponding SGS contribution. The filtered viscous stress tensor is modeled as:

$\overline{\tau}_{ij}=\overline{\mu}\left[\frac{\partial \widetilde{u}_i}{\partial x_j}+\frac{\partial \widetilde{u}_j}{\partial x_i}-\frac{2}{3}\frac{\partial \widetilde{u}_k}{\partial x_k}\delta_{ij}\right]$, where $\overline{\mu}=\mu(\widetilde{T})=\mu_0\left(\frac{\widetilde{T}}{T_0}\right)^b$, b=0.76.

With these choices, we have the following momentum equations.

$$\boxed{\frac{\partial \overline{\rho}\widetilde{u}_i}{\partial t}+\frac{\partial \overline{\rho}\widetilde{u}_i\widetilde{u}_j}{\partial x_i}+\frac{\partial \overline{p}}{\partial x_i}=-\frac{\partial T_{ij}}{\partial x_i}+\overline{\rho}g_i+\frac{\partial \overline{\tau}_{ij}}{\partial x_j}} \tag{23}$$

where $T_{ij}=\overline{\rho u_i u_j}-\overline{\rho}\widetilde{u}_i\widetilde{u}_j$. In equation (23), a closure model for T_{ij} is needed.

We choose to describe energy variations using the following filtered variable $\widetilde{e}=c_v\widetilde{T}$.

$$\frac{\partial \overline{\rho}\widetilde{e}}{\partial t}+\frac{\partial \overline{\rho e u_j}}{\partial x_j}=-\overline{p\frac{\partial u_j}{\partial x_j}}+\overline{\tau_{ij}\frac{\partial u_i}{\partial x_j}}+\frac{\partial}{\partial x_j}\left(\overline{\lambda\frac{\partial T}{\partial x_i}}\right)+\overline{\dot{q}}$$

Where $\overline{\dot{q}}=-\sum_{k=1}^{N}h_k^0\overline{\dot{\omega}}_k$ is the LES-filtered heat release rate per unit volume. We use here again the standard LES decomposition: $\overline{\rho e u_j}=\overline{\rho}\widetilde{e}\widetilde{u}_j+(\overline{\rho e u_j}-\overline{\rho}\widetilde{e}\widetilde{u}_j)$, where the first term is the LES grid-resolved convective flux of internal energy and the second term the corresponding SGS contribution.

For the pressure dilatation term, using the equation of state we have:

$$\begin{aligned}
\overline{p\frac{\partial u_i}{\partial x_i}} &= \frac{\partial}{\partial x_i}\left(\overline{pu_i}\right)-\overline{u_i\frac{\partial p}{\partial x_i}} \\
&= \frac{\partial}{\partial x_i}\left(\overline{\rho\frac{R}{M}Tu_i}\right)-\overline{u_i\frac{\partial p}{\partial x_i}} \\
&= \frac{R}{M}\frac{\partial}{\partial x_i}\left(\overline{\rho}\widetilde{T}\widetilde{u}_i\right)+\frac{R}{M}\frac{\partial}{\partial x_i}\left(\overline{\rho Tu_i}-\overline{\rho}\widetilde{T}\widetilde{u}_i\right)-\overline{u_i\frac{\partial p}{\partial x_i}} \qquad ; \\
&= \frac{\partial}{\partial x_i}\left(\overline{p}\widetilde{u}_i\right)+\frac{R}{M}\frac{\partial}{\partial x_i}\left(\overline{\rho Tu_i}-\overline{\rho}\widetilde{T}\widetilde{u}_i\right)-\overline{u_i\frac{\partial p}{\partial x_i}} \\
&\cong \overline{p}\frac{\partial \widetilde{u}_i}{\partial x_i}+\left(c_p-c_v\right)\frac{\partial}{\partial x_i}\left(\overline{\rho Tu_i}-\overline{\rho}\widetilde{T}\widetilde{u}_i\right)+\left[\widetilde{u}_i\frac{\partial \overline{p}}{\partial x_i}-\overline{u_i\frac{\partial p}{\partial x_i}}\right]
\end{aligned}$$

The contribution in the square bracket is neglected. It is argued that the fluctuation Mach number for the small scales is small and therefore this term may be neglected. Using low Reynolds number DNS data of isotropic turbulence at several Mach numbers, this

neglected term was found to be at most 5% of the heat flux (Moin et al. 1991). Similar approximations were made for the other terms where their small-scale components were neglected. For example, we approximate $\overline{\lambda \frac{\partial T}{\partial x_i}} \cong \overline{\lambda} \frac{\partial \widetilde{T}}{\partial x_i}$ where $\overline{\lambda} = \lambda(\widetilde{T}) = \frac{\mu(\widetilde{T}) c_p}{\Pr}$;

and $\overline{\tau_{ij} \frac{\partial u_i}{\partial x_j}} \cong \overline{\tau}_{ij} \frac{\partial \widetilde{u}_i}{\partial x_j} - \overline{\rho} \widetilde{\varepsilon}_{SGS} \cong \overline{\tau}_{ij} \frac{\partial \widetilde{u}_i}{\partial x_j} - T_{ij} \frac{\partial \widetilde{u}_i}{\partial x_j}$

where $\widetilde{\varepsilon}_{SGS}$ is the SGS dissipation rate of kinetic energy and is assumed to be balanced by the production term for SGS turbulent kinetic energy.

Finally, we have the following equation for the LES grid-resolved temperature.

$$\frac{\partial \overline{\rho} c_v \widetilde{T}}{\partial t} + \frac{\partial \overline{\rho} c_v \widetilde{T} \widetilde{u}_j}{\partial x_j} = -\overline{p} \frac{\partial \widetilde{u}_i}{\partial x_i} - \gamma \frac{\partial Q_j}{\partial x_j} + \overline{\tau}_{ij} \frac{\partial \widetilde{u}_i}{\partial x_j} - T_{ij} \frac{\partial \widetilde{u}_i}{\partial x_j} + \frac{\partial}{\partial x_i} \left(\overline{\lambda} \frac{\partial \widetilde{T}}{\partial x_i} \right) + \overline{\dot{q}} . \qquad (24)$$

where $Q_j = \left(\overline{\rho T u_j c_v} - \overline{\rho} \widetilde{T} \widetilde{u}_j c_v \right)$. In equation (24), closure models are needed for Q_j and $\overline{\dot{q}}$.

The equations (18)(19)(21)(23)(24) form the filtered equations for a LES description of a chemically reacting flow. To close the system, several models are needed to account for unresolved subgrid scale effects.

2.4. SGS sub-models

2.4.1. Classical Smagorinsky model

In large-eddy simulations the effect of the large scales is directly computed, and only the small subgrid scales are modeled. Since small scales tend to be more isotropic than the large ones, it should be possible to parameterize them using simpler and more universal models than standard Reynolds stress models. Most subgrid scale stress models are based

on the eddy-viscosity assumption. The Smagorinsky model for eddy-viscosity is combined with the Yoshizawa model for SGS turbulent kinetic energy. The later is important in compressible flow simulations, particularly in combustion modeling formulations. The subgrid terms in species mass and energy equations are also adopting the gradient-transport models, whose role will rely to some extent on the correct choice/determination of the eddy-viscosity.

The SGS stress T_{ij} can be decomposed into anisotropic and isotropic tensors, which are modeled separately.

$$T_{ij} = (T_{ij} - T_{kk}\frac{\delta_{ij}}{3}) + T_{kk}\frac{\delta_{ij}}{3} = \text{anisotropic tensor } T_{ij}^{a} + \text{isotropic tensor } T_{ij}^{i}$$

The anisotropic part is modeled based on the concept of a turbulent viscosity:

$$T_{ij}^{a} = -2\overline{\rho}\nu_t \widetilde{S}_{ij}^{a} \tag{25}$$

Where $\widetilde{S}_{ij} = \frac{1}{2}\left(\frac{\partial \widetilde{u}_i}{\partial x_j} + \frac{\partial \widetilde{u}_j}{\partial u_i}\right)$, $\widetilde{S}_{ij}^{a} = \widetilde{S}_{ij} - \frac{\delta_{ij}}{3}\widetilde{S}_{kk}$, $\widetilde{S}_{kk}$ is the dilatation of the LES resolved velocity field.

In the following, the classical Smagorinsky model is adopted:

$$\nu_t = (C_S\Delta)^2\left|\widetilde{S}\right|, \tag{26}$$

Where $\left|\widetilde{S}\right| = \sqrt{2\widetilde{S}_{ij}\widetilde{S}_{ij}}$ and C_S is a model coefficient (C_S is a constant, or is dynamically computed from the LES solution, see below). So for the anisotropic part,

$$T_{ij}^{a} = -2\overline{\rho}(C_S\Delta)^2\left|\widetilde{S}\right|\widetilde{S}_{ij}^{a}$$

The isotropic part of the SGS stress tensor is modeled based on the Yoshizawa model (Yoshizawa, 1986). Following the argument that $k_{SGS} = (C_I\Delta)^2\left|\widetilde{S}\right|^2$, we have

$$T_{kk} = 2\overline{\rho}\left(C_I\Delta\right)^2\left|\widetilde{S}\right|^2. \tag{27}$$

where C_I is a model coefficient (see below). Erlebacher et al. (1992) neglected this term on the grounds that it is negligible compared to the thermodynamic pressure. In contrast, in Moin et al. (1992), this term is preserved for reactive flow simulations.

So the full SGS stress tensor is then modeled as:

$$T_{ij} = -2\overline{\rho}\left(C_S\Delta\right)^2\left|\widetilde{S}\right|\widetilde{S}_{ij}^{\,a} + \frac{\delta_{ij}}{3}2\overline{\rho}\left(C_I\Delta\right)^2\left|\widetilde{S}\right|^2 \tag{28}$$

For SGS mass species transport, a gradient-transport modeling assumption is also used.

$$\lambda_{kj} = -\overline{\rho}\frac{\nu_t}{Sc_t}\frac{\partial\widetilde{Y}_k}{\partial x_j} \tag{29}$$

where Sc_t is the turbulent Schmidt number and ν_t is the Smagorinsky viscosity (equation (26)).

Similarly, the SGS heat transport is expressed as:

$$Q_j = -\overline{\rho}\frac{\nu_t}{\mathrm{Pr}_t}\frac{\partial\widetilde{e}}{\partial x_j} = -\overline{\rho}c_v\frac{\nu_t}{\mathrm{Pr}_t}\frac{\partial\widetilde{T}}{\partial x_j} \tag{30}$$

where Pr_t is the turbulent Prandtl number.

In analogy to the description of molecular transport, where $\lambda = \frac{\mu c_p}{\mathrm{Pr}}$, $D_k = \frac{\mu}{\rho Sc_k}$, we have similar relations between the turbulent transport coefficients $\lambda_t = \frac{\mu_t c_p}{\mathrm{Pr}_t}$, $D_{kt} = \frac{\mu_t}{\rho Sc_t}$. At this point, the LES formulation for turbulent inert flows is almost complete. Four model coefficients have been introduced (C_S, C_I, Pr_t, Sc_t) and remain to be specified. We turn to this question in the next section.

2.4.2. The dynamic model

The Smagorinsky model always assumes a positive eddy viscosity, even in laminar flows. Although this property makes this model not suitable for transitional flows, its dissipative character helps stabilize numerical solutions. As pointed out by Moin et al. (1992), the limitations of the Smagorinsky model are the following:

1. The optimal model constant must be changed in different flows;
2. The model does not have the correct limiting behavior near walls;
3. The model does not vanish in laminar flows, and it has been shown to be too dissipative in laminar/turbulent transition regions;
4. The model does not account for backscatter of energy from small scales to large scales, which has been shown to be of importance in transition regions;
5. Compressibility effects are not included in the model.

The key element that has been lacking in most SGS modeling efforts prior to the introduction of the dynamic model has been the effective utilization of the large-scale field, which is computed directly.

To overcome some of the limitations of the Smagorinsky model, Germano et al. (1991) introduced a dynamic procedure, based on the application of the Smagorinsky model at two different filter levels, this procedure allows to calculate the Smagorinsky coefficient. The coefficient can be negative in some regions and thus does not totally exclude backscatter; it provides for the proper asymptotic behavior of the stresses near the wall without ad hoc damping functions; and it vanishes in laminar flows without ad hoc intermittency functions.

2.4.2.1. Application of the dynamic model to the calculation of C_S

We start from the expression of the SGS stress at the grid filter level $\overline{\Delta}$

$$T_{ij}^{M} = -2\overline{\rho}(C_S\overline{\Delta})^2\sqrt{2\widetilde{S}_{ij}\widetilde{S}_{ij}}\widetilde{S}_{ij}^{a} + \frac{2\delta_{ij}}{3}\overline{\rho}\left(C_I\overline{\Delta}\right)^2\left(2\widetilde{S}_{ij}\widetilde{S}_{ij}\right) \tag{32}$$

The key element of the dynamic model concept is the utilization of the spectral data contained in the resolved field. This information is brought to bear by introducing a test filter, defined with a filter width $\hat{\overline{\Delta}}$ larger than the resolved grid filter, which generates a second field with scales larger than the resolved field. A point to be made about this second filtering is that it is realized through explicit filtering, while the first filtering is done implicitly at the grid level.

The SGS stress at the test filter level $\hat{\overline{\Delta}}$ (also noted $\hat{\hat{\Delta}}$ if more than 2 variables are present under the hat) is defined as:

$$t_{ij} = \widehat{\overline{\rho u_i u_j}} - \frac{\widehat{\overline{\rho u_i}}\,\widehat{\overline{\rho u_j}}}{\hat{\overline{\rho}}} \tag{33}$$

and is modeled as

$$t_{ij}^{M} = -2\hat{\overline{\rho}}(C_S\hat{\overline{\Delta}})^2\sqrt{2\hat{\widetilde{S}}_{ij}\hat{\widetilde{S}}_{ij}}\hat{\widetilde{S}}_{ij}^{a} + \frac{2\delta_{ij}}{3}\hat{\overline{\rho}}\left(C_I\hat{\overline{\Delta}}\right)^2\left(2\hat{\widetilde{S}}_{ij}\hat{\widetilde{S}}_{ij}\right) \tag{34}$$

Where $\hat{\widetilde{S}}_{ij} = \frac{1}{2}\left(\frac{\partial}{\partial x_j}\left(\frac{\widehat{\overline{\rho u_i}}}{\hat{\overline{\rho}}}\right) + \frac{\partial}{\partial x_i}\left(\frac{\widehat{\overline{\rho u_j}}}{\hat{\overline{\rho}}}\right)\right)$, $\hat{\widetilde{S}}_{ij}^{a} = \hat{\widetilde{S}}_{ij} - \frac{\delta_{ij}}{3}\hat{\widetilde{S}}_{kk}$

Applying Germano's identity, we have

$$L_{ij} = t_{ij} - \hat{T}_{ij} = \left(\frac{\overbrace{\rho u_i \rho u_j}}{\overline{\rho}} \right) - \frac{\overbrace{\hat{\rho u}_i \hat{\rho u}_j}}{\hat{\overline{\rho}}} \tag{35}$$

where L_{ij} is known as the Leonard stress tensor.

The right hand side may be obtained from the filtered variables. In other words, L_{ij} is known and this may be used to provide valuable expressions of C_S or C_I.

For instance, the anisotropic part of the Leonard stress tensor L_{ij} is

$$L_{ij}^a = t_{ij}^a - \hat{T}_{ij}^a = 2(C_S\overline{\Delta})^2 \overbrace{\overline{\rho}\sqrt{2\widetilde{S}_{ij}\widetilde{S}_{ij}}\widetilde{S}_{ij}^a} - 2(C_S\hat{\overline{\Delta}})^2 \hat{\overline{\rho}}\sqrt{2\hat{\widetilde{S}}_{ij}\hat{\widetilde{S}}_{ij}}\hat{\widetilde{S}}_{ij}^a = C_S^2 M_{ij}^a, \tag{36}$$

where

$$M_{ij}^a = \left[\overbrace{\overline{\rho}\sqrt{2\widetilde{S}_{ij}\widetilde{S}_{ij}}\widetilde{S}_{ij}^a} - 2\left(\frac{\hat{\overline{\Delta}}}{\overline{\Delta}}\right)^2 \hat{\overline{\rho}}\sqrt{2\hat{\widetilde{S}}_{ij}\hat{\widetilde{S}}_{ij}}\hat{\widetilde{S}}_{ij}^a \right] \overline{\Delta}^2 \tag{37}$$

Equation (36) corresponds to 5 independent relations for C_S (L_{ij}^a is symmetric and trace-free). The ratio of test filter size to grid filter size is proposed as $\kappa = \frac{\hat{\overline{\Delta}}}{\overline{\Delta}} = 2$ by Germano et al. (1989), and $\kappa = \sqrt{5}$ by Vreman et al. (1997). Germano et al. (1989) found the computed turbulence statistics to be insensitive to this ratio. With 5 relations, C_S is over-specified, a least-squares approach is followed to calculate the model coefficients (Lilly, 1992),

$$C_S{}^2 = \frac{\left\langle L_{ij}^a M_{ij}^a \right\rangle}{\left\langle M_{ij}^a M_{ij}^a \right\rangle} \tag{38}$$

Note that in order to prevent numerical instability caused by negative values of C_S^2, the numerator and denominator are averaged over homogeneous flow directions, as expressed by the symbol <>. In the absence of a homogeneous flow direction, some form of local averaging may be used. Furthermore, the model coefficient is artificially set to zero at locations where the right-hand side of equation (38) still has negative values to prevent any unrealistic backscatter. One assumption in the formulation above is that variations of C_S on the scale of the test filter are small.

A note should be made on the local averaging of the model coefficients. The original choice by Germano et al. (1989) is to average in the homogeneous directions, while Meneveau et al. (1996) proposed an averaging method based on the fluid imaginary particle trajectory, *i.e.*, in a Lagrangian way. The later is suitable for complex geometries. Here both jet and plume configurations are spatially evolving flows, there is one homogeneous direction for plane configurations, and no homogeneous direction in round configurations. In the absence of a homogeneous direction, as an alternative to the Lagrangian model, we use have a simple local averaging in order to stabilize the calculation of C_S.

2.4.2.2. Application of the dynamic model to the calculation of C_I

The dynamic model has been extended to compressible flow problems by Moin et al. (1991). The isotropic part of the Leonard stress tensor is

$$L_{kk}^i = t_{kk}^i - \hat{T}_{kk}^i = -2(C_I\overline{\Delta})^2 \overline{\rho}\overbrace{\left(2\widetilde{S}_{ij}\widetilde{S}_{ij}\right)} + 2(C_I\hat{\overline{\Delta}})^2 \hat{\overline{\rho}}\left(2\hat{\widetilde{S}}_{ij}\hat{\widetilde{S}}_{ij}\right) = C_I^2 M_{kk}^i \tag{39}$$

$$M_{kk}^{i} = \left[-\overbrace{\overline{\rho}\left(2\widetilde{S}_{ij}\widetilde{S}_{ij}\right)}^{\widehat{\quad}} + 2\left(\frac{\hat{\Delta}}{\overline{\Delta}}\right)^{2} \hat{\overline{\rho}}\left(2\hat{\widetilde{S}}_{ij}\hat{\widetilde{S}}_{ij}\right) \right] \overline{\Delta}^{2} \tag{40}$$

Equation (39) corresponds to one relation for C_I. We get

$$C_I{}^2 = \frac{\left\langle L_{kk}^{i} \right\rangle}{\left\langle M_{kk}^{i} \right\rangle} \tag{41}$$

2.4.2.3. Application of the dynamic model to the calculation of Sc_t

The dynamic strategy may be easily extended to a calculation of Pr_t and Sc_t. We start from the SGS species *k* mass flux at the grid filter level:

$$\lambda_{ki} = \overline{\rho u_i Y_k} - \overline{\rho}\widetilde{u}_i\widetilde{Y}_k = \overline{\rho u_i Y_k} - \frac{\overline{\rho u_i}\,\overline{\rho Y_k}}{\overline{\rho}} \tag{42}$$

This flux is modeled as:

$$\left(\lambda_{ki}\right)^{M} = -\overline{\rho}\frac{\nu_t}{Sc_t}\frac{\partial \widetilde{Y}_k}{\partial x_i} = -\overline{\rho}\frac{\left(C_S\Delta\right)^2\sqrt{2\widetilde{S}_{ij}\widetilde{S}_{ij}}}{Sc_t}\frac{\partial \widetilde{Y}_k}{\partial x_i} \tag{43}$$

Similar expressions are also assumed at the test filter level.

$$\Lambda_{ki} = \overbrace{\overline{\rho u_i Y_k}}^{\widehat{\quad}} - \frac{\overbrace{\overline{\rho u_i}}^{\widehat{\quad}}\,\overbrace{\overline{\rho Y_k}}^{\widehat{\quad}}}{\hat{\overline{\rho}}} \tag{44}$$

This species mass flux is modeled as

$$\left(\Lambda_{ki}\right)^{M} = -\hat{\overline{\rho}}\frac{\left(C_S\hat{\Delta}\right)^2\sqrt{2\hat{\widetilde{S}}_{ij}\hat{\widetilde{S}}_{ij}}}{Sc_t}\frac{\partial \hat{\widetilde{Y}}_k}{\partial x_i} \tag{45}$$

Applying Germano's identity, we have

$$\Lambda_{ki} - \hat{\lambda}_{ki} = \overbrace{\left(\frac{\overline{\rho u_i}\,\overline{\rho Y_k}}{\overline{\rho}} \right)} - \frac{\overbrace{\overline{\rho u_i}}\,\overbrace{\overline{\rho Y_k}}}{\hat{\overline{\rho}}} \tag{46}$$

The RHS is obtained from the LES solution, while the left hand side is expressed as:

$$L_{ki}^{Y_k} = \Lambda_{ki}^{M} - \hat{\lambda}_{ki}^{M} = \frac{C_S^2}{Sc_t}\overline{\Delta}^2 \left[\left(\overbrace{\overline{\rho}\sqrt{2\widetilde{S}_{ij}\widetilde{S}_{ij}}\,\frac{\partial \widetilde{Y}_k}{\partial x_i}} \right) - \left(\frac{\hat{\overline{\Delta}}}{\hat{\overline{\Delta}}} \right)^2 \left(\hat{\overline{\rho}}\sqrt{2\hat{\widetilde{S}}_{ij}\hat{\widetilde{S}}_{ij}}\,\frac{\partial \hat{\widetilde{Y}}_k}{\partial x_i} \right) \right] = \frac{C_S^2}{Sc_t} M_{ki}^{Y_k} \tag{47}$$

where

$$M_{ki}^{Y_k} = \overline{\Delta}^2 \left[\left(\overbrace{\overline{\rho}\sqrt{2\widetilde{S}_{ij}\widetilde{S}_{ij}}\,\frac{\partial \widetilde{Y}_k}{\partial x_i}} \right) - \left(\frac{\hat{\overline{\Delta}}}{\hat{\overline{\Delta}}} \right)^2 \left(\hat{\overline{\rho}}\sqrt{2\hat{\widetilde{S}}_{ij}\hat{\widetilde{S}}_{ij}}\,\frac{\partial \hat{\widetilde{Y}}_k}{\partial x_i} \right) \right] \tag{48}$$

Equation (47) corresponds to 3 independent relations (for each species *k*).

The Schmidt number is finally computed from a least-square expression:

$$Sc_t = \frac{C_S^2 \sum_{i=1}^{3} M_{ki}^{Y_k} M_{ki}^{Y_k}}{\sum_{i=1}^{3} L_{ki}^{Y_k} M_{ki}^{Y_k}} \tag{49}$$

2.4.2.4. Application of the dynamic model to the calculation of Pr_t

The calculation of the turbulent Prandtl number follows a similar approach. We start from the SGS heat flux at the grid filter level.

Here the subgrid heat flux at grid level is defined as

$$Q_i = \overline{\rho c_v u_i T} - \overline{\rho} c_v \widetilde{u}_i \widetilde{T} = c_v \left(\overline{\rho u_i T} - \frac{\overline{\rho u_i}\,\overline{\rho T}}{\overline{\rho}} \right) \tag{50}$$

This flux is modeled as

$$Q_i^{\ M} = -c_v \overline{\rho} \frac{\nu_t}{\mathrm{Pr}_t} \frac{\partial \widetilde{T}}{\partial x_i} = -c_v \overline{\rho} \frac{\left(C_S \Delta\right)^2 \sqrt{2\widetilde{S}_{ij}\widetilde{S}_{ij}}}{Sc_t} \frac{\partial \widetilde{T}}{\partial x_i} \tag{51}$$

At the test filter level, the SGS heat flux is defined as

$$q_i = c_v \left(\overbrace{\overline{\rho u_i Y_k}} - \frac{\overbrace{\overline{\rho u_i}}\,\overbrace{\overline{\rho Y_k}}}{\hat{\overline{\rho}}} \right) \tag{52}$$

Applying the gradient transport model, the modeled heat flux is computed as

$$q_i^M = -c_v \hat{\overline{\rho}} \frac{\left(C_S \hat{\overline{\Delta}}\right)^2 \sqrt{2\hat{\widetilde{S}}_{ij}\hat{\widetilde{S}}_{ij}}}{Sc_t} \frac{\partial \hat{\widetilde{T}}}{\partial x_i} \tag{53}$$

Applying Germano's identity, we have

$$q_i - \hat{Q}_i = c_v \left[\frac{\overbrace{\overline{\rho u_i \rho T}}}{\overline{\rho}} - \frac{\overbrace{\overline{\rho u_i}}\,\overbrace{\overline{\rho T}}}{\hat{\overline{\rho}}} \right] \tag{54}$$

The RHS is obtained for the LES solution. The LHS is expressed as

$$L_{ki}^T = q_i^M - \hat{Q}_i^M = c_v \frac{C_S^2}{\mathrm{Pr}_t} \overline{\Delta}^2 \overbrace{\overline{\rho} \sqrt{2\widetilde{S}_{ij}\widetilde{S}_{ij}} \frac{\partial \widetilde{T}}{\partial x_i}} - \left(\frac{\hat{\overline{\Delta}}}{\overline{\overline{\Delta}}} \right)^2 \left(\hat{\overline{\rho}} \sqrt{2\hat{\widetilde{S}}_{ij}\hat{\widetilde{S}}_{ij}} \frac{\partial \hat{\widetilde{T}}}{\partial x_i} \right) = \frac{C_S^2}{\mathrm{Pr}_t} M_i^T \tag{55}$$

Where

$$M_i^T = c_v \overline{\Delta}^2 \overbrace{\left(\overline{\rho} \sqrt{2\widetilde{S}_{ij}\widetilde{S}_{ij}} \frac{\partial \widetilde{T}}{\partial x_i} \right)} - \left(\frac{\hat{\overline{\Delta}}}{\overline{\overline{\Delta}}} \right)^2 \left(\hat{\overline{\rho}} \sqrt{2\hat{\widetilde{S}}_{ij}\hat{\widetilde{S}}_{ij}} \frac{\partial \hat{\widetilde{T}}}{\partial x_i} \right) \tag{56}$$

Equation (55) corresponds to 3 independent relations. The Prandtl number is finally computed from a least-square expression,

$$\mathrm{Pr}_t = \frac{C_S^2 \sum_{i=1}^{3} M_i^T M_i^T}{\sum_{i=1}^{3} L_{ki}^T M_i^T} \tag{57}$$

2.4.3 A subgrid-scale model for turbulent mixing

We present here a simple SGS model proposed to describe unresolved fluctuations in mixture composition. In the majority of fire configurations, the combustion correspond to diffusive burning and is limited by the rate of mixing between fuel and air. In this situation, a turbulent mixing model is all that is required to describe the rate of combustion ($\dot{\omega}_k$ and $\dot{q}$ in the LES equations). We limit our discussion here to the turbulent mixing SGS model.

Assuming that the information is available on the first two statistical moments of the scalar field, it is possible to start to reconstruct a description of the instantaneous scalar distribution at any point in the flow by generating a quantitative prediction of the scalar probability density function (pdf). Use of the pdf is common practice in turbulent combustion problems where thermochemical properties (and reaction rates) are strong non-linear functions of the instantaneous gas state (e.g. fuel/air ratio or mixture fraction). With information on the mean and the variance (standard deviation), the easiest route would be to use these to generate a normal (Gaussian) distribution at any point in the flow. This is unwise for two reasons. Firstly the Gaussian pdf is unbounded, whereas the scalars in question are bounded to lie between maximum and minimum values determined by the experimental boundary conditions. Secondly, because the scalars are bounded, skewed, non-normal distributions are to be expected when the mean value lies

close to one of its bounds (e.g. at the edges of a plume). To overcome these defects, an alternative assumed shape for the pdf has acquired popularity in combustion modeling, namely the β-function pdf. This shape is therefore adopted here for use in combustion problems, it is defined as.

$$\widetilde{p}(Z) = \frac{Z^{\alpha-1}(1-Z)^{\beta-1}}{\int_0^1 Z^{\alpha-1}(1-Z)^{\beta-1}dZ} \tag{58}$$

Where Z represents the local mixture fraction. The denominator is introduced as a normalizing factor, so that the integral of $\widetilde{p}(Z)$ over the allowable scalar range (0<Z<1) is identically unity. The β-function shape has two free parameters, which may be determined from the available information on the first two moment of Z, *i.e.*,

$$\widetilde{Z} = \int_0^1 Z \cdot \widetilde{p}(Z)dZ \tag{59}$$

$$\widetilde{Z}''^2 = \int_0^1 \left(Z - \widetilde{Z}\right)^2 \cdot \widetilde{p}(Z)dZ \tag{60}$$

These relations lead to the following conditions on the two parameters (α, β)

$$\alpha = \widetilde{Z}\left[\frac{\widetilde{Z}(1-\widetilde{Z})}{\widetilde{Z}''^2} - 1\right] \tag{61}$$

And

$$\beta = (1-\widetilde{Z})\left[\frac{\widetilde{Z}(1-\widetilde{Z})}{\widetilde{Z}''^2} - 1\right] \tag{62}$$

And hence, with knowledge of (α, β), the pdf may be generated.

The presumed pdf model allows intermediate species formation, dissociation effects and the coupling between turbulence and chemistry to be accounted for. Only mixture fraction is solved, other species are predicted based on state relationships.

In a large-eddy simulation (LES) framework, $\widetilde{Z}$ is the LES grid-resolved mixture fraction; $\widetilde{p}(Z)$ represents the subgrid-scale statistical variations of Z at a given location and time; and σ_Z is the standard deviation of these subgrid-scale fluctuations. σ_Z may be obtained from an algebraic model expression:

$$(\sigma_Z)^2 = C_Z \, \Delta^2 \left|\nabla \widetilde{Z}\right|^2 \tag{63}$$

C_Z is a model coefficient that may be expressed in terms of the Smagorinsky constant; and Δ is the LES filter size usually taken as the local grid size.

2.5. Numerical developments

While S3DLES builds up on the numerical framework previously developed for the DNS solver S3D, the larger domains and time scales found in LES applications require some adaptation in terms of boundary conditions and time integration. These adaptations are presented in this section.

2.5.1. Buffer-zone treatment for outflow boundaries

For both jet and plume simulations, the flow is injected into the computational domain across an inflow boundary with or without a coflow. The outflow boundaries are required to let spurious perturbations leave the domain smoothly while maintaining the ambient pressure. Here due to the nature of the compressible flow, a constant-pressure condition (Zhou et al. 2001) could not be specified. Nor did the 'traction-free' boundary condition

used by Boersma et al. (1999). Both schemes work for incompressible or weakly compressible flows. The essence of such boundary conditions is to maintain the ambient pressure while allowing the entrainment to happen without restrictions. In S3DLES, the non-reflecting boundary conditions of Poinsot and Lele (1992) are used. The form of these conditions is allowed to switch between non-reflecting inflow and outflow at each point on the computational domain boundary depending on the instantaneous local normal velocity.

It should be noted that these characteristic-based boundary conditions were derived based on linearized waves propagating normal to the boundary (LODI treatment, Local One-Dimensional Inviscid) and, thus, are not strictly non-reflecting in a multi-dimensional nonlinear flow. When the direction of wave propagation at the boundaries deviates from normal incidence, the amount of spurious reflection increases, the tilted part of the exiting waves will still be bounced back, possibly causing the jet profile to sway, and contaminating the flow structure (as shown in Figure 1a). In addition, in case of local flow reversal, the boundary condition treatment is known to have limited accuracy. To isolate the interior of the domain from the effects of the boundary conditions, several approaches can be followed in the boundary treatments for compressible flows (Colonius, 2004):

1. Grid stretching to keep the artificial boundaries as far away from the region of intense flow activity as possible.
2. Numerical dissipation, as provided by low-order numerical schemes, to damp the perturbations generated near the boundaries. This is a common practice for most

low-order scheme simulations. It is not adopted in S3DLES, which has a minimum spatial resolution of 6^{th} order.

3. Explicit filtering to damp high frequency oscillations. It is an optional choice in S3DLES, but the filtering operation must be fine-tuned in order to avoid the unwanted dissipation of turbulent motions.
4. Numerical dissipation as provided by an additional term in the governing equations. Stretching the grid is equivalent to a kind of artificial viscosity. No artificial viscosity is adopted here.
5. Applying absorbing buffer layers to minimize acoustic wave reflection at the boundary interfaces.

In this study, an absorbing buffer layer is used near the outflow boundaries (downstream and lateral boundaries) in order to damp out numerical errors and improve the non-reflecting performance of the outflow boundaries. This buffer zone is a numerical construct that consists of a stretched grid, where exponential damping terms are added to the governing equations, so that the disturbance are damped prior to exiting the computation domain. The stabilizing effect is significant at large Reynolds number flow conditions. An example of the stabilizing effect resulting from the application of a buffer layer treatment is presented in Figure 1b.

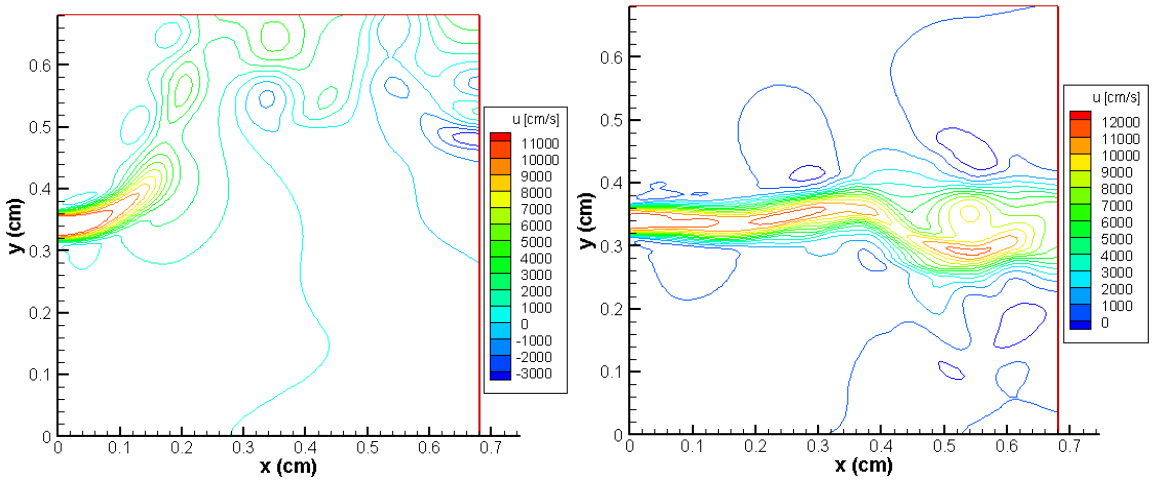

(a) (b)

Figure 1: LES simulation of a three-dimensional high-speed plane jet. Instantaneous iso-contours of u velocity at z=0 without (left) and with (right) a buffer zone.

An absorbing layer treatment typically provides for a damping effect on disturbances prior to interaction with boundary surfaces. Some obvious ways to do this are to introduce artificial dissipation (by up-winding), to increase the value of physical viscosity (or add hyper-viscosity), and perhaps most simply, to add relaxation terms to the governing equations. Provided the relaxation factor σ is large enough, then disturbances are exponentially damped during their residence in the layer. Whatever disturbances are reflected by the boundary are returned but similarly damped as they propagate back through the layer before reaching the domain as reflection errors.

$$\frac{\partial \overline{\rho}\widetilde{u}_i}{\partial t} + \frac{\partial \overline{\rho}\widetilde{u}_i\widetilde{u}_j}{\partial x_i} + \frac{\partial \overline{p}}{\partial x_i} = -\frac{\partial T_{ij}}{\partial x_i} + \overline{\rho} g_i + \frac{\partial \overline{\tau}_{ij}}{\partial x_j} - \sigma(x)(u_i - u_i^{\text{target}}) \tag{65}$$

where $$\sigma(x) = \sigma_m \left(\frac{x - x^*}{L_b} \right)^{\beta}$$

For the strong-jet simulations described in Chapter 3, we use $\beta = 2.0$ and $\sigma_m = 2.0$ on the sidewall boundaries, x^* is the lateral boundary, and L_b is the thickness of the buffer

layer. On the downstream boundary, $\beta = 2.0$ and σ_m is made a function of the cross-stream spatial coordinates. $\sigma_m(y)$ is specified as an inverted "top-hat" profile with smooth transitions. The minimum value of $\sigma_m(y)$, near the centerline, is 0.1 and the maximum value is 2.0. This choice provides for strong damping in the co-flow region and weaker damping in the jet region.

The absorbing layer treatment requires specifying u_{target}, *i.e.* the reference velocity profile at the outflow boundary. Choosing a target profile as the co-flow velocity is not a good choice as it will block the volume flux, and the jet will diverge at the buffer zone due to the conservation laws (Stanley et al. 2002). An experimental profile (empirical approximate expression) is a good choice, but its usage is limited, as the experimental conditions may be different from the current simulation (Stanley et al. 1999). Here the profile is calculated based on the spatially averaged stream-wise velocity profile in the buffer zone. The averaged profile is expected to keep the mass flux conserved (without disturbing the interior domain solution), and the jet can exit the domain in a non-reflecting way.

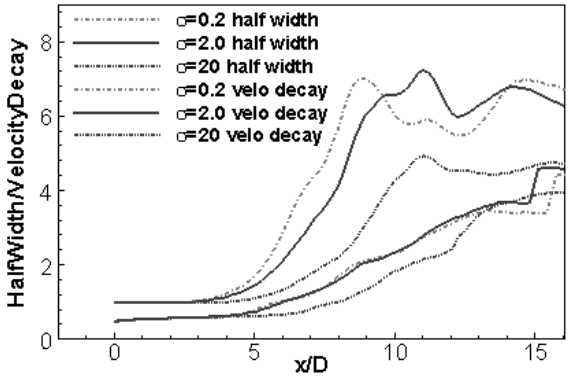

Figure 2: Effect of σ in buffer layer on the jet parameters.

Figure 2 shows the effect of different damping intensities on the jet parameters. Here the jet halfwidth is defined as the radial distance from the centerline to the position where the jet velocity is half of its centerline value. The velocity decay is represented by the quantity $\left((u_1 - u_0)/(u_c - u_0)\right)^2$. The numerator is constant, while the denominator is decreasing with the distance from the injector, so the velocity decay is expressed as a value larger than one. It is shown that the buffer layer will change the jet-spreading rate. Strong damping will maintain the jet initial profile for longer distances, while weak damping have less impact on the jet spreading. Choosing the right damping factor is a matter of balance between accuracy and stability. In chapter 3, $\sigma = 2.0$ is chosen, and the computational domain is made longer (instead of 16D used in Figure 1, the domain in Chapter 3 is 32D), so the impact is supposed to be less than those shown here.

Another parameter to be tested is the thickness of the buffer zone. It is better to have a large layer, which can exert the damping force on the jet gradually, but the effective simulation domain is shortened by using a larger buffer layer. And the presence of a buffer layer close to the important zone of jet spreading will affect the process significantly. Figure 3 shows the effect of changing the buffer layer thickness on the jet evolution. δ_l is the number of grid points adopted in the layer treatment. Choosing the right damping layer thickness between valid data zone and minimum disturbance to the flow field is again a matter of balance.

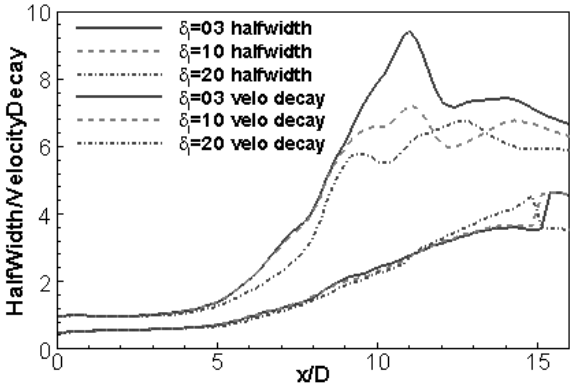

Figure 3: Effect of buffer layer thickness on the jet parameters.

After comparing these parameters for applying the buffer zone, we will choose $\sigma = 2.0$, and $\delta_l = 10$ in the simulations of chapter 3.

2.5.2. A pseudo-compressibility method for a more efficient time integration of slow flow problems

Fire is a complex combustion phenomenon with heat generation. After ignition, the fuel is vaporized (or pyrolyzed from the solid fuel) from the fuel surface, mixes with ambient air and burns, and rises vertically due to buoyancy. In some fire scenarios, the fire-induced flow may be large, such as in a flash fire or a fireball, where the flow speed can reach several tens of meters per second; but these situations are extremely rare. For a typical pool fire in a stagnant environment, the flow speed is only a few meters per second and the flow Mach number is about 0.01.Thus the plumes from most accidental fires correspond to low Mach number flow conditions.

Generally, the flow problems with variable temperature are treated either as incompressible constant density flow with a special treatment for buoyancy effects, or variable density flow with a special treatment for pressure effects. The former is

applicable to weak (small density variations) plumes, as found in environmental flows. For instance, the classical buoyant plume theory is treated with the Boussinesq approximation. The density variations are ignored in the equations except in the body force term due to buoyancy. The Boussinesq approximation has been the corner stone of the classical weak (small density variation) plume theory (Morton et al. 1956). A different treatment is applied in strong (large density variations) plumes, as found in combustion and fire problems. The pressure term in the momentum equation is decomposed into a background pressure, which satisfies the ideal gas law, and a pressure perturbation, which drives the turbulent flow (Zhou et al. 2001a, McGrattan, 2004). This approach is also called the zero or low Mach number approach, in which the acoustic waves are filtered out intentionally to increase computational efficiency. This is achieved at the cost of a reduced domain of application (the flow must remain in the incompressible range, *i.e.* the Mach numbers remain below 0.3) and increased complexity in the numerical algorithms.

An alternative to the zero Mach number approach is the pseudo-compressibility approach, where compressibility effects, meaning the propagation of acoustic waves, are intentionally controlled to achieve faster time integration. More specifically, the computational efficiency is increased by decreasing the gap between flow and acoustic speeds. One such method is the Pressure Gradient Scaling (PGS) method (Ramshaw et al. 1985), where the modification of acoustic speeds is directly achieved by the modification of the pressure gradient term in the momentum equations. Since the pressure is rescaled

everywhere, a side effect of PGS method is that the pressure variations are dramatically amplified.

A variation of the PGS method has been proposed by Wang and Trouvé (2004) and we adopt this variation in our plume simulations (chapter 5, 6). The variation is called the Acoustic Speed Reduction (ASR) method. In S3DLES, the fully compressible flow formulation uses explicit time integration, which leads to the following acoustic-limited time step restriction:

$$\Delta t = CFL(\Delta x / \max|u \pm c|) \approx CFL(\Delta x / \max|u|) \times Ma$$

With the ASR method, the acoustic speed is reduced, *Ma* is artificially increased and the time step Δt may then take large values. The goal of ASR is to achieve the gains in computational efficiency allowed by PGS, while preserving the pressure field. Preserving the pressure field is believed to be important in situations where it is externally imposed (for instance by gravity). It is found in this work that the original ASR method has to be modified to accommodate the gravity-induced hydrostatic pressure field.

We start from the generic equation for energy conservation modified by the Acoustic Speed Reduction method (equation B.25 in Wang and Trouvé, 2004).

$$\rho c_p \left(\frac{\partial T}{\partial t} + u_j \frac{\partial T}{\partial x_j} \right) - \frac{\gamma - \alpha^2}{\gamma - 1} \left(\frac{\partial P}{\partial t} + u_j \frac{\partial P}{\partial x_j} \right) = \tau_{ij} \frac{\partial u_i}{\partial x_j} + \frac{\partial}{\partial x_j} \left(\lambda \frac{\partial T}{\partial x_j} \right) + \dot{q} \qquad (66)$$

The first term on the left hand side is the temperature change of the fluid, while the second term is the pressure change, which directly supports acoustic wave propagation. Here α is the ratio of the original acoustic speed to the modified acoustic speed. When ASR is not activated, $\alpha = 1$, *i.e.* the acoustic speed is unchanged. The terms on the right

hand side are the rate of viscous dissipation, the transport of heat due to conduction, and the generation of heat due to combustion.

From the ideal gas law, $p = \rho RT/M$, and assuming that M is constant, we have

$$\frac{Dp}{Dt} = \frac{p}{T}\frac{DT}{Dt} + \frac{p}{\rho}\frac{D\rho}{Dt} \tag{67}$$

Combining the 2 previous equations, we get:

$$\alpha^2\left(\frac{\partial P}{\partial t} + u_j\frac{\partial P}{\partial x_j}\right) + \gamma p\frac{\partial u_j}{\partial x_j} = (\gamma - 1)\left[\tau_{ij}\frac{\partial u_i}{\partial x_j} + \frac{\partial}{\partial x_j}\left(\lambda\frac{\partial T}{\partial x_j}\right) - \dot{q}\right] \tag{68}$$

or

$$\frac{\partial u_j}{\partial x_j} = -\frac{\alpha^2}{\gamma p}\left[\frac{\partial p}{\partial t} + u_j\frac{\partial p}{\partial x_j}\right] + \frac{\gamma - 1}{\gamma p}\left[\tau_{ij}\frac{\partial u_i}{\partial x_j} + \frac{\partial}{\partial x_j}\left(\lambda\frac{\partial T}{\partial x_j}\right) + \dot{q}\right] \tag{69}$$

The essence of the ASR method is to scale the acoustic dilatation term (the first term in the expression of $\frac{\partial u_j}{\partial x_j}$) while keeping the other terms due to heat transfer, viscous dissipation, and chemical reaction unchanged (the second term in the expression of $\frac{\partial u_j}{\partial x_j}$).

It is noticed that in the presence of an external pressure gradient (Wang and Trouvé, 2004), the decomposition may have to be reformulated to properly account for non-acoustic pressure variations. The ASR method has been tested previously in a number of flow and flame configurations, but without an external pressure gradient.

To properly account for the presence of the hydrostatic pressure gradient, the decomposition of flow dilation into a small acoustic component and an order 1 heat transfer component is now re-written as.

$$\frac{\partial u_j}{\partial x_j} = \left\{\frac{\partial u_j}{\partial x_j}\right\}_{ac} + \left\{\frac{\partial u_j}{\partial x_j}\right\}_{ht}$$

$$\left\{\frac{\partial u_j}{\partial x_j}\right\}_{ac} = -\frac{\alpha^2}{\gamma p}\left[\frac{\partial p}{\partial t} + u_j\left(\frac{\partial p}{\partial x_j} - \rho_0 g_j\right)\right] \tag{70}$$

$$\left\{\frac{\partial u_j}{\partial x_j}\right\}_{ht} = +\frac{\gamma - 1}{\gamma p}\left[\tau_{ij}\frac{\partial u_i}{\partial x_j} + \frac{\partial}{\partial x_j}\left(\lambda\frac{\partial T}{\partial x_j}\right) + \dot{q}\right] - \frac{\rho_0 g_j u_j}{\gamma p}$$

The newly corrected ASR modified energy equation is

$$\rho c_p\left(\frac{\partial T}{\partial t} + u_j\frac{\partial T}{\partial x_j}\right) - \frac{\gamma - \alpha^2}{\gamma - 1}\left(\frac{\partial P}{\partial t} + u_j\frac{\partial P}{\partial x_j}\right) = \tau_{ij}\frac{\partial u_i}{\partial x_j} + \frac{\partial}{\partial x_j}\left(\lambda\frac{\partial T}{\partial x_j}\right) + \dot{q} + \frac{\alpha^2 - 1}{\gamma - 1}\rho_0 g_j u_j \tag{71}$$

The ASR method corresponds to minor changes in the solvers S3D or S3DLES. These changes allow in turn for an increases in the integration time step by a factor α. The value of α is typically up to 10 to 50.

We present here basic tests of the modified ASR treatment in the presence of a hydrostatic pressure gradient. We simulate the test problem TP3 introduced in Wang and Trouvé (2004). This problem corresponds to a 1-D, steady flow problem, with gravity and without diffusion and reaction.

The corresponding ASR system of equations may be written as

$$\begin{cases} \dfrac{\partial}{\partial x_1}(\rho u_1) = 0 \\ \dfrac{\partial \rho u_1^2}{\partial x_1} + \dfrac{\partial p}{\partial x_1} = \rho g_1 \\ u_1\dfrac{\partial p}{\partial x_1} + \dfrac{1}{\alpha^2}\gamma p\dfrac{\partial u_1}{\partial x_1} = \rho g u_1(1 - \alpha^2) \end{cases} \tag{8}$$

For small spatial variations, $\frac{\partial p}{\partial x_1} = \frac{c^{*2}}{c^{*2} - u_1^2}\rho g_1 \approx \rho g_1$, where $c^{*2} = \alpha^2 c^2 = \alpha^2\frac{\gamma p}{\rho}$ which shows that the pressure gradient is almost independent of the ASR parameter α and is a

good approximation to the exact solution. However, as shown in Figure 5, while the pressure gradient is correct, the velocity gradient is not (using the original ASR formulation). It may be shown that the velocity gradient is in that case multiplied by a factor α^2. Figure 4 also shows that the proposed correction to ASR successfully cancels the velocity errors.

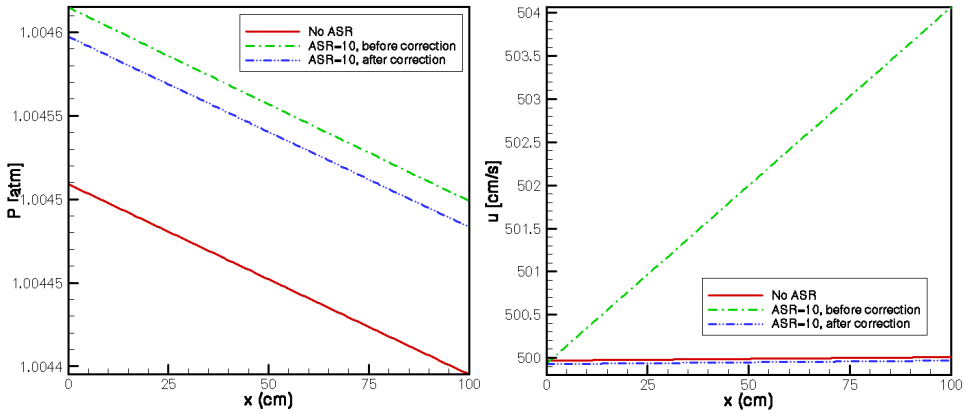

Figure 4: Pressure and velocity variations in the test TP3. Comparison of the original and modified ASR formulations.

Additional tests are presented below for different values of the ASR parameter α and different flow velocities.

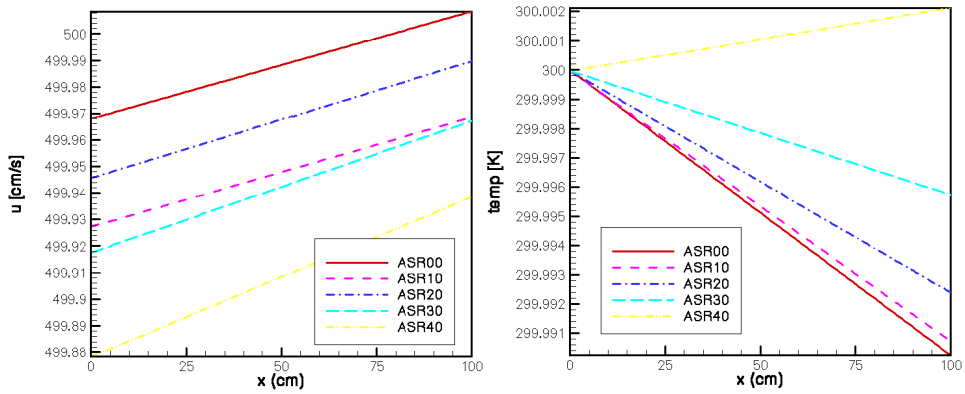

Figure 5: Velocity and temperature variations in test TP3, u=5.0m/s, $0 \le \alpha \le 40$

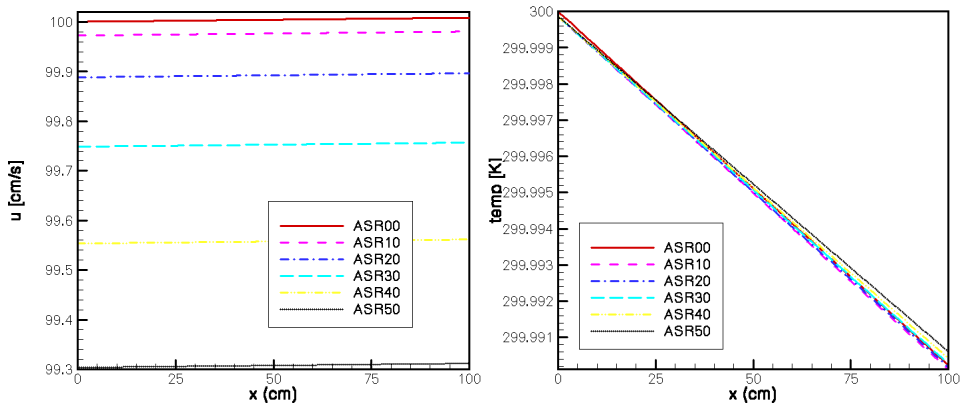

Figure 6: Velocity and temperature variations in test TP3, u=1.0m/s, $0 \le \alpha \le 40$

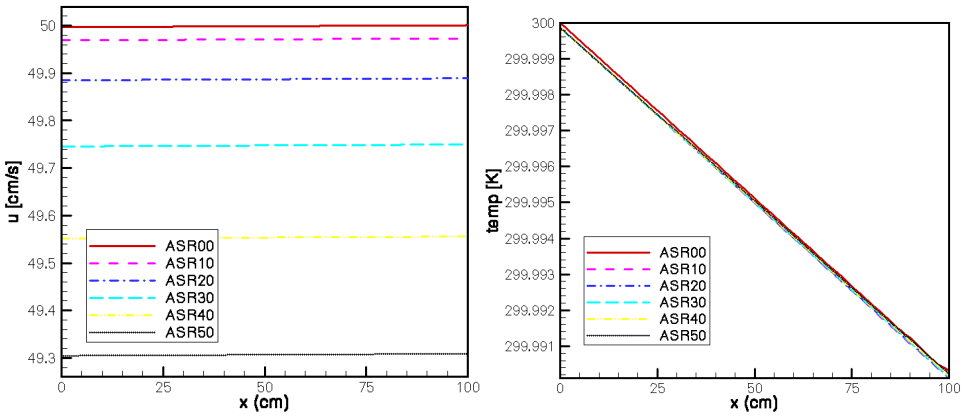

Figure 7: Velocity and temperature variations in test TP3, u=0.50m/s, $0 \le \alpha \le 50$

The results in Figure 5-7 suggest that the errors introduced by an ASR treatment are small while the increase in computational efficiency is large (for α=50, the calculations proceed at a speed that is about 50 times faster than in the non-ASR calculations). It is important to note, however, that the ASR acceleration should be such that the flow Mach numbers remain below 0.3. For instance, in Figure 6, the simulation corresponding to α=40 exhibits an unrealistic temperature variation. This result may be explained by the introduction of significant non-physical compressibility effects (in this case the flow Mach number has been artificially increased by ASR to a value above 0.5, the compressibility is no longer negligible).

2.5.3 Non-uniform computational grid

The effect of non-uniform computational grid is difficult to quantify. Here a 2-D numerical simulation of 3 streams (case selected from Chapter 4, 3 streams without density variations), shows the dilation change at the interface between uniform and non-uniform computational grid. It is observed that high-frequency oscillation of dilatation terms appear near the transition interface from uniform to non-uniform meshes. This error is localized and supposed to be not affecting the result at other locations.

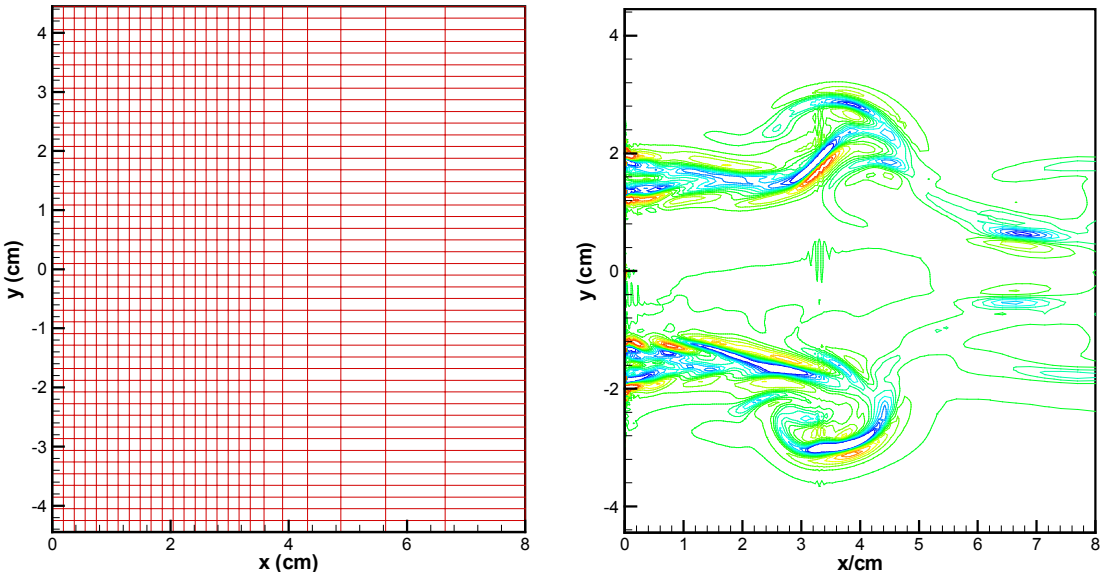

(a) non-uniform computational mesh (1 out of 5 shown) (b) flow dilatation

Figure 8. Flow dilation distortion showing the impact of non-uniform meshes.

Beside the numerical error, there is additional error due to the non-commutable feature of LES filter. This is even more difficult to quantify. But it serves to damp the incoming waves from outside, improving the boundary treatment, so it is an advantage to our flow simulations.

Chapter 3: Numerical simulation of a plane jet

Turbulent plane jets are prototypical free shear flows on which fundamental research can expand the overall understanding of turbulent flows. Here the S3DLES code is validated against a plane jet simulation to test the performance of the SGS models adopted and to accumulate experience for further simulations. We compare our results to previous studies performed by Ribault et al. (1999) and Ribault et al. (2001) where the dynamic Smagorinsky model was used. Since in the reference studies, the governing equations and the numerical scheme are comparable to those of S3DLES. We view the present simulation as validation tests that serve to establish the performance and accuracy of S3DLES.

3.1. Numerical configuration

The techniques used in this study to numerically solve the governing equations are summarized here. The governing equations correspond to a fully compressible flow formulation (see Chapter 2). A sixth-order finite difference discretization is utilized to evaluate the spatial derivatives. This otherwise center-difference scheme is biased at the boundaries using one-sided, third order finite difference expressions. This 3-6-3 scheme allows the simulation of problems on an open, non-periodic domain while maintaining at least an overall fourth-order spatial accuracy. In order to eliminate high-wave-number errors resulting from numerical boundary closures, a 6^{th} order filter is utilized to damp the high-wave-number modes. The role of filters is discussed in more detail by Kennedy et al. (1997). The Euler and viscous terms in the governing equations are marched in time

using a low storage third-order Runge-Kutta explicit time integration (Kennedy et al., 1998)

The open boundaries are described using characteristic-based boundary conditions enhanced with an inflow forcing treatment for turbulent inflow boundaries and a buffer zone treatment for outflow boundaries. A conventional structured rectangular Cartesian uniform/non-uniform computational mesh is adopted. The current turbulence sub-model in S3DLES is a Smagorinsky model to describe subgrid-scale turbulent stresses with a static or a dynamic implementation using explicit top-hat filtering. The flow field dynamics near the nozzle in plane turbulent jets are initially dominated by the shear layer instabilities at the jet edges. Near the nozzle the most strongly growing disturbances are those corresponding to the shear layers (Ho and Huerre, 1984). The shear layers grow downstream and interact to form a fully developed jet. This reorganization as the flow field develops from the shear layers near the nozzle to the fully developed jet downstream has a strong influence on the mixing of the jet. Note that the flow is sensitive to the initial shear layer instabilities and we need to specify the inflow turbulence forcing carefully.

In our study, the turbulence forcing is slightly different from that used in the paper by Ribault et al. (2001). Instead of using broadband forcing, we have a forcing scheme that corresponds to a synthetic flow field with a specified characteristic turbulence intensity and a specified characteristic length scale associated with the most energetic eddies (Passot and Pouquet, 1986). The generated velocity fluctuations are superimposed upon the mean velocity profile at the inlet. The generated turbulence field is recycled after each

sweep-over of the synthetic field. A full discussion on the role of the discrete forcing is presented in Stanley and Sarkar (2000) and will be discussed in the next section.

3.2. Simulation parameters

The configuration is three-dimensional and corresponds to a "strong" jet. The jet is called strong because the co-flow velocity is small and the resulting shear large. The velocity ratio between the co-flow and jet streams is 0.09. The jet Reynolds number is $\mathrm{Re}_d = (\rho \Delta \overline{u}_j D / \mu) = 3000$, where $\Delta \overline{u}_j$ is the differential velocity between the jet and the co-flow, and D is the jet slot width. The Mach number of the high-speed stream is 0.35 ($u_1 = u_{jet}$=121.5 m/s) and the convective Mach number for the jet shear layers is 0.16 ($\Delta \overline{u}_j / 2 =$ 55.5 m/s, $u_0 =$ 10.4 m/s). The Mach numbers are moderate and the flow dynamics are essentially incompressible.

The computational domain is (32D) in the streamwise direction, (40D) in the cross-stream direction, and (6D) in the spanwise direction. The domain is larger than that used in the reference study (16Dx16Dx4D). The reason is due to the outflow boundary treatment and the requirement for a fully developed flow. Stretched grids cover the extra domain area, so the computational cost is not significantly increased. The computational grid size is 136x126x26. The grid is uniform in the near-field region of the jet and stretched in the stream-wise and cross-stream directions in the far field. For the near injector region, a uniform grid is chosen: $\Delta x = 0.164D$, $\Delta y = 0.066D$ and $\Delta z = 0.24D$. Compare to the reference studies, the gridsize in the x direction is finer (0.25D), while comparable in the other 2 directions. Boundary conditions correspond to prescribed

velocity at the injection plane, non-reflecting conditions at the outflow and cross-stream boundaries, and periodic conditions in the spanwise direction. The prescribed velocity field at inlet corresponds to a pre-computed turbulent flow with well-characterized *rms* intensity and integral length scale. The outflow boundary condition is also stabilized by introducing a buffer zone treatment in its vicinity. The buffer zone treatment consists in adding damping terms to the governing equations (different implementations are available in the literature, here only the momentum equations are treated); the effect of those damping terms is to reduce the strength of flow perturbations prior to their interactions with the outflow boundary. The damping terms are calibrated in terms of an empirical damping coefficient and a target outflow velocity profile; this target profile is a priori unknown and is determined in the simulations from spatial averaging across the buffer zone interface (see Chapter 2). A series of tests have shown that: the buffer zone treatment is required to get stable solutions; and that the constraints that are introduced are strong enough to stabilize the simulations, but remain weak enough not to affect the flow solution in any significant way.

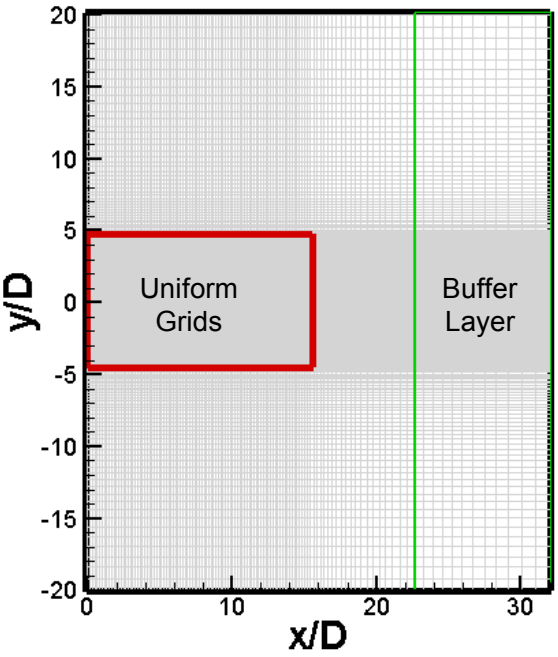

Figure 1: Computational grid on in a constant-z plane.

The configuration is treated as a mixing problem, both in terms of temperature and species composition. The mixture fraction is unity in the jet and zero in the co-flow field. Also the jet is hot and the co-flow cold. Since the flow is momentum driven and buoyancy effects are small, temperature behaves like a passive scalar. The jet temperature is 420K and the co-flow field temperature is 300K. Both passive scalars should have similar behavior. The evolution of mixture fraction is studied in more detail by Ribault et al. (2001).

For the inflow condition, hard-inflow conditions (prescribed velocity conditions) are set. The mean u-component is set using a hyperbolic tangent function. The mean v- and w-components are set to zero. The inlet profiles are specified as:

$$\begin{cases} u = (u_1 - u_0)\Omega + u_0 + u' \\ v = v' \\ w = w' \\ T = (T_1 - T_0)\Omega + T_0 \\ Z = 1 \times \Omega + 0 \end{cases} \tag{1}$$

where u_1, u_0 are the velocities of the jet and co-flow streams, respectively; u', v', w' are the fluctuations due to turbulence; T_1 is the jet temperature, and T_0 is the ambient temperature. The function Ω is defined as

$$\Omega = 0.5 * \left[\tanh\left(\frac{y - y_{0.5w}}{2\theta} \right) - \tanh\left(\frac{y - y_{-0.5w}}{2\theta} \right) \right] \tag{2}$$

where θ is the shear layer momentum thickness, $y_{0.5w}$ and $y_{-0.5w}$ are the location of the jet orifice boundaries respectively. The momentum thickness θ determines the magnitude of inlet flow gradients, so it is important for the transition to turbulence due to Kelvin-Helmholtz instability of the shear layer flows. Equation (2) is a normalized smoothed top-hat profile, with peak 1 and background 0. The mean pressure is initially set as uniform.

3.3. Effect of the turbulence forcing scheme

Here several tests are performed on a smaller domain (76x126x16 grids for a physical domain of 16Dx16Dx4D) to show the effect of turbulence forcing. The grid-size is approximately the same as that used for the formal study, and a buffer zone treatment is applied to stabilize the computations.

In most experimental studies, the fluctuation intensity at the jet nozzle is only reported on the centerline. However, because of the boundary layers upstream, the fluctuation intensity peaks in the shear layers on either side of the jet, so does the peak mean shear. So the fluctuation intensity in this region of the jet will have a strong influence on the initial jet-flow evolution. As seen in Figure 2, when the inflow fluctuation intensity is increased from $u'/\Delta\overline{u}_j$ =0.025 to 0.10, the length of the potential core decreases from 5D to 3D. (The potential core is defined as the region of the flow where the center-line means excess velocity remains constant.)

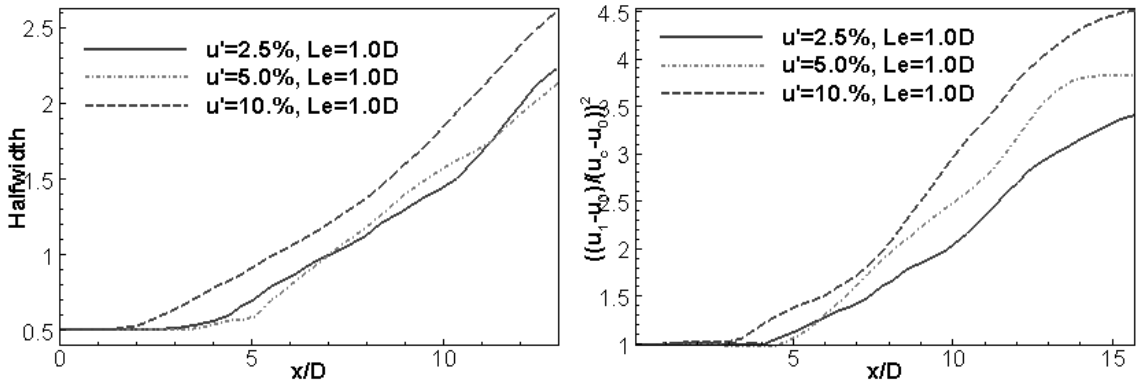

Figure 2: Downstream evolution of the jet half-width and the centerline mean excess velocity for different inflow turbulence intensities: thick line, $u'/\Delta\overline{u}_j$ =0.025; dotted line, $u'/\Delta\overline{u}_j$ =0.05; dashed line, $u'/\Delta\overline{u}_j$ =0.10.The centerline mean excess velocity is normalized and presented as $((u_1-u_0)/(u_c-u_0))^2$, with u_c the mean centerline x-velocity.

Another important factor for turbulence forcing is the length scale associated with the most energetic eddies. Figure 3 presents the results of different simulations performed for different values of this length scale. High values of the facing length scale will make the potential core shorter. Again, the near-field dynamics are sensitive to the details of the inflow-forcing scheme, whereas the far-field exhibit growth rates that seem independent from these details.

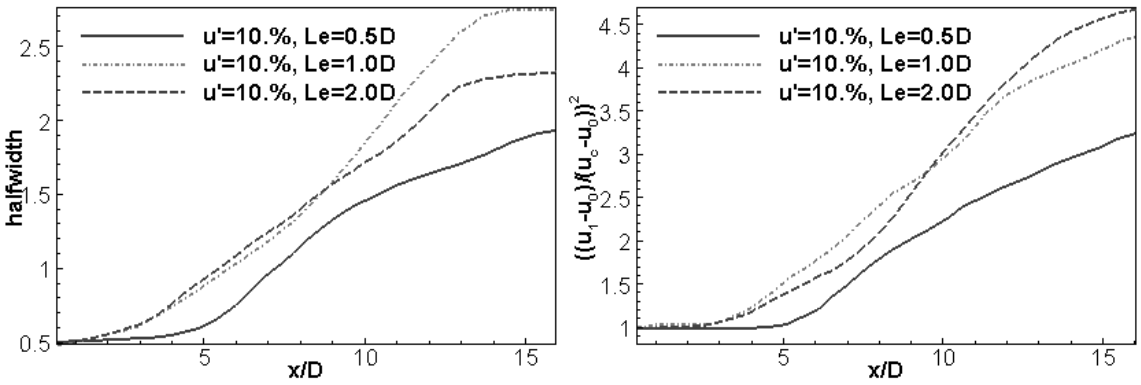

Figure 3: Downstream evolution of the jet half-width and the mean centerline excess velocity for different values of the inflow turbulence integral length scale.

Based on these tests above, it is decided to choose $u'/\Delta\overline{u}_j$ =0.10 and *Le=1.0D* for the simulations below.

3.4. Simulation results

3.4.1. Instantaneous view of jet variables

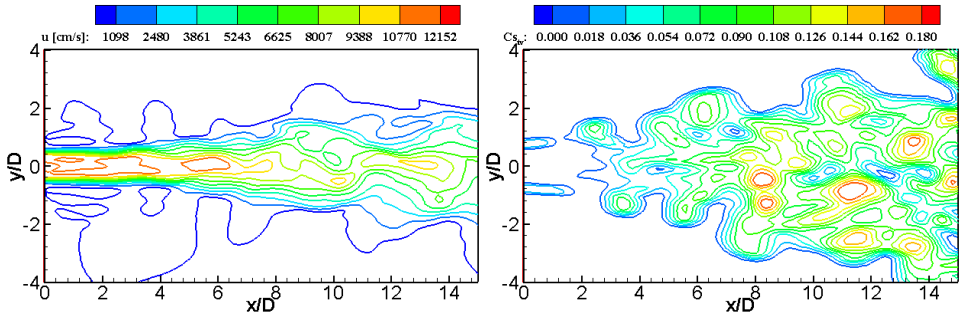

a. u-velocity b. C_S

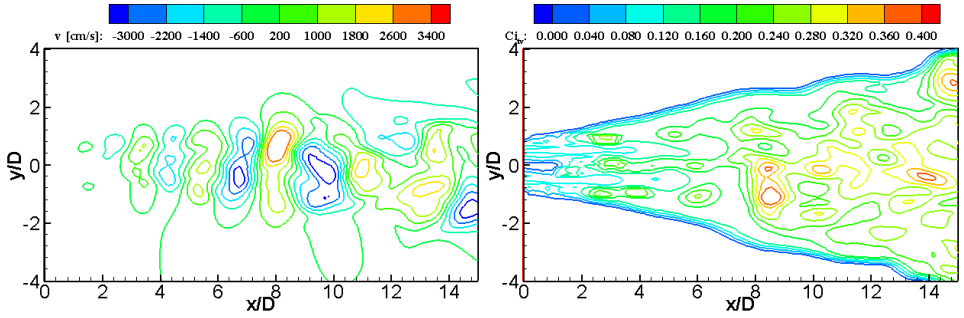

c. v-velocity d. C_I

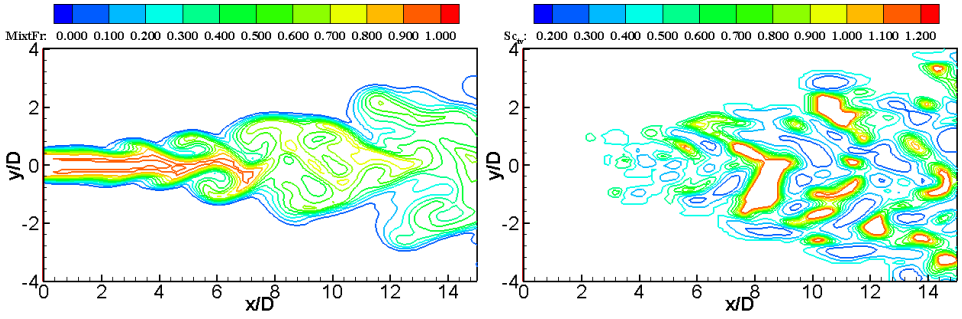

e. mixture fraction f. S_C

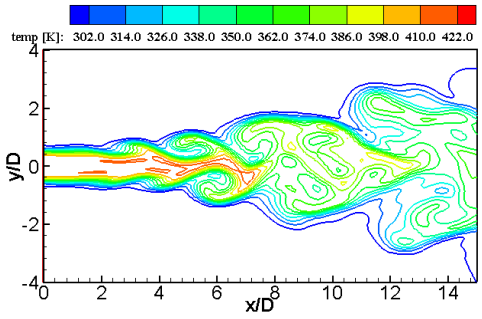

g. temperature

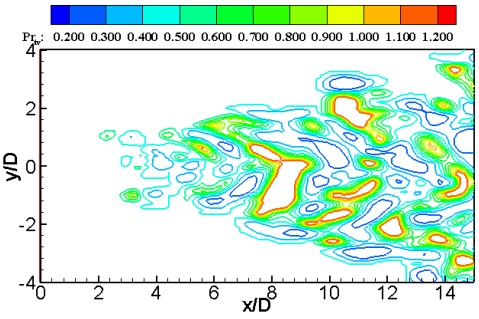

h. Pr

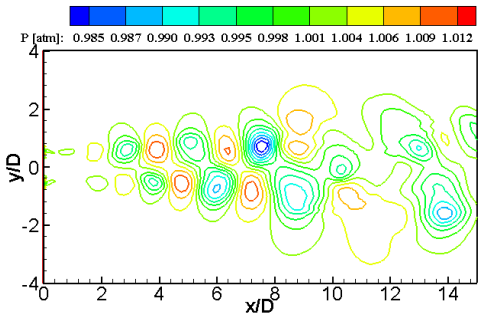

i. pressure

Figure 4: Instantaneous snapshots of the solution. The data are taken in a median plane, z =0, a uniform grid zone (0<x<15D, -4D<y<4D)

Figure 4 presents a series of snapshots from the S3DLES solution. On the left hand side are the primitive variables, while the model coefficients are on the right hand side. This simulation corresponds to a solution with the dynamic Smagorinsky model. The Smagorinsky model is sensitive to the local strain rates, and the effect of local filtering is clearly shown in figure 4(b). Due to the same initial profiles and similar governing equations, the Pr and Sc fields are similar to each other. It should be pointed out that the background values of model coefficients (Sc, Pr only) are not zero, rather a certain default value is used, to avoid numerical difficulties of dividing by zero.

3.4.2. *Evolution of the mean properties*

Figure 5 presents a test of the similarity of cross-stream variations of stream-wise velocity. The right figure shows that the slight backflow observed on the edge of the jet vanishes in the far field. It is seen that the velocity profile features a classical transition from an initial top-hat shape to a fully developed Gaussian-like shape.

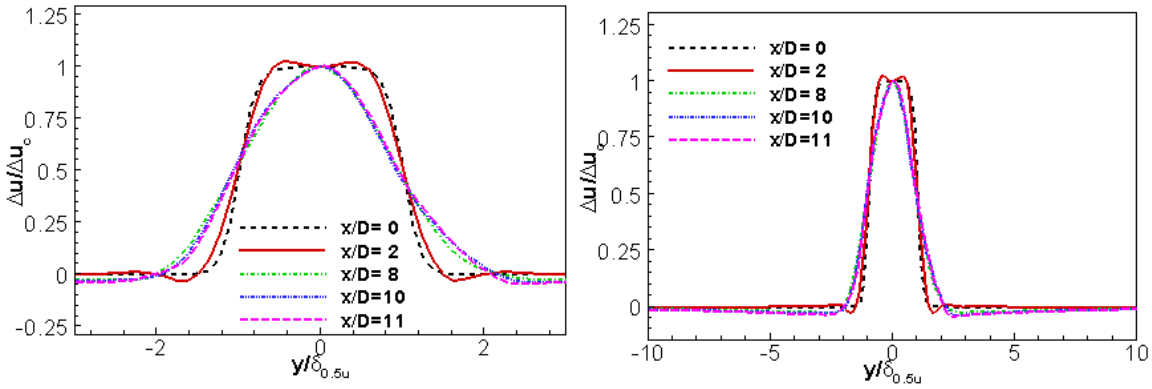

Figure 5: Time-averaged cross-stream variations of u-velocity at different stream-wise locations. (The right plot shows a wider view of the curves presented in the left plot.)

Figures 6 and 7 present the stream-wise evolution of the jet half-width and time-averaged centerline velocity. The total length of the calculation is 1.5e-3 sec, or approximately 10 flow-over time. The variations are compared to previous results from the literature (Ribault et al. 1999). The comparison is good; some discrepancies are observed, however, and in particular the velocity decay is delayed.

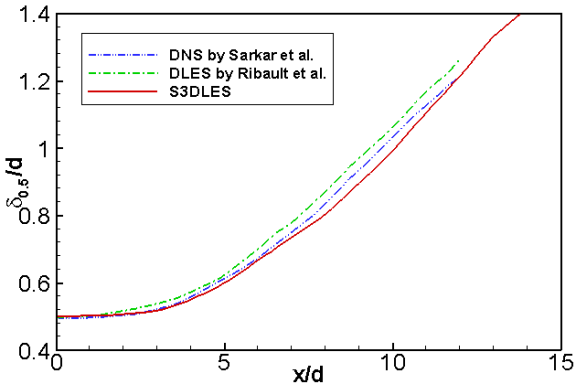

Figure 6: Time-averaged stream-wise variations of the jet half-width

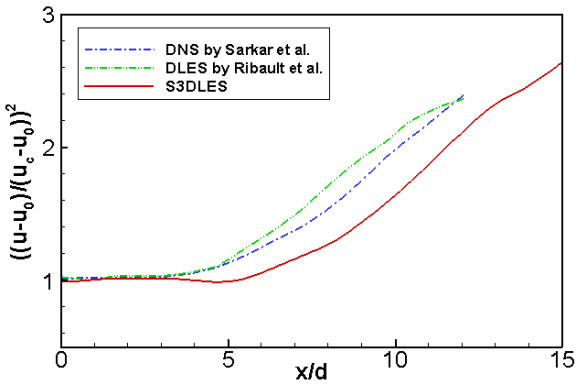

Figure 7: Time-averaged stream-wise variations of the mean centerline u-velocity

3.4.3. Velocity Fluctuations

The downstream evolution of the longitudinal centerline fluctuation intensity is presented in Figure 8. The fluctuating quantities develop slowly toward a self-preserving behavior. Compared to the study by Ribault et al. (1999), the stream-wise *rms* value increases later than expected, but achieves about the same level as in the reference study. The cross-stream variations of stream-wise turbulence intensity are shown in Figure 9. This section *x=10D* is chosen because it belongs to the region where self-similarity in the fluctuating quantities applies and is still far from the outflow boundary. The overall agreement between S3DLES and the previous study is good.

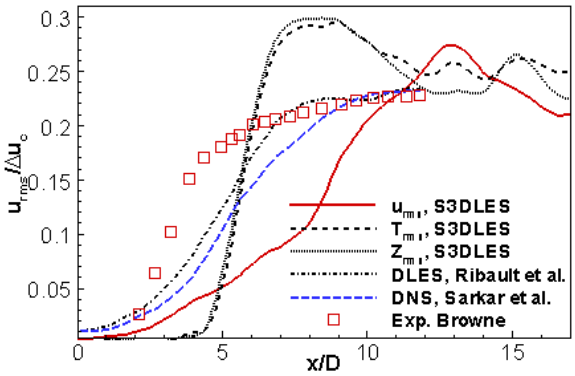

Figure 8: Downstream evolution of the fluctuation of the longitudinal velocity

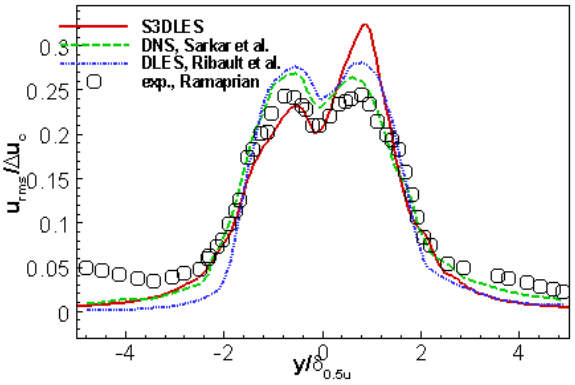

Figure 9: Time-averaged cross-stream variations of stream-wise turbulence intensity at x=10D

3.4.4. Variation of the dynamical Smagorinsky coefficient

Here the time-averaged dynamic Smagorinsky coefficient is compared to Ribault's data at *x=10D (Figure 10)*. Our results are slightly lower and smoother than the published result. This is possibly introduced by the local spatial averaging of the coefficients used to get stable computations. The level is still close, as the same filter-size is used.

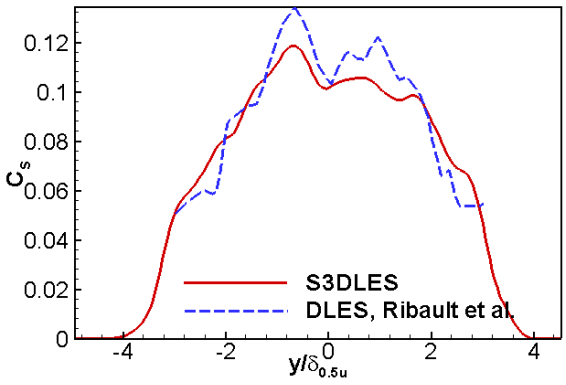

Figure 10: Time-averaged cross-stream variations of the dynamic Smagorinsky coefficient at the section x=10D

3.4.5. Iso-contours of vorticity

A snapshot of iso-contours of spanwise vorticity is presented in a *xy*-plane in Figure 11. For *x<5D* the Kelvin-Helmholtz rollers of the two mixing layers at the jet edge appear clearly. These mixing layers develop symmetrically and start breaking down into small scales. Downstream of *x=5D*, the two mixing layers merge, causing a rapid breakdown of the large structures with a growth of smaller structures, and the development of a sinuous motion in the jet.

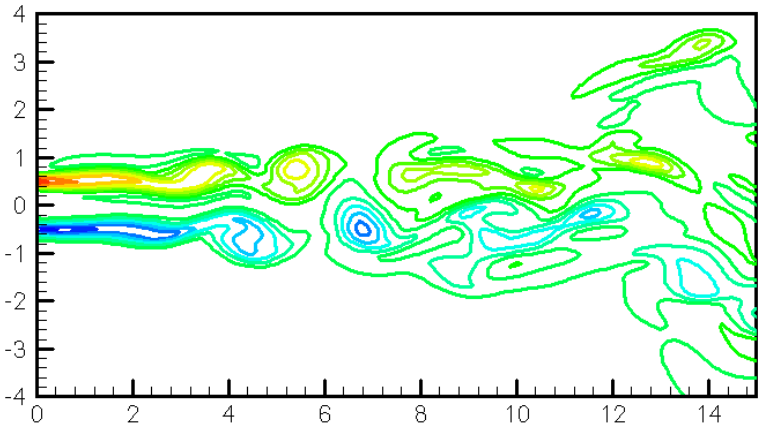

Figure11: Spanwise vorticity showing the vortex breaking-up process

3.4.6. *Evolution of passive scalars*

An instantaneous snapshot of the mixture fraction field is shown in Figure 4(e), with the dynamically determined turbulent Schmidt number field in Figure 4(f). Here the jet halfwidths based on temperature and mixture fraction are shown in Figure 12. The similarity profiles of temperature and mixture fraction are shown in Figure 13.

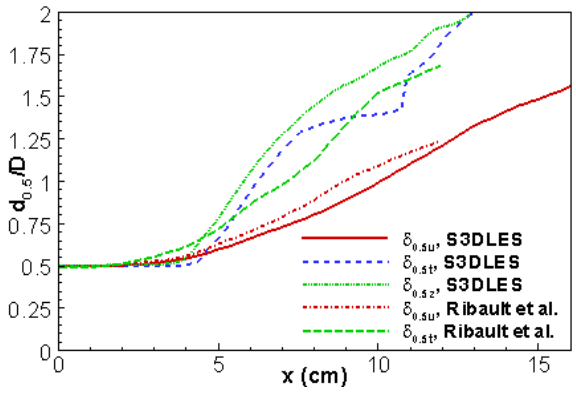

Figure 12: The jet halfwidth based on velocity, temperature and mixture fraction.

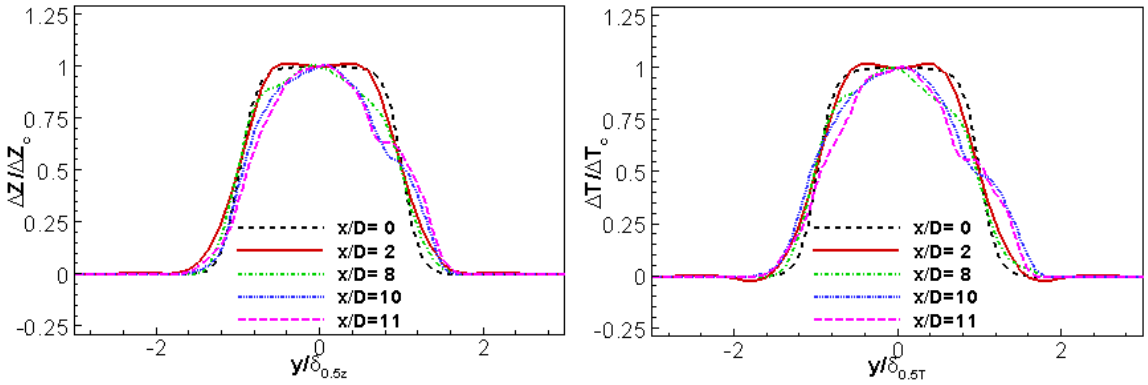

(a) *(b)*

Figure 13: Time-averaged cross-stream variations for (a) mixture fraction and (b) temperature

3.5. S3DLES performance study

To test the performance of S3DLES running on multi-processors, a scalability test is performed for the simulation of the planar jet described above. The order for spatial and temporal integration is 6^{th} and 3^{rd} respectively (8^{th} order in space and 4^{th} order in time will increase the computing time by a factor of 90%). The grid size is 128x128x64. There is no initial turbulence. The computational cost is evaluated in Table 1. The data corresponds to a calculation duration of 2500 time-steps (1-flow-over time) on 12 cpus in a Titan cluster at NCSA super-computing center at University of Illinois. Global quantities are evaluated at every 10 time-steps and saved in a history file. The full solution is saved every 50-time step in a *Tecplot*–ready data file.

	With data-dumping (sec)	Without data-dumping (sec)	Computing Load (without damping)
No dynamic procedure	13915	10738	1.00
Dynamic LES with 2 coefficients	23541	20469	1.91
Dynamic LES with 3 coefficients	29678	27057	2.52

Table 1. Computational cost of S3DLES with different input parameters.

The data indicate that dynamically evaluating the Smagorinsky and Yoshizawa coefficients approximately doubles the computational cost. In addition, if the Schmidt number is also dynamically determined, the cost is increased by a factor of 50%.

The next test shows that S3DLES has a good scalability up to 64 processors (Figure 14). This test is done on different combination of cpus without initialization and data damping. The test case is allowed to run strictly 50 time steps. The calculation on 2 processors will have a longer running time than the total time on one processor divided

by 2, which is the ideal situation, due to the cross-communication between nodes and waiting time requirement.

It is interesting to notice that the computational time in 8-cpu is smaller than the time of the one-cpu case divided by 8. The same is true for the 64-cpu case. The reason may be due to the heavy memory requirement on one-cpu running case, which is less efficient.

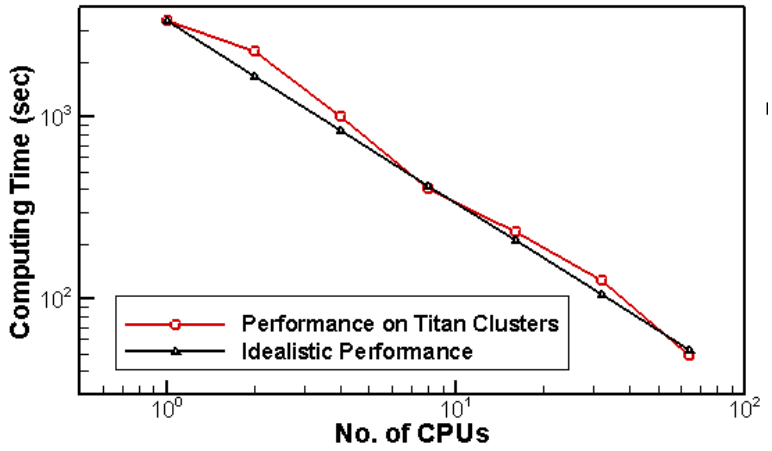

Figure 14: Scalability of S3DLES on a Titan cluster

Generally, the scalability of the MPI-based parallel code is very good. This is reasonable, as the code was well optimized during the conversion process from Fortran77 with special emphasis on parallel optimization. These tests provide the guidance for future parallel computing allocation.

For the plane jet simulation, the domain length is 1.3568 cm (=32D) with a coflow speed of 10.9m/s, so the flow-through time is 1.56e-3sec. The characteristic length is the plane jet width (D=0.0424 cm). The jet Re number is 3000 (based on velocity difference between the jet and the coflow), the Mach number is 0.35 for the jet velocity, and Richardson number is zero (no gravitational force). Here the dimensionless parameters are defined as in equation (3):

$$\mathrm{Re} = \frac{uD}{\nu},\ Ma = \frac{u}{c},\ Ri = \frac{g\alpha\Delta TL}{u^2} = \frac{gD}{u^2}\cdot\frac{\Delta\rho}{\rho_0} \tag{3}$$

Here the D is the characteristic length scale, usually the jet width (plane jet) or the jet diameter (round plume). α is the thermal expansion coefficient. The DNS grid requirement is based on the Kolmogorov scale, which is estimated as:

$$\eta = l_t \cdot \mathrm{Re}_t^{-3/4} \tag{4}$$

Here the turbulent Reynolds number is based on the rms velocity and the integral length scale (commonly using diameter).

The computing cost ratio between different computational grids is defined as grid size ratio to the 4th power, because of the 3 coordinates and the time restrictions.

$$\frac{COST_{DNS}}{COST_{LES}} = \left[\frac{dx_{DNS}}{dx_{LES}}\right]^4 \tag{5}$$

A grid resolution study shows that for such a Re=3000 flow ($\mathrm{Re}_t \approx 600$), the DNS resolution would be on the order of 2 μm, while the resolution for a well-resolved LES is 10.6 μm (based on the jet thickness divided by 40, D/40), as compared to the current choice (dx=27.8 μm). The difference of cost between DNS and LES based on the above choices are 789 and 37,330, respectively. Only a marginal resolution for LES is chosen here due to the limitation of computing resources. The advantage of LES over DNS for such a problem is obvious.

3.6. Conclusions

For the strong jet simulations, the buffer layer can successfully control the disturbances at the outflow boundary by matching the exit velocity profile with a target profile. This method proves valuable in strong jet simulations.

Detailed comparison with published results is satisfactory. The jet parameters: velocity decay, jet width, and fluctuation level are comparable with the reference study. The Smagorinsky model and relating submodels are playing its role by damping the high-frequency oscillations (due to the unresolved turbulence scales). However, some oscillation of scalar variables outside of physical boundary are noted. They are the byproduct of higher order differencing schemes, commonly called Gibbs error, which will be discussed more in Appendix B.

The parallel performance of S3DLES is also tested. The scalability of the code is good. The computation cost follows the log-linear relationship with the number of processors. The computational cost of the dynamic Smagorinsky procedure is significant. So the dynamic procedure is not resorted in later chapters.

Chapter 4. Acoustic response of jets in a chamber

4. 1. Introduction

Combustion noise has plagued the liquid rocket engine since its early appearance in 1940s. With the NASA plans to re-land the moon and exploration to Mars, there is a new wave of interests on the combustion noise (thermoacoustic instability) for liquid rocket engines. To fully understand the noise problem in the liquid rocket engine, duct acoustics provides the simple problem toward the understanding of the detail instability mechanisms.

Combustion instability problem in liquid rocket engines usually occurs following a sequence of events:

1. Initialization of the perturbation;
2. Selective amplification of the perturbation;
3. Combustion-acoustic coupling

The combustion oscillation can be overcome by removing any of the 3 events in the acoustic excitation loop. The instability of the combustion process requires an excitation source and the interaction between the unsteady heat release and the acoustic waves.

There are several mechanisms leading to the onset of instability in a liquid rocket engine. The combustion of propellants in liquid rocket engines consists of several major component processes. These processes have all been considered to be candidates for combustion instability mechanisms and may be categorized following the general sequence of events affecting an elemental mass of liquid propellant (Santoro, 2006)

1. Injection;
2. Atomization of a liquid stream to form drops;

3. Drop heating and vaporization
4. Mixing of drops, vapors, and gases
5. Chemical reaction

These mechanisms belong to two schools of thought. The heat release fluctuations are caused by the local mixing rate or mass flux (Richards, 1998) or by the flow instabilities such as vortex rollup (Poinsot et al. 1987). However, there is not a single mechanism to explain all the observed combustion instability phenomena. It is postulated that several mechanisms potentially are important in establishing combustion instability. And the local environment produced by the rocket engine determines the specific mechanism responsible for a particular combustion instability event. A series of direct numerical simulations (Colonius et al. 2004) show that the sound generation is in fact the leakage of otherwise trapped wave modes facilitated by the vortices. Details of physical mechanisms that generate sound in complex flows can be revealed by carefully conducted numerical simulations.

Depending on the geometry and local information, the acoustic perturbation generated by these processes may be enhanced or damped by the ambient conditions. Here the wall and the local density interfaces play an important role on exciting or damping certain acoustic modes. Depending on the phase relationship between the source and the response from the media and the boundary, acoustic waves may successively increase in energy leading to large-amplitude self-excited oscillations. Some early research work focused on providing passive control measures (such as baffles, resonators, and acoustic liners) to damp the troubling modes. The essential point is to force the resonance to occur

in frequency ranges where the driving mechanisms are inadequate to sustain oscillations or to directly damp the mechanical energy of unsteady motions (Culick and Yang, 1995).

When the acoustic wave is strong enough to affect the combustion process, the Rayleigh's criterion (Rayleigh, 1896), of the acoustic type oscillations observed in a Rijke tube, specifies the conditions that must be met for driving a periodic pressure disturbance by energy addition. Due to the high density of energy release in a volume having relatively low losses, conditions normally favor excitation and the source of excitation is difficult to remove. If the addition of energy is periodic and in phase with local pressure oscillations, the excitation is amplified until limited by the non-linear effects. This is the general guideline for acoustic instability generation. This theory has been validated by numerous experimental results (Culick and Yang, 1995). Addition of energy out of phase with the local pressure oscillation provides a damping effect. This provides a basic route toward active noise control (Dowling, 2005).

The excitation of the perturbation and the combustion-acoustic coupling have attracted most research interests in the literature. Detail research work is summarized by the literature reviews on combustion instability in liquid rocket engines (such as most recent ones: Yang and Anderson, 1995, Santoro, 2006). Other reviews on general combustion-oscillation control are also useful to understand the problem (Ffowcs Williams, 1983, Candel et al. 2004, Dowling et al. 2005). The intermediate process, the selective enhancement of the acoustic wave, is usually included in the combustion-acoustic coupling studies.

Acoustic wave propagation in fluids has been studied for a long time. Most of modern methods are summarized in Crighton et al. (1992). Analytically, Sujith and his coworkers

(for example, 2000) derived many exact, transient solutions for sound propagation in inhomogeneous media. Dowling (1995) compared the analytical methods for computing thermoacoustic oscillations and found that the mean flow effects are significant even at modest inlet Mach numbers. Experimentally, Liuwen (1999) studied combustion instability in premixed gas turbines. Numerically, Eccardt et al. (1996) studied the wave propagation in flowing media using finite element simulations on linear wave equation. These methods study either the wave propagation or the resulting modes. The interaction between inhomogeneous fluids, wall and acoustic wave are simplified. Ducruix et al. (2004) developed the external flow modulation for flow-acoustic interactions and applied in Richecoeur et al. (2006) for simulations.

This chapter presents an application of S3DLES to the simulation of acoustic phenomena. In contrast to the next chapters in which acoustic waves are considered as a numerical nuisance to be handled by specialized treatments (e.g., NSCBC boundary conditions, the ASR pseudo-compressibility method, etc.), this chapter considers a problem in which acoustics are an integral part of the flow solution, and thereby takes advantage of the compressible flow formulation adopted in the LES solver. Here we will perform some numerical analysis on chamber acoustics with flow and density effects, which provides a basic problem towards the understanding of the whole combustion-instability problem in liquid rocket engines. Historical experience shows that the best approach to eliminate combustion instability in rocket engines is to modify the injector and incorporate passive controlling methods. These methods are supposed to change the energy release process and the acoustic response of the chamber. This requires a thorough understanding of the

duct acoustics and the working mechanism of the wall (including other density interfaces). This provides another motive to study the chamber acoustics. To predict the onset of acoustics in a combustor is one important goal toward controlling the combustion noise.

The combustion instability can be separated into three effects: wall and density effects, flow effects and combustion effects. In this paper, we will focus on the passive environment for the resonance behavior inside a duct (to mimic the situation in a combustor). Study is limited to gas phase effects, while the spray and vaporization effects are neglected. Also no combustion is involved. The main research tool is a fully compressible LES flow solver for 3-D flow-acoustics simulations. Another 1-D acoustic solver is developed to validate the CFD result. They are also validated by the experimental work on the acoustic behavior in homogeneous and density-stratified flow fields.

The organization of the chapter is to present the numerical theory and the experimental work first, followed by the data analysis on 1-D numerical, experimental and analytical results. Then 2-D simulation is performed to test the effectiveness of the wall boundary treatment. Now turbulence is involved. Large-eddy simulation requires 3-D flow information, so here 3-D simulations are also performed to predict the effects of acoustic excitation at the density interface. The simulation results are compatible with the experimental results. Due to the details of CFD results, the numerical work can provide some insights about the acoustic phenomena, which are difficult to observe and measure in experiments.

4.2. Numerical and experimental configuration

4.2.1. Experimental configuration

The tested configuration is shown in figure 1. It is a simplified version for the real situation, which is a combination of hydrogen/oxygen/hydrogen with reaction and two-side-forcing (Details can be found in Ghosh et al. [4]). The dimension of the chamber is 15x3.5x0.375 in (38.1x8.9x0.95 cm). Three injectors for Helium/Air/Helium are ¼, ¾, and ¼ inch in width respectively. The slot for acoustic forcing speaker is 1 inch in length. The four black dots in the graph are the pressure sampling points in the centerline of the acoustic forcing. The pressure measurement is accomplished with 4 Kistler 211B5 piezoelectric transducers along with a 4 Channel Kistler 5134A1 Piezotron coupler. Pressure transducers are mounted on the sidewall along the centerline of the lateral forcing. Their relative position is shown in the plot (see figure 1). The speaker is 75 watts 16 ohm trumpet horn driver, where we use a sine wave generator to simulate its function.

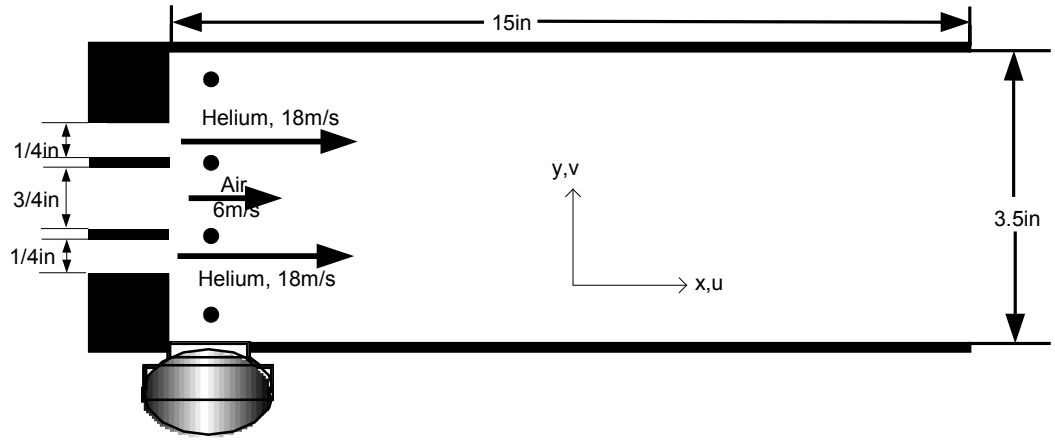

Figure 1: Experimental mixing chamber (used as a simplified representation of a liquid-rocket engine configuration).

The above configuration is enough for a homogeneous static field, without density variations. If a stream of different density is introduced into the field, the stream profile is

not easy to maintain, and the injector will introduce more acoustics associated with the cavities and the walls. The resulting response is complex and difficult to differentiate the density effects. So we have to resort a static pipe test with density inhomogeneity to find the effect of the density (see figure 2). The arrangement is made of a plastic pipe commonly used for indoor plumber system. It is 2 inch in diameter and made of PVC material. The pipe is cut into blocks of 1, 2, 3, 5 inch in length, so we can adjust the position of the density inhomogeneity easily. The cutting surface is smooth, so there is no significant leakage. After a few try runs, the sealing of the space between these blocks are proved to be unnecessary. The density inhomogeneity is introduced by a 5-inch segment with 2 plastic films on both sides. The film is the kind commonly used to wrap the food in a refrigerator. The thickness of the film is 0.127mm in thickness. The film is glued to the both end with a fast-hardening glue. The hydrogen filling process is happened in a plastic container, where the hydrogen environment is maintained for a few seconds. This is enough for the glue to do its work.

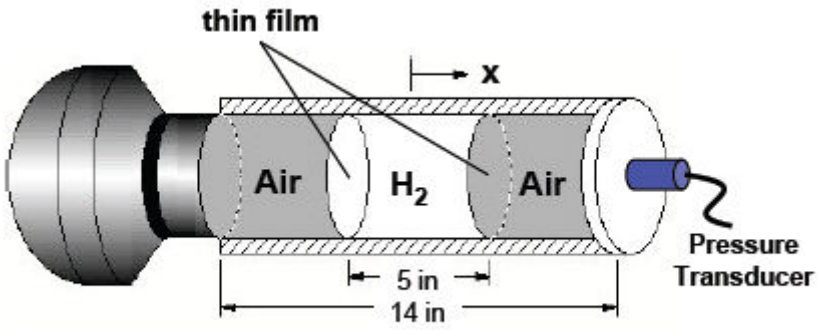

Figure 2: Auxiliary one-dimensional set-up.

For any confined domain, the sequential-broadband forcing is applied to find the natural frequencies. This is realized by quickly scanning the specified frequency range. The duration for each frequency is short, so it is an approximation to the broadband forcing.

4.2.2. 3-D Navier-Stokes flow solver

To mitigate the Gibbs error commonly associated with high-order schemes, a forth-order finite difference discretization is utilized to evaluate the spatial derivatives. In order to eliminate high-wave number errors resulting from numerical boundary closures, a 4^{th} order optimized filter is utilized to damp the high-wave-number modes (Kennedy et al. 1994, Bogey et al. 2004). The purpose of such optimization is to improve the spectral performance at the price of global resolution. Since the target of the simulation is not acoustic wave generation or propagation, but the spectral mode selection, this is an acceptable choice. The governing equations are marched in time using a low storage third-order Runge-Kutta explicit time integration (Kennedy et al. 2000). The parallel programming is based on the Message Passing Interface (MPI) protocols. The conventional structured uniform/non-uniform computational mesh is adopted. For 1-D and 2-D simulations, no turbulence model is used.

The boundaries are described through the characteristic-based boundary conditions treatment. For the walls of the pipe, the slip wall condition is used (except the excitation velocity v term, which has to be specified). For the downstream boundary, the non-reflecting boundary conditions of Poinsot and Lele (1992) are used. The form of non-reflecting conditions is allowed to switch between that for non-reflecting inflow and outflow at each point on the boundary depending on the instantaneous local normal flow

velocity. Moreover, to isolate the interior of the domain from the effects of the boundary conditions, a buffer zone based on the approach of Hu (1997) is used on the nonreflecting boundaries. The buffer zone is an artificial boundary consists of non-uniform grids around the exit outlet where exponential damping terms are added to the governing equations. Buffer zone technique for computational Aeroacoustics is reviewed by Colonius (2004).

For numerical simulations, since the governing equations are not simply wave equations, but the full Navier-Stokes equations which support the propagating waves in the gaseous media. So we can have a separated wave source superimpose upon the flow field. Depending on the domain geometry and purposes, the excitation can be applied in different forms. The excitation signal is a specified velocity signal, while the pressure is floating depending on the local flow conditions.

The perturbation source can be a harmonic-wave generator of known frequency.

$$\text{Permanent harmonic forcing: } v_1(t) = V_0 \cdot \sin\left[2\pi(\omega_0)t\right] \tag{1}$$

$$\text{Finite-duration excitation: } v_2(t) = \begin{cases} V_0 \cdot \sin\left[2\pi(\omega_0)t\right], t \le t_c \\ 0, t > t_c \end{cases} \tag{2}$$

Temporarily, the excitation source is either permanent forcing (equation 1) or finite-duration-forcing (equation 2). The former provides a source of known frequency and phase, those frequencies close to its natural resonance have the largest response. It is commonly used to find the duct acoustics experimentally. The later is only used for a closed domain. Since the viscosity is small for wave propagation, let the wall damp those modes away from the natural frequencies. The wall will redistribute the acoustic energy in the frequency domain to fit the geometry. It is commonly recognized as the energy

transfer method for duct acoustics. Both methods can be used to find the acoustic response of the system.

For 2-D and 3-D simulations, the whitenoise (equation 3) is used to find the natural frequencies of the duct. This method is commonly used for the open domain, where a continuum of multi-mode excitation is supplied and let the duct select its natural frequencies

White noise excitation: $v_3(t) = V_0 \cdot 2 \cdot (randomnumber - 0.5)$ (3)

Here random number generator in Fortran generates a number in the range of (0,1), so we need to convert it into (-1,1). (The conversion is not important as the broadband frequency inherent in these random numbers).

4.2.3. 1-D acoustic solver

As will be provided later, the numerical simulations can provide details of mode information missing from the experiments. It is necessary to find a theory to explain such behaviors in a consistent way. The acoustic wave traveling in air can be treated as a pneumatic spring, thus we can make a direct comparison using the classical mass-spring theory. In this theory, the resonance of a multi-degree-of-freedom system is determined by its total inertia (mass) and elasticity (stiffness) (Kinsler, 1982).

The acoustic equation usually appears in a pressure form. A measurement of the pressure at a fixed location shows, roughly, a time dependence similar to that for the displacement of a simple mechanical oscillator. Hence, it is natural to suppose that the fluctuation of pressure satisfies the oscillator equation with damping constant α, natural frequency ω_0, and forcing $f(t)$.

$$\frac{d^2 p'}{dt^2} + 2\alpha \frac{d\, p'}{dt} + \omega_0 p' = f(t) \tag{4}$$

Analogy between the pressure perturbation and local displacement is already known. Here start from the Newton's law, the equation of motion based on displacement is set up as

$$M\frac{d^2 x}{dt^2} + R\frac{dx}{dt} + Kx = F_0 e^{j\omega t} \tag{5}$$

Where M, R, K are mass, resistance, and stiffness of the media respectively. $F_0 e^{j\omega t}$ is an external forcing of the sinusoidal function, where ω is the angular frequency. From the Ohm's law, it is established that the velocity is force over impedance, as in Equation (5)

$$v = \frac{F_T}{Z_T} = \frac{F_0 e^{j\omega t}}{j(M\omega - K/\omega) + R} = \frac{F_0 e^{j(\omega t - \beta)}}{\left\{(M\omega - K/\omega)^2 + R^2\right\}^{1/2}} \tag{5}$$

When the resonance happens, the impedance is lowest, which means

$$M\omega - K/\omega = 0 \tag{6}$$

Here we can set up the K and M for an infinitely small element as.

$$K = \gamma P \cdot A / dy \qquad\qquad m = \rho \cdot dy \cdot A \tag{7}$$

If treating this element as a piece of pneumatic spring, we can get a matrix of linear springs with individual stiffness and mass components. Then the system performance is determined by this multi-degree-of-freedom system. Each element forms a one-degree-of-freedom resonator, and the chamber boundary conditions allow solutions only at discrete modal frequencies. This idea was originally proposed by John Bernoulli and his son David and got its wide application on solid vibration problems. It is also restated (Culick and Yang, 1995) that a continuum, such as the gaseous environment inside a combustion chamber, is basically an infinite degree of freedom system.

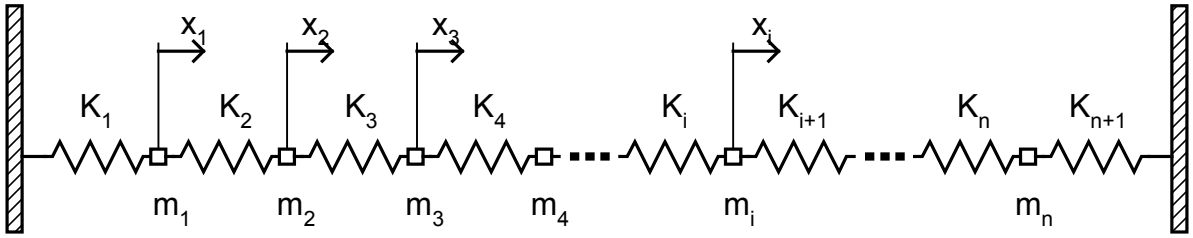

Figure 3. Distributed system approach

For each distributed node in a multidegree freedom system, we have the force balance.

$$m_i\ddot{x}_i - K_i x_{i-1} + (K_i + K_{i+1})x_i - K_{i+1}x_{i+1} = F_i \tag{8}$$

The resistance is assumed low (for acoustic wave in air). This can further be simplified as

$$[m]\{\ddot{x}\} - [K]\{x\} = \{F\} \tag{9}$$

where [M] and [K] are called the mass and the stiffness matrix, respectively, and are given by

$$[M] = \begin{bmatrix} m_1 & 0 & 0 & \dots & 0 \\ 0 & m_2 & 0 & \dots & 0 \\ & & & \dots & \\ 0 & 0 & 0 & \dots & m_n \end{bmatrix} \tag{10}$$

$$[K] = \begin{bmatrix} K_1 + K_2 & -K_2 & 0 & \dots & 0 \\ -K_2 & K_2 + K_3 & -K_3 & \dots & 0 \\ & & & \dots & \\ 0 & 0 & 0 & \dots & K_n + K_{n+1} \end{bmatrix} \tag{11}$$

For free vibrations, F is zero. The characteristic equation of the system is that the determinant equate to zero; that is

$$M^{-1}K - I\omega^2 = 0 \tag{12}$$

Equation (12) is commonly recognized as the eigenvalues problem. This is also known as the characteristics equation or frequency equation of the physical system. MATLAB provides a function EIG to solve equation 12 in this form:

$$[\omega^2 \quad X_i] = eig(M, K) \tag{13}$$

The roots ω_i^2 of the characteristic equation are called the eigenvalues, and they are the natural frequencies of the system. The eigenvector $[X_i]$ is the corresponding mode shape for vibration displacement. Such a solution is often referred to as being obtained by modal superposition or simply modal analysis. This is the physical model (mass-spring theory) approach to find the natural modes. More rigorous development can be found using Finite Element Technique, which will be provided in appendix.

Equation (10) (11) and (13) provide the governing equations for the characteristic system. To find the response of a specific system, we need to know the boundary conditions. If the domain is closed at both ends, there are n pieces of mass with n+2 stiffness constants. The springs at both ends should be counted twice. If one side is open, the number of stiffness will be n+1, since the open side spring does not work. This is the physical reasoning for the boundary condition.

The acoustic solver has no input requirement on signal generation, since it solves the characteristic equation and the eigenvalue analysis is fundamental to any mechanical system.

4.3. Result Analysis

To start with a simple case, the mixing chamber is simplified as a 1-D homogeneous domain with walls on both sides. The source velocity is specified on one side, and the pressure is floating depending on the boundary conditions. The acoustic modes are found by spectrum analysis and some statistical calculations.

For the auxiliary 1D configuration, there is not flow involved. So the density inhomogeneity is maintained fixed in position. It is realized via decoupling the species equation with others and enforcing the density profile at each time step. The acoustic wave will change the propagating speed and mode shape in the density inhomogeneity. Some pseudo-gases with a different molecular weight but same bulk modulus as air are tested within the background air. So the physics of acoustic propagation is preserved. Again the perturbation can only be measured statistically as done in experiments. This configuration will help to find the role of density inhomogeneity toward wave propagation.

For the above 1-D cases, the acoustic solver can solve the system response given the distribution of mass and elasticity via the eigenvalues analysis.

For 2-D simulation, the flow could not be set up realistically (Turbulence is in-essence a 3-D flow phenomenon), so an excitation of whitenoise is introduced into the uniform density chamber, and let the chamber wall to select (or damp) certain modes. Here the transverse mode is the main focus. Longitudinal modes could not be found due to the non-reflecting boundary treatment and the buffer layer treatment at the outlet. Unlike Longatte et al. (2000), where only Euler equations are used, here the full Navier-Stokes equations are used, so they are more sensitive to the backflows at the outlet.

For 3-D LES simulations, the variable density flows can be set-up into the domain. The purpose the flow is to maintain a density inhomogeneity. The transverse mode will be found based on the numerical measurement of pressure sensor. The mixing behavior of different excitation will researched based on the relationship between the hydrodynamic instability and excitation frequency. This will provide some insights on the density effect on the acoustic response of a certain chamber.

4.3.1. 1D analysis of transverse modes in homogeneous domain

For the standing wave problem in a tube, it is well established that the fundamental mode in an open-open tube is the half-wave mode ($f_1 = \frac{c}{2L}$), while the fundamental in a closed-open tube is the quarter-wave mode ($f_1 = \frac{c}{4L}$) (Kinsler, 1982). In this experiment, the injectors are sealed with an aluminum tape to avoid unnecessary cavity acoustics. The source speaker occupies a small fraction of the wall, so it is a condition of closed wall on both sides. Here the source speaker is simulated with a velocity generator on top of a wall. This arrangement has a problem that the resonance is so strong, that the acoustic wave growth will be limited only by non-linear effects, but the resonance frequency will be unaffected by this limitation. Figure 4 shows the response (pressure) signal in the numerical simulations. While the source has a perfect sine wave specified velocity, the response will have the perturbation due to the reflection at the walls. If the incoming and outgoing waves at the wall are out-of-phase (for example, f=900Hz, figure 5(a)), the response is a linear wave with some imposed high frequency term introduced by the geometry. If in-phase (f=1950Hz, figure 5(c)), then the pressure wave will be enhanced

upon each reflection at the wall, until limited by the non-linear effects (figure 5 (d)). This process is commonly recognized as resonance, which is most harmful for the safe operation of any combustors.

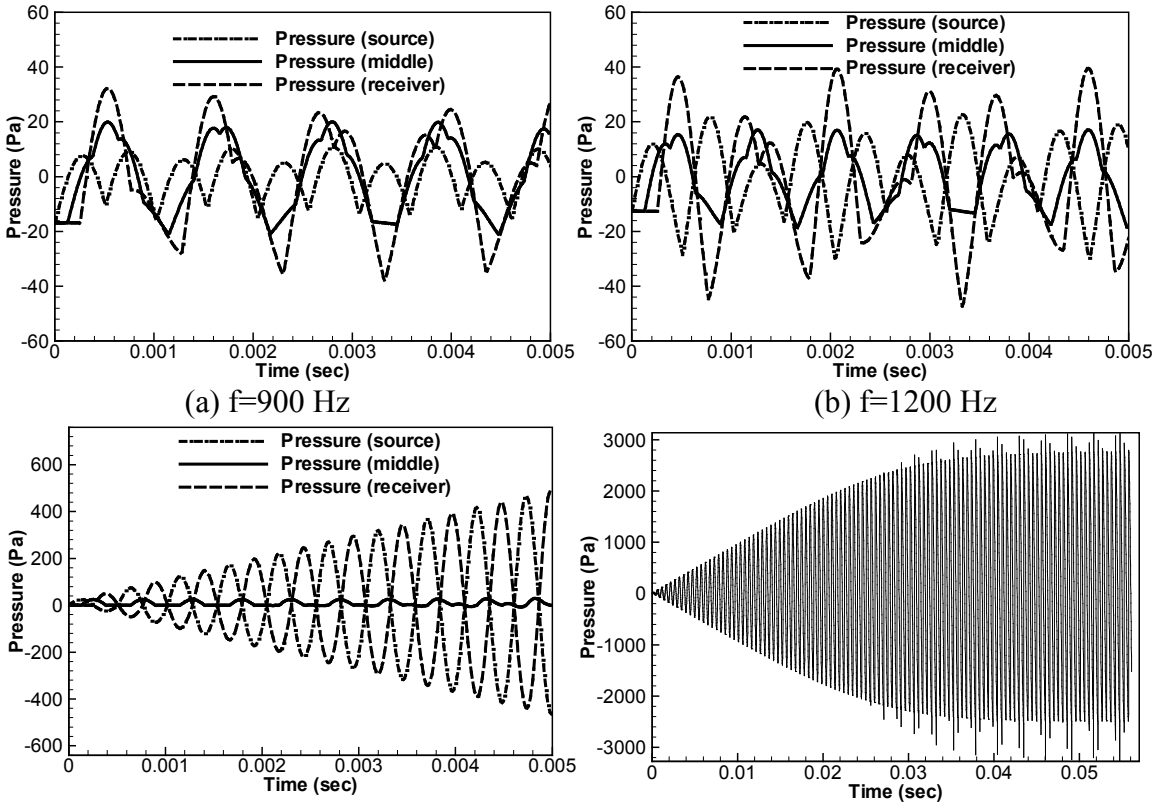

Figure 4. Time series of excitation (velocity) and pressure response for (a) f=900Hz; (b) f=1200Hz and (c) f=1955Hz. (d) is the pressure (receiver) signal in (c), but reaches the steady state due to non-linear effects.

The resonance behavior is better shown in the graph of mode shape (figure 5). The root-mean-square (RMS) pressure tells the spatial distribution of pressure fluctuation. Figure 5 shows that the pressure amplitude is enhanced at the resonance frequencies. For those harmonics, the pressure perturbation is symmetric and has a full integer number of cycles covering the domain. For those frequencies not harmonics (such as f=900 Hz in figure 5), the reflected wave are not in phase with the incoming wave, so the amplitude is small and

a steady state is reached quickly. Most passive combustion instability control methods utilize this property explicitly or implicitly.

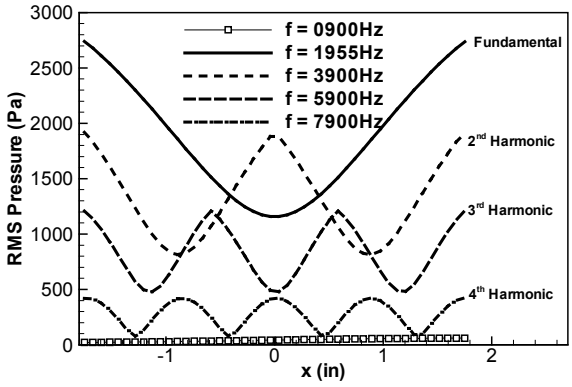

Figure 5. Pressure fluctuation level (mode shape) under different excitation frequencies

It is also observed that the pressure fluctuation is not zero at some nodes for both graphs. As will be discussed with mode analysis in figure 9, the pressure fluctuation here has the contributions from all excited harmonics. The node is defined as the zero pressure fluctuation point. The node for a certain frequency may not be the node for another harmonics. Here the mode shape is dominated by the fundamental harmonic, so it is still useful in predicting the resonance.

Knowing how the response pressure behaves temporally (figure 5) and spatially (figure 6), we can use this information to find the chamber characteristic acoustics. Figure 7 shows the acoustic response of a two-sides-closed domain on a variety of frequencies (The sampling point is on the receiver wall side). Here the mixing chamber is used and the injectors are sealed to avoid any unnecessary cavity acoustics. The pressure measurement is sampled at the receiver wall side. The resonance amplitude is finite, since it is limited by the non-linear effect (see figure 5(d)). From the relative strength of the response, it is found that the fundamental frequency is 1957Hz, while the theory gives

1951Hz for half wave mode ($f_1 = \frac{c}{2L}$, for two-sides closed pipe, listed in table 1). This discrepancy is mainly introduced by the choice of different acoustic speeds. The others harmonics are clearly shown to be full-integer multiples of the fundamental.

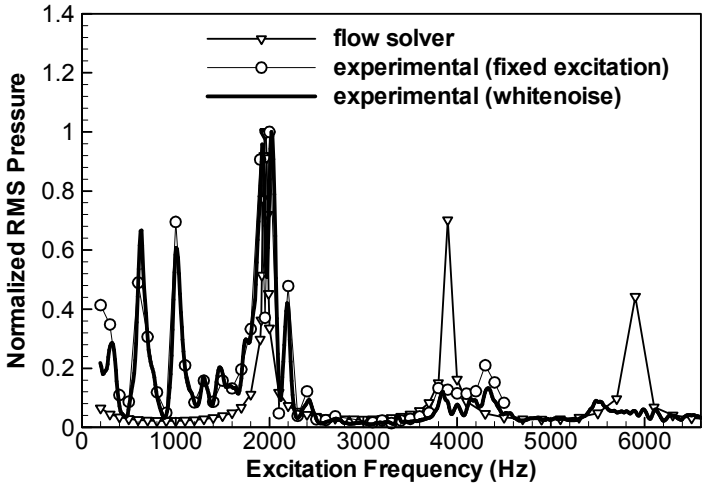

Figure 6. Acoustic response of 1-D domain between 2 walls

	first	second	third	forth	fifth
Longitudinal Modes (Hz)	228	684	1139	1595	2050
Transverse Modes (Hz)	1951	3903	5854	7806	9757

Table 1. Theoretical modes with first 5 harmonics (The numbers are based on the acoustic speed of 347.2m/s, which is based on 20 ^{o}C and 1 atm.)

The experimental data are gained via two methods (discrete forcing and whitenoise forcing). The excitation pressure amplitude is not a constant (constant voltage operation mode for the speaker), so the exact amplitude of pressure perturbation is unknown and not important here. For the discrete forcing, the sampling point is the closest to the receiver wall and the data are sampled at 100Hz intervals. For the continuous forcing, a whitenoise signal is introduced into the duct. It is found that both methods produce the same result. Here all signals are scaled by the maximum amplitude in each data series for comparison purposes. It is also found that the duct acoustic spectrum has many

contributions from the longitudinal modes. The first 3 peaks are those induced by the longitudinal modes. The peak at 1957 Hz and its multiples are those induced by transverse modes. The occurrences of these transverse harmonics are in good agreement with the theoretical prediction and numerical results.

The numerical results are gained through flow solver with velocity excitations. Only 1D configuration is used, so only the transverse modes are simulated here. The fundamental harmonic in the transverse mode is close to the fifth harmonic (2050 Hz = 9c/4/L) in the longitudinal mode, shows the limitation of this experimental arrangement in 1-D acoustics. In a rigid-wall waveguide, only plane waves propagate if the frequency of the sound is lower than the cutoff frequency of 0.5c/L (Kinsler, 1982), which is not our case here. The auxiliary test setup (figure 2) is designed to overcome this dimensional effect.

To determine the resonance frequency in a waveguide, the commonly used way is to introduce a whitenoise and let the boundary conditions to determine which frequency has the resonant effects (Kinsler, 1982). Here an energy transfer method can be used for the duct acoustics in a static domain. A wave of known frequency is introduced into the domain, and after the balance is reached, the source is shut-off. The residual acoustic energy will transfer into those dominant modes via the wall. The process is like a puff at the open end of an empty bottle, the buzzing will linger for some time before being damped completely. This buzzing is the initial excitation energy being transferred into the residual energy by the bottle walls.

A cyclic wave of 200Hz is introduced into the domain on the left side. It reached a steady state quickly, since the reflected wave is out-of-phase with the incoming wave, so the energy is quickly balanced. Then the source is shut-off, leaving the residual energy

trapped inside and being worked by the wall over time. The frequency spectrum shown in figure 7(c) is that before the shutoff and figure 7(d) is that after shut-off. All raw data are treated with Hamming windows before FFT, which is good at increasing the signal-noise-ratio for this situation.

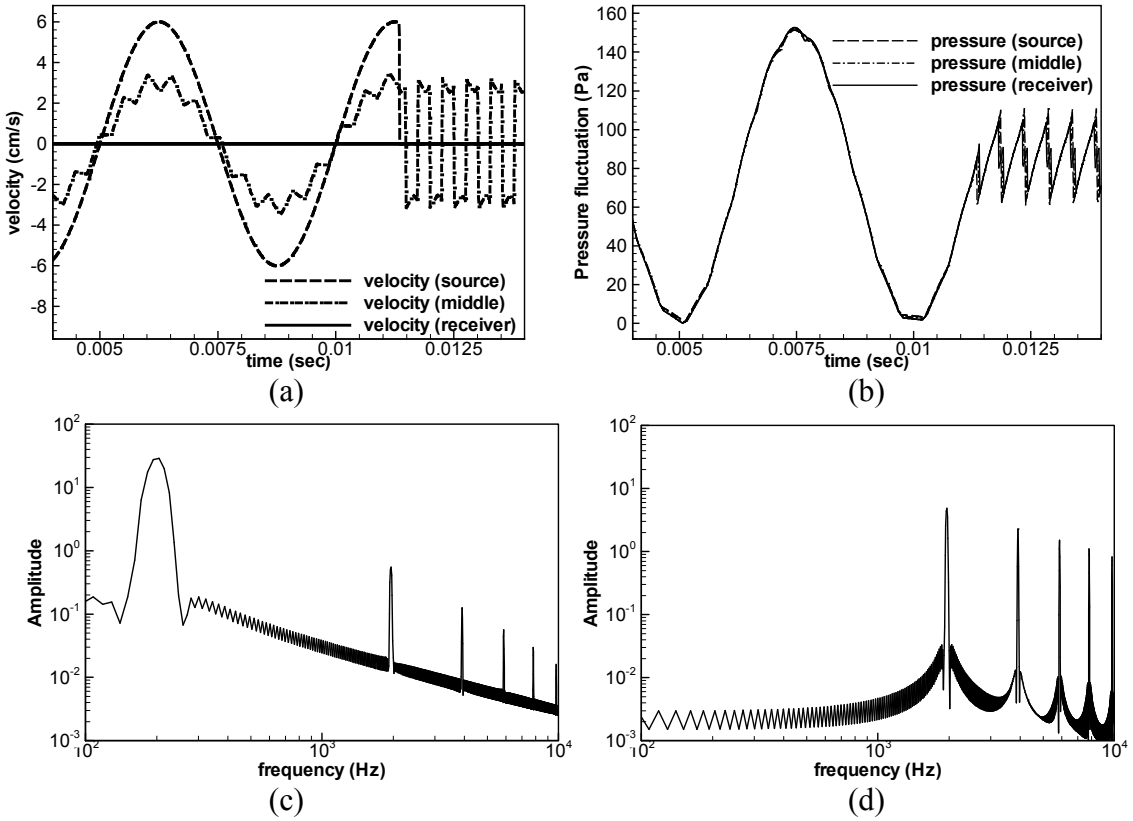

Figure 7: Wall effect on mode selection. (a) Velocity before and after shutoff; (b) pressure before and after shutoff; (c) spectrum before the shutoff; (c) spectrum after the shutoff

The left figure shows that even in the cyclic forcing mode, the pressure spectrum has its characteristic harmonics due to the wall. After the source signal shutoff (right figure), the residue acoustic energy redistribute in spectrum from 200Hz to its geometry-dependent value, the harmonics, but not simply into the fundamental harmonic. This is the reason

that even under the excitation of the fundamental harmonic, the center pressure fluctuation is not zero (figure 5), but has the contributions from other harmonics. When decomposed into normal modes (as seen in figure 8), the pressure fluctuation at each harmonic has zero fluctuation point(s), i.e., pressure nodes. This method can be used to find the acoustic response for a non-homogeneous flow field, as will be discussed next.

Since almost all mechanical structures have their own natural modes of vibration (dynamic response), the modal analysis can help us understand the nature of resonance in any domain. These modes can be readily computed given the elastic and inertia characteristics of the structure. Here the gaseous medium is treated as a coupled system of mass spring arrangement. When assembled together, the stiffness (elasticity) matrix and the mass (inertia) matrix can be used to find the system eigenvalues (natural/resonant frequencies) and eigenvectors (spatial-temporal mode structure).

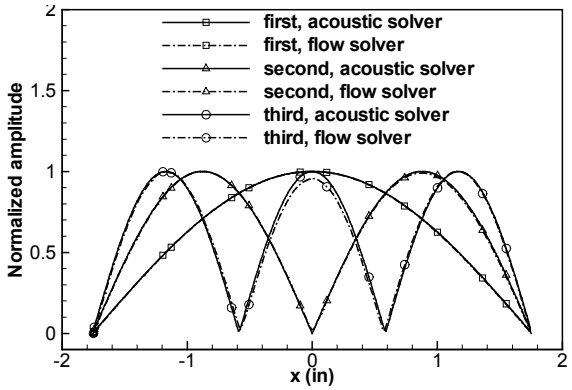

Figure 8: Mode shape for velocity fluctuation (Flow solver) and displacement (Acoustic solver)

A comparison of flow solver (via statistical analysis) result and acoustic solver (via eigen value analysis) result is shown in figure 8. They are normalized to unity for comparison purpose. For the numerical simulations, the characteristic displacement used in the eigenvectors is most closely related to the velocity fluctuation, since they share the same

governing equation (Helmholtz wave equation) and the same boundary conditions (no-slip wall on both sides). By definition, the velocity is the time derivative of the displacement. So they share the same governing equations in steady state.

It is found that the characteristic displacement from the acoustic solver has the same mode shape as the velocities fluctuations for the flow solver. The only difference is the velocities shown here are RMS values (always positive). Beside this difference, they are exactly the same, which means these theoretical mode shapes can be used to validate each other.

A further experimental validation of the mode shape is shown (figure 9) below. Here the pressure is chosen since it is easily measurable. The acoustic wave is manifested more as a pressure perturbation wave than a velocity perturbation wave. The rescaled pressure RMS fluctuations fit well with the predicted mode shape. Due to the limited number of pressure measurements, the experimental data could not match the numerical simulation completely. According to Nyquist Sampling rule, the number of pressure samplings is far from enough to produce the perturbation structure in the domain. Given the numerical results known, the experimental result can be better explained from the theory. Here for f=1900Hz and f=3900Hz, which are close to the harmonics in the domain, the acoustic structure is symmetric, while for f=900Hz and f=2900Hz, the structure is asymmetric. The numerical result provides details that are unavailable in the experiments, while the experimental results validate the theory qualitatively.

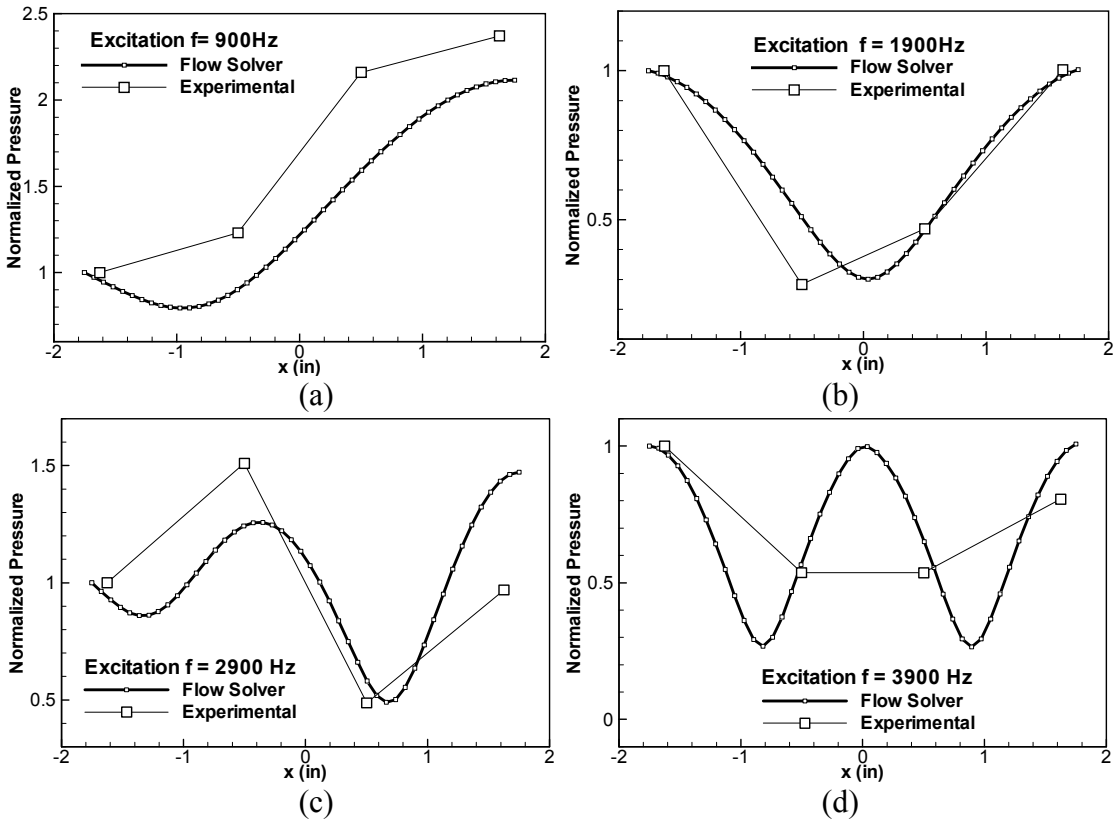

Figure 9: Mode shape comparison with experimental data

4.3.2. 1-D analysis of transverse modes in inhomogeneous domain

The incoming acoustic/pressure wave will experience the reflection and transmission behavior at the density interface. For a general density interface, there is no separation or interpenetration of the two media at the boundary. So the continuity of displacement and velocity at the interface is valid. Also the interface can be treated as a free-body diagram of forces acting on a thin layer of material, where the pressures on either side of the layer are equal. These two boundary conditions form the basis for analyzing the wave behavior at the interface.

From the above boundary conditions, it can be found in most textbooks (for example, see Kinsler, 2005) on acoustics that the amplitude ratio of the reflected acoustic (pressure) wave to the incoming wave is

$$\frac{A_r}{A_i} = \frac{\rho_2 c_2 - \rho_1 c_1}{\rho_1 c_1 + \rho_2 c_2} = \frac{r_{12} - 1}{r_{12} + 1} \tag{20}$$

Where $r_{12} = \frac{\rho_2 c_2}{\rho_1 c_1}$ is the ratio of impedance (ρc) at the density interface. From this equation (20), we can find the reflected pressure is in-phase with the incident pressure if $\rho_2 c_2 > \rho_1 c_1$ (figure 10d), otherwise, the reflected wave is out-of-phase when traveling from high to low-density fluid (figure 10b). If the interface is between gas and wall, which means $\rho_2 c_2 \to \infty$, the incoming wave is 100% bounced back and in-phase (figure 10f).

The amplitude ratio of the transmitted wave to the incoming wave is

$$\frac{A_t}{A_i} = \frac{2\rho_2 c_2}{\rho_1 c_1 + \rho_2 c_2} = \frac{2r_{12}}{1 + r_{12}} \tag{21}$$

From this equation, there is no phase change between incoming and transmitted waves. The amplitude of transmitted wave will be higher or lower solely depending the impedance ratio r_{12}. According to the conservation of the acoustic energy, we will have

$$\left(\frac{A_r}{A_i}\right)^2 + \left(\frac{A_t}{A_i}\right)^2 = \frac{A_i^2}{A_i^2} = 1 \tag{22}$$

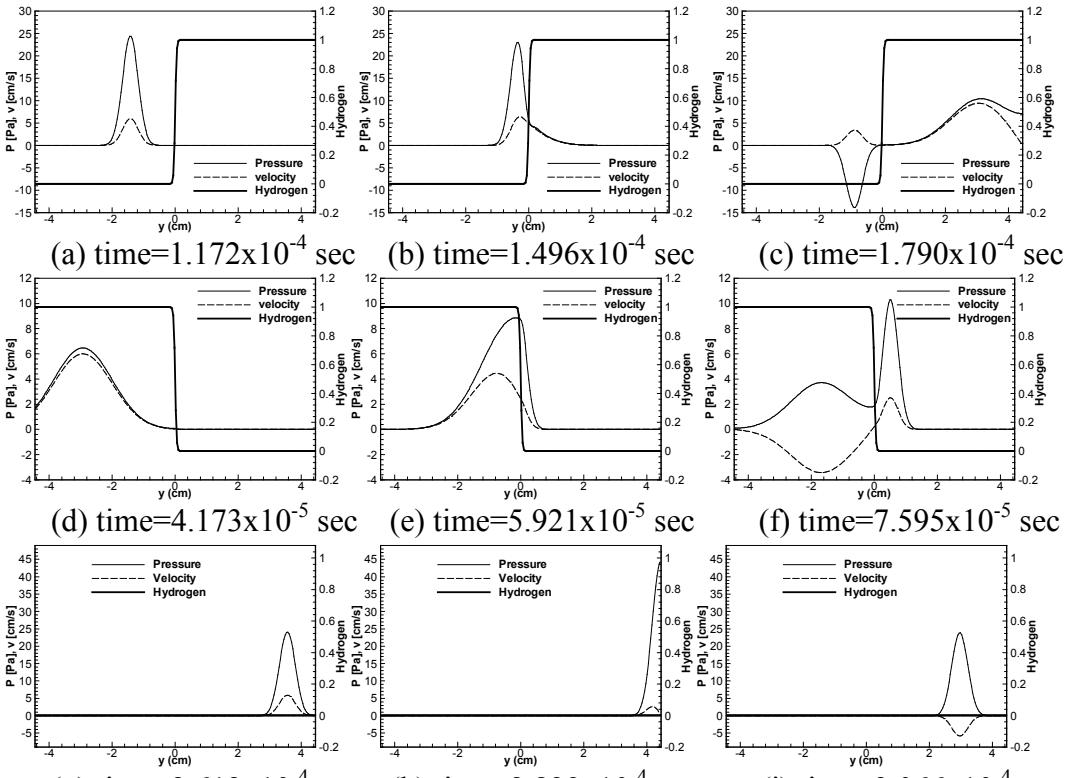

(a) time=1.172×10^{-4} sec (b) time=1.496×10^{-4} sec (c) time=1.790×10^{-4} sec

(d) time=4.173×10^{-5} sec (e) time=5.921×10^{-5} sec (f) time=7.595×10^{-5} sec

(g) time=2.612×10^{-4} sec (h) time=2.839×10^{-4} sec (i) time=3.066×10^{-4} sec

Figure 10: Traveling wave behavior at different density interfaces

Figure 10 shows the transmission and reflection behavior for a single incoming Gaussian-shaped wave. They are generated using the flow solver and show the time-evolution result of velocity and pressure at high-to-low-density interface (a~c), low-to-high-density interface (d~f), and wall interface (g~h). The default/background gas is air (28.84g/mol). Here the wall is treated as the infinite density difference, where all outgoing waves are bounced back into the computational domain completely. From the above relationship (for acoustic pressure only), the amplitude change of the incoming, reflecting and transmitting waves are clearly defined and computable. It is also observed that the pressure fluctuation is smaller and wider in low-density zone due to its high acoustic speed, and higher and thinner in high-density zone due to its low acoustic speed. This is the reason proposed by G.G. Stokes (1867) on successfully explaining the hydrogen-in-air stifling sound phenomena.

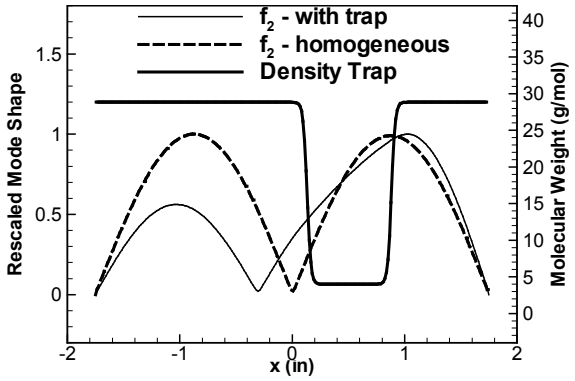

Figure 11. Mode shape with and without a density trap (for the second harmonic only: f2=3899Hz for homogeneous domain, and f2=5078Hz for density-stratified domain)

	first	second	third	forth	fifth
Transverse modes (without density trap)	1949	3899	5848	7797	9746
Transverse modes (with density trap)	2420	5078	6455	9816	13129

Table 2. Theoretical transverse modes with first 5 harmonics with and without density trap

Mode shape can further be used to understand the resonance behavior in a closed domain with a density trap. Here in figure 11, a mode shape for the second harmonic is generated (using the acoustic solver) to show the effect of the inhomogeneity on the mode structure. Here the inhomogeneity is introduced not at the center (to break the symmetry). Basically, the mode shapes are all changed (or more precisely stretched) over the low-density part. The full integer number of cycles over the closed domain is preserved for the resonance frequencies, since the zero amplitude at the wall is determined by the boundary conditions. Comparing with the homogeneous case, the low-density zone has a larger fluctuation and the zero-amplitude node is shifted. This information is important for the placement of pressure sensors, which are sensitive to the location of pressure nodes. It is expected that with a priori knowledge of the mode shape, the pressure sensor can record the power spectrum and the acoustic field better by avoiding these nodes. The

frequency shift due to the location and profile of density trap is listed in table 2, and will be discussed more in figure 15/16/17.

Once we know the wave behavior at the density interface and mode structure for inhomogeneous field, it is natural to find some experimental results to validate the theory. Here the experimental setup in figure 1 is not good enough for setting-up variable density field. The inhomogeneous flow is easy to set up, but the injector will bring some cavity noise and the 3-D effects are strong (as shown in figure 6). So we devised the simple arrangement in figure 2 to test the role of a static density inhomogeneity on the transverse modes.

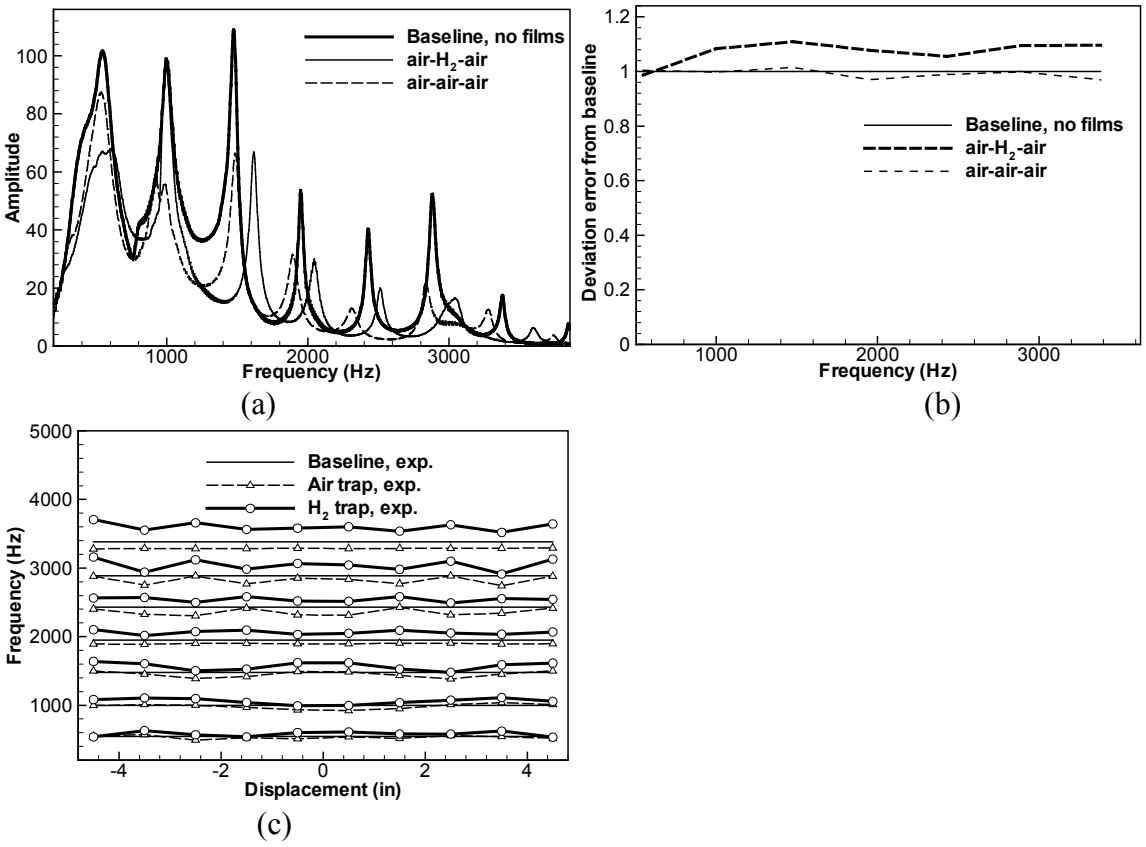

Figure 12. Frequency response of the density trap (a)FFT spectrum for sampling point near the center (b)Comparison with theory (c) measurements at different positions

Figure 12 shows the frequency response of different density trap positions. Displacement means the distance from the center of the density trap to the center of the domain. The

frequency values are local peaks on the power spectrum. They are obtained via converting the raw signal into the frequency domain (using FFT) as shown in figure 12(a). Here the trap is placed near the center of the domain. The frequency shift due to the films and the hydrogen trap is also shown. The difference introduced by the films and the hydrogen trap is better presented in figure 12(b). It clearly shows that the effect of films is to decrease the resonance frequency since the density of the film is higher than the air. The hydrogen introduced as a light medium, so the resonance frequencies are higher even with the films. Figure 12(c) shows the frequency shift at different position by the films and the trap. The base line case is the 14 inch pipe with air inside only, to serve as the reference. With a 5-inch air trap (plus 2 plastic films on both sides), the response frequency change is small, only some phase change due to the position changes. The air-trap can be looked as a heavy density trap (The density of the film is larger than the air), so the characteristic frequencies are a little lower than the baseline case. The hydrogen trap case (with 2 films) has a significant frequency shift, but the phase change is almost the same as the air-trap-only case. So it is believed that the 2 films will introduce some phase change due to the elasticity of the film, while the hydrogen trap will cause a frequency shift systematically.

The experimental hydrogen trap case is predicted with the numerical result from the acoustic solver (figure 13). Here the numerical result is based on a density profile without any correction for the plastic films. The f2 and f3 are correctly predicted, while the high frequency responses show some phase difference. The film has some effect under high frequency noise, while transparent to the acoustic wave of f2 and f3.

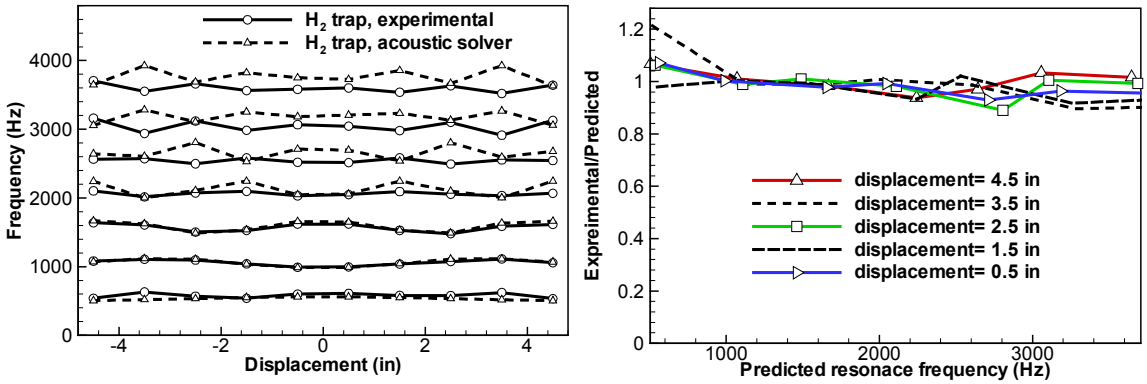

Figure 13. Comparison with analytical predictions (left) and Experimental vs. Predictions at 5 positions on one side (right).

If given the element (or pneumatic spring) at the position of the films with more mass to mimic the film (here only 2 points with 10 times of the original mass), the frequency response will be improved (as shown in figure 14.). Though there are still some phase difference, the magnitude of higher harmonics are closer to the experimental data. It is equivalent to say that adding the mass effect of the film will improve the prediction. Further improvement is not made, since the film modulus is missing and it is not worthwhile to model the impact of the film separately. It has a minor effect on the frequency shift introduced by the density trap.

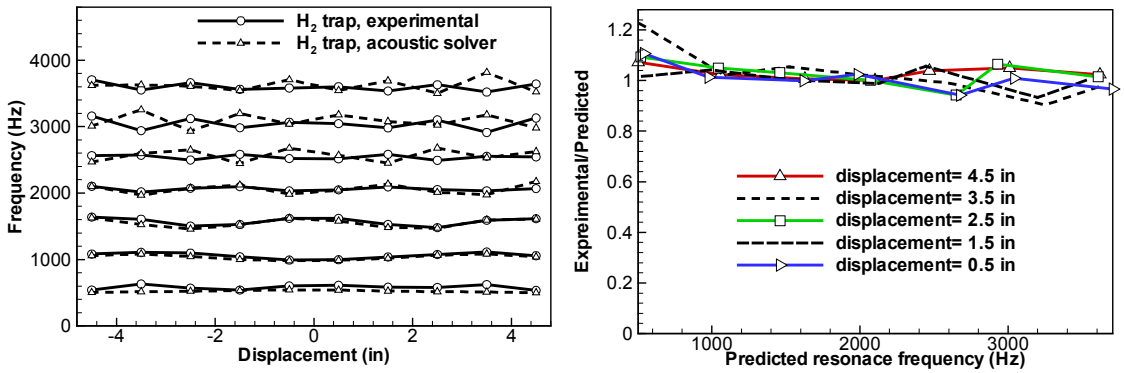

Figure 14. Better prediction with improved film effects.

Having partially validated the solvers in inhomogeneous field, we can make some predictions on the role of the inhomogeneous zone on the duct acoustics. The experimental validation is difficult to perform, so we will use these two solvers to validate each other. The purpose of these tests is to find the acoustic response of a closed system with density and location effects.

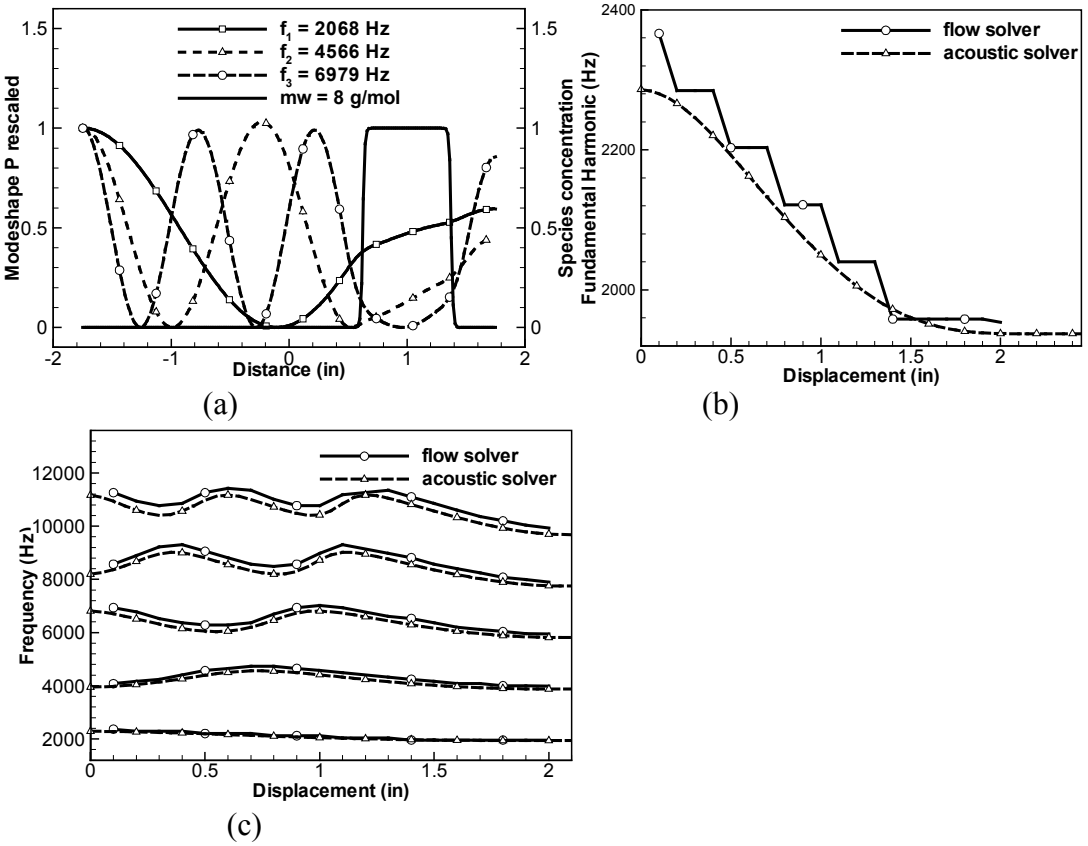

Figure 15. Mode selection on the position of a light density trap (mw=8g/mol)(a) mode shape (b) fundamental harmonic (c) other harmonics

Figure 15 shows the pressure mode shape and the mode selection on the different positions of a light density trap. The molecular weight of the density trap is 8 g/mol out of 28.84 g/mol (air). The trap is 0.75 inch in width (top-hat profile) and moves from the center (zero displacement) to the right until out of the domain. The pressure mode shapes are those at the instant when the displacement is 1 inch from the center (figure 15(a)).

Consistent with figure 11, the pressure fluctuation level is lower in the trap. Again the light density trap stretches the mode shapes. The frequency shift for the fundamental harmonic is shown in figure 15(b). The result from the acoustic solver is also shown with the dashed lines. The trends are closely preserved and the prediction difference comes from the number of points for spectrum analysis (for flow solver) and the number of pneumatic springs for mass-spring analysis (for acoustic solver). This difference is expected to diminish with finer grids in both cases.

The frequency shift for other harmonics is shown in figure 15(c). Only the fundamental harmonics is monotonously decreasing and transits to the value in the homogeneous field of air, while the other harmonics follow a pattern that looks like a mode shape. Physically, it means the acoustic wave of the fundamental harmonic travels once across all media, while the other waves travel more than once locally (near the density interfaces). The global effect is that the system response is a function of local position and local density. This provides the possibility to avoid certain acoustic modes via initial design control. In theory, all system response can be controlled by organizing the position and strength of the density inhomogeneity. And this is implicitly practiced in the pass liquid rocket engine development (Hulka et al. 1995). In reality, shifted system response may be another acoustic modes to be damped. So there sill need some research work on predicting the onset of resonance in a combustor. Our work is a step forward on completely avoiding the resonance in a combustor.

This prediction can be used to explain the experimental result reported by Marshall et al. (2006). They provide carefully designed combustor details and use 1-D unsteady Euler equation solver for numerical simulations. All effects, including wall, density, flow and

combustion, are involved in modeling the acoustics. Here we find their result on the acoustic response to different injector locations supportive to our needs. In studying transverse modes, the location of the single injector is varied to find the system response. The fundamental harmonic for the injector near wall is around 2700 Hz, while the same harmonic is shifted to 3900 Hz when the location is moved to the center. The second harmonic is almost unchanged (around 5000Hz). We made following observations according to our theory:

> The advanced harmonics are no longer full integer multiple of the fundamental harmonics, because the density field is no longer homogeneous.
>
> The centerline light density trap has the highest fundamental harmonic. The fundamental frequency will decrease when shifted to the wall side. That is to say, the injector (or the density trap) near the center will have a larger role on changing the duct acoustics.
>
> The second harmonic can be the same with different positions of the density trap (injector with combustion), since they are not the monotonous function of the location.

Their result is consistent with our result. It seems possible to make a prediction of the characteristic response based on the measured density profile, given the concentration and temperature distribution in the domain.

A similar prediction is performed on the position of the heavy density trap. Again the pressure fluctuation in the trap is higher, and the mode shapes are distorted by the trap and its position (figure 16(a)). The mode selection on the right figure is correctly performed and predicted (figure 16(b)(c)).

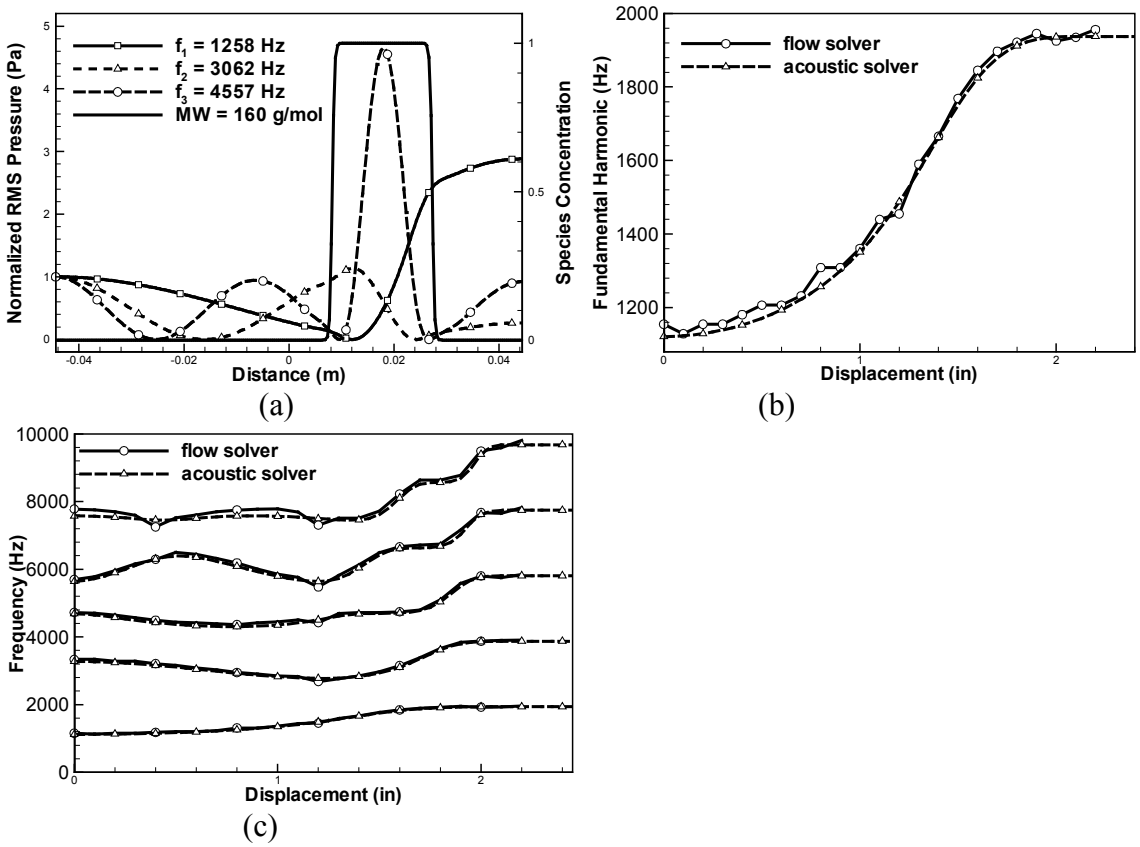

Figure 16. Mode selection on the position of a heavy density trap (mw=160g/mol)

A further study is to find the role of the trap width on mode selection. Here we have only a light density trap and expands until flooding the domain (figure 17a). Thus we have a smooth transition from one medium to another, which is correctly predicted on the right figure. It is noticed that the transition for higher harmonics are not monotonous, probably due to the complex coupling between the two density interface and the two walls.

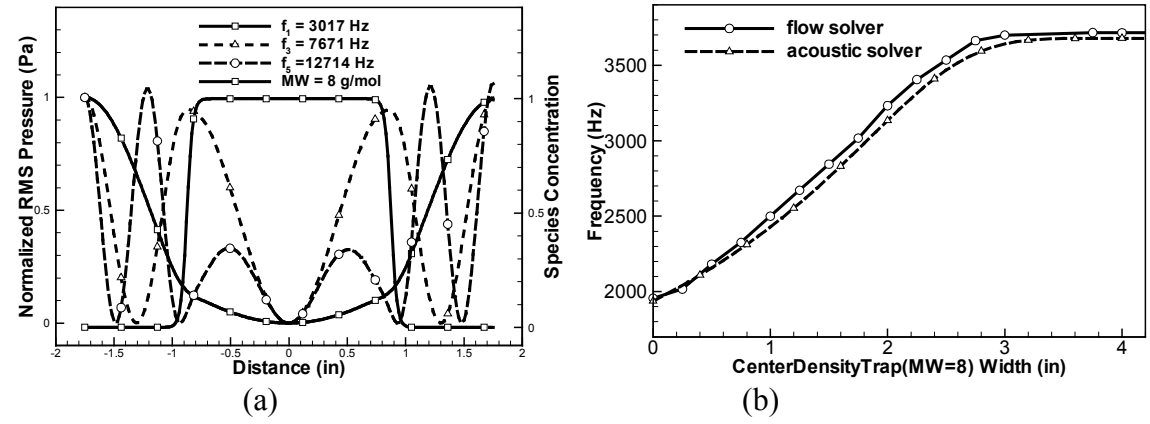

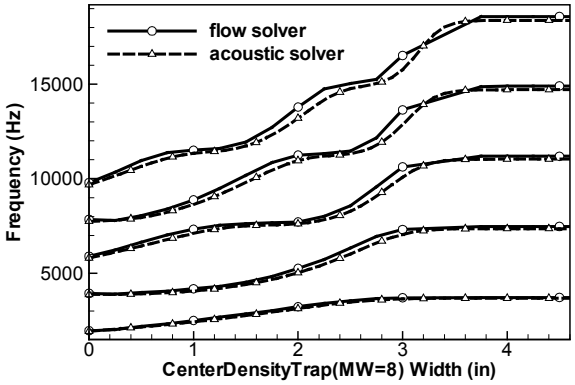

(c)

Figure 17. Density trap width and its role on harmonics

It is no surprise that the two solvers produced almost the same prediction on the density and location effects. The characteristic harmonics are the system response of any mechanical system. With the same mass (inertia), stiffness (elasticity) and the boundary condition, both solvers behaves properly.

The above successful simulation and prediction seems to pave the way for an inverse problem approach to find the density position, width and/or profile in an acoustically excited flow field. The theory says yes while in reality we need to measure the higher order harmonics, which is low in energy, and the background noise is usually strong. The 2D or 3D acoustics is further complicated by the geometry functions and the source terms inside the domain. In some simpler cases, such as those encountered in underwater acoustics, the inverse acoustic problem is actively researched (Taroudakis et al., 2001).

4.3.3. 2-D simulations of chamber acoustics in a homogeneous domain

Real combustion-instability problem are mostly 3-dimensional flow with reactions within a certain chamber. Here with the flow solver, we can find the chamber acoustic modes in a 2-D domain without flow and density effects. Here the source is the sinusoidal wave generator modulated by the amplitude of whitenoise. The whitenoise is generated based

on the random number generator in FORTRAN and the Gaussian distribution function (Press et al., 1996).

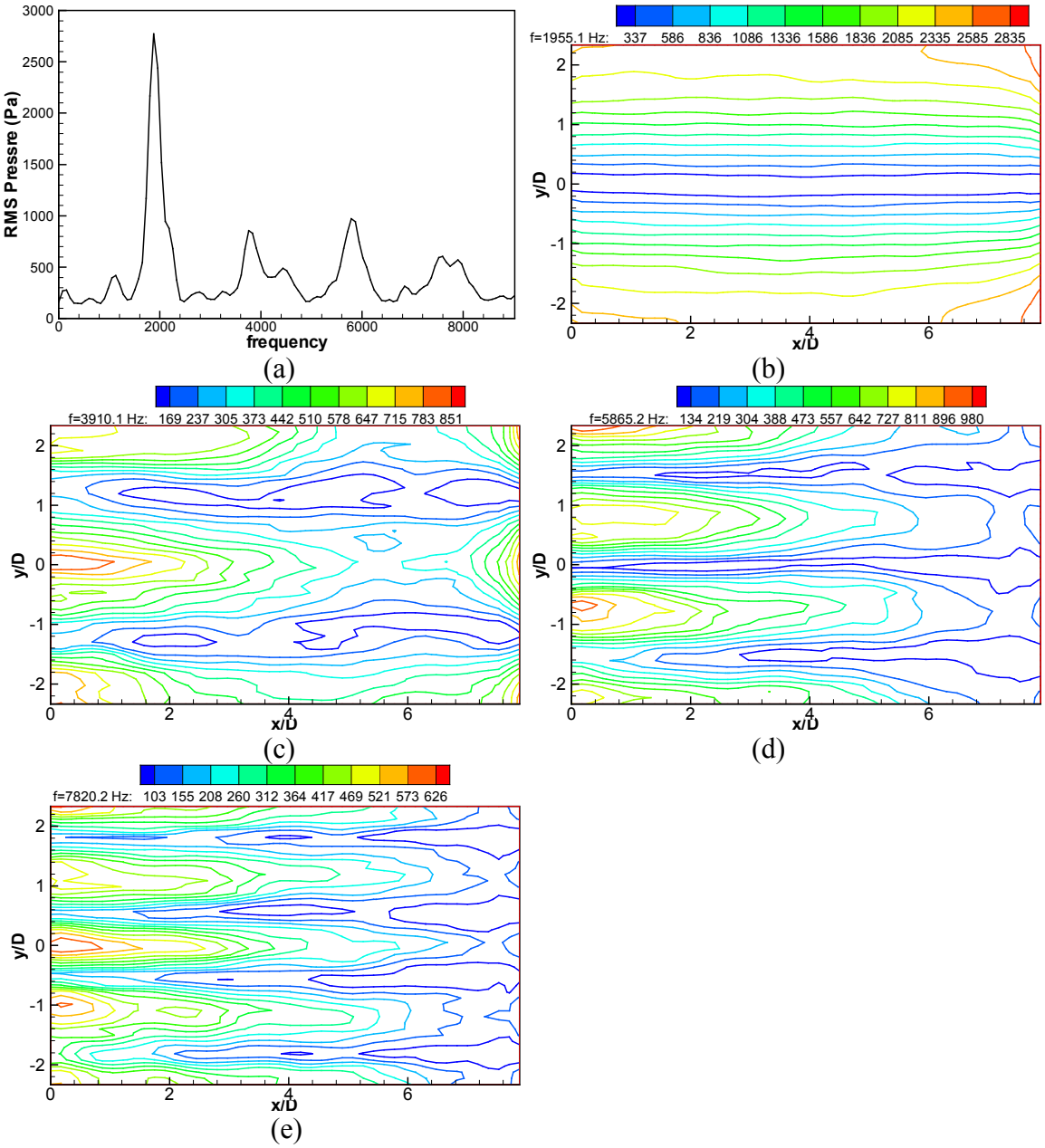

Figure 18. 2-D DNS simulation of acoustic waves (whitenoise) in homogeneous chamber a) spectrum at the wall opposite to speaker, pressure fluctuation at b) f=1955Hz, c) f=3910Hz, d) f=5856Hz, e) f=7820Hz.

Figure 18(a) shows the spectrum response of pressure sampling at the wall opposite to the excitation speaker. The transverse modes are clearly shown. It is also observed that the amplitude of these modes is variable depending on locations, so the amplitude distribution for these modes (b/c/d/e) are selected to show the patterns of these modes. This result is consistent with previous 1-D simulations, and also with the mode pattern studies of Longatte et al. (2000). No matter what is the source of the speaker, the chamber will select its preferred modes based on the boundary conditions. The correct prediction of these modes shows the right boundary treatment in this code.

4.3.4. 3-D simulations of chamber acoustics with inhomogeneous flow

In real test conditions, the density in-homogeneity is maintained within streams in a complex domain (injector cavities, flow dampers, acoustic-liner, etc.). So we need to simulate a 3D flow to show the capability of the flow solver under these conditions. Here the Smagorinsky model is used to provide the additional turbulent viscosity for the stabilization of the computation. For the safety operating conditions, the Helium is chosen as the light gas instead of hydrogen, while the heavy gas is the normal air. The flow solver uses a constant ratio of specific heats, while this ratio for Helium is different from the common di-atomic gases. This will cause a minor effect by different bulk-moduli of the medium. Since some flow parameters (turbulence level, initial pressure drop, etc) are missing, and the jet profile measurement also has some uncertainties, we accept this error.

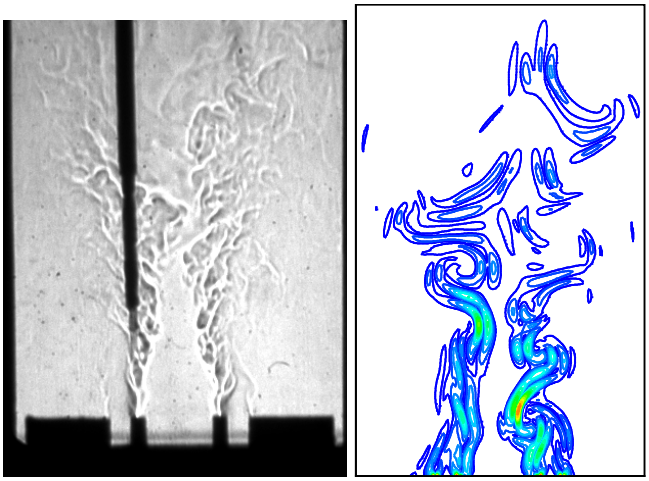

Figure 19. Snapshot of inhomogeneous flows a) Schlieren image in experiments. b) Numerical Schlieren image.

Here the flows in experiment and simulation are shown in figure 19. The black sensor in the helium stream is a hotwire for velocity measurement. The Schlieren image is the common method for density variable flows. The numerical Schlieren image is based on the second order derivative of the density field. Due to the dissipative nature of Smagorinsky model, the fine turbulence structure in the experiment is smoothed in the numerical result.

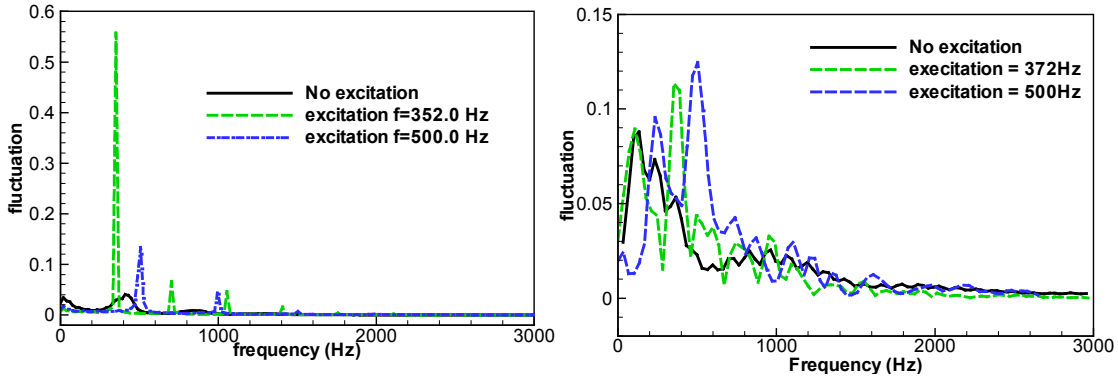

(a) Experimental (b) numerical

Figure 20. Spectral measurement in the acoustically excited flows. The role of acoustic excitation on the density-variable flow is shown in figure 20. The sampling point is 2cm

from the injector plane and 3.5 cm from the speaker (transversely). For the unforced cases, the experimental results (a) are subject to various mechanism of flow instability (flow instability and longitudinal acoustic mode), while the numerical test on the right (b) are predominantly perturbed by the initial forcing. This artificial perturbation is a little strong (comparing with experiments) and mostly covers the low frequency range (near 120 Hz). These frequencies are subject to the impact of the outflow boundary treatment, where a buffer layer is imposed. For the sideway acoustically excited cases, both graphs show that the specified mode will be excited in the stream, no matter whether the excitation is related to a peak or valley (in spectrum diagram) or not. The external forcing will modulate the flow and lead to an enhanced mode, while the neighboring modes are suppressed. For the numerical streams, the initial turbulence forcing creates significant perturbation in the low frequency range. Though not significant as the experimental result, the effect of modulation is observable. Here the data for statistical analysis is about 10 cycles (of excitation) comparing with more than 1000 cycles in the experiment. So the peak amplitude is still under-resolved as the experiment. Longer simulation time will produce better statistics.

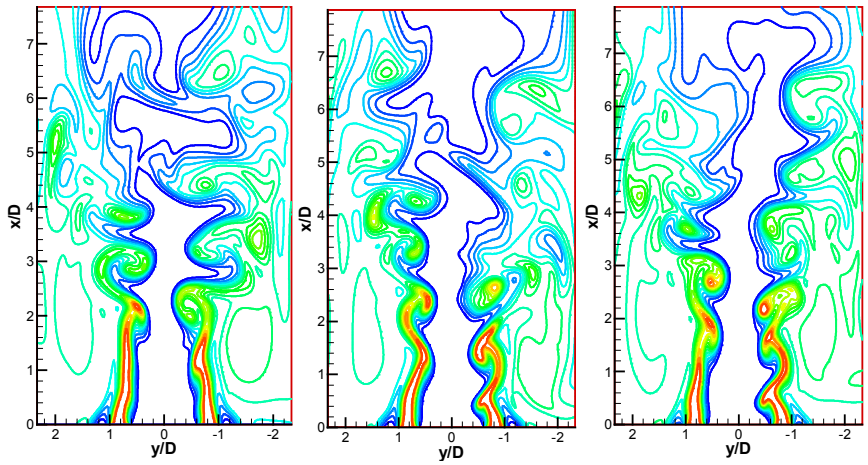

Snapshots: a) unexcited b) excited with 372Hz c) excited with 500Hz

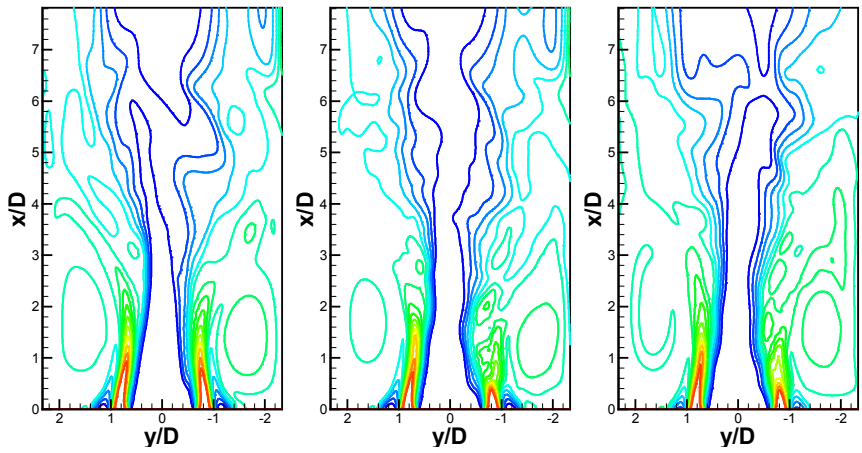

Averaged-shots: d) unexcited e) excited with 372Hz f) excited with 500Hz

Figure 21. Effect of acoustic excitation on the density stratified flow field.

The role of excitation is also shown in figure 21. Here the streams are superimposed with a turbulence spectrum (Passot et al. 1986). So the flow will transit into turbulence in a later stage. The acoustic source will modulate the flow with its inherent frequency, so the vortex is generated earlier due to the external forcing. The right stream is perturbed more than the left stream due to its proximity to the source.

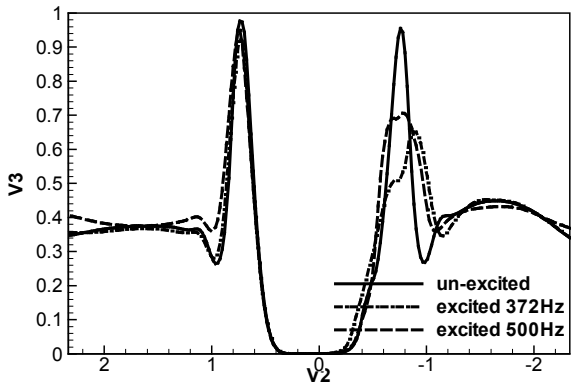

Figure 22: Averaged species profile at x/D=0.75.

The effect of mixing is shown in figure 22. Here all 3 averaged species profile at x/D=0.75 are shown. The excitation of 372Hz has the better mixing effect, since it is the most dominant mode in the unforced streams. The acoustic mode close to the jet preferred mode would have the most significant effect on the mixing, which is also

shown in figure 21. This enhanced mixing effect is also studied by Richecoeur, et al. (2006).

4.4. Discussion and future work

4.4.1. Summary of the simulation

For the plane variable-density streams simulation, the domain size is 15 cm with a jet speed of 6 m/s, so the flow-through time is 0.025 sec. The characteristic length scale is ¼ inch, or 0.00635m. The jet Re number is 6781 (based on the Helium speed and Helium plane jet width), the Mach number is 0.052 for the jet velocity, and Richardson number is zero (no gravitational force).

A grid resolution study shows that for such a Re=6781 flow ($\mathrm{Re}_t \approx 1356$), the DNS resolution is on the order of 28.4 μm, while the resolution for a well resolved LES is 158.8 μm (based on jet thickness divided by 40), as compared to the current choice (dx=395 μm). The cost ratios for DNS over LES based on the above choices are 978 and 37420, respectively. Only the last one is chosen here due to the limitation of computing resources. The advantage of LES over DNS for such a high-Re flow problem is obvious.

4.4.2. Brief overview of the previous experimental work on LRE

The fire triangle is well established for analyzing the fire prevention and suppression problems. Here the noise is unwanted sound, just like the fire is unwanted combustion. So we can setup a combustion noise triangle following the fire triangle. Removing any of the 3 elements in the fire triangle will lead to un-sustained combustion. Similarly, improving any of the 3 elements in combustion noise triangle will lead to stable

combustion without combustion oscillations. A review of the literature shows most of the research in combustion instability control focused on either the source or the boundary, while there is not enough understanding on the media supporting the propagation of the sound waves. It is the main purpose of the paper to find the role of medium density in selectively supporting the acoustic waves.

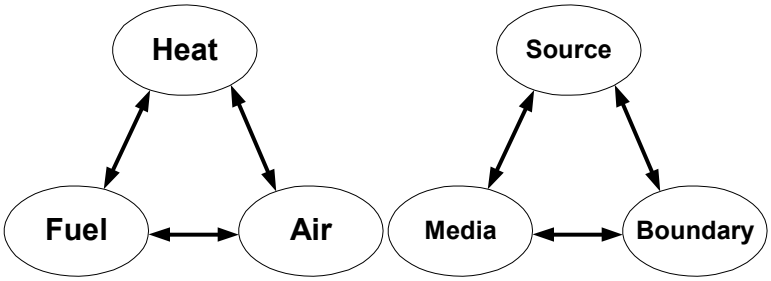

Figure 23. Analogy between fire triangle and combustion noise triangle

According to Culick and Yang (1995), the term "passive control" means the change of the geometry parameters to suppress acoustic waves in the chamber. Usually the passive part means the baffles, resonators, or acoustic liners which need no additional energy to suppress the noise. So it is a modification to the boundary. The essential point is to force the resonance to occur in frequency ranges where the driving mechanisms are inadequate to sustain oscillations or to directly damp the mechanical energy of unsteady motions. The effectiveness of the baffles is associated with the possibility for shadowing regions of sensitive processes from disturbances. Whatever devices are used, limitations always arise because of the issues such as the rigid frequency response, the structural integrity and the flow loss, etc.

Active control of combustion instabilities has received more attention recently since the limitation of passive control is well understood. The most important means of control is to control the supply of propellant. The transfer function for pressure and controlling

force is established very early, but the instrumentation and transducers limit this method from successfully controlling the noise. Also the internal process for propellant supply is lacking understanding. So this method is far from mature. A second method is based on the idea of antisound in which destructive interference is caused by injecting an appropriate acoustic field to cancel unwanted noise. There is a series of applications with various means to generate antisound, including using a secondary flame to produce the noise anti-phase with the primary noise source. Since the acoustic energy is only a tiny fraction of the chemical energy released in combustion, it is hoped that an acoustic source, such as a loudspeaker, primary fuel control or secondary fuel control will lead an acoustic source into the field. This source is anti-phase with the original source, so the noise is cancelled or damped. This idea works for some simple laminar flame apparatus, such as Rijke tube, and some limited work on real combustors. The main problem is a lack of the understanding on combustion noise generation process and the complexity of the turbulent mixing. The problem lingers as when, where and how to introduce the antisound, so current experiments are mostly simple and one-dimensional.

Due to the high density of energy release in a volume having relatively low losses, conditions normally favor excitation and the source of excitation is difficult to remove. Though not explicitly stated, the density effects were utilized in finding the instability boundaries for some combustors. For example, the importance of propellant density on the combustion instability problem was long recognized in the cryogenic oxygen/hydrogen propulsion industry. Different adjustment methods, such as Hydrogen injection temperature, momentum ratio, velocity ratio, contraction ratio, etc. were proposed to find the unstable region of the combustor operation. They have gained

variable success in practice for some specific combustors. The essential point from the density point of view is that phase-shift due to the density interface, so that there could have some anti-node (to the dominant combustion induced frequency) at the wall. Thus the wall damps the dominant waves indirectly. This method is a spatial phase-shift via density control. This idea has to be validated by further experiments.

4.4.3. Predicting the instability zone for design purpose

It was found that the combustion stability of many LRE program is represented by a particular injection element type – the concentric or coaxial orifice - and particular conditions for developing high-frequency acoustic instability – low-hydrogen injection temperature. The later means the background density determines the over-all behavior in the combustor. From the source side, the high density of energy release in a volume having relatively low losses, conditions normally favor excitation and sustenance of oscillations in any combustion chamber intended for a propulsion system. So it is difficult to modify the disturbance from the source side, while the role of background density field is predictable. This leads a new cluster of methods controlling the combustion instability, i.e., control the resonance via density field control. This idea look new, but some measures are already practiced in the industry. With the analysis result in section 3, we can have a new look at some practice in this field. Here are a few examples:

Various mechanisms describing the instabilities were theorized as engine parameters were correlated and empirical stability boundaries defined. Hutt and Hulka (1995) provide a summary of the numerous LOX/hydrogen coaxial injector studies that have identified hydrogen temperature and the ratio of gas to liquid propellant flow velocity as the primary determinants for the onset of combustion instability. Recommended design

practices are velocity ratios greater than ten and hydrogen temperatures greater than 55K. It has also been observed that a small cup recess has a beneficial effect on stability. Based on the result in this work, increasing the hydrogen temperature will lower the density. So the system dynamics are changed by the boundary through different spatial distribution of inertia and elasticity.

The injection velocity ratio needs some attention, since it maintains the density traps (Oxygen is heavier than Hydrogen). This condition is close to the ideal condition set by Prof. Ffowcs Williams, " The hope is that physically connected regions might one day be acoustically separated by a sparse array of secondary sources that constitute an acoustic screen." This screen can be understood as a complete shield with not sound wave in and out, but it can also be looked as a selective filter to change the phase of the dominant acoustic wave. The stiffness of the stream will enhance its role as an acoustic screen. In the perspective, the flame can be treated as both a source and a damper/phase-shifter.

With better knowledge on the role of density in fine-tuning the phase of the combustion noise, we can design the future combustor in the following way (figure 24).

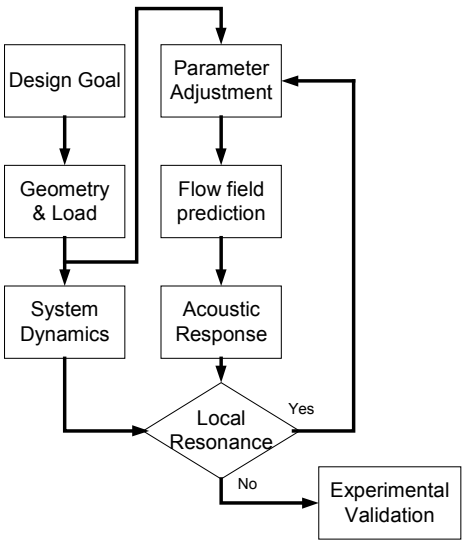

Figure 24. Conceptual flowchart for future liquid rocket engine design with special emphasis on combustion noise control.

Here there are two difficulties still lingering: system dynamics and acoustic response. This paper tries to find a method to predict the acoustic response, while system dynamics looks predictable from the historical data. For example, when hydrogen level reaches a certain level, all combustion oscillations are killed at the wall or some density interface, so the combustion is stable. This fact was usually explained from the chemical kinetics perspective. Here this study shows this may be a possible criterion for system dynamics, which is beyond our research in this work.

4.5. Conclusions

To find the role of density and wall on the acoustic response of a duct, 2 numerical solvers are developed to prediction the system response with variable complexities. They are validated by carefully designed experiments.

The 3-D compressible flow solver can predict the transverse modes from 1D to 3D conditions, with and without flow, and/or with the variable density conditions. The excitation is specified as a source of velocity fluctuation, and the floating pressure fluctuation field shows the acoustic response of the system. Several experiments are performed to validate the numerical results. The results show the role of density and wall on changing the acoustic wave propagation, so leading to different mode selections. The modal analysis can be used to demonstrate the mode identification.

Originally developed for any mechanical devices, the 1D characteristic-based acoustic solver used the idea of modal superposition and eigenvalue analysis to find the natural frequency of a certain system. The resonance property is based on the inertia, the elasticity and the boundary conditions, so it is inherent to any system disregarding the perturbation source. The acoustic solver is independent to the perturbation and can be applied to validate some simple resonance cases.

As commented by Colonius et al. (2004), the sound generation is in fact the release of the trapped wave modes in the vortices, here the mode selection process is the release of the predetermined modes due to the density field (including the density interfaces, such as wall). The flow has a secondary role in mode selection, since it is the density profile maintained by the flow determining the system response. With smaller viscosity damping, the non-dissipative wave in chamber will shift the acoustic energy into those

predetermined modes. The selected and enhanced acoustic wave will play an important role in flame-acoustic interaction, which is still actively researched.

The experimental and numerical results show that the externally applied mode will work on the stream better when the acoustic mode are coincide with the jet-preferred mode. Excitations at other modes can still modulate the flow to a lesser extent than the jet-preferred mode. The effect of external forcing on mixing is correctly simulated.

Chapter 5. Numerical simulation of a strong plume

5.1. Background

Fire-induced flow is one kind of plumes (featuring temperature variation) usually important in transporting the combustion products to other locations outside the combustion zone. So it is of great interest to fire detection, sprinkler actuation and fire suppression processes. When the variable-density jet is flowing in a gravitational field, the flow speed will increase or decrease due to the action of gravity. A jet is the discharge of fluid from an orifice or slot into a large body of the same or similar fluid. A plume is a flow that looks like a jet, but is driven by the potential energy source that provides the fluid with positive or negative buoyancy relative to its surroundings. The primary difference between a jet and a plume is that the jet is momentum-dominated while the plume is buoyancy-dominated. The buoyancy is generated from the density difference, which can be caused by either thermal difference (such as fire) or concentration difference (such as salt water). In most plume situations, fluid either at high temperature or at a different density is injected into ambient air. After a certain distance, the initial momentum is lost while buoyancy effects become dominant. Depending on the initial momentum strength, the plume can be either a forced plume (characterized by a strong momentum at the injector) or a purely buoyant plume (no initial momentum). Forced plumes share some common features with jets, such as: transition from a laminar to a turbulent state in the near-field, self-similarity in the far field, air entrainment by large eddies that control spreading, etc. In this perspective, the plume is controlled by flow dynamics that are similar to those found in cold jets.

The classical jet and plume theory is based on the application of dimensional analysis and similitude arguments. A typical example is the buoyant momentum jet (*i.e.* the forced plume). Integration of the equations of momentum and mass conservation across the jet leads to the conclusion that the total specific momentum flux is preserved as the jet develops spatially, thus the volume flow rate μ associated with a momentum-dominated flow is given by a relationship of the form.

$$\mu \sim M^{1/2} x \tag{1}$$

On the other hand, the volume flow rate associated with a buoyancy-dominated flow is given by

$$\mu \sim B^{1/3} x^{5/3} \tag{2}$$

Where *B* is the initial specific buoyancy flux, *M* is the momentum flux, which are defined as

$$B = 2\pi \int_0^{r_0} Wg \frac{\Delta\rho}{\rho} r dr \tag{3}$$

$$M = 2\pi \int_0^{r_0} W^2 r dr \tag{4}$$

Where r_0 is the source radius.

For forced plumes (plume with non-negligible initial momentum), the jet solution (1) is appropriate for $x << M^{3/4} / B^{1/2}$, and the plume solution (2) is valid for $x >> M^{3/4} / B^{1/2}$, since the only length scale that can be constructed from *M* and *B* is $L_M = M^{3/4} / B^{1/2}$, the Morton length scale. It is argued that though buoyancy effects become dominant over momentum at $(x - x_0) / L_M = 5$ (Shabbir and George), self-preserving profiles of mean and fluctuating mixture fraction can only be achieved at roughly $(x - x_0) / L_M > 10$ (Dai

et al. 1994). Failing to collect data in the well-established zone leads to different constants supported by different work by different authors (Basu et al. 1999).

The work of Nam and Bill (1993) dealing with free plumes shows that the standard $k-\varepsilon$ model over-predicts velocities and temperature on the centerline of a plume, leading to an underestimation of the width of the plume. Correction is made by tuning the turbulent viscosity coefficient and the effective Prandtl number; thereby reported agreement is improved within 2 % error. Hara and Kato (2004) simulated the thermal plumes with a standard $k-\varepsilon$ model, and found that the cell Reynolds number determines the quality of the numerical results. Besides the above work, the simulation of plumes with RANS approaches are limited, partly due to the unsteady nature of the plume, and partly due to the many empirically-determined constants in RANS approaches.

McGrattan et al. (1998) developed a numerical model based on a simplified set of equations, applicable to buoyancy-driven flows of perfect gas. The weakly compressible approximation is made, so that acoustic waves are filtered out. This model was originally developed to model smoke dispersion from large pool fires, then down-scaled to simulate fire plumes and fires.

Based on the DNS code of Boersma et al. (1997), a dynamic LES (Basu et al. 1999) in a spherical polar coordinate system is performed to compare with the experimental data of Shabbir and George (1994). The governing equations correspond to an incompressible flow with the Boussinesq assumption. Similarity solution and turbulence levels of the plume are compared. This work provides some insights on the boundary conditions and the validity of Boussinesq hypothesis. A low-Mach-number weakly compressible flow with variable density is simulated with a standard Smagorinsky model (Zhou et al. 2001).

The pressure is decomposed as the zeroth-order thermodynamic pressure that follows the ideal gas law, and the hydrodynamic pressure, which is solved by a projection method with a Poisson equation solver. This formulation has no need to capture the acoustic wave, but is still expensive to solve (using multi-grid method and the Poisson equation solver), so no dynamic model is used. DesJardin et al. (2004) developed a LES code to simulate the instability modes and flow dynamics of a Helium plume. Their simulation is computationally expensive, since the full compressible flow formulation is adopted and a combination of different schemes are employed to prevent the generation of nonphysical overshoot and undershoot (Gibbs error), and to prevent the occurrence of odd-even decoupling errors (i.e., checkerboarding) from appearing in regions of the flow where the Mach number approaches zero.

Most of the experimental and theoretical work on plume has been concentrated on the far-field self-similar region. Dai et al. (1994) studied the fully developed turbulent plume extending far from the source (up to 150 diameters). According to their observation, the self-similar region can only be achieved after about 80 diameters. So most previous research results are questionable as to the state of turbulence. On the other hand, the plume experiment by George et al. (1979) and Shabbir et al. (1992) presented results in a self-similar region in the range of 8-25 diameters from the inlet. So their work is a good choice for a computational study.

Here we look at a round turbulent plume discharging into a quiescent environment with strong initial momentum, buoyancy and turbulence at the source (so it is called a turbulent forced plume), using the tools of large-eddy simulation. A strong plume means

large density variations (buoyancy flux). The emphasis of the simulation will be on the similarity assumption and the decay laws (plume structure).

The text in this chapter is organized as follows. The simulation inputs are presented first. The result from plume simulations will be compared with a similar numerical study and the original experimental measurements. The purpose of this work is to reproduce the correct decay laws appearing in classical buoyancy-dominated flows.

5.2. Simulation Inputs

One of the advantages of LES is to predict the transition and subsequent turbulent mixing (or spreading) process that occurs in spatially developing flows. A free jet is known to be susceptible to Kelvin-Helmholtz instability, which in turn means that the flow is unstable to small exponentially growing disturbances and many linear instability analyses have confirmed this growth. The thin shear layers in a spreading jet with an initially top-hat profile undergoes several stages of development: Kevin-Helmholtz instability followed by the rolling up of vortices, pairing and merging process and the breakdown of the potential core with the increase of spreading by a secondary three-dimensional instability mechanism. Vortex dynamics are also expected to be important in the control of plume instability, transition from the momentum to buoyancy dominated region and even the plume development further downstream. According to the experiments by George et al (1978) and Shabbir and George (1994), the plume achieves its turbulent state within 2 diameters. Other investigators, however, have shown that the length of the potential core lies between 5-8 jet diameters if white noise is imposed on the jets. Here following Zhou et al. (2001) a sinusoidal forcing is imposed at the inlet boundary to generate the

turbulence for an early transition to a turbulent state. A survey of free jets shows that the evolution of an azimuthal instability mode can lead to an earlier breakdown and transition from laminar to turbulence. The same forcing scheme with both vertical forcing and an azimuthal mode of instability is adopted to get consistent results with the experiments. The outflow conditions are similar to those used in Chapter 3. The inflow conditions correspond to prescribed velocity and temperature profiles.

To excite the flow, the fluctuating axial velocity at the inflow plane takes the following form:

$$u' = AU_0(r)\sum_{n=1}^{6}\sin\left(\frac{2\pi ft}{n}+\theta\right) \tag{5}$$

where A is the amplitude of forcing and N is the number of modes (set to 6). Therefore the fluctuating axial velocity is specified as a function of time, t, and azimuthal angle, θ. The frequency f is the passage frequency of the vortical structures at the end of the potential core, which is determined by the jet-preferred mode corresponding to $St = fD/U_0 = 0.3$. That is, the response of a round jet to a monochromatic excitation, (measured as the gain or ratio of the peak amplitude to initial amplitude of the wave along the jets axis), reaches a maximum near a Strouhal number of 0.3. This value comes from forcing experiments on round jets by Crow and Champagne (1971) and was validated by the numerical experiments by Zhou et al. (2001b).

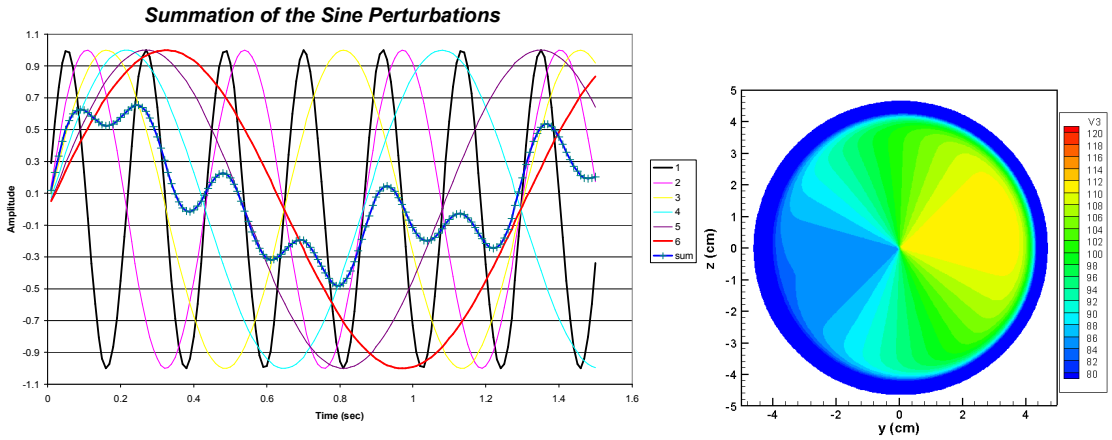

Figure 1. Summation of the temporal modes of equation (5) and azimuthal variations.

A vertical round jet of heated air is injected upward, which is subjected to a positive buoyancy force. Although the use of a rectangular grid for the circular jet may cause some stepped edges around the jet boundary, especially close to the plume source, the effect is considered to be negligible in the reference study by Zhou et al. (2001a). The heat source diameter is 6.35 cm, the exit velocity 0.98 m/s, the inflow temperature 568 K (295 C). The corresponding Reynolds number is 1273, based on the inflow mean velocity, viscosity and diameter. The reference study has 256x128x128 uniform grid cells for a domain of 16x8x8 diameters. In the present study, in order to keep the domain boundaries far from the flow region of interest, the grid is uniform in the center and stretched (with a stretch ratio of 6%) near the side boundaries. More specifically, 45-46-45 grid cells are allocated for the *y* and *z* directions. The grid in the direction of gravity (in the *x* direction) is uniform up to the first 180 grids, and then a grid stretching of 3% is used down stream. Overall a 256x136x136 grid is used to simulate a domain of 16Dx16Dx16D, with a resolution that is about twice higher than that used in the reference study.

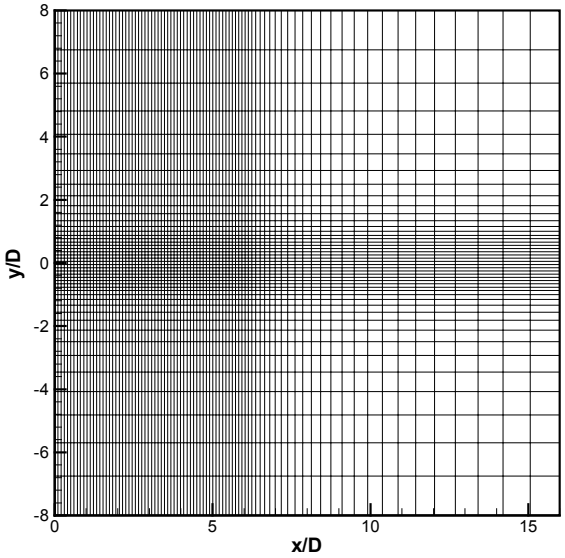

Figure 2. Grid adopted in the present plume (only 1 out of 3 grid lines is shown here)

Comparison	Current Study	Zhou et al.
Temporal discretization	3rd order Runge-Kutta scheme	2nd order Adams-Bashforth time integration
Spatial discretization	6th order central difference scheme + 6th order central-stencil filter	2nd order central difference scheme
Grid	256x136x136	256x128x128
Domain	16x16x16D (D=0.0635m)	16x8x8 D (D=0.0635m)
Best Resolution (D/dx)	29	16
Time step	0.00028 sec	0.00025 sec
Running cost	10 (sec) x 4 (cpus) x 34.0 (hours)	6.5(sec) x 64 (cpus) x 10 (hours)
Acceleration ratio	ASR = 100	None

Table 1. Summary of computational inputs and comparison with Zhou et al. (2001a)

We now turn to the specification of initial conditions. This specification is affected by the ASR method. As the background flow speed is small, the chance of initial perturbations (due to incorrect initial profiles) being flushed away is small. So it is important to set-up correct initial conditions. The initial conditions are specified as a hydrostatic solution. Here the flow problem in the gravitational field can be simplified into a 1-D steady flow case as shown in equation (6). This problem corresponds to a 1-D, steady flow problem

in the gravitational field, without diffusion and reaction. It was first introduced by Wang and Trouvé (2004).

$$\begin{cases} \dfrac{\partial}{\partial x_1}(\rho u_1) = 0 \\ \dfrac{\partial \rho u_1^2}{\partial x_1} + \dfrac{\partial p}{\partial x_1} = \rho g_1 \\ u_1 \dfrac{\partial p}{\partial x_1} + \dfrac{1}{\alpha^2}\gamma p \dfrac{\partial u_1}{\partial x_1} = 0 \end{cases} \tag{6}$$

The solution to the above equation is

$$\begin{cases} u = u_0 \left(1 - \dfrac{\gamma - 1}{\gamma}\dfrac{\rho_0 g x}{p_0}\right)^{\frac{-1}{\gamma-1}} \\ T = T_0 \left(1 - \dfrac{\gamma - 1}{\gamma}\dfrac{\rho_0 g x}{p_0}\right) \\ p = p_0 \left(1 - \dfrac{\gamma - 1}{\gamma}\dfrac{\rho_0 g x}{p_0}\right)^{\frac{\gamma}{\gamma-1}} \\ \rho = \rho_0 \dfrac{T_0}{T}\left(1 - \dfrac{\gamma - 1}{\gamma}\dfrac{\rho_0 g x}{p_0}\right)^{\frac{1}{\gamma-1}} \end{cases} \tag{7}$$

With the introduction of variable flow profiles, the initial condition for a plume simulation is set up as

$$\begin{cases} u = \left[u_0 + (u_1 - u_0)\Omega\right]\left(1 - \dfrac{\gamma - 1}{\gamma}\dfrac{\rho_0 g x}{p_0}\right)^{\frac{-1}{\gamma-1}} \\ T = \left[(T_1 - T_0)\Omega + T_0\right]\left(1 - \dfrac{\gamma - 1}{\gamma}\dfrac{\rho_0 g x}{p_0}\right) \\ p = p_0 \left(1 - \dfrac{\gamma - 1}{\gamma}\dfrac{\rho_0 g x}{p_0}\right)^{\frac{\gamma}{\gamma-1}} \end{cases} \tag{8}$$

where Ω is a hyperbolic-tangent profile in the *y*-direction that corresponds to a smooth step function. Here the density is directly computed from the state equation, so only u, T and p need to be specified.

The conventional Smagorinsky model is adopted, as the reference numerical study has shown that the effect of the SGS model is small (Zhou et al. 2001b). A Smagorinsky constant of 0.1 is chosen to facilitate the flow transition from laminar to turbulent state. The time step is limited by the CFL condition with the ASR method, so the total running time is limited by the pseudo-acoustic speed. Roughly 35 seconds is needed for a time step of 0.00028 second on 4 processors (2.8 GHz CPU of the Opteron PC/cluster). A total simulation time of 10 flow-over times is computed.

5.3. Data Analysis

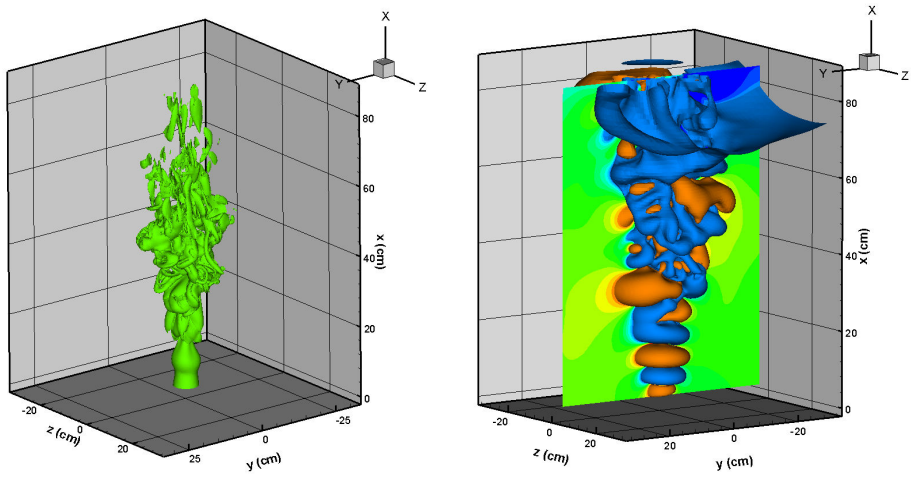

Figure 3. 3D Snapshots of vorticity magnitude and hydrodynamic pressure (perturbation only)

Figure 3 shows a snapshot of the vorticity magnitude and pressure field. The unsteady puffing near the injector is clearly seen. Though the grid near the outflow boundary is coarse, the buoyancy-induced turbulence can be recognized from the vorticity magnitude field. The helical pressure surface shows the azimuthal forcing. The regular/orderly structure breaks in the second half of the domain, showing the role of buoyancy in forcing transition from momentum-dominated to buoyancy-dominated state.

Since the experimental work by Shabbir and George (1994) was performed in the well-established plume region (8~25 D), there is no experimental data available for the near field. Here the numerical results of Zhou et al. (2001a) are used as the reference study. Simulation was found to agree well with experimental data.

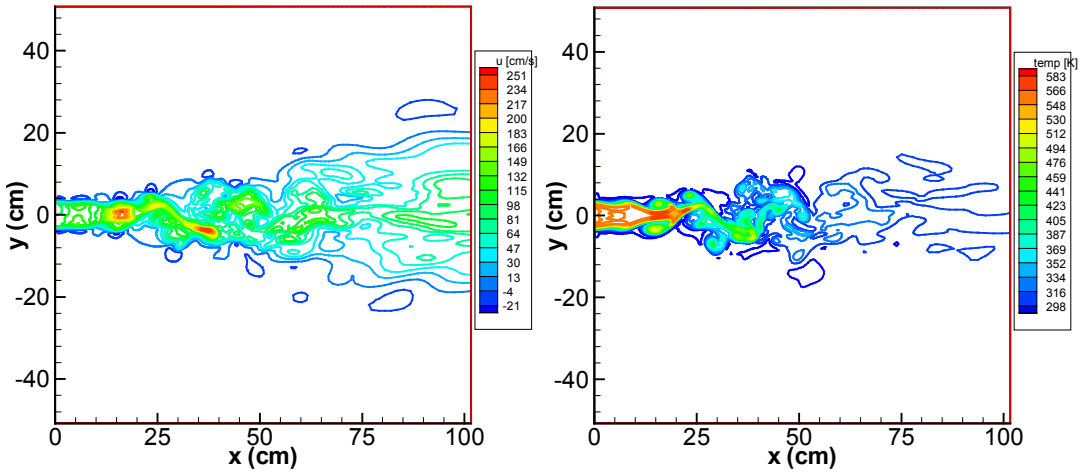

Figure 4. Instantaneous snapshots of velocity and temperature field in center XY plane

Figure 4 shows an instantaneous velocity and temperature contour plot in the center x-y – plane with azimuthal forcing. The acceleration of the flow due to buoyancy can be clearly seen. The laminar flow dominates the near-field region until the end of the potential core. Some overshooting of temperature near the rim of the potential core and at the tip region can also be observed.

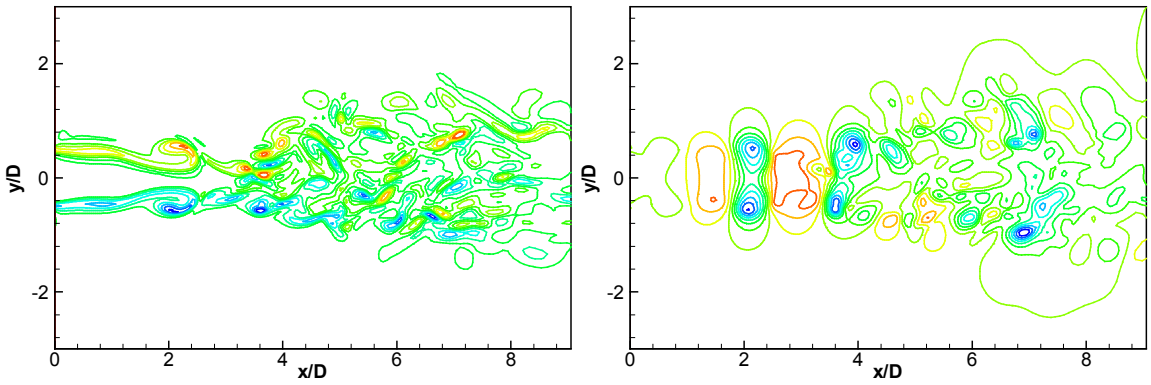

Figure 5. Instantaneous snapshots of 2D azimuthal vorticity and pressure

Figure 5 shows a snapshot of the z_vorticity and pressure. The helical instability mode and the entrainment vortex are clearly seen.

The centerline mean velocity and temperature distributions are shown in figure 6. The initial acceleration of axial velocity is due to the buoyancy acceleration and has been observed by Lingens et al. (1996) who experimentally investigated buoyant jet diffusion flames. The underlying physical mechanism is that the positive body force constitutes a major part to the mean flow in the near-field region of the buoyant jet. The flow is accelerated while the mass flux is not increased much, so the velocity keeps increasing until the tip of the potential core. The temperature curves follow a stable plateau, which is the potential core, and then drop due to the turbulent mixing/entrainment. The rapid decrease of velocity downstream is also caused by turbulent mixing with the surrounding fluid. Though the temperature is still higher than the background, (so that the buoyancy force is still acting), the entrained ambient fluid offsets the buoyancy-induced acceleration. The result is a rapid decay of the velocity and temperature in the far-field.

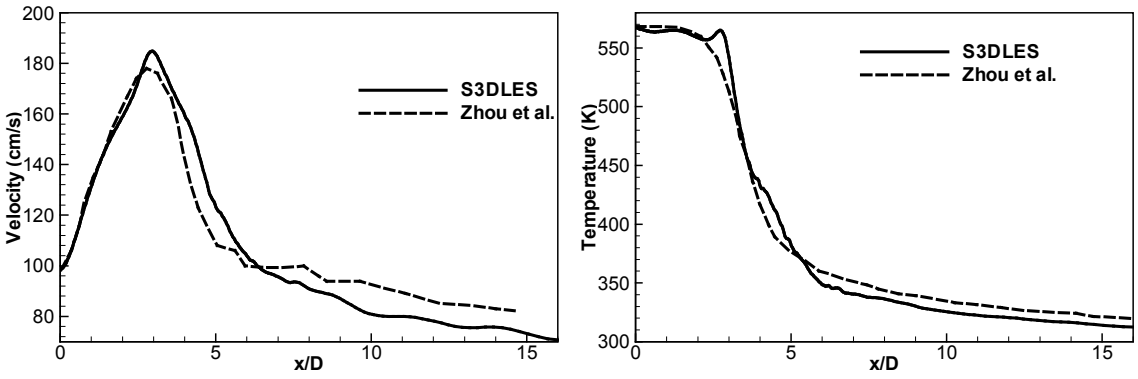

(a) *(b)*

Figure 6. Centerline mean velocity and temperature variations.

In the present study, the mean temperature variations show a local peak at the end of the potential core. This behavior is believed to be due to the Gibbs error commonly associated with higher order schemes. Also the potential core is a little longer than those of the reference study. The reasons may come from 3 sources:

1. The soft-inflow conditions adopted here have some relaxation effects on the imposed turbulence forcing scheme, so the gradient near the momentum thickness is smoothed to some extent. This effect will be less significant if the boundary profile is constant (i.e. without turbulent forcing). With the turbulent forcing both in temporal and spatial domains, the soft-inflow works like a spring, it will absorb any sharp changes, and smear some gradients. A difference between the imposed velocity and actual velocity profile at a random instant is shown in Figure 7. Here the data are shown within each cpu block. It shows that the most changes happen near the momentum thickness, which smears the gradient to some extent and is important for the flow transition from laminar to turbulent state.

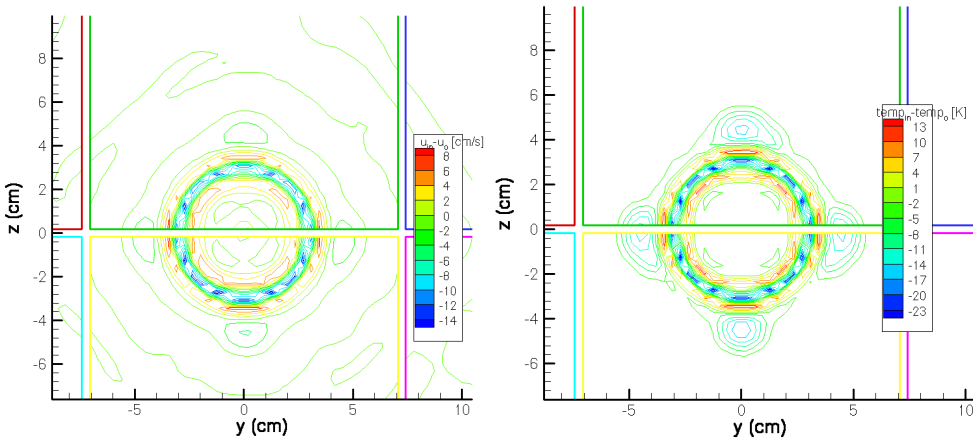

(a) *(b)*

Figure 7. The relaxation caused by the soft-inflow conditions.

2. S3DLES used a high-order central difference scheme. High-order schemes works well as long as there are enough grid cells to resolve sharp gradients. If not enough grid cells are used, the so-called Gibbs phenomenon will appear at the locations where the largest gradients are found. The resulting effect is overshoots and undershoots of the primitive variables, such as velocity, temperature and mixture fraction. At the same time, the high-order central-differencing filter also fails when variations are under-resolved, so it cannot be used to control the Gibbs phenomenon. This will be discussed more in Appendix B. Figure 8 shows examples of non-physical oscillations formed downstream of step variations.

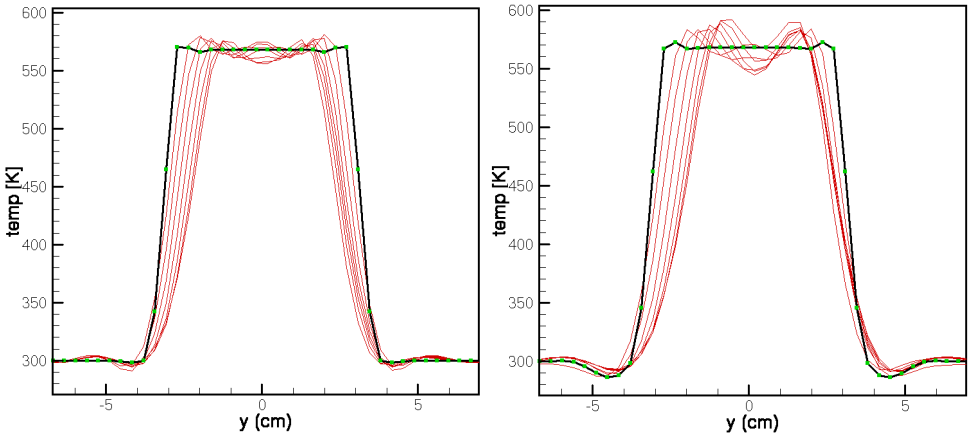

(a) 8th order scheme *(b) 6th order scheme*

Figure 8. Gibbs phenomenon on the specified input temperature profile.

3. 3-D round plumes have a degraded resolution in an orthogonal coordinate system. Due to the entrainment behavior, all errors produced near the edge converge at the tip of the potential core. This leads to a significant overshooting at the end of the core.

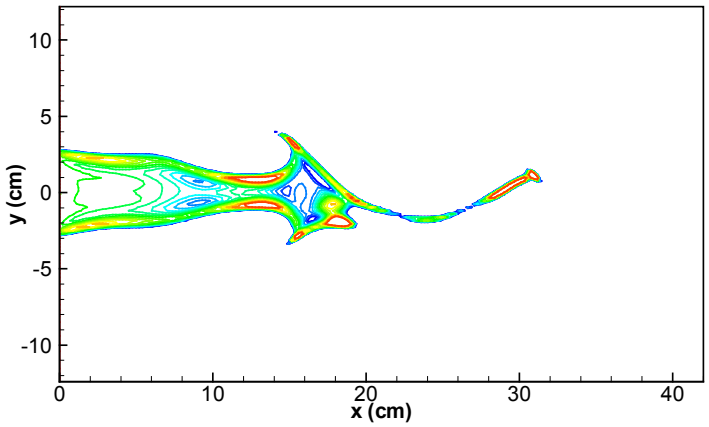

Figure 9. Spatial distribution of errors in the near field of the plume.

Of these 3 factors, the second one is believed to be dominant for all the simulations in this work. The unphysical overshooting of the parameters will delay the transition, so it helps explain the delay of the velocity decay, and the longer potential core, and under-development in the far-field regions. The first factor only delays the turbulence transition, but will produce no overshooting of primary variables.

The centerline values of the non-dimensionalized mean velocity $u_c x/\sqrt{M_0}$ as a function of non-dimensional vertical distance $\zeta = x/L_m$ are plotted in Figure 10. The experimental correlation of $3.4\zeta^{2/3}$ as a function of ζ is also shown by the dash-dot line. The results from S3DLES show the correct scaling law for the far-field velocity decay.

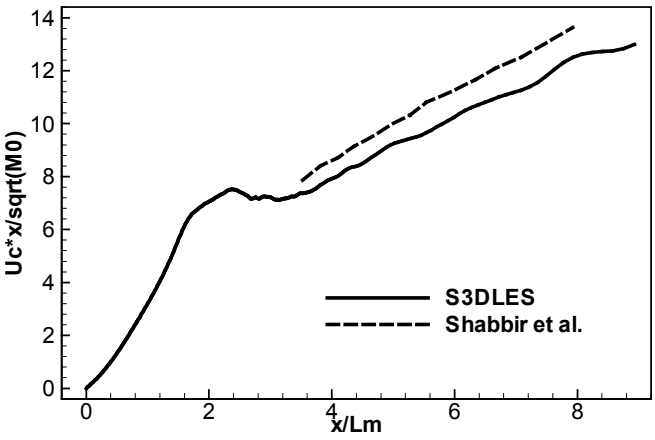

Figure 10. Centerline mean axial velocity profiles in dimensionless form

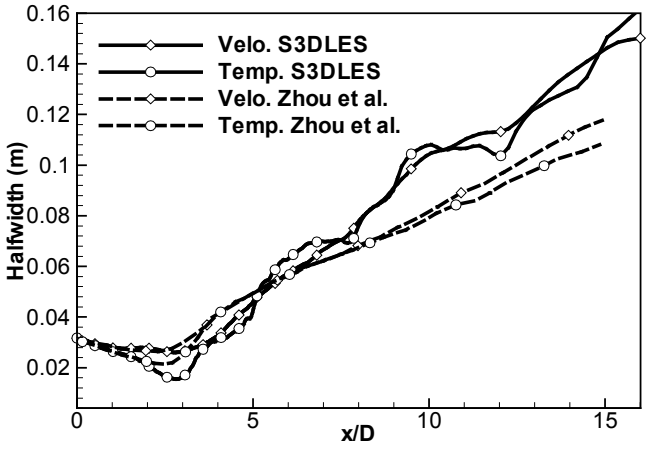

Figure 11. Half-width of the mean velocity and temperature profiles

Figure 11 shows the half-width of the plume compared with the reference study. The half-width based on velocity is slightly wider than the half-width based on temperature (defined as where the excess mean temperature to the ambient value is half the temperature difference between centerline and ambient) in the far-field. This means that the velocity field in a round plume spreads faster than the temperature field and is consistent with the experimental observations of Shabbir et al. (1994). Consistent with Figure 4(b), the plume has a longer potential core. It shows that the simulated plume has a correct behavior in the far-field while the near-field is affected by the inflow conditions.

It seems that the initial forcing is not enough, which can be explained by the relaxation due to soft-inflow conditions, and the high order scheme also has some impact on transition effects. The flow in the potential core is laminar, which means less entrainment, and leads to less spreading. The trend is reversed when the buoyancy begins to dominate the flow and when the impact of the initial momentum is lost over distance. The spreading rates obtained with S3DLES are larger than the reference study.

The centerline *rms* values of velocity and temperature normalized by the mean velocity and temperature difference between the local and ambient values are shown in Figure 12. It can be seen that the *rms* velocity and temperature reach nearly-constant values in the downstream self-similar region and are very close to the experimental of George et al. (1977), who reported the following values: $\left(\overline{T'^2}\right)^{1/2} / \overline{\Delta T} = 0.4$, $\left(\overline{u''^2}\right)^{1/2} / \overline{u} = 0.28$.

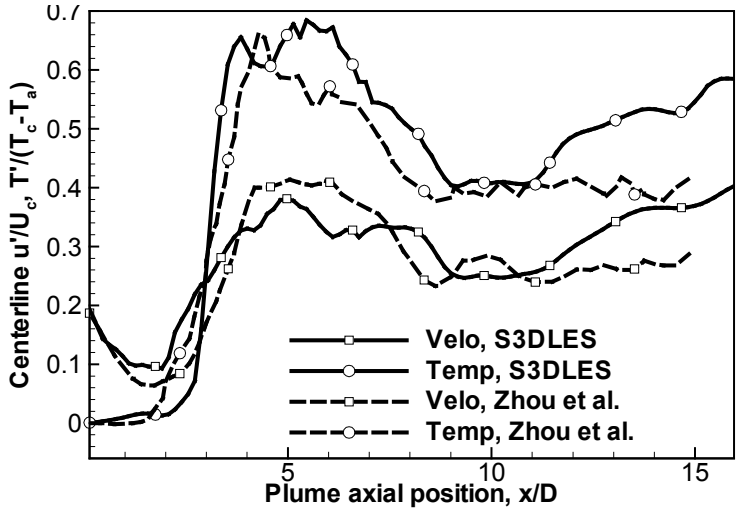

Figure 12. Centerline velocity and temperature fluctuations

The tendency for a plume to become self-similar some distance downstream of a plume means that the turbulent flow depends only on the initial momentum flux and initial weight deficit. The overall properties at all vertical heights above the plume follow the same dimensionless rule.

$$\frac{U}{U_c} = \exp\left(-55\frac{r^2}{x^2}\right) \qquad \frac{T - T_a}{T_c - T_a} = \exp\left(-65\frac{r^2}{x^2}\right)$$

These imply a slightly greater spread of momentum relative to buoyancy (as also shown in Figure 8). If self-similarity is achieved in a plume, the radial profiles of mean velocity, temperature and their fluctuations will maintain the same shapes at different downstream locations. Four axial positions (x/D=8, 10, 12, 14) are chosen to examine the radial profiles across the plume. The radial profiles of velocity and temperature from our LES results and the experiments of Shabbir et al. (1994) are shown in Figure 13 where x_0 is the origin of the jet. Note that x_0 = -1.8D is different from the reference study, which is calculated as the slope of a plot of $u_c^3 x$ versus u_c^3 as suggested in appendix A of George et al. (1977)

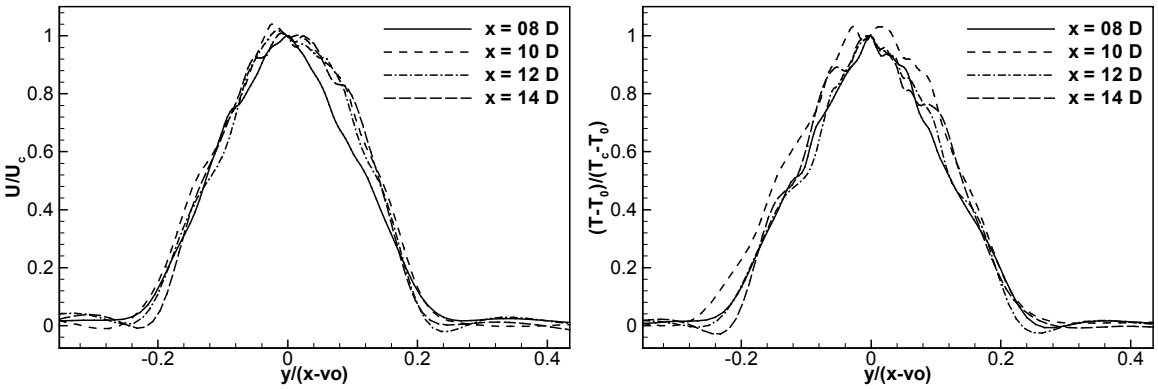

Figure 13. Radial profiles of mean (a) axial velocity, and (b) temperature at different axial positions.

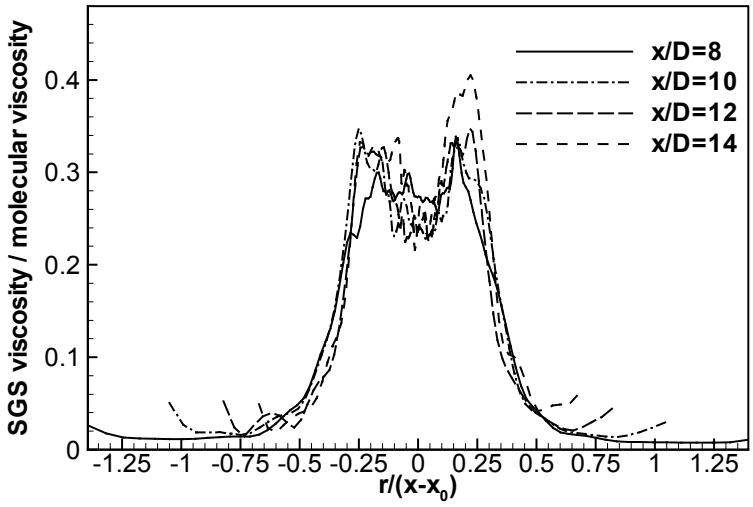

Figure 14. Ratio of SGS viscosity divided by molecular viscosity

Figure 14 shows the SGS/molecular viscosity ratio in the plume region. This is slightly smaller than the result by Zhou et al. (2001a), but the levels are similar. Comparing with the strong jet simulation, the Smagorinsky model plays a smaller role here. Larger values of the Smagorinsky constant will damp the turbulence and mask the nature of the buoyancy-induced-turbulence-transition. So a smaller Smagorinsky constant (Cs=0.1) is chosen here.

The streamlines of the mean velocity field are plotted in Figure 15. It can be seen that the plume draws in ambient fluid through the lateral boundary. This is generally called entrainment. Cortesi et al. explained that the entrainment was a direct consequence of the engulfment of fluid by the coherent, vortical structures after the roll-up and pairing (amalgamations) events. The entrainment or mixing of surrounding fluid into the plume engulfed by the turbulent eddies is the key to understanding turbulent plumes.

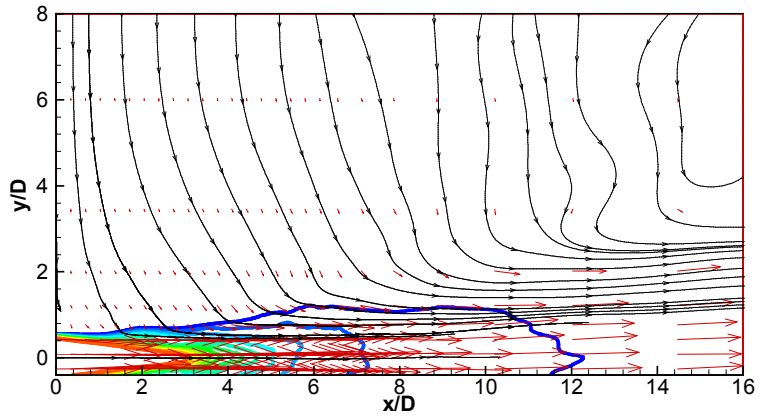

Figure 15. The streamlines of mean velocity field in the plume.

The classical plume theory by Morton et al. (1956) is based on the following 3 important assumptions: similarity profiles, the Boussinesq assumption and a linear entrainment rate assumption. The assumption of linear entrainment states that the mean entrained flux across the edge of the plume E (entrainment rate) is proportional to the local upward velocity u (a function of plume height). The plume theory is simplified by the integral solution/assumption of top-hat profiles of velocity, temperature, and plume radius. Of most importance is the determination of the entrainment rate on the basis of the assumption introduced by Morton et al. (1956).

The calculated plume width b from the simulation data is shown in Figure 16. The experimental slope of 0.18 is also plotted in the same graph. It can be seen that agreement is roughly acceptable, the discrepancy comes from the insufficient statistics (longer simulation time needed).

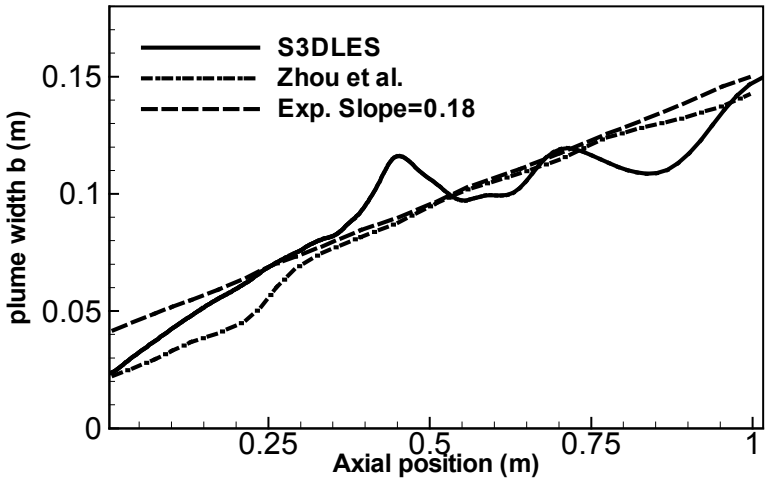

Figure 16. The plume width distribution along axial position

5.4. Conclusions

For the round hot-air plume simulation, the domain size is 120 cm with a initial speed of 0.98 m/s, so the flow-through time is 1.224 sec. The jet Re number is 1273, the Mach number is only 0.0028 for the jet velocity, and Richardson number is 0.579. The characteristic buoyant velocity is 0.746 m/s ($u_c = \sqrt{\frac{\Delta\rho}{\rho_0} gD}$).

A grid resolution study shows that for such a Re=1273 ($\mathrm{Re}_t \approx 969$) plume, the DNS resolution would be on the order of 366 μm, while the resolution for a well-resolved LES is 1588 μm (based on plume diameter over 40), as compared to the current choice (dx=3216 μm). The cost ratios for DNS over LES based on the above choices are 354 and 5961, respectively. Only the last one is chosen here due to the limitation of computing resources. The advantage of LES over DNS for such a plume simulation is obvious.

A forced plume has been simulated using LES at a Reynolds number of 1273 and a density ratio of about 2.0. The initial turbulence scheme is forced azimuthally at the inlet to facilitate an early transition to turbulence. An ASR ratio of 100 is chosen to decrease the acoustic speed, thus increasing the computing efficiency by two orders of magnitude. The primary objective of this study was to establish the validity of the ASR method and the boundary treatment in treating a low Mach number flow. The results were encouraging.

The far-field of the plume shows the correct statistical behavior (and follows the correct decay laws). Basic statistical plume variables (averaged values and rms values) are consistent with the reference study. In the far-field, the buoyant jet (or forced plume) eventually loses its initial momentum and becomes plume-like far away from the jet origin even with a large initial momentum flux at the source. In the near-field, the current grid resolution is not adequate to resolve the sharp gradients, and the Gibbs phenomenon is observed at the rim of the potential core. The longer potential core and overshoots in temperature and velocity lead to an incorrect near-field behavior. A finer mesh is required to capture the near-field behavior, which will increase the computational cost significantly. Further improvements on the numerical schemes are presented in Appendix B.

Chapter 6: Numerical simulation of a weak plume

6.1. Introduction

Most of the fire-induced flows become buoyancy-dominated. Compared to jet configurations, buoyant plumes have a strong large-eddy motion due to the external gravitational force; this motion generates shear and promotes entrainment and the mixing with the ambient fluid. The entrainment of fresh air into the mainstream determines the plume structure and associated hazards to the environment. The plume structure is very important to determine the threshold of detection and optimal position of fire detectors. From a combustion perspective, the mixing with fresh air determines the non-premixed flame location, or in other words, the flame structure. Since most engineering plumes are turbulent, the turbulent mixing behavior will be fundamental to the study of buoyant flows.

Integral models based on the similarity assumption have been successful in predicting the averaged properties of jet and plume behavior. These models were applied to a salt-water plume by Morton et al. (1956) in their classical work on plume theory. Subsequent work focused on the measurement of transient properties. As pointed out by List and Dugan (1994), although we have a perfectly good theory to describe the long-term average concentration of a tracer in a jet or plume, it is the peak concentration that is frequently of particular interest. The similarity assumption is valid only in an averaged sense. So we need to know the detail structure of the flow, to resolve the apparent contradiction that a peak concentration may be equal to 4.2 times the value of the average concentration (Papanicolaou et al. 1988). In a fire situation, this peak concentration in the plume may

still have the capability to trigger a smoke detector, although the time averaged value may be far below the critical level.

Early work focused on the integral and similarity theory and the plume structure, while later work focused on the turbulence and mixing behavior (Papantoniou et al. 1989). The numerical approach has made significant progress in recent years. The capacity, efficiency and cost of computation have improved at a fast pace. Now, with clusters of conventional PCs, it is possible to routinely carry out computational tasks that were designated as super-computer applications only 10 years ago. So there is a revival of interests on plume structures, with the purpose of developing numerical modeling tools (Basu et al., 1999, 2000, Zhou et al. 2001).

Salt-water modeling has been used in the fire community primarily as a qualitative tool to explore smoke dispersion in complex geometries. In salt-water modeling, plumes are created by carefully introducing salt-water into fresh-water. The salt-water dispersion closely simulates the dispersion of hot exhaust gases (smoke) in a fire plume. The salt-water plume has the advantage of small-size, is less sensitive to ambient perturbation and facilitate visualization. Here the fine-resolution of the plume structure provided by PLIF images can be compared as DNS results, so we can study the plume mixing behavior with DNS-like resolution data. The experimental images can be used to validate numerical sub-models used under the framework of Large Eddy Simulation. This provides the background and benchmark work for the large-eddy simulations of turbulent plumes.

Following the experimental work on the detailed plume structures, the purpose of this work is an extension of the study presented in the previous chapter and an application to weak plumes, as found in salt-water experiments. The aim of the simulations is two-fold,

to validate the ability of S3DLES to simulate weak plumes, and to validate the subgrid-scale mixing model used in the LES framework. The numerical results from the simulation will be compared with the experimental results of a salt-water plume study (Yao, 2006).

The structure of the chapter is organized as follows. First, the direct analogy between salt-water plume and thermal air plume is discussed. Then the LES mixing sub-models to be tested will be presented. The simulation results will form the main body of the chapter. Potential applications of this comparison will be finally discussed.

6.2. Salt-water/fire plume analogy

Many researchers interested in buoyant flows are environmentalists or meteorologists and the experimental fluid is often water. Also the water pollution problems are always associated with density variations. So early research in water plumes has been motivated by environmental problems. With a growing interest in fires, the advantage of simulating fire plumes using salt-water began to be recognized. Early work on fire plume includes Baum et al. (1982). Linden et al. (1990) studied the smoke-filling problem for natural ventilations using salt-water experiments. It is a useful scaled simulation tool among HVAC (including smoke management) communities.

Since the density of water is about 800 times larger than that of air, high Reynolds number flows can be more easily achieved and the experiment can be performed in a small configuration (at a reduced scale). The additional benefit comes from the increased easiness in visualization and measurements. Reduced experiments in a liquid container are subject to less perturbation than a gaseous plume in a large space. For example, the

classical study by Morton et al. (1956) has shown the effectiveness of studying plume dynamics by injecting fresh water into salt-water. Papantoniou et al. (1989) studied the large-scale structure in the far field of buoyant jets. Dahm et al. (1990) characterized the large Schmidt number effects in the self-similar far-field of turbulent jets.

Plumes and jets share several common features. The similarity profiles in plume, first proposed by Zeldovich (1937) and Schmidt (1941) are basically irrespective of the fluid used. The similarity profiles for jets and plumes are covered in current textbooks on turbulence (for example, Pope, 2002).

The major difference between a salt-water plume and a thermal air plume is due to the Schmidt number: while air has a Schmidt number of order unity, water has a Schmidt number of around 600. So the mass transport behavior is different at the molecular level. This problem is partly overcome by the fact that transport in turbulent buoyant flows is determined by the turbulent flow properties, not by molecular transport. Bejan et al. (1984) has studied the critical value for laminar plume transition to turbulent state. The source-based critical Rayleigh number, $Ra_{crit} = 10^{10}$, has been proposed as the criterion for axisymmetric plume transition to turbulence. The other limitation in using salt-water plumes is that the range of buoyancy intensities (Froude numbers) is limited by the density ratio (too small if salt-water is used, too large if air bubbles are used). For the best quality of the visualization, only weak buoyancy fluxes can be realized with salt-water plume. In addition, the near-field region is still dominated by the initial momentum, the analogy breaks down before the plume gains its turbulent state. So the salt-water plume is used for comparison with the far-field region in a buoyant air plume.

In addition to the universality of the similarity profile in well-developed plumes, the salt-water plumes and fire plumes have additional common features in the distribution of source and strength terms. The early work in developing the salt-water analogy for fire plume application is due to Baum, Quintiere and Rehm (1982). Further work includes studies of fire-induced flows by Kelly (2000), and Zhang et al. (2002), natural ventilation studies by Linden et al. (1996), *etc*. The focus of these studies are the global properties, such as the entrainment ratio, travel times, decay law, etc. With the improvement on instrumentation hardware, more detailed work on direct comparisons between salt-water and fire plumes was performed by Jankewitz (2004) and Yao (2006). Here a numerical simulation of a gaseous liquid-like plume is performed with the intent of comparing numerical results with the salt-water plume experiments performed by Yao (2006). The purpose is to test turbulent mixing models for LES and the overall ability of the LES solver to capture the correct flow physics.

In salt-water modeling, plumes are created by careful introduction of salt-water into fresh-water. The salt-water dispersion closely simulates the dispersion of hot exhaust gases (smoke) in a fire plume. The salt concentration and exhaust gas temperatures downstream of the flame zone behave like passive scalars and are transported by similar turbulent convective and diffusive processes. Proper scaling of the fire and salt-water flows allows for direct comparison of fire measurements and salt-water measurements.

While most of the previous studies are macroscopic study of the plume structure, in the study by Yao (2006), the microscopic structure of local mixing is studied with a high-resolution camera and high-resolution simulation of buoyant plumes. Interest in the transport and mixing processes in turbulent shear flows stems mainly from their importance in a wide

range of technological applications including turbulent combustion, which in the fast chemistry limit can be determined from the transport and mixing of a conserved scalar. Classically, turbulent transport has been treated as a diffusion-like process, resulting from vertical motions whose scales are presumed small relative to the lateral extent of the flow and characteristically lacking any persistent large-scale organization. However, contrary to this classical picture, experiments over the past years have established that transport in fully turbulent plane shear layers is dominated by a characteristic large-scale and roughly periodic organization that ultimately results from the dynamics of large vertical structures. This organized character of the fully developed shear layer has been found to have particularly important implications for turbulent mixing. A further consequence is that the range of mixed fluid compositions encountered at different lateral location across the layer is far less uniform than what the mean concentration profile might suggest. So it is widely presumed that some form of large-scale organization may also play a significant role for transport in other turbulent free shear flows. Large-eddy simulation provides such an attractive tool to study the mixing behavior due to large-scale organizations.

6.3. Comparison strategy

The methodology for the PLIF based salt-water plume measurements and the LES based CFD plume analysis is provided. The PLIF experiments provide quantitative visualization of large cross-sections of the flow for comparison with CFD model predictions. Highly resolved salt-water concentration measurements also provide detailed turbulent mixture fraction data for comparison with LES modeling results at the resolved grid scales and sub-grid scales.

Conventionally, the salt-water simulation results are used to explain a thermal gaseous plume behaviour using scaling laws. Here the salt-water plume results are used to compare the turbulence details. While S3DLES is a gas-phase solver and uses the ideal gas law, a set of modified gas parameters are proposed to mimic a liquid flow. The direct analogy can be established by modifying the transport properties of the gas to match those of the salt-water. In the analogy, it is assumed that the turbulent transport is dominant over molecular transport. Inlet boundary conditions for S3DLES are specified as close to the experimental injection state as possible, though the turbulence levels of the salt-water plume are unknown. The turbulence level in the simulation is specified so as to promote an early transition to turbulent state to match the experimental results. Comparisons between numerical results and experimental data will be made at the same location measured from the virtual origin based on the classical plume theory. So here the self-similarity assumption of the plume is implicitly used. The sampling point is a point in the fully-developed turbulent region.

Controlled parameters

Physical geometry	$D_{inj} = 5.6\,\text{mm}$
Initial velocity	$u = 7.5\,\text{cm/sec}$
Source strength (buoyancy flux)	$B = g\dot{V}\Delta\rho / \rho_{inj} = 1.8\times10^{-6} m^3 s^{-3}$
Turbulent Mixing Properties	$\text{Pr}_t = Sc_t$
Turbulent state	$Ra = \dfrac{Gr\cdot\text{Pr}}{Gr\cdot Sc} = 3.8\times10^{10} > Ra_{critical}$

Uncontrolled parameters

Turbulent inlet conditions	u'
Mixing at molecular levels	Sc , Pr

Table 1. List of important parameters in the comparison between salt-water experiments and S3DLES simulations.

For a direct comparison to be made, several adjustments are to be made to the gaseous plume simulation. 1). The geometry is kept the same, so the length scales are subjected to a direct comparison; 2). The initial velocity is the same, so the specific momentum flux is the same for both plumes; 3). The source specific buoyancy flux in the model is equal to that in the experiment. The source buoyancy flux is given by

$$B = g\dot{V}\,\Delta\rho/\rho_{inj} \tag{1}$$

where $\dot{V}$ is the volumetric source flow and $\Delta\rho$ is the density difference at injection, and ρ_{inj} is the density at injection. The inhomogeneous density is caused by a density difference in the water experiment, and a temperature difference in the gas simulation. Thus the velocity scale will be preserved by these 3 conditions. 4). The Pr of gas is also set equal to the salt-water Sc for direct comparison of the results. Thus the transport of the conserved scalar will be comparable at the molecular level. 5) Furthermore, the modelled viscosity is artificially modified to match the experimental Rayleigh number. Matching *Ra* provides dynamic turbulence similarity between the experiment and the LES model.

To clarify this comparison, further points are made on the direct comparison. Flow conditions were prescribed for the experiment and the CFD analysis to ensure that the flow was turbulent and buoyancy-dominated. The appropriate specification of these criteria is essential to ensure that the mixing dynamics are similar to those in a fire-induced flow. The flows created in the salt-water modelling study have non-negligible initial momentum and are thus considered as forced plumes. If the initial momentum is small, these flows will become buoyancy-dominated and exhibit plume-like behaviour

very near the source. As discussed previously, Morton defined a length scale based on the relative proportions of the initial momentum flux and specific buoyancy flux, $L_M = M^{3/4}/B^{1/2}$. Morton demonstrated and others have verified that plume-like behaviour is achieved at a streamwise location of $5\times L_M$. Although plume-like mixing behaviour is achieved beyond $5\times L_M$, it is necessary to introduce a virtual origin, z_0, to correct for the initial injection momentum and finite injector geometry before the results are compared with point source plume theory. Furthermore, the flow is not necessarily turbulent at the exit of the injector because of the small injection velocities required to achieve a buoyancy-dominated flow near the injector. Turbulence in plumes results from the buoyancy-induced inertial forces. A source based critical Rayleigh number of $Ra_{crit} = 10^{10}$ has been proposed by Bejan (1984) and used as a criterion for axisymmetric plume transition to turbulence. The locations of interest in this study correspond to $Ra = 3.8\times10^{10}$ significantly larger than this value. The observed turbulent flow dynamics are consistent with these results.

6.4. Results

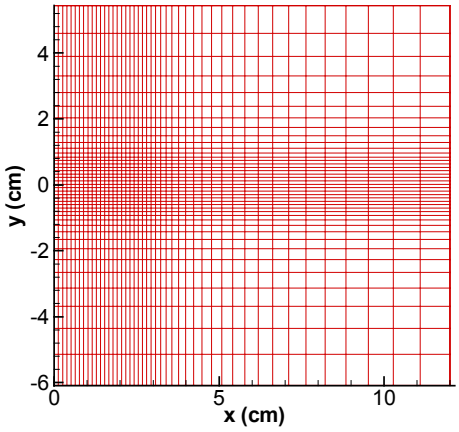

Figure 1. *Grid configuration for current simulation (only 1 out of 3 grids is shown here)*

Figure 1 shows the computational grid for this simulation. The grids are stretched by 6% on both sides, and 3% along the jet flow region. About $\left(\frac{1}{2}\right)\cdot\left(\frac{1}{3}\right)\cdot\left(\frac{1}{3}\right)$ of the total mesh (136x126x126) are kept uniform to capture the near-field flow dynamics. The non-uniform mesh grids are adopted to keep the boundary away from the point of interest. In this problem, a longer domain is needed for the flow to develop into a turbulent state, which means 20-30 D from the injector.

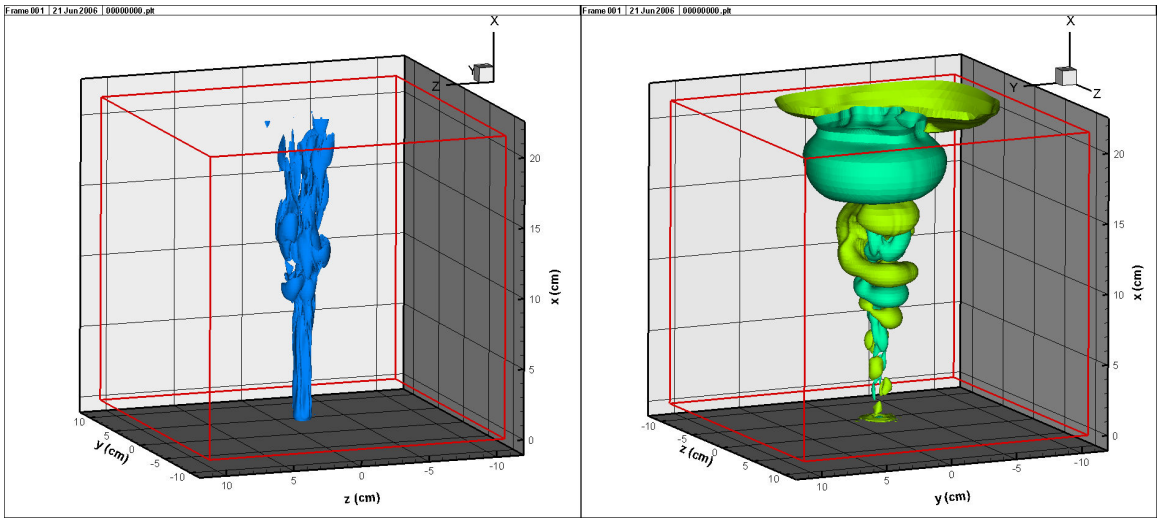

Figure 2. Instantaneous 3D snapshots of vorticity magnitude and hydrostatic pressure

An instantaneous view of the vorticity magnitude and hydrostatic pressure field is shown in Figure 2. The azimuthal forcing is seen to create an organized helical pressure field. This weak plume has much less turbulent activity than the previous strong plume case (see Chapter 5) due to its liquid-like properties.

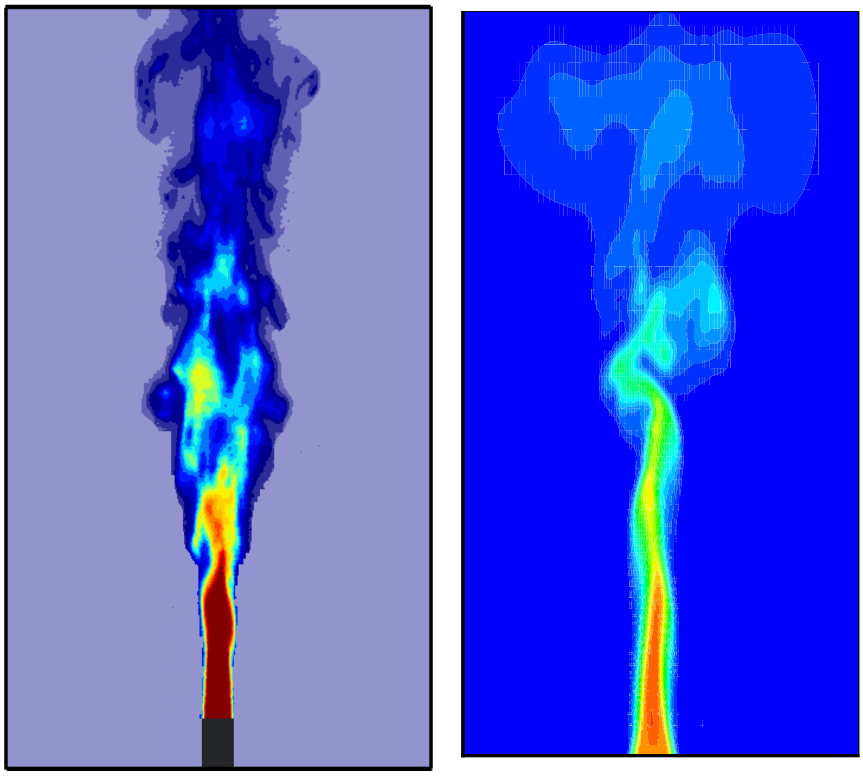

Figure 3. Instantaneous distribution of density (salt-water plume) and temperature (air plume) at central xy-plane.

An instantaneous temperature distribution is compared in Figure 3 with an instantaneous concentration profile from the salt-water experiment. The experimental image shows fine structure in the far field while the LES result appears more smoothed due to the turbulent viscosity and the stretched grids. Also the unmatched initial forcing plays some role on the development of the plume. The S3DLES have a thicker plume due to the stretched grids in the far field region.

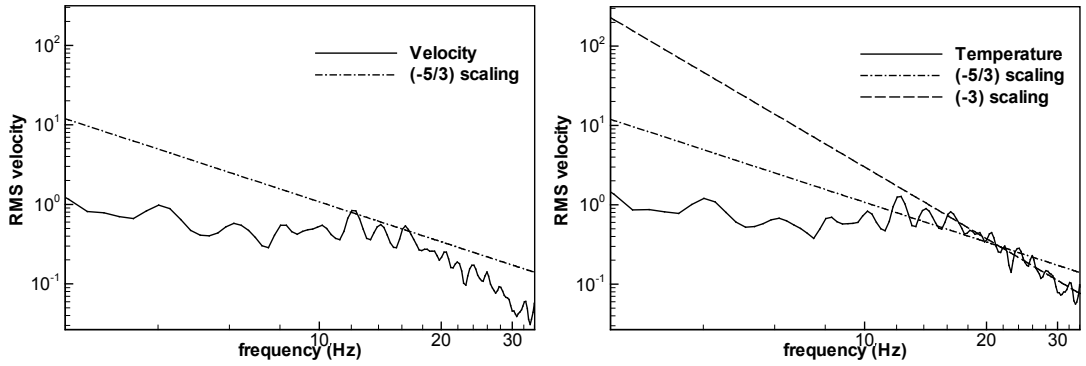

Figure 4. Power spectrum of pointwise velocity and temperature fluctuations in the plume

Figure 4 shows the energy-spectrum of velocity and temperature fluctuations at x/D=8 along the centerline. (The statistics are accumulated over a period corresponding to 40 forcing periods). It is expected that the inertial range in the velocity spectrum obey the –5/3 Kolmogorov power law. The power spectrum for temperature fluctuations is similar to the velocity spectrum. The high-frequency region corresponds to a –3 power law. Kotsovinos argued that the 'jump' from a –5/3 to a –3 power law is a result of a stronger energy cascade due to large plume vortices driven by buoyancy forces.

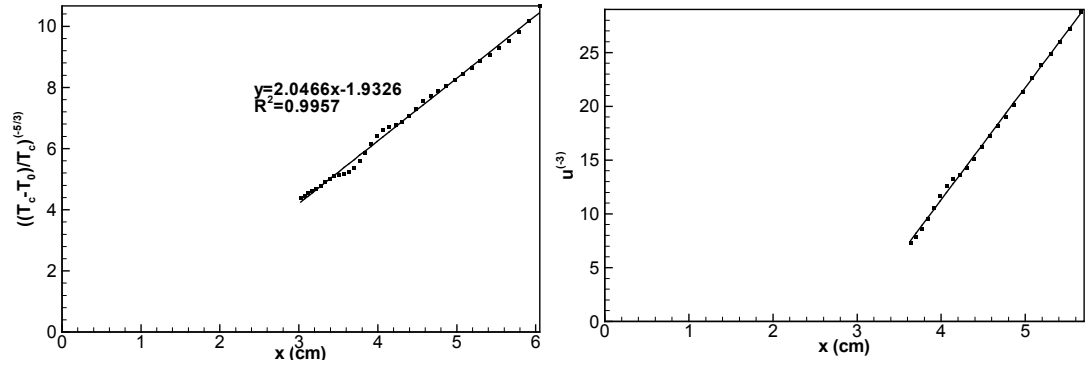

Figure 5. Virtual origin determined from the plume decay law

The time-averaged velocity and temperature profiles show the correct decay behavior in the region where the grid is still uniform. The behavior is obscured in the down-stream

non-uniform grid region, where the linear curve has another slope. Due to the different transport coefficients, the temperature and the velocity profiles produced different virtual origins (0.944cm for temperature and 3.12cm for velocity). The experimental virtual origin is -1.18 cm for temperature and 5.36cm for velocity. The similarity profile will be corrected based on the respective virtual origins.

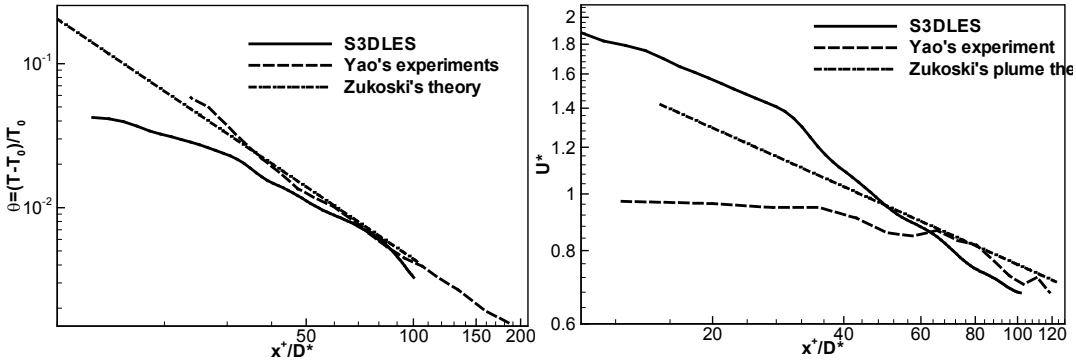

Figure 6. Non-dimensional evolution of temperature and vertical velocity along the plume centerline. Comparison between experimental data and numerical result.

Figure 6 shows a comparison between experimental and computational results for centerline scaling laws. Here all parameters are dimensionless to have better comparison between different plume conditions. Here $x^+ = x - x_0$ is the distance corrected by the virtual origin location. $D^* = \left[\frac{\rho c_p \Delta T A V}{\rho c_p T_0 g^{1/2}}\right]^{2/5}$ is the characteristic dimension of the point source plume. The dimensionless velocity $u^* = \frac{u}{(gD^*)^{1/2}}$ is the velocity scaled by the characteristic velocity. The scaled representation of the simulation results is close to that observed in the far field region in the experiments. The scaling laws are partially validated from the theory.

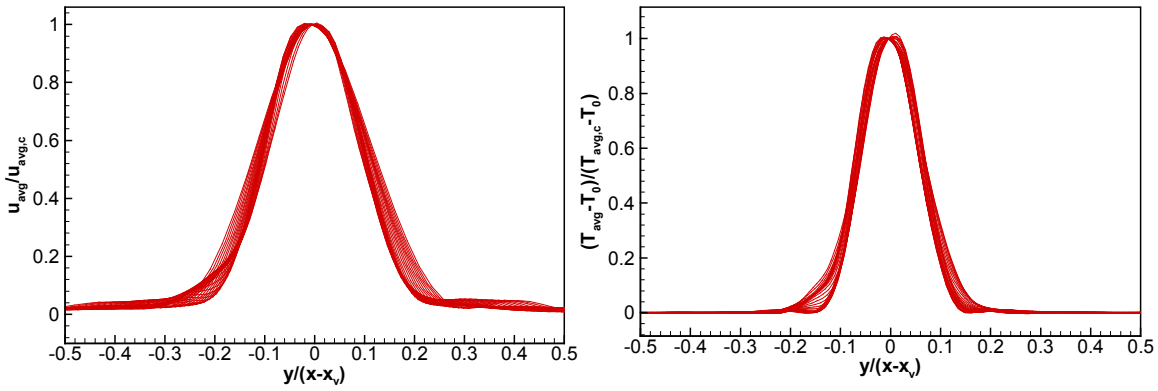

Figure 7. Similarity profiles in the fully developed plume region

The similarity profiles of velocity and temperature are shown in Figure 7. The velocity profiles are wider than the temperature profiles, which explains why the virtual origin for velocity is located farther upstream than that of temperature.

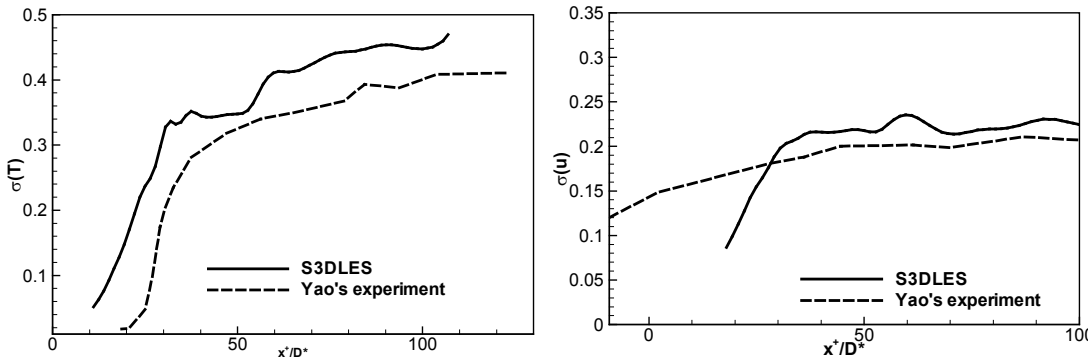

Figure 8. Turbulence fluctuations along the centerline.

Figure 8 shows LES results for the velocity and temperature fluctuation intensity. Values of 0.28 and 0.4 are given respectively for velocity and temperature fluctuation intensities in George's experiments.

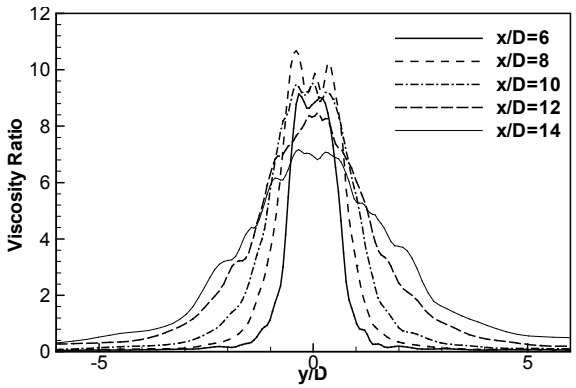

Figure 9. Time-averaged cross-stream profiles of the turbulent/molecular viscosity ratio

The role of the Smagorinsky model is shown in figure 9, where the turbulent/molecular viscosity ratio is shown at different x-locations. Here for comparison with salt-water plume, the reference thermal conductivity is 500 times smaller than that of air. So the molecular viscosity of this 'liquid-like' gas is also smaller. The averaged turbulent/molecular viscosity ratio is about 10 times more than that of air.

The PDFs of mixture fraction (based on the temperature ratio) at different positions along the centerline are shown in figure 10. Here a total of 1050 slices are sample over a time interval of 0.0146 sec. That is a total of 10 flowover time are accumulated for data sampling. Away from the injector, the peak value of the PDF shifts to the lower values, which is consistent with the mixing process.

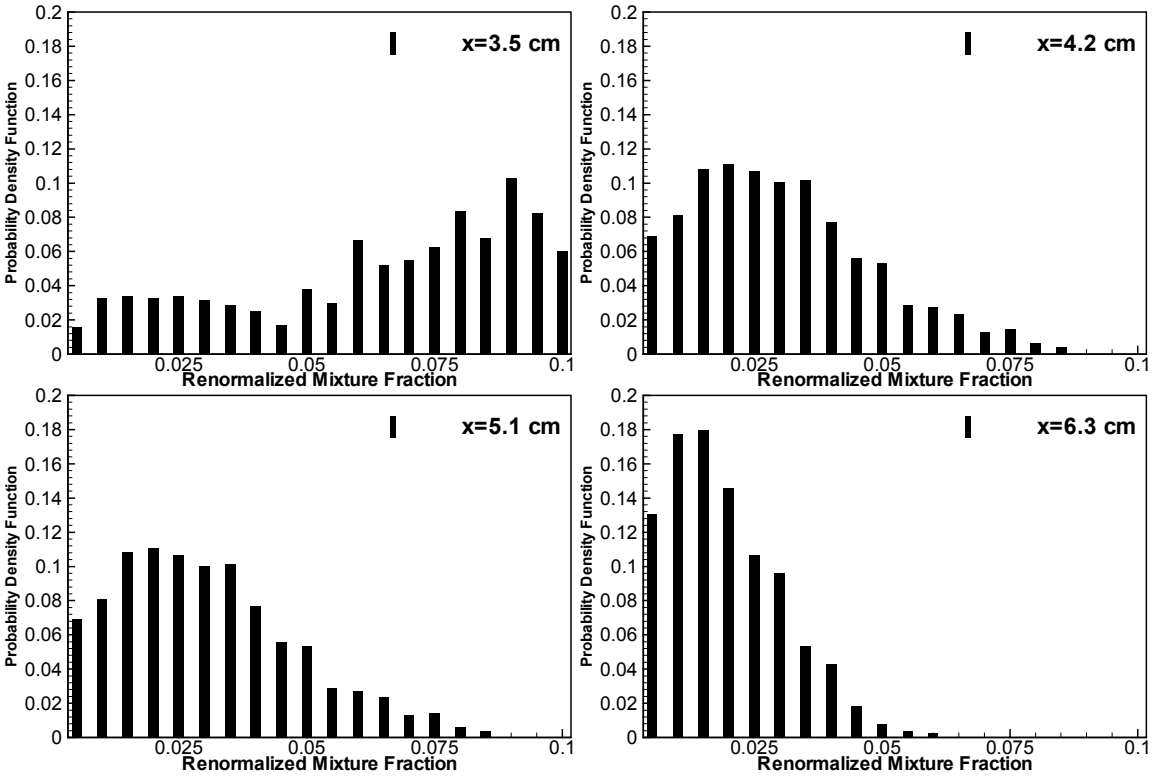

Figure 10. Statistical distribution of mixture fraction at different locations on the centerline

6.5. Conclusions

For the round hot-air plume simulation, the domain size is 12 cm with an initial speed of 0.075 m/s, so the flow-through time is 1.6 sec. The initial Re number is 11031, the Mach number is only 2.16e-4 for the jet velocity, and Richardson number is 0.975. . The characteristic buoyant velocity is 0.074 m/s ($u_c = \sqrt{\frac{\Delta\rho}{\rho_0} gD}$). The turbulent Re number is 10884. A grid resolution study shows that for such a weak plume, the DNS resolution is on the order of 5.2 μm, while the resolution for a well-resolved LES is 139.7 μm (based on plume diameter divided by 40), as compared to the current choice (dx=172 μm). The

cost ratio for DNS over LES based on the above choices are 5.2e5 and 1.2e6, respectively. Only a course LES is chosen here due to the limitation of computing resources.

Compared to the strong plume case discussed in the previous chapter, the weak plume displays similar features except for the extremely small characteristic velocities and the relatively large domain size when scaled by the injector diameter. To overcome this first problem, an ASR ratio of 200 is chosen for decreasing the acoustic speed, thus increasing the computational efficiency.

The second problem is a difficult one, since it is directly related to the computing resources at hand. Currently, the small cluster for this project has only 4 cpus of 2.8GHz each. So the grid size is constrained to be less than 3 million grid points. Also great care is taken to resolve the initial jet profile before reaching the fully developed stage. Currently, more than half of the grids are allocated uniformly around the potential core, though test results show it is still not sufficient to get rid of the Gibbs phenomena and the resulting overshooting behavior. Simulation results are not grid-independent and finer grids are likely to improve the simulation flow structure.

The direct comparison between variable-density salt-water plume and the thermal air plume is a new concept to validate the subgrid models used in LES. The essence of this method is that the flow is fully turbulent and turbulent transport over-powers molecular transport. Transition from an initial momentum-dominated laminar plume into a buoyancy-dominated turbulent plume is correctly observed. The direct comparing of air plume with liquid-water plume shows encouraging results and supports the analogy. The small Mach number flow is compensated by a large ASR ratio.

The fundamental feature of the plume, the decaying law, is validated by the simulation result. The fully compressible simulation of plume dynamics combined with the pseudo-compressibility method successfully captures many of the flow features. Due to the numerical problems of the solver, the code could not produce a grid-independent result under current computing resources. Further work is still needed on improving the numerical schemes and performing direct comparisons of detailed structure of the plumes.

Chapter 7. Conclusion and discussion

7.1. Simulations summary

The numerical development in this work is based on the fully compressible DNS flow solver S3D. So the main numerical work is the adaptation of a DNS solver to LES filtered equations and submodels. Here Favre-averaged governing equations are formulated first, supplemented with the classical Smagorinsky model and the dynamic procedure. To simulate low-Mach number flows, the speed of sound is artificially reduced while the zero-Mach number physics are modeled correctly. The LES framework of governing equations and the ASR method provide the basis for several simulations in the thesis work.

The boundary treatment in S3DLES (or its original version S3D) is based on the characteristic-based non-reflecting boundary treatment. The LODI formulation is precise for one-dimensional conditions, while approximate under 2-D or 3-D conditions. For plane jet simulations, the Mach number is 0.35, which is strong and causes some trouble at the exit boundary (usually associated with backflow events). To stabilize the solution, a buffer layer treatment is introduced to reduce the acoustic reflection at the outflow. The resulting flow is stable and produces comparable results with a reference study. Following the study by Ribault et al. (1999), the Smagorinsky model and other relating sub-models are validated using published results with clearly defined flow and perturbation conditions.

The next simulation in chapter 4 is devoted to test the turbulent mixing and acoustic response capabilities of the code in a confined domain. Three streams of different densities and momentum are introduced into the chamber-like domain. The wall is treated

as a slip-wall while a velocity perturbation (modulation) is introduced on the speaker wall. This arrangement provides a platform for flow-acoustic interaction simulations. The amplitude and phase of the excitation source can be adjusted easily. The mode shape prediction from the code compares well with the experimental work. A variety of numerical tests on 1D, 2D and 3D domain show the mechanism of transverse resonance, and resulting flow-acoustic interactions. It will be a good prediction tool for future combustion noise control studies.

The above two cases are flows of intermediate Mach number, so the computational efficiency is not as constrained as for the low Mach number flows. The time-advancing steps for compressible flow are determined mainly by the acoustic speed. The acoustic wave is important to propagate pressure information across the full domain, while its contribution to convective flow dynamics is a small fraction. This leads to the idea of a pseudo-compressible method, where the acoustic speed is manipulated in order to allow larger time steps and faster calculations. For buoyancy-induced flows (such as air streams), this acceleration can be 20 times or more. Thus the computational efficiency for low Mach number flows can be greatly improved. The problems in applying the ASR method to gravitational flows are the distorted gravitational field (initial conditions) and the correct gravitational gradient scaling, which are developed in this work. The simulation results of the Shabbir plume (1992) are close to the reference study (Zhou et al. 2001) and to the experimental results (Yao, 2006). The turbulence-forcing method produced the expected early transition to the turbulent state; and the plume parameters meet the theoretical predictions and the scaling laws.

One of the primary goals of this code development is simulating fire-induced flows. So the reaction-modeling capability is an important feature to be tested. Here the condensed (reduced-scale) saltwater plumes are used to test the mixing properties of the LES sub-models, a valuable intermediate step in the development of a non-premixed combustion capability. The analogy between a buoyant plume and a saltwater plume is based on the fully turbulent state, where the mixing is predominantly based on turbulent transport instead of the molecular transport (different by orders of magnitude). The scaling laws of the turbulent plume are correctly predicted. The mixing behavior of the 'liquid-like' air plume is close to the saltwater plume under the buoyancy- and turbulence-dominated states. This analogy shows the possibility of validating turbulence models using saltwater measurements.

	Reynolds No.	Mach No	Richardson No.
Plane jet	3000	0.35	0
Acoustics	6781	0.052	0
Round plume	1273	0.0028	0.580
Saltwater plume	13013	2.16e-4	0.977

Table 1. Summary of input parameters for cases in this work.

In summary, the test cases used in this work feature a wide range of flow velocities of 121m/s, 18 m/s, 1 m/s and 0.075 m/s. When the flow velocity is small, the buoyancy plays a more important role in determining the flow state. Depending on the characteristic speed and the purpose of the study, the pseudo-compressible method (ASR) is used to improve the computational efficiency under low-Mach number conditions. The global prediction capability of the code is encouraging, while there remain several problems associated with the computational costs and the numerical methods.

7.2. Computational costs

One of the difficult problems in applying this code is the large computer power requirement. Here the code is based on the fully compressible flow formulation with a high order spatial discretization and a high-order explicit Runge-Kutta method. The filtering of the solution variables at each time step is also intensive. Although the code uses MPI and takes advantage of current parallel computing technology, additional problems arise due to the global data exchange and the relating synchronization requirement. The current platform used in this work is one Opteron with 4 cpus of 2.0GHz each. It is a good platform for debugging purposes, while still limited for production runs. The computational cost for the plume cases are listed in table 2.

Comparison	Strong (hot air) plume	Weak (saltwater) plume
Ma number	0.0028226	0.00021531
Velocity	98 cm/s	7.5 cm/s
Diameter	6.35 cm	0.5588 cm
Re	626	23170
Grid	136x136x256	126x126x136
Domain	16x16x16D	22x22x22D
Acceleration ratio	ASR = 100 (cfl_no=1.0)	ASR =200 (cfl_no=0.8)
Maximum D/dx	29.4	29.0
Time step (sec)	2.88e-4	1.47e-4
Running cost	10 (sec) x 4 (cpus) x 34.4 (hours/sec)	16 (sec) x 4 (cpus) x 23.2 (hours/sec)

Table 2. Computational cost for a plume simulation of 10 flow-through times.

To accomplish the simulation of 10 flow-through times in a certain time period, the finest grid size and the domain size are carefully chosen to fit the time constraints. Here the ASR method is pushed to its limits, that is, the acoustic speed is lowered so that the modified Mach number is close to 0.3 without considering the compressibility effects. Other factors, such as the background temperature gradient, the easiness of applying soft-inflow conditions are also considered in choosing the right combinations. For the weak

plume, in theory ASR=1000 can be adopted for the acoustic speed reduction. The current choice is based on the consideration of boundary treatment, so a lower value is used.

The only comparable plume research is performed by DesJardin et al. (2004). Besides different numerical choice to control numerical overshoots and undershoots, only a cubic domain of 4 diameters was chosen, which decreases the computational cost significantly. In current saltwater plume simulation, the plume becomes buoyancy-dominated after 5 Morton length scales, which means that the best sampling region for plume turbulence is in the region 20D-30D from the injector. This condition plus previous requirements puts a strong constraint on the grid allocation and resulting computational costs. The injector needs fine grids, while the sampling point in the turbulent plume region needs uniform mesh. To meet the 2 constraints significant computer power is required.

7.3. Numerical problems in S3DLES for plume simulations

The numerical framework of S3D is based on higher-order central finite difference schemes. Though more computational cost is required for larger stencils used in high-order schemes, the overall computational efficiency is generally increased by adopting high-order schemes (Ekaterinaris, 2005). When these high-order schemes are used in the LES framework, the unresolved gradients will lead to dispersion and aliasing errors. The important Gibbs phenomenon is a byproduct of such numerical schemes. Currently there is not a conclusive method on avoiding the Gibbs phenomenon except the demand for finer meshes. Many numerical improvement and/or physical models are developed for avoiding such behavior. Here are some partial results that provide directions for future work.

When centered difference schemes are used in hyperbolic systems of linear first-order PDEs, it was found that they disperse, but do not dissipate, the Fourier components of the solution. When higher wavenumbers cannot be represented on the grid, their energy is aliased onto the resolved wavenumber. Higher order schemes have the effect of increasing the aliasing error, although to a first approximation, the aliasing error may be considered independent of the finite-difference scheme. Even for an eighth-order scheme, the error is smaller than the subgrid term for only about half of the wavenumber range (Ghosal, 1996). An increase in grid resolution makes the errors increase faster than the dissipation due to subgrid models, so the situation cannot be improved by grid refinement alone as long as the cutoff wavenumber remains in the inertial range.

According to Colonius and Lele (2003), spurious waves are generated due to initial conditions, boundary conditions, nonlinear cascading, and stretching/coarse grids. If not generated by the coupling with the boundary treatment, the spurious waves arise due to insufficient resolution of relevant length scales in a given problem. In linear, constant coefficient problems, where the relevant length scales are determined solely by initial and boundary conditions, smoothing of spurious waves only changes the nature of the error for the poorly resolved components from dispersive to dissipative. As the problem is linear, the solution at the resolved scales is unaffected by the presence of errors of either type. This puts some requirement on a spatial filter for smoothing/removing the spurious waves. For nonlinear problems, smoothing amounts to an ad hoc turbulent model or shock-smoothing scheme. If spurious waves cannot be reduced by using higher-order schemes or more grid points, they can be attenuated by artificial dissipation (e.g. the

upwind scheme), by adding an artificial viscosity term to the governing equations, or by directly filtering them from the solution.

As pointed out by Kennedy et al. (1997), the finite difference derivative scheme used in S3D is not so important as the effect of the filtering scheme. This has been tested with some simple tests. The modification of filtering order indeed changes the plume turbulence while a change in the spatial discretization scheme has no significant effect on the global properties. There are several tests in appendix B for the behavior of the numerical schemes.

The role of filtering is partially validated by the simulation of the strong plume in a small domain. Here a conserving variable mixture fraction is introduced into the domain. The left figure in figure 1 is filtered with an 8^{th} order standard filter, while the right figure is filtered with an optimized 8^{th} order filter (with an overall 4^{th} order resolution). The Gibbs phenomenon is significant in the figure 1(a), while the gradient in figure 1(b) is improved at the rim of the potential core. The overshoots are not completely overcome at the tip of the potential core remain. So the solution of an optimized filter is only a partial solution. Further work on the governing equations is still needed.

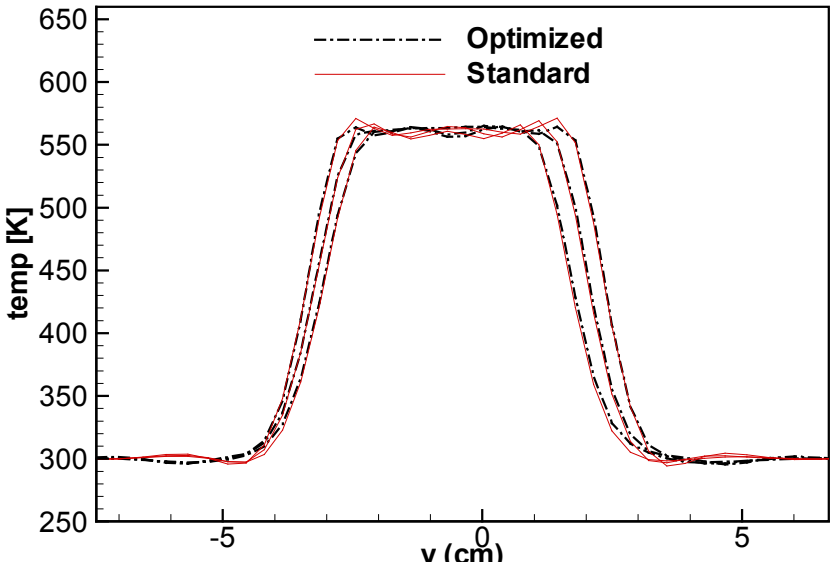

Figure 1. Gibbs phenomena improved by the optimized schemes on real plume simulations. Other conditions are same. (6^{th} order derivative, 4^{th} order Runge-Kutta time advancing, ASR=100).

Aliasing errors result from evaluation of the nonlinear terms on a discrete grid. Unlike truncation errors, aliasing errors can be removed from some simulations and a method of controlling aliasing errors is known in the Fourier space. Dealiasing has primarily been performed in incompressible flow simulations. Suppression of aliasing errors in compressible flow simulations is difficult due to the division by density required in numerical formulations. To minimize the aliasing error, the nonlinear terms has been rewritten in the skew symmetric form (Kravchenko et al., 1997).

$$\frac{\partial \rho u_i u_j}{\partial x} = \frac{1}{2}\left(\frac{\partial \rho u_i u_j}{\partial x} + u_i \frac{\partial \rho u_j}{\partial x} + \rho u_j \frac{\partial \rho u_j}{\partial x} \right) \tag{1}$$

Most of the current compressible jet simulations are medium or high Mach number flow (such as Ribault et al., 1999, Bogey et al. 2004). Nonlinear cascading of energy to smaller scales is a feature of turbulent flows. While artificial dissipation can be introduced to eliminate them, it imposes in essence, a grid-dependent turbulence model.

For LES, the effects of spurious waves are not well understood at present. The Reynolds number is high so the dissipative effect by the Smagorinsky model is also strong. For such flow, the turbulent viscosity vs. molecular viscosity ratio is on the order of 10, while in the low Mach number plume case this ratio is typically on the order of 0.5. Large values of the Smagorinsky coefficient will dissipate the turbulence, while small values will not damp the spurious waves. There is some research work aiming at model-free simulations with the utilization of the artificial diffusion caused by upwind schemes. Low order scheme will have a dissipative effect on turbulent scales. DesJardin et al (2003) used high order schemes for a plume simulation, but their high-order scheme has the special dissipation introduced by the upwinding and the ENO schemes. So the dissipative nature of the scheme is important for a successful CFD simulation.

7.4. Other candidate solutions

Most computational Aeroacoustics (CAA) simulations on jet acoustics are those for subsonic flows, using compact scheme and explicit filtering. Sometimes the compact scheme is optimized and is also filtered with an optimized compact filter. The scheme itself has a lower dissipation than the classical standard (central) scheme. The associated high Reynolds number favors the gradient-type Smagorinsky model to damp the unwanted spurious waves. Comprehensive reviews are produced almost yearly on this hot research topic in the CAA community (Bogony et al. 2005, Colonius et al. 2004).

The non-density weighted LES formulation, which provides a subgrid diffusive term in the density equation, was helpful for numerical stability. Other work has used a direct approach of explicitly filtering the spatial scales by the addition of artificial selective

damping (Constantinescu, 1999). This approach is also used in the jet study by Bogey, Bailly and Juve (2000). Approaches to achieve robust simulations, without degrading the wideband spatial resolution of the calculations remains an active research area.

Comparison	Compressible jet	Saltwater plume
Characteristic Flow	Ma=0.9	Ma=0.0002153
Physical model	Non-Favre-weighting	Favre-averaging
Aliasing error treatment	Skew-symmetric	Rotational
FD scheme	6^{th} Compact scheme	6^{th} order central differencing
Coordinate	Cylindrical	Orthogonal
Time integration	4^{th} order RK	3^{rd} order RK
Filters	4^{th} central on Sij only	6^{th} order central

Table 3. Comparison of the numerical choices (Boersma et al. 1999).

Table 3 shows several choices for a round jet/plume simulation. Each item on the left column is chosen so that the numerical overshooting will be damped either by turbulent diffusion (via Smagorinsky model), an additional damping term (non-Favre-averaging), better-resolution (cylindrical meshes), a skew-symmetric form of the convective term (dealiasing) and additional filtering.

There is only one closely related research topic on plumes by DesJardin et al. (2003) where a similar compressible flow solver and a pseudo-compressibility method are adopted. Here is a table comparing our current simulation parameters with those provided by DesJardin et al. (2003). Their work is close to this work in the following aspects.

1. Fully compressible flow solver
2. Characteristic-based boundary treatment;
3. Pseudo-compressibility method for acoustic speed reduction;
4. Buoyancy-induced flow.

5. High-order discretization schemes
6. Chemically-inert flow

Their study is focused on the plume instability modes and flow dynamics. So only the near field is simulated. Our simulation work is focused on the far-field plume dynamics, so the near field is not as well resolved. Besides these dense grids for the near-field flow, the combination of high-order upwind scheme and ENO scheme plays an important role in overcoming the overshooting error.

Table 4 shows the computational details for the current simulation with a published result. The main difference is the choice of the numerical scheme and the resolution. While the grid size in both cases is on the order of 2~4 million grid cells, the choice of the discretization scheme and the dynamics procedure is more time-consuming.

Comparison	Helium plume	Hot-air plume
Temporal discretization	4^{th} order Runge-Kutta scheme	3^{rd} order Runge-Kutta scheme
Spatial discretization	9^{th} order upwind biased schemes + 5^{th} order ENO scheme + 4^{th} order flux/stress terms	6^{th} order central difference scheme + 6^{th} order central-stencil filter
Grid	136x136x136	136x136x256
Domain	4x4x4 D	16x16x16D
D/dx	62.5/12.9	29
Subgrid model	Dynamic Smagorinsky	Smagorinsky model
Running cost	20(sec) x 128 (cpus) x 5.5 (hour/sec)	10 (sec) x 4 (cpus) x 34.0 (hours/sec)
Acceleration ratio	PGS = 20	ASR = 100

Table4. Comparison with a plume simulation (DesJardin et al. 2004)

The numerical work in this thesis is limited by the computing resources and the choice of numerical methods. In a long run, S3DLES can have the following solutions for a good simulation of round plume:

Optimized FD derivative and filters

Compact FD derivative and filters

Optimized upwind FD derivative and filters

Non-density averaging governing equations

Hybrid methods (central differencing with WENO scheme applied locally)

Turn the orthogonal grids into cylindrical coordinates

Appendix A. Finite element technique for acoustics

Linear spring as a finite element is commonly used as an introductory material leading to the formal finite element analysis. Here we can derive the above theory from the famous Galerkin method, with applications in the field of structural dynamics.

The governing equation for any solid or gaseous bar (1-D case only) is

$$E\frac{\partial^2 u}{\partial x^2} = \rho\frac{\partial^2 u}{\partial x^2} \tag{A.1}$$

Here E is the modulus for solids and bulk modulus for gases ($E = \gamma p$).

In the dynamic case, the axial displacement is discretized as

$$u(x,t) = N_1(x)u_1(t) + N_2(x)u_2(t) \tag{A.2}$$

Here we chose the commonly used linear interpolation functions.

$$N_1(x) = \frac{x_{j+1} - x}{x_{j+1} - x_j},\quad N_2(x) = \frac{x\ - x_j}{x_{j+1} - x_j},\ x_j \le x \le x_{j+1} \tag{A.3}$$

Applying Galerkin method to equation B.1 yields the residual equation ass

$$\int_0^L N_i(x)\left(E\frac{\partial^2 u}{\partial x^2} - \rho\frac{\partial^2 u}{\partial x^2}\right)Adx = 0 \tag{A.4}$$

Assuming constant material properties, we have

$$\rho A\int_0^L N_i(x)\frac{\partial^2 u}{\partial t^2}dx = AE\int_0^L N_i(x)\frac{\partial^2 u}{\partial x^2}dx \tag{A.5}$$

Substitute (A..2) into (A.5), we can further have

$$AE\int_0^L N_i(x)\frac{\partial^2 u}{\partial x^2}dx = AE\int_{x_1}^{x_2}\frac{dN_i}{dx}\left[y_1\frac{dN_1}{dx} + y_2\frac{dN_2}{dx}\right]dx \tag{A.6}$$

$$\rho A\int_0^L N_i(x)\frac{\partial^2 u}{\partial t^2}dx = \rho A\int_0^L N_i(N_1\ddot{u}_1 + N_2\ddot{u}_2)dx \tag{A.7}$$

If rewrite the (A.6) and (A.7) into matrix form for only 2 elements, we have

$$\frac{\rho AL}{6}\begin{bmatrix}2 & 1\\ 1 & 2\end{bmatrix}\begin{Bmatrix}\ddot{u}_1\\ \ddot{u}_2\end{Bmatrix} + \frac{AE}{L}\begin{bmatrix}1 & -1\\ -1 & 1\end{bmatrix}\begin{Bmatrix}u_1\\ u_2\end{Bmatrix} = \begin{Bmatrix}f_1\\ f_2\end{Bmatrix} \tag{8}$$

For the system response, the external force is zero. So the right hand side of (A.8) is zero matrix. The stiffness matrix is the same as (equation 11 in chapter 4), but the mass matrix is different with (equation 10 in chapter 4). This is because here the consistent mass matrix is used. The consistent means the interpolation function used in formulating the mass matrix are the same as (consistent with) those used to describe the spatial variation of displacement. For the spring mass examples, the lumped mass matrix is used, where half the total mass of the element is assumed to be concentrated at each node and the connecting material is treated as a mass less spring with axial stiffness. The lumped mass matrix for a bar element is then $[m] = \frac{\rho AL}{2}\begin{bmatrix}1 & 0\\ 0 & 1\end{bmatrix}$, which is consistent with the distribution used in the mass-spring system.

For the finite element technique, the boundary is treated as node with various degrees of freedom. If the domain is closed, the 2 nodes at the walls have no degree of freedom, so only n nodes are involved, with a matrix of the form, but with n x n terms. The mass is also distributed into n nodes. If one side is open, this node is counted like others with one degree of freedom, so the total number of nodes is n+1, and $K_{n-1} = k_n$ instead of $K_{n-1} = k_n + k_{n+1}$ for internal nodes. This treatment is exactly the same as the physical reasoning in the text.

The prediction error is shown in figure A.1. The error is mainly physical, since the modeling error comes from the closeness of each element to the Helmholtz resonator model. The finer the grids, the better a Helmholtz model can be used as an element.

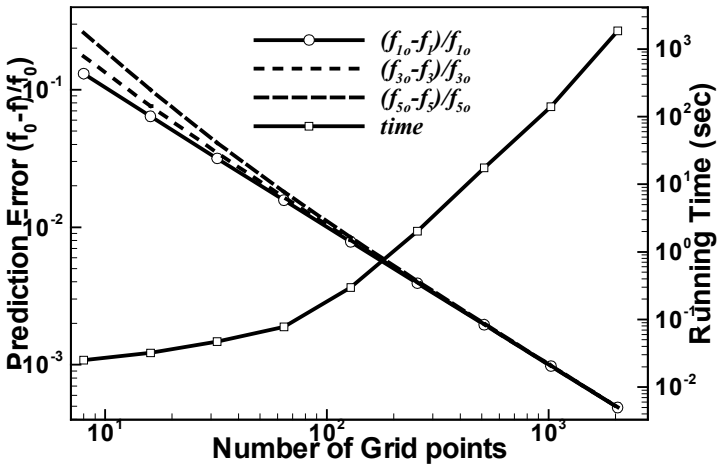

Figure A.1. Modeling errors for mass-spring method

```
%Matlab code for eigen-value analysis
clear all;close all;clc;
p0=101325;t0=300;mw0=0.02884;rho0=p0*mw0/8.3144/t0;c0=sqrt(1.4*p0/rho0);
c=zeros(ny-1,1);M1=zeros(ny-1,1);S1=zeros(ny-1,1);f=zeros(ny,1);
M2=zeros(ny-1,ny-1);S2=zeros(ny-1,ny-1);
djet   =  1.25*2.54/100.d0;theta   = 0.25*.0254/30.d0;dhjet   = .75*2.54/100.d0;
yhl    = djet-.5d0*dhjet;yhu     = djet+.5d0*dhjet;ny=100;
L0=3.5*.0254;dy=L0/(ny-1);
for j=1:ny
  y(j)=.0254*(-1.75)+dy*(j-1);
end
for k=8:8                % Molecular weight
mw(k)=k*.001; mass=0.d0;stiff=0.d0;
for j=1:ny
  temp1=5.d-1*(tanh((y(j)-yhl)/4.d0/theta)-tanh((y(j)-yhu)/4.d0/theta));
  p(j)=p0; s(j)=temp1; t(j)=t0;   m(j)=(1-temp1)*mw0+temp1*mw(k);
  rho(j)=rho0*m(j)/mw0;
end
for i=1:ny
  M1(i)=rho(i)*dy/pi;  S1(i)=1.4*p0*pi/dy; %-p0*(1-rho(i)/rho0)/dy;
end
for i=1:ny-1
  mass=mass+M1(i);   M2(i,i)=M1(i);   stiff=stiff+1.d0/S1(i);
    if i==ny-1
       S2(i,i)=S1(i)*2;         S2(i,i-1)=-S1(i);
    else if i==1
       S2(i,i)=S1(i)+S1(i+1);          S2(i,i+1)=-S1(i+1);
       else
       S2(i,i)=S1(i)+S1(i+1); S2(i,i+1)=-S1(i+1);      S2(i,i-1)=-S1(i+1);
    end
  end
  c(i)=sqrt(S1(i)/M1(i))/pi*dy;   f(i)=sqrt(S1(i)/M1(i))/2/pi;
end
[v d]=eig(S2,M2);stiff=1.d0/stiff;
for i=1:ny-1
  ff(i)=sqrt(d(i,i))/2/pi/pi;
end
ff3=sort(ff);ff2=sqrt(stiff/mass)/2/pi
figure(1);hold on;plot(y(1:ny-1),ff3,'-rx');
end
```

Appendix B: Numerical study on schemes used in LES

The S3DLES used for this thesis is based on the DNS code, S3D, developed by Sandia National Laboratory. S3D is a fully compressible solver with high-order central finite-difference scheme. This scheme is strictly non-dissipative in nature. This choice and other measures (such as filtering and time integration) prove to be a good choice for DNS on studies of combustion and acoustic phenomena, with the limitations clearly defined and tested by Kennedy et al. (1997). When tailoring to the LES framework, additional problems occur due to the numerical properties of the spatial discretization scheme. During the development of S3DLES, the resolution problem constantly lingers in all the simulations. Here the problems in LES will be discussed in different aspects of the numerical properties. Special attention is paid on the spectral improvement on the current numerical choices. Several numerical tests are performed to show the improvements. Finally, other candidate solutions to the problem are also proposed and discussed. Currently, there is still no conclusive idea on best high-order scheme for Large-eddy-simulations (usually application-dependent), so this study is some preliminary work for future decisions.

1. Analysis of the current numerical schemes

High-order methods typically have at least third-order spatial accuracy. Traditionally, second-order accurate numerical methods are often preferred in practical CFD simulations due to their simplicity and robustness. In many practical fluid problems, the solution structures are so complicated and their time evolution is so long, that it is impossible to obtain an acceptable solution with today's computing speeds using high-

grid density and low-order methods. So there is a need for high-order schemes. Vortical flow fields are especially challenging for low-order numerical methods that are typically found in current Euler and Navier-Stokes flow solvers. The main cause for this deficiency is that these vortical flow features deform and dissipate prematurely due to excessive numerical diffusion in the solution algorithms. High-order methods can minimize the numerical diffusion due to low-order finite difference schemes (Ekaterinaris, 2005).

High order central finite difference (CeFD) schemes are straightforward, easy to implement, and sufficiently accurate to capture the smallest resolvable scales presented at these problems with a small number of points per wavelength. Comparing with compact schemes, the demand on exchanging information from neighboring cells is acceptable for parallel computing. For this reasons, central difference schemes are very popular in DNS of compressible flow, Unfortunately, the standard central difference approximations tend to be unstable when the gridsize is not enough, which is usually encountered in LES, unless some kind of artificial numerical dissipation (damping or filtering) is added.

The inherent limitation of any numerical method is that any wavenumber k greater than $\pi/\Delta x$ on a uniform mesh cannot be resolved. Even in a well-resolved computation, numerical errors are still present and are introduced primarily at high wave number. This can be readily be seen by plotting the modified wave number versus wave number (see figure 1). In many situations such as those encountered in Large Eddy Simulation, high wavenumber couldnot be resolved by the grids, the oscillation between grids will not only degrade the order of the scheme, but also induce numerical instability. Experience with the use of high-order central difference schemes for LES indicates that grid-to-grid

oscillations can become locally dominant. This is commonly called Gibbs errors (numerical grid uncertainty) caused by a finite representation of a continuous function.

The uncertainty for a finite representation of a continuous function can be shown in the following numerical test. Here the spatial derivative can be approximated by a central 2N+1 points stencil, finite-difference scheme in the form as

$$\frac{\partial u}{\partial x}(x_0) = \frac{1}{\Delta x}\sum_{j=-N}^{N} a_j u(x_0 + j\Delta x) \tag{1}$$

The coefficients are derived to cancel the Taylor series in (1) so that the maximum order of resolution is reached. Applying Fourier transform to (1), the effective wavenumber of the scheme is given by,

$$k^*\Delta x = 2\sum_{j=1}^{N} a_j \sin(jk\Delta x) \tag{2}$$

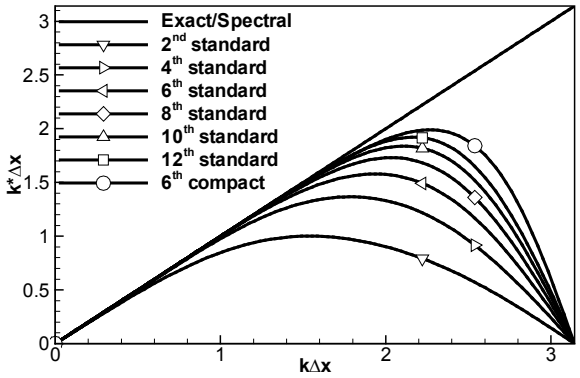

Figure 1. Modified wavenumber versus wavenumber (Fourier images) of first-derivative spatial operator for standard different finite difference schemes

Figure 1 shows the accuracy of various centered-difference first derivatives relative to the exact spectral derivative. Using the scaled wavenumber $\omega = 2\pi k\Delta x/\lambda$ where λ is the wavelength and the number of grid points per wavelength is $2\pi k/\omega$. Therefore, the lower the scheme's resolving ability the higher is the number of points per wavelength

required to resolve accurately certain predetermined portion of the range $[0,2\pi]$. The spectral method gives an exact representation of the first derivative up to a grid resolution. In contrast, finite-difference methods exhibit large errors at high wavenumbers. Even though more accurate finite-difference schemes provide better approximations at higher wavenumbers, the accuracy is always better at low wavenumbers than at high wavenumbers. All derivative operators except the spectral method have no resolution at $k\Delta x = \pi$ and have marginal resolution for wavenumbers near π. Nonlinear interaction of these unresolved nonphysical waves of various wavenumbers generates higher wave-number oscillations.

As a comparison, one compact scheme (will be discussed more later) is also shown in figure 1. It is noticed the compact derivative operators are more accurate than their explicit counterparts because the compact scheme has an implicit nature. Additional cost is needed for matrix inversion in solving the derivative from the implicit schemes.

When the grid is unable to resolve the highest wave-number information, the error is introduced into low wave numbers and eventually contaminates the solution. In addition, successive application of the first derivative operator to obtain a second-order derivative results in an amplification factor of unity at $k\Delta x = \pi$ for centered-difference operators; this application facilitates what is commonly referred to as "odd-even" decoupling. To suppress these effects, a numerical filter is used to create artificial viscosity. The important feature of these filters is that the eigenvalues corresponding to low wave numbers that are resolved should be virtually untouched; the relatively unresolved high wavenumbers should be removed. So it is a matter of selecting the bandwidth for the damping function of the filters.

Though Lele (1992) uses the compact filters up to the sixth order, S3D adopts an explicit filter because it is computationally more efficient and its design is more conceptually straightforward. Filtering is applied to the solution vector after the full predictor-corrector and central-difference stages in order to remove spurious information before it could move to lower wave numbers. The appropriate filter order was chosen based on the interior or boundary accuracy of the differencing scheme. The fact that the filters had such a significant effect indicates that the simulations may not have been completely resolved (Kennedy et al. 1994). Without filtering, the high-frequency spurious wave will be easily shown in dilation terms, which are sensitive to the resolution issues.

The grid-to-grid oscillation introduced by central finite-difference schemes must be removed because they can lead to numerical instabilities. Practically, the elimination of these spurious short waves is obtained by introducing artificial dissipation through additional damping terms in the equations or more efficiently through filtering without affecting the physical long waves. Applying a central 2N+1 point stencil filter to variable u on a uniform mesh provides

$$u^f(x_0) = u(x_0) - D_u(x_0), \text{ with } D_u(x_0) = \sum_{j=-N}^{N} d_j u(x_0 + j\Delta x) \tag{3}$$

where the coefficients are such as $d_j = -d_{-j}$ ensuring no dispersion. The standard approach for determining constants in canceling the terms resulting from the Taylor series of (3) for $k\Delta x \to 0$.

The spatial Fourier transform of (3) is

$$D_k(k\Delta x) = d_0 + \sum_{j=-N}^{N} 2d_j \cos(jk\Delta x) \tag{4}$$

Here $D_k(k\Delta x = 0) = 0$ and $D_k(k\Delta x = \pi) = 1$. The damping function shows the amount of dissipation for any wavenumber (figure 2).

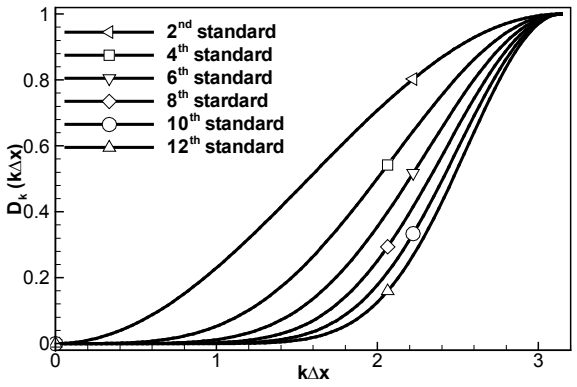

Figure 2. Performance of different finite-difference filters.

Figure 2 shows the damping function $D_k(k\Delta x)$ for some explicit filters used in S3D. Note the transfer function shown in Lele's paper (1992) is $1 - D_k(k\Delta x)$, the band passing zone in a frequency domain.

2. Numerical problems in LES

Since the main problem in plume simulation is associated with the high order scheme, we can devise some tests to show the problem. Here we have 2 typical test profiles for testing the performance of the derivation operation:

Case 1. Sinusoidal profile

$$y(x) = \sin(x), \frac{dy}{dx} = \cos(x) \tag{5}$$

Case 2. Hypertangent profile

$$y = \tanh\left(\frac{x}{\theta}\right), \frac{dy}{dx} = \frac{1}{\theta}\left[\sec h\left(\frac{x}{\theta}\right)\right]^2 \tag{6}$$

Here θ is 2 times momentum thickness. The raw signal and its derivative are shown in Figure 3(a) and 4(a) respectively. Case 1 is used for testing the global property of any scheme, since there is no special gradient appeared in the series. The wavenumber is discrete; the gradient is smooth and can easily be captured. Case 2 has a central gradient at the center of the domain. This special gradient needs enough grids to cover or special treatment to capture, so it is commonly used to test the local behavior of a difference scheme.

Applying the 6th order central scheme to case 1 shows that the global performance of the scheme is 6th order. The 6th and 8th order filtering will not change the order of the derivative operator, while lower order filters change the performance significantly (figure 3b). This shows the explicit filter play an important role in the derivative operation. The round-off error for current simulations is about 10^{-14}, so the error curves couldn't go beyond this limit.

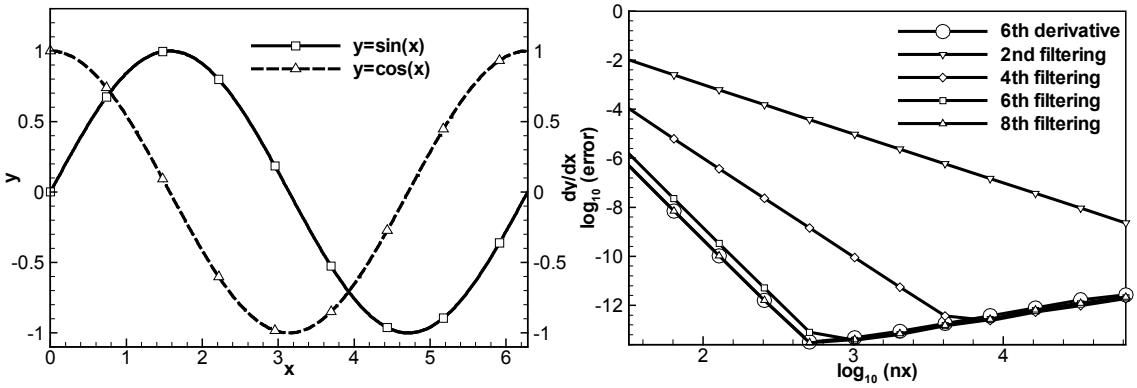

(a) *(b)*

Figure 3. Sinusoidal wave and performance curve

When case 2 is used, the global resolution behavior is not monotonous. Instead, the system error will not decrease much until the grid is fine enough to cover the gradient. Then the scheme gains its nominal performance with finer resolutions. Below a certain grid density level, the error lingers and cannot be overcome simply by increasing the number of grids. Unfortunately, most grids requirement at LES level falls bellow this grid density. So the simulation error cannot be smaller simply by increasing the grid density, while the derivative operation has no problem at the resolution of DNS. The Gibbs error (shown in figure 5) is not a simple function of grid number, so improvement is little when refining the grids, unless a grid level of DNS is reached. This behavior is discussed by Boran and Oris (1987) and also mentioned in DesJardin et al. (2003).

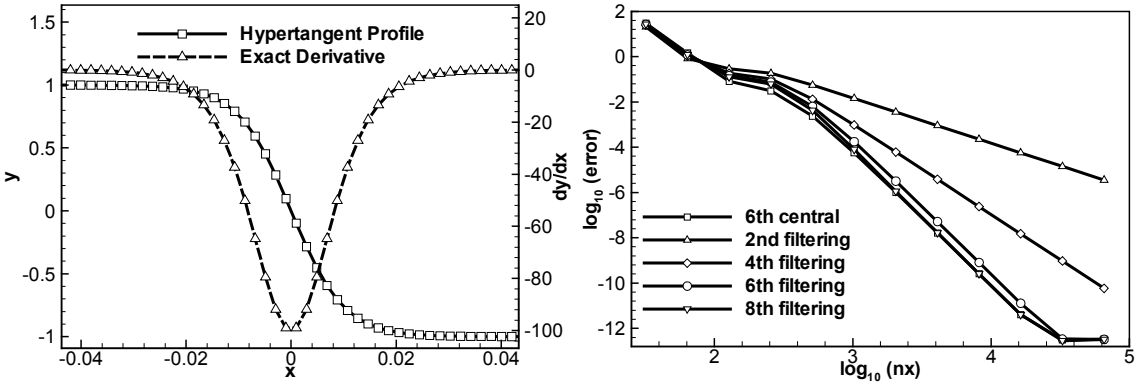

(a) *(b)*

Figure 4. Hyper-tangent profile and the performance curve for derivative and filters.

A systematic increase of grid number on Gibbs behavior is shown in figure 5. According to the Nyquist sampling rule, when there are not enough grid cells to cover the gradient, the numerical solution on grid cells will not be representative of the real value. The true derivative value is also sparsely sampled. The Gibbs phenomenon is usually appeared when the central scheme (usually non-dissipative) is used to capture the gradient. The

central schemes are usually non-dissipative, so the oscillation at the sharp gradient could not be simply damped.

The SGS viscosity commonly used in LES has the capability to be dissipative. But it is not designed to do this work, so there is some calibration work needed to use this property. Too much or not enough viscosity will lead to problems. If the eddy (SGS) viscosity is too much, it will kill the turbulence and laminarize the flow. When the flow is laminar, the computation is more DNS like, and the important feature of plume mixing is missing. If the SGS viscosity is not enough, the numerical oscillation induced by the central scheme could not be damped. This is true especially for low Mach number flow, where the turbulent behavior is not significant. This error will accumulate in the computational domain and contaminate the solution finally. So the computation needs other means of numerical damping to get the stabilized solution.

Figure 5 shows the Gibbs error when the grid number is not enough to capture the sharp gradient and filtering is not enough to remove the high-frequency oscillations. The high-order central-stenciled filters are designed to remove the high wave number oscillation associated with high-order derivative, and they fail to work properly when the derivative operator fails to capture the gradient. Figure 5 (a) shows that the high-order filter shifts the local energy, while the oscillation is not damped, but shifted. Only when enough grids are provided, both the derivative and the filter will capture the gradient to their designed purpose. So they are popular choices for DNS codes.

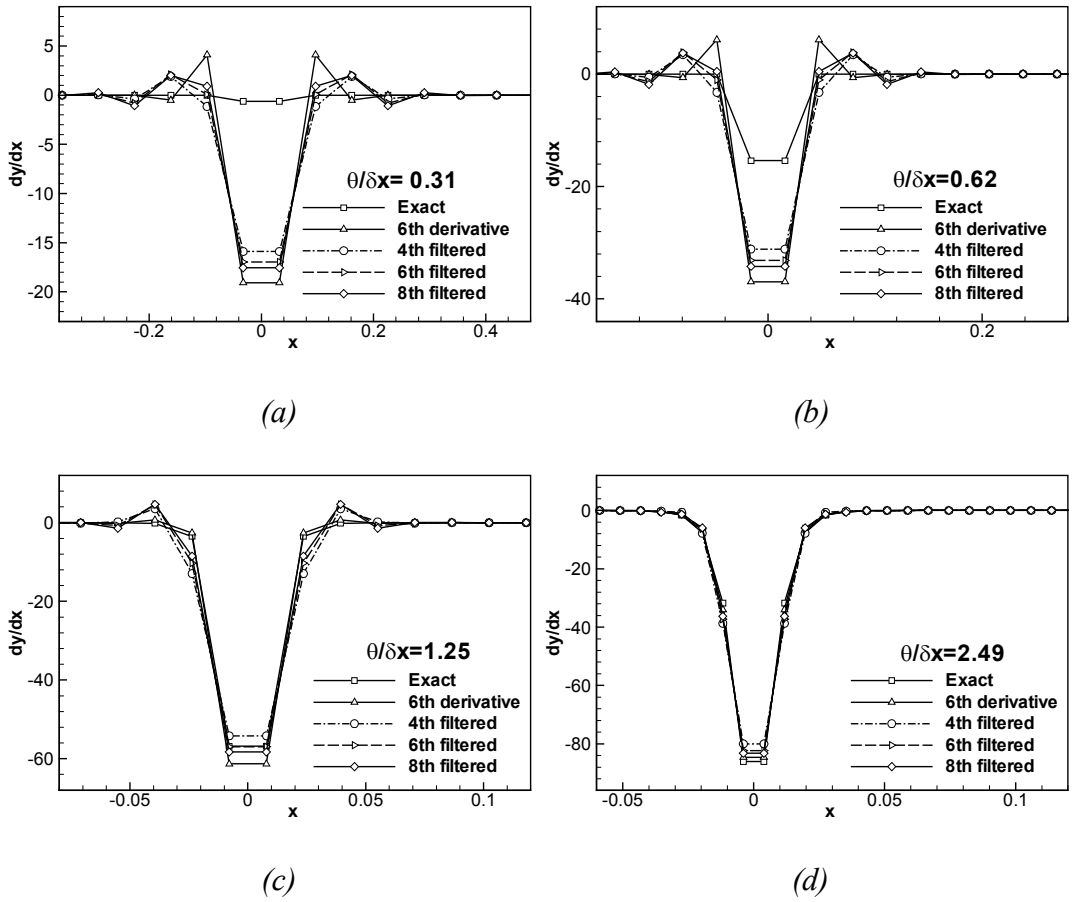

Figure 5. Gibbs error associated with not-enough grid cells covering the gradient.

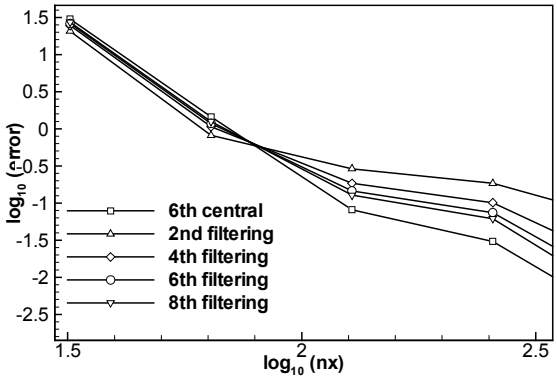

Figure 6. Role of filters at coarse grids

Figure 6 shows the role of the numerical filter at coarse grids, where the gradient is not fully resolved. The improvement is not significant, but also not zero. Along with the

finite-difference schemes, the filters fail significantly at coarse grids. So the filters cannot overcome the Gibbs error.

From figure 5 and figure 6, we can also see that the low order filter could not damp the strong oscillations at coarse grids. The improvement by the filters is limited at coarse grids. Since the code relies heavily on the filters to damp unwanted high-wavenumber oscillation, the error introduced by the high order scheme and not enough grids is difficult to remove by the filter. In other words, the filters determine the performance of the derivatives.

3. A family of low dispersive and low dissipative explicit schemes

For the Gibbs phenomena associated with high order schemes, there are 2 directions for improving to the schemes: decreasing the dispersion error (commonly adopted in CAA community) and increasing dissipation (commonly adopted in CFD community)

Taylor analysis is a tool that provides the order of accuracy, while Fourier analysis is used to investigate the dispersion properties. Utilizing a concept of often called bandwidth optimization in aero-acoustics, the formal accuracy can be sacrificed in exchange for better dispersion properties in the construction of an explicit center-difference scheme to represent the derivative.

The most promising candidate solution is the optimized finite difference scheme, with only minor modification to the coefficients to CeFD. A family of such optimized scheme is developed with the purpose of developing a low dispersive and low dissipative (LDD) explicit schemes for CAA (Bogey et al. 2004).

Following Tam and Webb (1993), the optimized finite difference schemes are developed so that the dispersion error is small for a large range of wave numbers up to $k\Delta x = \pi/2$. They are of fourth order and their coefficients are defined to minimize the integral error

$$\int_{\ln(k\Delta x)_l}^{n(k\Delta x)_h} \left| k^* \Delta x - k\Delta x \right| d(\ln(k\Delta x)) \tag{7}$$

where the wavenumber limits are $(k\Delta x)_l = \pi/16$, $(k\Delta x)_h = \pi/2$ for optimized schemes. The Fourier image of modified wavenumber for the optimized schemes is shown in figure 7.

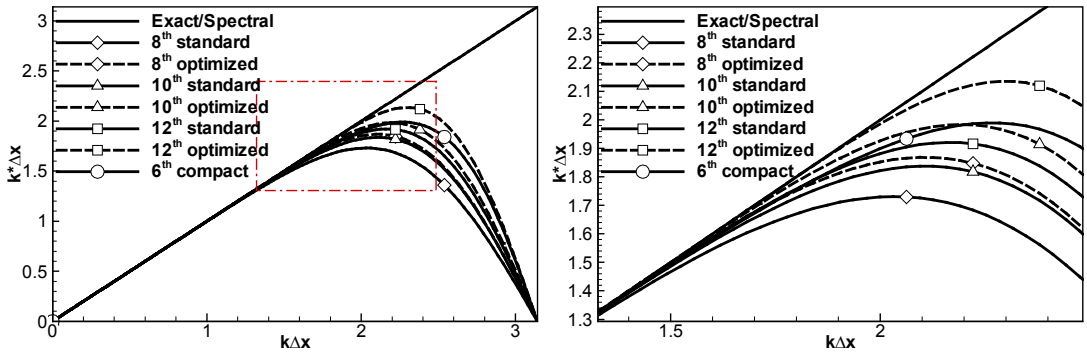

Figure 7. The modified wavenumber versus wavenumber for optimized schemes.

The standard center-stenciled finite difference filter has the coefficients derived from the canceling the terms resulting from the Taylor series of equation (3) for $(k\Delta x) \to 0$. To develop selective filters, the spatial transform function $D_k(k\Delta x)$ is optimized so the integral dissipation is small in a certain range (in accordance with the optimized derivative scheme (7)).

$$\int_{\ln(\pi/16)}^{n(\pi/2)} D_k(k\Delta x) d(\ln(k\Delta x)) \tag{8}$$

The damping functions of the optimized filters are displayed in figure 8. As expected, the dissipation is small for long waves and is significant for the wavenumber near $k\Delta x = \pi$.

Increasing the number of stencil points, from N=3 to N=6, allows to construct more selective, spectral-like filters.

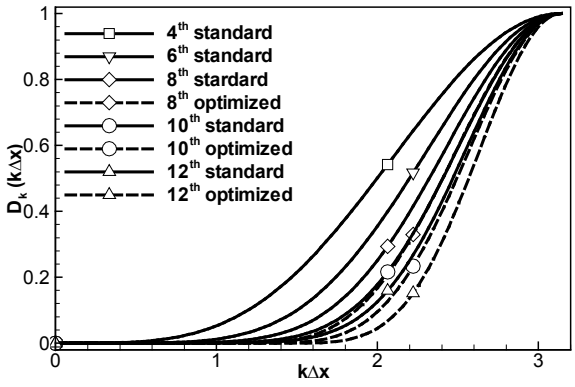

Figure 8. Performance of different finite-difference filters.

The standard Runge-Kutta time integration scheme can also be optimized to improve their dispersion and dissipation properties. Following the idea of Hu et al. (1997), the optimized scheme coefficients are derived via optimizing the dissipation and the dispersion error up to the angular frequency $\omega\Delta t = \pi/2$. Both are of second order and are defined by coefficients γ_l minimizing the following error:

$$\int_{\ln(\pi/16)}^{n(\pi/2)} \left|1 - G_{RK}(\omega\Delta t)\right| d(\ln(\omega\Delta t)) + \int_{\ln(\pi/16)}^{n(\pi/2)} \left|\omega^* \Delta t - \omega\Delta t\right| d(\ln(\omega\Delta t)) \qquad (9)$$

with these two conditions for the dissipation rate

$$\begin{cases} 1 - \left|G_{RK}\right| > 0 \\ \dfrac{\partial(1 - \left|G_{RK}\right|)}{\partial\left[\ln(\omega\Delta t)\right]} \geq -5 \end{cases}$$

for $0 \leq \omega\Delta t \leq \pi$, as for the selective filters. The performance of the optimized Runge-Kutta scheme is shown in figure 9.

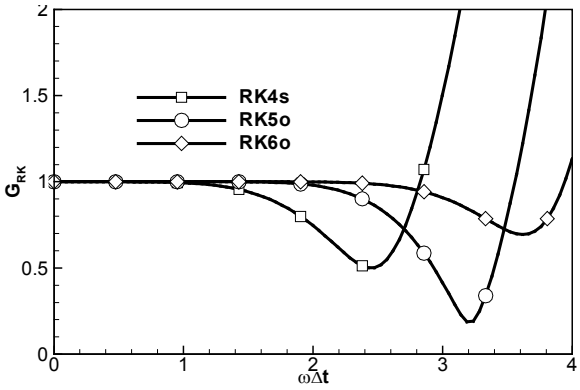

Figure 9. Performance of optimized Runge-Kutta time advancing Scheme

Due to the pseudo-compressibility method used in S3DLES, the time advancing steps are limited by the reduced acoustic speeds. The dispersion behavior of the Runge-Kutta scheme gains more importance with this acceleration. Though it is difficult to discern any significant error from the spatial error due to time advancing scheme, it is expected that the optimized scheme will have better performance over the conventional scheme.

It is expected that the d8 optimized derivative, f8 optimized filter, and Rko5 time integration will form a LDD scheme under the current framework of S3DLES. Here a test case with Hypertangent profile is used to test the performance of the optimized schemes.

4. Test of the optimized schemes

The numerical derivative is performed on case 2 (equation (6)) with different schemes and variable resolutions shown below (figure 10). Here the resolution is defined as $L/dx = 2\theta/dx$, the number of grid points covering the full gradient (4 times the momentum thickness).

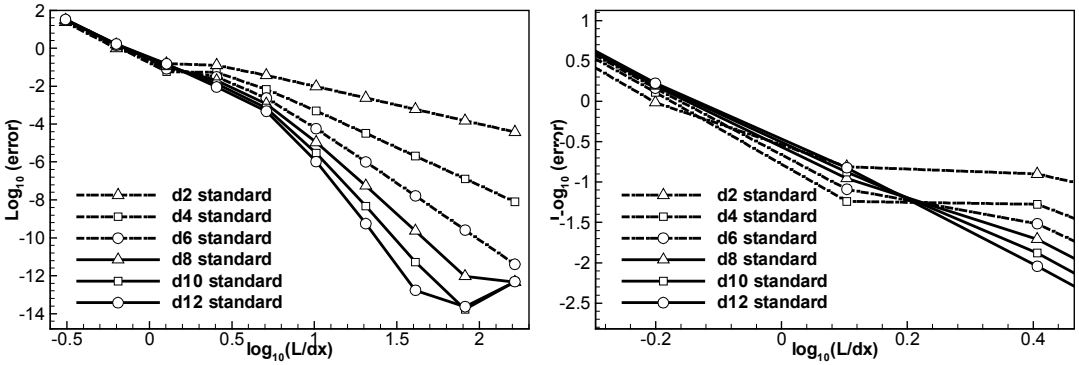

Figure 10. Performance of Standard derivatives

Figure 10 shows the performance of standard FD derivatives on the Hypertangent profile. The nominal order of the high order scheme only was gained after a certain resolution $L/dx \approx 2 \sim 5$. When the gradient is under-resolved, all schemes produced poorer behavior. It is also noticed that the lower order scheme behaves better at low wavenumber, because the shorter stencils and their dissipative nature.

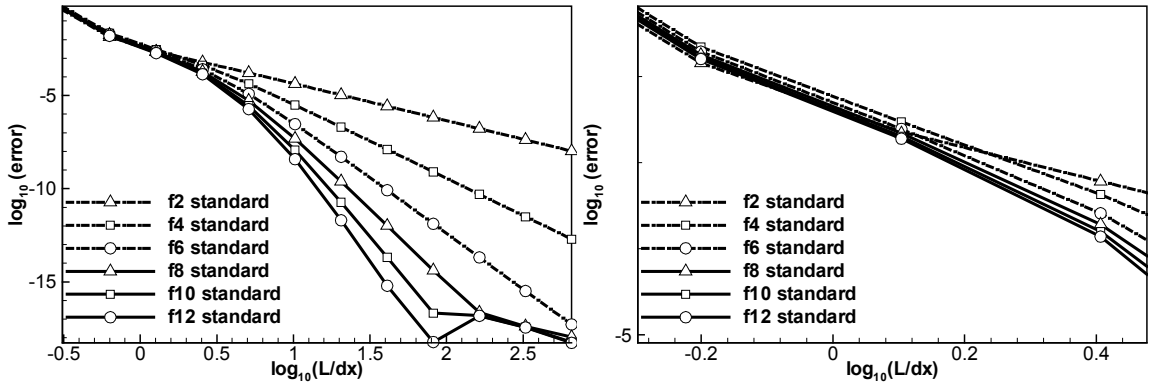

Figure 11. Performance of Standard filters

Figure 11 shows the performance of standard FD filter on the Hypertangent profile. The low order filters are always poorer than the high order schemes.

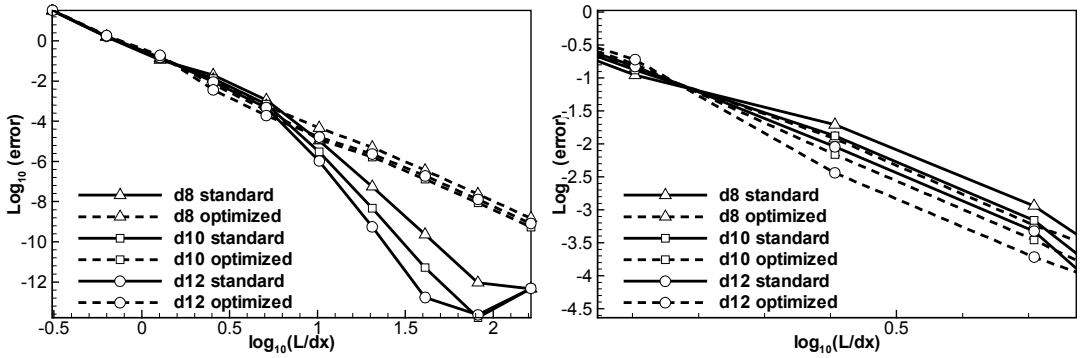

Figure 12. Performance of optimized derivatives comparison with standard derivatives.

Figure 12 shows that the optimized schemes are poorer than the standard schemes globally (in the full spectrum). But they are superior only in a certain range as the dash-dot line marked and zoomed up in the right figure. From this figure, it is clear that the optimized scheme have better performance in a certain region while sacrificing the global behavior in the high wavenumber region. The improved region is located in a range right around the grid resolution for large eddy simulation, so it is a better choice for LES, with improved dispersive and dissipative properties over the conventional high-order derivatives. The spectral resolution is improved at the price of degrading the overall resolution. The details of the improvement are shown in the coming figure 13.

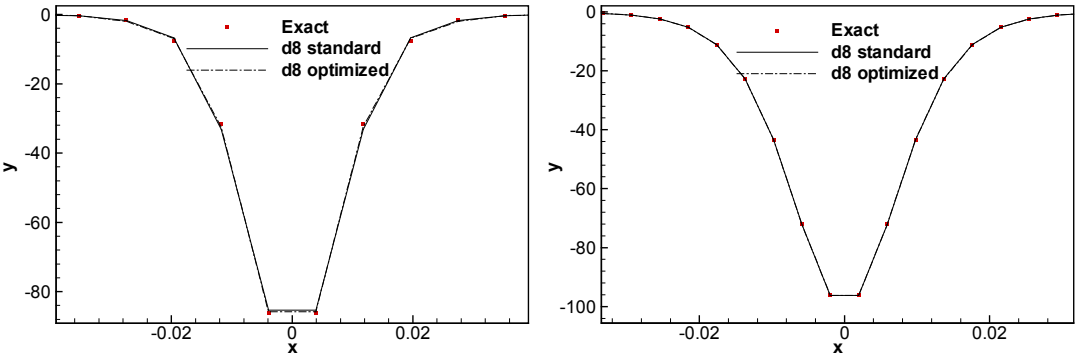

Figure 13. The derivative for Hypertangent profile.

Figure 13 shows the local behavior of the optimized scheme over the standard schemes. Only around the resolution L/dx=2.6~5.1 (nx=256~512), the optimized scheme is better

than the standard schemes. The error improvement is not significant in these graphs, which shows from the error perspective that the derivative operation is not so important as the filtering operators (Kennedy et al, 1997).

The performance of any derivative scheme is limited by the accompanying filter. Here the optimized filter over the Hypertangent profile is shown in figure 14. Again, the optimized filter is better only up to the resolution of around L/dx=2.6. All filters have their designed behavior in the high wavenumber region, and deteriorate significantly when the grid is not dense enough. The optimized filters improve the overshooting behavior in the under-resolved region.

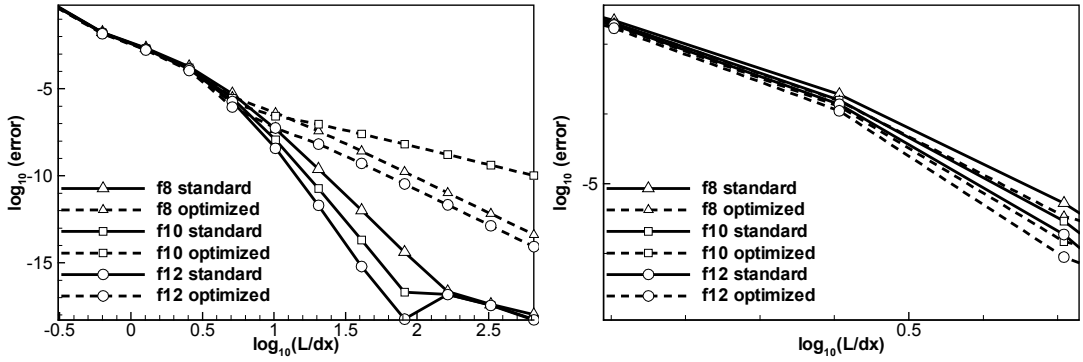

Figure 14. The performance of optimized filters on a Hypertangent profile.

Again, the optimized filters gained their improved spectral resolution by sacrificing their overall resolution. Here f8 and f12 optimized are 4^{th} order while the f10 optimized has only 2^{nd} order resolution.

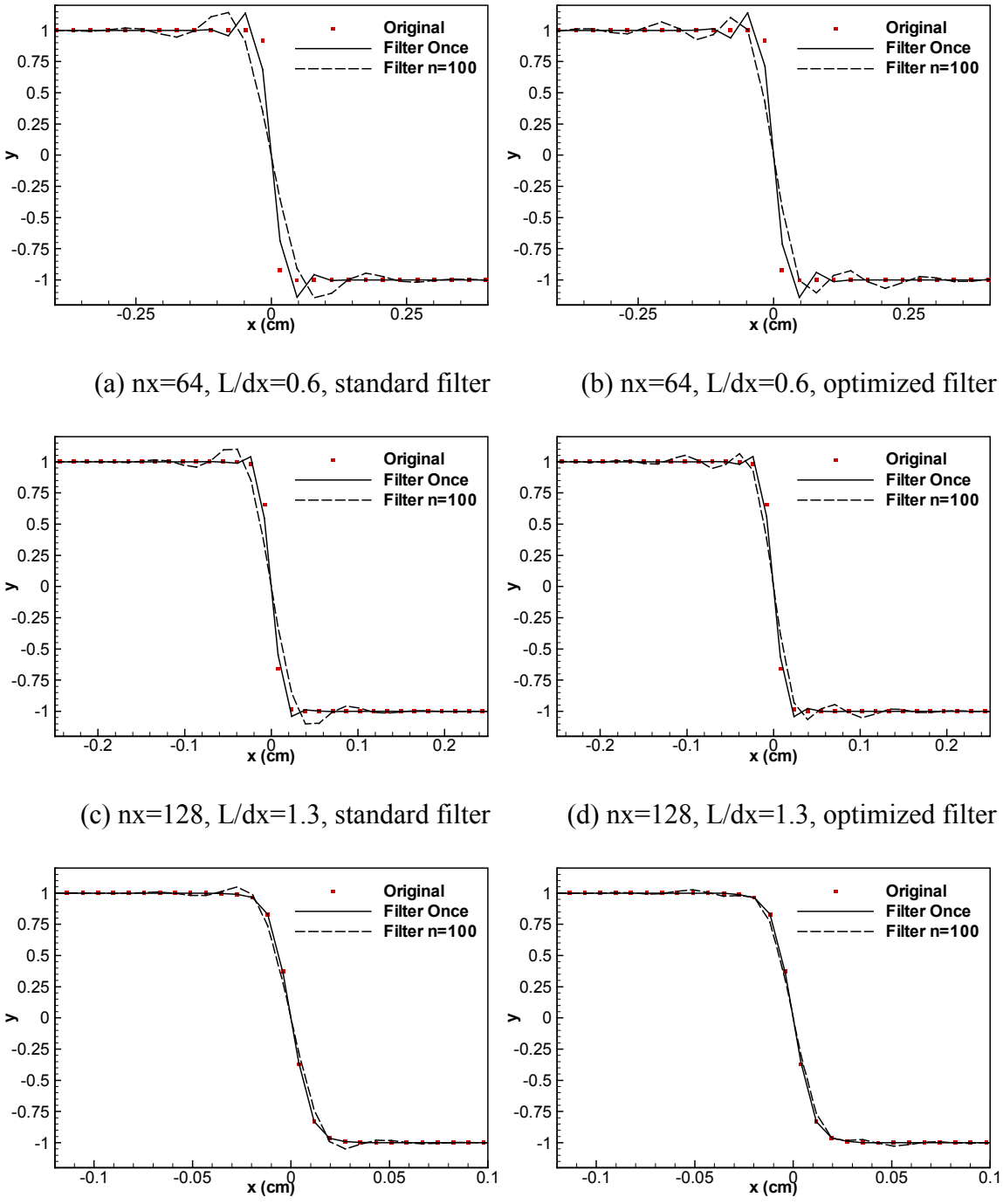

(a) nx=64, L/dx=0.6, standard filter

(b) nx=64, L/dx=0.6, optimized filter

(c) nx=128, L/dx=1.3, standard filter

(d) nx=128, L/dx=1.3, optimized filter

(e) nx=256, L/dx=2.6, standard filter

(f) nx=256, L/dx=2.6, optimized filter

Figure 15. Filtering of the Hypertangent profile

Figure 15 shows the local behavior of the optimized filtering scheme over the standard filtering schemes. The optimized scheme shows better performance than the standard

schemes up to the resolution of L/dx=2.6. When the gradient is not fully resolved, the application of filters will degrade the resolution. So multiple applications of filters will propagate the error away from the gradient. It also shows that the optimized selective filter has better performance in low wave number but poor behavior at high wave number, so after 100 times of filtering, the error travels more distance than those of the standard filter, but the maximum amplitude is significantly smaller.

5. Family of upwind schemes for CFD

Another line of thoughts for improving the robustness of the simulation is to increase the dissipation in the finite difference operations. This is a commonly adopted approach in CFD community. For nonlinear problems, straightforward application of high-order accurate central difference schemes is not possible, because the spurious modes that develop from the irresolvable by the numerical discretization high frequency models lead to instabilities (Ekaterinaris, 2005). Rai and Moin (1991) found that high-order upwind schemes are more promising to simulate turbulent flows. Upwinding alleviated some of the problems encountered with centered schemes and yielded some promising results for both incompressible and compressible flow DNS.

Upwind schemes (2n-1 order) can be considered as the corresponding central schemes (2n order) plus a correction term that introduces the numerical dissipation (Li, 1997). So it is commonly resorted as an alternative when the numerical dissipation is not enough to overcome the overshooting and under-shooting behavior. Comparing with the central scheme, it is more close to the flow physics, since the biased stencil can be chosen such that it favors the incoming flow.

The general form of the upwind scheme is

$$\frac{\partial u}{\partial x}(x_0) = \frac{1}{\Delta x}\left(\sum_{j=1}^{N} a_{-j}u(x_0 - j\Delta x) + a_0 u(x_0) + \sum_{j=1}^{N} a_j u(x_0 + j\Delta x)\right) \tag{9}$$

Depending on the flow direction, the a_N or a_{-N} is zero depending on local flow directions. Here only (N-1)-cells-stencil is chosen for upwind-biased schemes. It is a choice to provide the maximum formal order of accuracy for any partial upwind scheme when N is fixed. The coefficients determination process is the same as the standard schemes (using Taylor table).

The modified wave number is a complex function with real and imaginary parts. The real part and the imaginary part are associated with the dispersion error (phase error) and the dissipative error (amplitude error) respectively.

$$\begin{aligned} k_r^*\Delta x &= \sum_{n=1}^{N}\left[(a_n - a_{-n})\sin(nk\Delta x)\right] \\ k_i^*\Delta x &= \sum_{n=1}^{N}\left[(a_n - a_{-n})\cos(nk\Delta x)\right] + a_0 \end{aligned} \tag{10}$$

For the centered difference schemes, the imaginary part is zero, so all the centered schemes are non-dissipative.

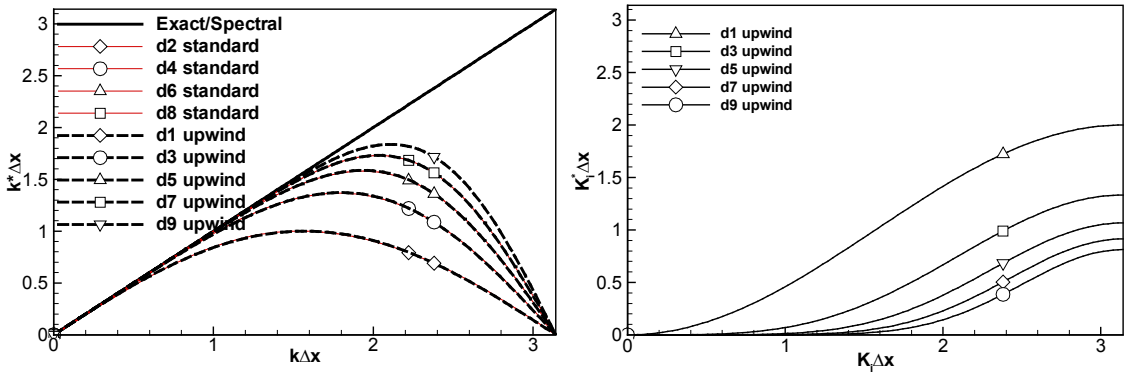

Figure 16. Modified wavenumber for standard and upwind schemes

Figure 16 shows the real part and the imaginary part of the wave number for upwind-biased schemes. The dispersion property of the (2N-1) upwind scheme is the same as the standard 2N standard scheme, while the same stencil is used. Upwinding introduced additional dissipative terms shown in the right figure. Note the wavenumber for central stenciled schemes is real, so central schemes are non-dissipative which is a good advantage in CAA.

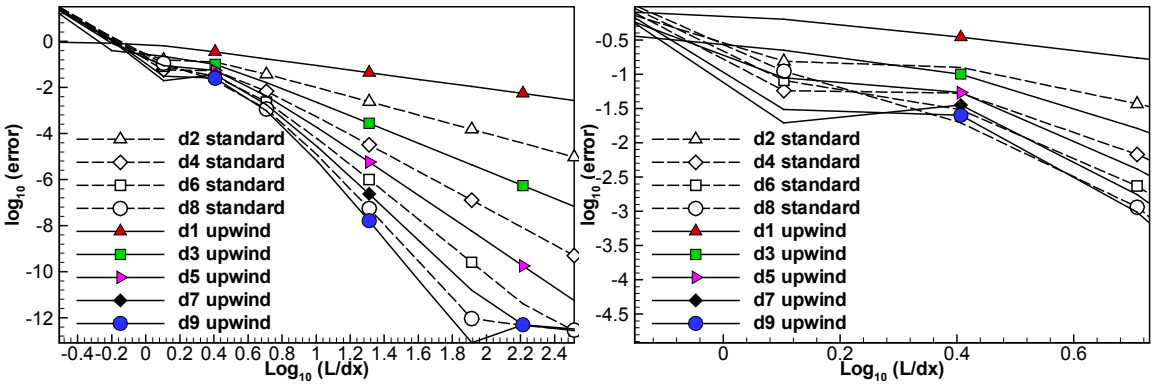

Figure 17. Performance of upwind-biased schemes on the Hypertangent profile

Figure 17 shows the global performance of upwind-biased schemes. Comparing with the standard central scheme of the same stencil size, the upwind schemes have additional dissipative terms, so the behavior is locally improved. Also the upwinding scheme has used one point smaller than standard scheme, so the resolution is one order smaller. The global resolution is slightly sacrificed in favor of the dissipation for robustness.

An extension to the upwind scheme is the wavenumber-extended high-order upwind-biased finite difference scheme, which provides the better resolution characteristics for the same order upwind scheme (Li, 1997). The coefficients are chosen to have better wavenumber performance using the integrated error minimization method (same as equation 7, but with different spectral interval for optimization), originally proposed by Tam and Webb (1992). The resulting new scheme is of 2N-2 formal order, which is one

order lower than the corresponding upwind-biased schemes. However, their high wavenumber oscillations are suppressed to a greater extent.

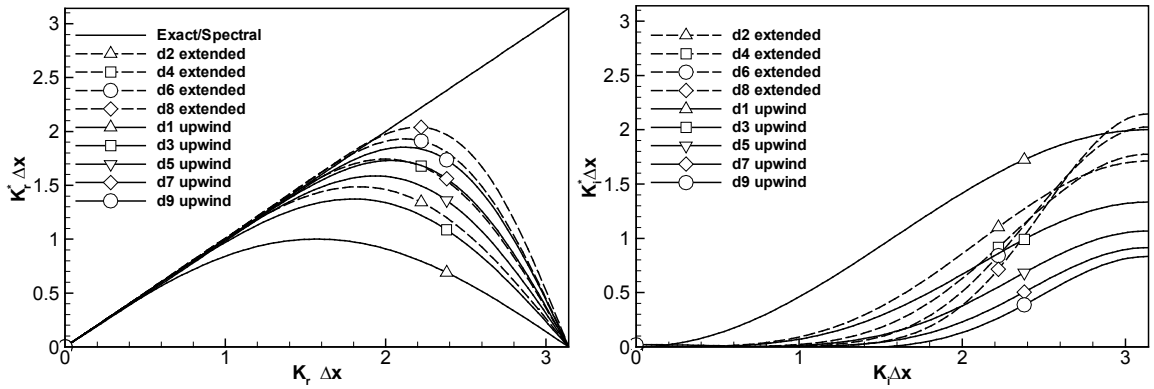

Figure 18. Performance of upwind and wavenumber-extended upwind schemes (Li, 1997)

Figure 18 shows the performance of the wavenumber-extended upwind schemes over normal upwind scheme. Basically, the spectral performance is tailored to favor the low wavenumber regime while sacrificing the high frequency resolution. The comparison between upwind and extended schemes on the Hypertangent profile is shown in figure 19. The comparison of standard and wavenumber extended schemes is show in figure 20.

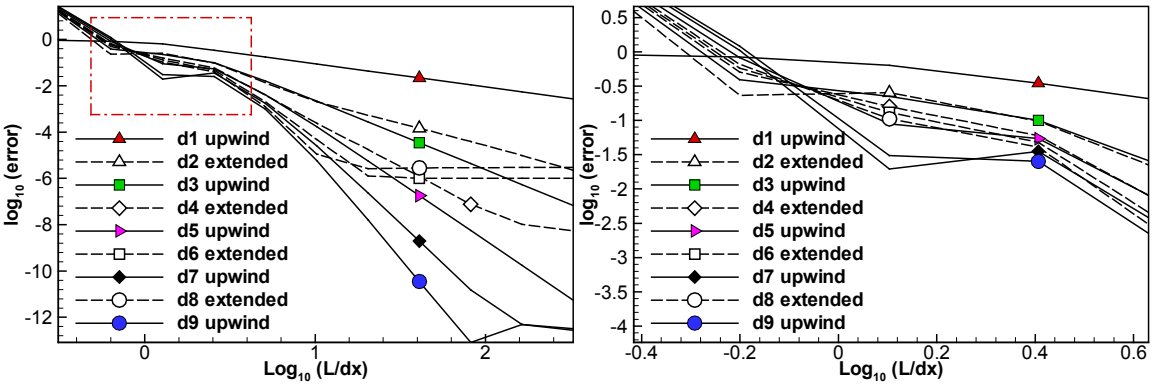

Figure 19. Tests of upwind and wavenumber-extended upwind schemes

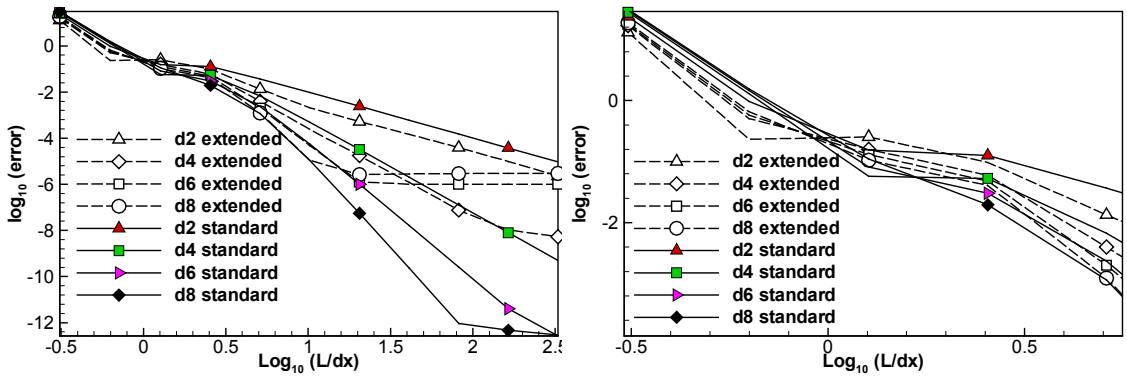

Figure 20. Tests of standard and wavenumber-extended upwind schemes

6. Family of compact schemes for CFD

The first systematic attempt to develop high-order accurate, narrow stencil, finite-difference schemes appropriate for problems with a wide range of scales was presented by Lele (1992). Compared with the traditional FD approximations, the compact schemes provided a better representation of the short-length scales. As a result, compact high-order scheme are closer to spectral methods and at the same time maintain the freedom to retain accuracy in complex stretched meshes. Emphasis in the development of compact schemes was given on the resolution characteristics of the difference approximations rather than formal accuracy. Compact schemes are variations or extensions of the Pade scheme, so they are also called Pade schemes in the literature.

Due to the high performance of the compact schemes and the leading work of Lele (1992), the family of compact schemes is popular in CAA community. Compact schemes using the neighboring derivative information, so it is an implicit scheme by nature, which requires numerical solver to reconstruct the local information for the global array of derivatives. This also put a strong demand on communication if running on multi-processors. Most of the current code adopted a compromise by recovering the derivative

matrix within one processor, thus the communication are reduced at the price of degrading the performance. The general form for a tridiagonal compact scheme has the following form.

$$\alpha\hat{f}_{i-1} + \hat{f}_i + \alpha\hat{f}_{i+1} = af_i + \frac{d}{2}(f_{i+3} - f_{i-3}) + \frac{c}{2}(f_{i+2} - f_{i-2}) + \frac{b}{2}(f_{i+1} - f_{i-1}) \qquad (11)$$

The stencil coefficients a,b,c,d are chosen to have the best resolution while the coefficient α determines the implicitness of the scheme. Here $-0.5 \le \alpha \le 0.5$, and $\alpha = 0$ leads to the standard (central-stenciled) high order finite difference schemes.

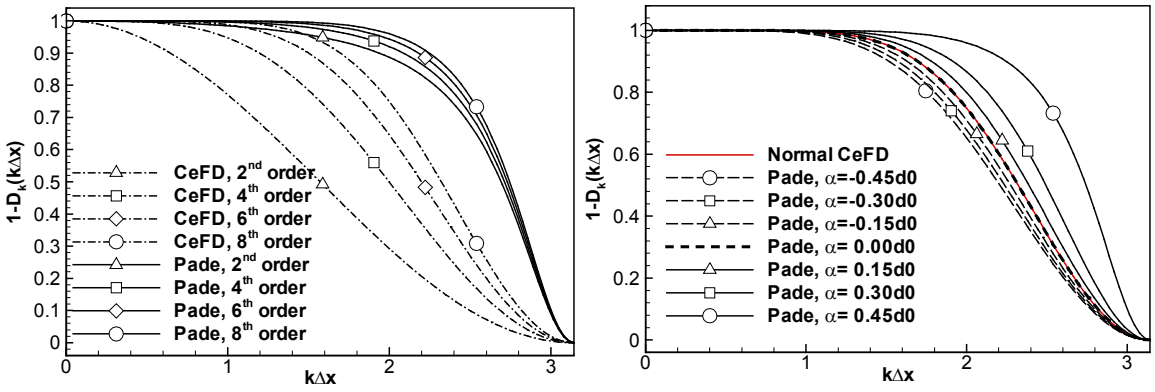

Figure 21. Fourier analysis for compact schemes

Fourier analysis of compact scheme with different α is shown in figure 21. Usually, α is close to 0.5 to have the best spectral performance.

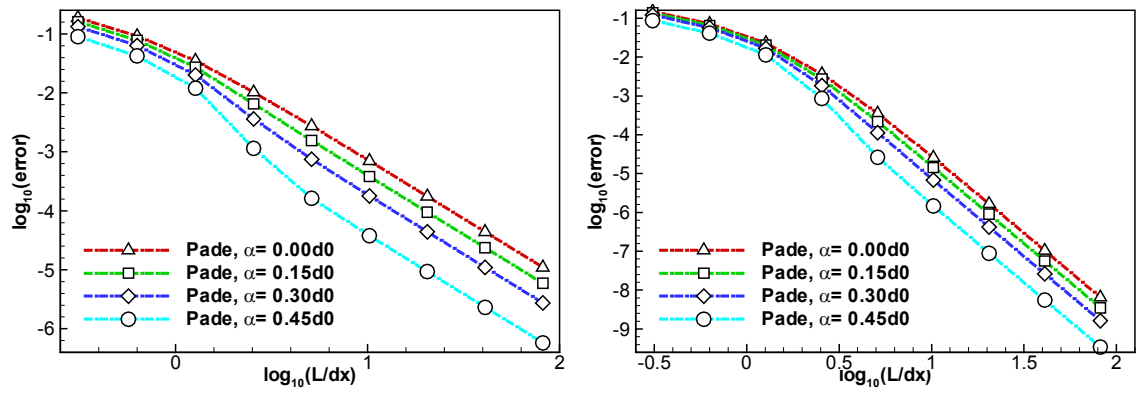

(a) *(b)*

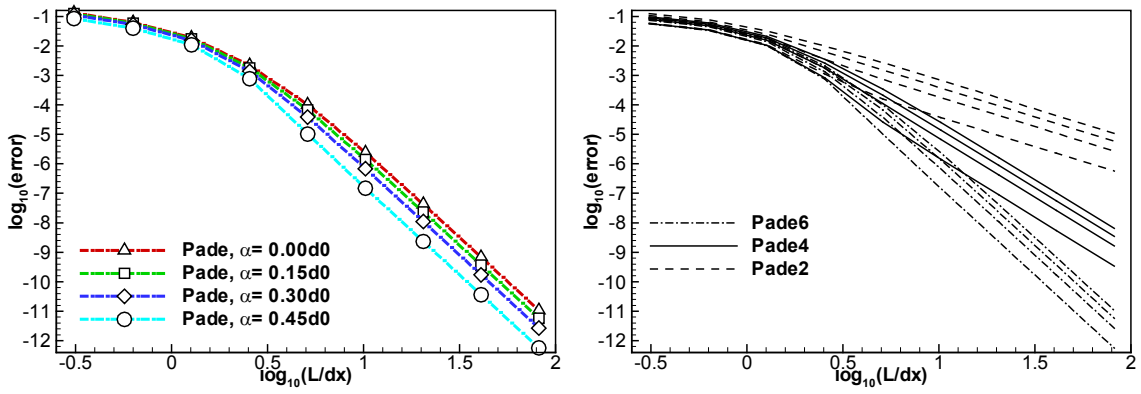

(c) *(d)*

Figure 22. Taylor analysis of compact schemes (a) 2nd order (b) 4th order (c) 6th order (d) all

Taylor analysis of the schemes is shown in figure 22. Like the usually central schemes, the nominal (theoretical) order of resolution is achieved after a certain resolution.

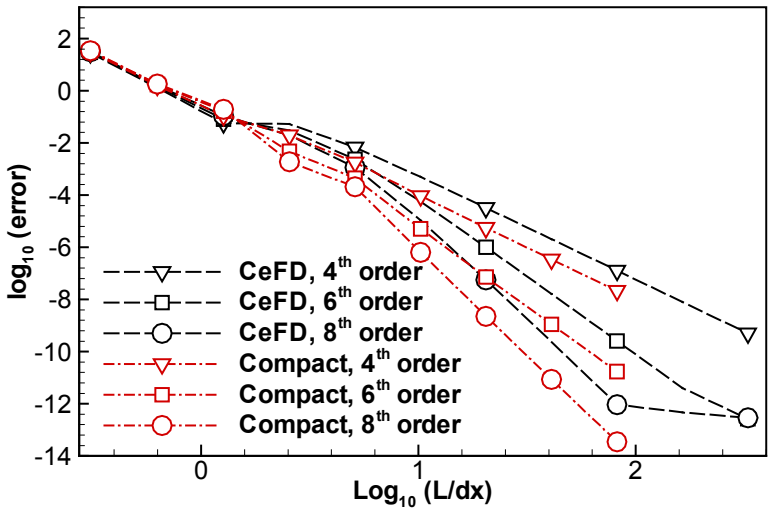

Figure 23. Comparison of compact scheme with central schemes

Figure 23 shows the performance of compact schemes with central schemes (α =0.45). The compact schemes gain no significant improvement in the low frequency domain.

7. WENO schemes

The Gibbs phenomenon is well known to appear with high order schemes. Several schemes are developed to overcome such unphysical oscillations. Usually, they are based on Finite Volume Approach. Here the popular WENO (Weighted Essentially-Non-Oscillatory) scheme is tested here to show its non-oscillatory nature.

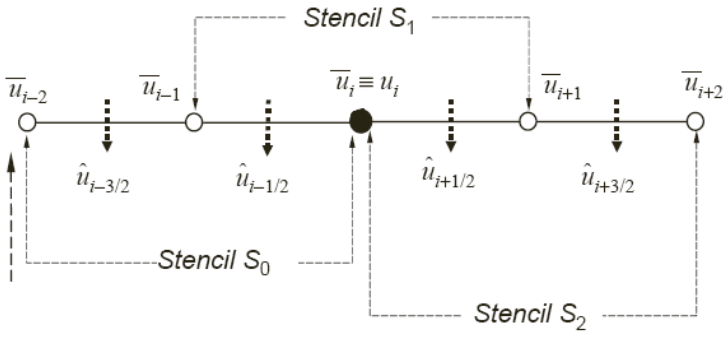

Figure 24. Stencils for WENO scheme

The combination of stencils used of WENO scheme in shown in Figure 24. The weights are chosen that the stencil covering sharp gradient have a small weight/contribution. So the scheme have local dissipative nature near gradients Like most TVD schemes, the sharp gradient is captured with first order upwind scheme while the higher order performance is resumed away from the sharp gradients. The purpose of such combination is to find the best stencil with a strong damping term (weight) for sharp gradients.

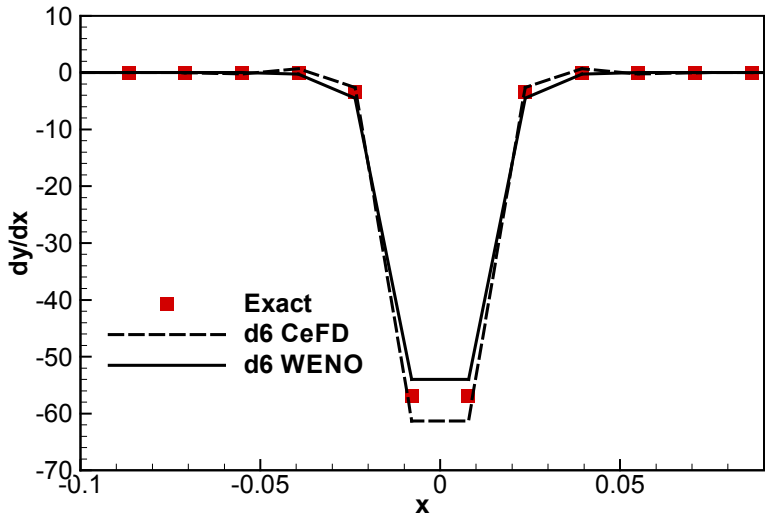

Figure 25. The non-oscillatory feature of WENO scheme

Figure 25 shows the non-oscillatory nature of WENO scheme. The oscillation behavior at sharp gradients is suppressed by the dissipation terms.

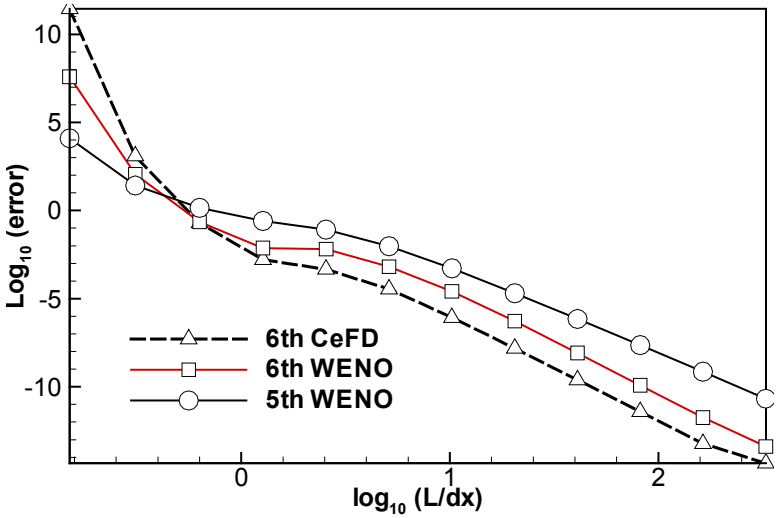

Figure 26. Comparison of 5th WNEO scheme with 6th order central scheme

Figure 26 compares the WENO scheme with 6th order central scheme. It can be seen that the WENO scheme performs better in the high wavenumber region, while resuming its higher order performance for low wavenumber components.

8. Other candidate solutions

Large-eddy simulations of turbulent flows are normally performed on grids that are just fine enough to resolve the important large flow structures, and numerical discretization errors on such grids can have considerable effects on the simulation results.

A point of concern related to the high order numerical schemes such as the ones used in this study is that the discretization does not numerically conserve kinetic energy for an inviscid low Mach number flow. This means that the calculation can become unstable when a flow scale is under-resolved, and there is not enough viscosity (molecular or subgrid) to damp this instability. Because in a LES setting the molecular viscosity is relatively low, the damping has to come from the subgrid model. The calculation of the subgrid stresses is subject to numerical errors to the point that $2\Delta x_i$ error waves become apparent. These $2\Delta x_i$ waves in the subgrid stresses can generate instabilities in the resolved quantities. To avoid numerical problem, such error waves are removed by filtering the strain rate tensor before the terms in the subgrid stress are calculated.

Dissipation can be added by using additional damping term, using upwind biased schemes, and/or using implicit filters or explicit filters. Following Boersma and Lele (1999), several treatments to the governing equations are proposed in LES framework. As a non-linear equation, Favre averaged continuity equation will be prone to numerical instabilities. Such instabilities are observed to lead to small grid point to grid point waves. These waves have to be removed from the flow field. This can be done by adding an artificial diffusion term to the right hand side of the continuity equation. Another way to do this is by using the non-Favre averaged LES equations. In this set of equations a damping term is already present in the continuity equation. The LES modeling of the

non-Favre averaged equations is a little bit more complicated due to the appearance of an additional unsteady term in the momentum equation. Here S3DLES adopted the first strategy, i.e., using explicit filtering to introduce the additional artificial diffusion term into the continuity equation.

In simulations where not all the relevant length and /or time scales of the problem are being resolved, dissipation must be added to ensure computational stability. Some numerical dissipation is desirable to remove spurious high-frequency information regardless of whether second-order derivatives are taken once with a second-order derivative operator or twice with a first-order derivative operator. The source of this high-frequency information may be intrinsic instability in the scheme, the misspecification of physical boundary conditions, the "odd-even" decoupling between grid points, or insufficient resolution (temporal and spatial). Upwind finite-difference schemes are one possible way of introducing numerical dissipation into the solution to damp high wavenumber components. DesJardin et al. (2004) used 9^{th} order biased upwind scheme together with ENO scheme to capture the derivatives.

When all above improvements on governing equations and on numerical schemes are not enough for removing the overshooting behavior, the more dissipative shock-capture schemes are resorted. The application of such schemes is still tentative in the CFD community.

1. ENO (Essentially Non-Oscillatory) and WENO (Weight Essentially Non-Oscillatory) schemes

2. Hybrid (High-order hybrid central-WENO finite difference scheme) and flux-splitting-limiting

Essentially Non-Oscillatory schemes (ENO) have been developed in order to overcome the Gibbs phenomenon (Harten, 1997). ENO schemes make use of nonlinear weights based on divided difference of the numerical solution in order to bias the local stencil when computing derivatives, avoiding interpolations across discontinuities. This method has been adopted partially in Runge-Kutta steps by DesJardin et al. (2003). Weighted Essentially Non-Oscillatory schemes (WENO) are an improvement over ENO schemes due to their higher order of accuracy with same stencil size (Jiang, et. al. 2000). A convex combination of all the possible sub-stencils of ENO achieves optimal order of accuracy at the smooth parts of the solution. Nevertheless, the intrinsic numerical dissipation of WENO schemes, although necessary to capture shock waves, might seriously damp relevant small scales.

Since the central finite difference scheme is numerically more efficient than the WENO scheme, it is natural to find an algorithm to combine the 2 schemes together, and use a numerical switch between the discontinuity-capturing schemes and the normal FD schemes for smooth parts of the solution. The important sensor is a switch algorithm that dynamically decide at any given time step which scheme to turn on at each grid point. A high order multi-resolution analysis is chosen to perform at every time step of the temporal integration process. The resulting adaptive scheme ensures that fluxes at grid points around discontinuities will always be computed by a WENO scheme, whereas smooth tendencies will not suffer any unnecessary extra damping since they will be

treated by a central scheme. A smart sensor (multi-resolution method) is designed to detect the sharp gradients (Figure 27, Costa et al., 2006).

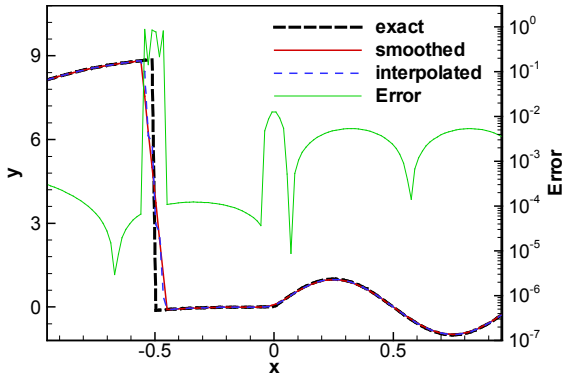

Figure 27. The difference between smoothed and interpolated data to find the sharp gradient for switching CeFD/WENO

Since the low-order filter has no Gibbs phenomena, a combination of low and high order filtering is realized to damp the physical noise. The solution is based on flux correction/limiting on the corrective fluxes, which is the difference between a high-order diffusion scheme and a low-order one. Over-shootings near sharp gradients are prevented, while the highly selective property of damping is retained (Xue, 2000).

9. Conclusions

While popular in DNS, the higher order CeFD schemes introduce high-wavenumber oscillations in LES of jet and plumes. Two approaches are adopted to remove the overshooting and undershooting behavior, decreasing the dispersion and increasing the dissipation. The CAA community adopted the first choice for better resolution, while CFD community adopted the second for better robustness. Most adjustments to the central schemes are to improve the spectral performance of the scheme (sharper spectral cutoff for the same stencil), while at the price of decreasing the order of the schemes.

Similar argument is also valid for finite difference filters and the time integration schemes. Tests are performed on a Hypertangent profile for these specially designed schemes.

Unlike the strict low-dispersion and low-dissipation requirement in CAA, the design objective of S3DLES is to simulate low-Mach number flows of practical dimensions. So the dispersion property of high order central FD scheme should be controlled. Here is a list of potential solutions to the simulation of buoyancy-induced flow using S3DLES:

1. Additional damping terms, such as the non-Favre-averaging procedure will introduce an additional damping term into the continuity equation;
2. Adopting skew-symmetric form for convection terms, avoiding the aliasing error due to unresolved non-linear terms;
3. Higher order scheme with better spectral properties, such as the compact scheme and Pade filters.
4. Optimized higher order finite difference scheme with optimized selective filters;
5. 4^{th} order Runge-Kutta scheme or optimized 5^{th} order Runge-Kutta scheme.
6. Hybrid scheme with variable upwinding, introducing more dissipation;
7. Hybrid scheme with ENO/WENO for local improvement;
8. Converting the orthogonal coordinate system into cylindrical only for round flow simulations.

Of these choices, only partial solution are realized and tested in S3DLES. The next important criterion is the computational cost. The final choice will be balanced among development easiness, accuracy, and running cost. The modification in the current

research work is not enough, given the fixed framework set in S3D. Further work is needed to tailor this code more suitable to low Mach number simulation purposes.

Reference:

1. Boersma BJ, Lele SK. Large eddy simulation of compressible turbulent jets. In: Annual Research Briefs. Center for Turbulence Research, Stanford University, 1999. p. 365 – 77.
2. Bogey, C., Bailly, C., A family of low dispersive and low dissipative explicit schemes for flow and noise computations, Journal of computational physics, 194 (2004) 194-214
3. Colonius, T., Lele, S.K., Computational aeroacoustics: progress on nonlinear problems of sound generation, Progress in Aerospace Science 40 (2004) 345-416
4. Constantinescu, G.S., Lele, S.K., Large eddy simulation of a near sonic turbulent jet and its radiated noise, AIAA 2001-0376
5. Costa, B., Don, W.S., High Order hybrid central-WENO finite difference scheme for conservation laws, submitted to Elsevier Science, 2006
6. Ekaterinaris, J.A., High-order accurate, low numerical diffusion methods, for aerodynamics, Progress in Aerospace science 41 (2005) 192-300
7. Harten A, Engquist B, Osher S, Chakravarthy SR. Uniformly high order accurate essentially non-oscillatory schemes. 3. J Comput Phys 1987;71:231 – 75.
8. Hu, F.Q., Hussaini, M.Y., Manthey, J.L., Low dissipation and low-dispersion Runge-Kutta Schemes for computation acoustics, Journal of computational physics, 124, 177-191 (1996)
9. Jiang, G.M., Shu, C.W., Efficient implementation of Weighted ENO Schemes, Journal of Computational Physics, 126, 202-228 (1996).
10. Li, Y., Wavenumber-extended high-order upwind-biased finite-difference schemes for convective scalar transport, Journal of computational physics, 133, 235-255, 1997
11. Rai & Moin (1991), Direct simulation of turbulent flow using finite-difference schemes, Journal of computational physics, 96: 15-53
12. Xue, M., High-order monotonic numerical diffusion and smoothing, Monthly weather review, vol. 128, pp. 2853-64, 2000
13. Tam, CKW, Webb, JC., Dong Z., (1993) A study of the short wave components in computational acoustics, Journal of Computational acoustics, 1 (1): 1-30

Appendix: Stencil Coefficients for modified numerical schemes.

	D8, standard	D10, standard	D12, standard	D8, optimized	D10, optimized	D12, optimized
a_1	4/5	5/6	6/7	0.841570125482	0.872756993962	0.907646591371
a_2	-1/5	-5/21	-15/56	-0.244678631765	-0.286511173973	-0.337048393268
a_3	4/105	5/84	5/63	0.059463584768	0.090320001280	0.133442885327
a_4	-1/280	-5/504	-1/56	-0.007650904064	-0.020779405824	-0.045246480308
a_5		1/1260	3/1155		0.002484594688	0.011169294114
a_6			-1/5544			-0.001456501759

Table 1. Coefficient of the standard and optimized finite difference first derivative schemes

	f8, std	f10, standard	fD12, standard	f8, optimized	f10, optimized	f12, optimized
d_0	35/128	63/256	231/1024	0.243527493120	0.215044884112	0.190899511506
d_1	-7/32	-105/512	-99/512	-0.204788880640	-0.187772883589	-0.171503832236
d_2	7/64	15/128	495/4096	0.120007591680	0.123755948787	0.123632891797
d_3	-1/32	-45/1024	-55/1024	-0.045211119360	-0.059227575576	-0.069975429105
d_4	1/256	5/512	33/2048	0.008228661760	0.018721609157	0.029662754736
d_5		-1/1024	-3/1024		-0.002999540835	-0.008520738659
d_6			1/4096			0.001254597714

Table 2. Coefficient of the standard and optimized finite difference spatial filter schemes

	U1D0, 1st order	U2D1, 3rd order	U3D2, 5th order	U4D3, 7th order	U5D4, 9th order	U6D5, 11th order
ϕ_{i-6}						1/2772
ϕ_{i-5}					-1/630	-1/210
ϕ_{i-4}				36/5040	1/56	1/336
ϕ_{i-3}			-1/30	-336/5040	-2/21	-5/42
ϕ_{i-2}		1/6	1/4	1512/5040	1/3	5/14
ϕ_{i-1}	1	-1	-1	-1	-1	-1
ϕ_i	-1	1/2	1/3	1260/5040	1/5	1/6
ϕ_{i+1}		1/3	1/2	3024/5040	2/3	5/7
ϕ_{i+2}			-1/20	-1/10	-1/7	-5/28
ϕ_{i+3}				48/5040	1/42	5/126
ϕ_{i+4}					-1/504	-1/168
ϕ_{i+5}						1/2310

Table 3. Coefficient of the upwind schemes

	U2D1, 2nd order	U3D2, 5th order	U4D3, 7th order	U5D4, 9th order
ϕ_{i-5}				-0.004191
ϕ_{i-4}			0.015825	0.041288
ϕ_{i-3}		-0.055453	-0.127442	-0.188962
ϕ_{i-2}	0.213933	0.360600	0.482326	0.552022
ϕ_{i-1}	-1.141798	-1.221201	-1.303877	-1.328033
ϕ_i	0.651798	0.554534	0.553877	-0.528033
ϕ_{i+1}	0.286067	0.389400	0.417674	0.447978
ϕ_{i+2}		-0.027880	-0.039225	-0.049133
ϕ_{i+3}			0.000842	0.000379
ϕ_{i+4}				0.000619

Table 4. Coefficient of the wavenumber-extended upwind schemes

Reference:

1. Alpert, R. (1972), Calculation of Response Time of Ceiling-Mounted Fire Detectors.Fire Technology, Vol. 8, No. 3, 181-195, May 1972.
2. Bardina, J., Ferziger, J.H., Reynolds, W.C., Improved subgrid scale models for large eddy simulations, AiAA paper 80-1357
3. Basu, A.J., Mansour, N.N., (1998). Large eddy simulation of a forced round turbulent buoyant plume in neutral surroundings, Center for turbulence Research Annual Research Briefs.
4. Basu, A.J., Narasimha, (1999), Direct numerical simulation of turbulent flows with cloud—like off-source heating, Journal of Fluid Mechanics, 385, 199-228
5. Batchelor, (1954), Heat convection and buoyancy effects on fluids. Q. J. R. Met. Soc. 80, 339-258
6. Baum, M., Poinsot, T. and Thevenin, D. (1995) Accurate boundary conditions for multi-component reactive flows, J. Comp. Phys. 116, 2:247-261.
7. Bejan, A., (1984), Convective Heat Transfer, Wiley, New York
8. Boersma, G.J., Brethouwer, G., Nieuwstadt, F.T.M., (1998), A numerical investigation on the effect of the inflow conditions on the self-similar region of a round jet, Phys. Fluids 10: 899–909.
9. Boersma, B.J., Lele, S.K., Large eddy simulation of compressible turbulent jet, Annual Research Briefs, 1999.
10. Chen, C.J., Rodi, W., (1980) Vertical Turbulent Buoyant Jets, (HMT, the science applications of heat and mass transfer; vol. 4. Pergamon Press
11. Chu, V.H., (1994) Lagrangian scaling of turbulent jets and plumes with dominant eddies, in Recent Research Advances in the Fluid Mechanics of Turbulent Jets and Plumes, ed. by Davies, P.A., Neves, M.J. V., NATO ASI Series, pp: 45-72.
12. Clement, J. M. (2000) Experimental Verification of the Fire Dynamics Simulator (FDS) Hydrodynamic Model, Ph.D Thesis, University of Canterbury, New Zealand
13. Cortesi, A.B., Smith, B.L., Yadingaroglu, G., Banerjee, S., (1999) Numerical investigation of the entrainemnet and mixing processes in neutral and stably-stratified mixing layer, Physics Fluids 11 (1) 163-185.
14. Cook, A. W., and J. J. Riley. 1998. "Subgrid-scale modeling for turbulent, reacting flows", *Comb. Flame*, Vol. 112, pp. 593-606.
15. Colonius, T., 2004, Modeling Artificial Boundary Conditions for Compressible Flow, Annu. Rev. Fluid Mech. 36:315-345.
16. Cox, G. (1995) Compartment Fires, in Combustion Fundamental of Fire, G. Cox, ed., New York, Academic Press.
17. Crighton, D.G., Dowing, A.P., Ffowcs Williams, J.E., Heckl, M., and Leppington, F.G., Modern methods in analytical acoustics, Springer Verlag,: London, 1992
18. Crow S.C., Champagne, F.H. (1971) Orderly structure in jet turbulence, J. Fluid Mechanics. 48: 547-591

19. Culick, F. and Yang, V. Overview of Combustion Instabilities in Liquid-Propellant Rocket Engines. Liquid Rocket Engine Combustion Instability, volume 169 of Progress in Astronautics and Aeronautics, pages 3–37. AIAA, 1995.
20. Dahm, W.J.A., Dimotakis, P.E., (1990), Mixing at large Schmidt number in the self-similar far field of turbulent jets, Journal of Fluid Mechanics, vol. 217, pp. 299-330
21. Dai, Z. Tseng, L.K., and Faeth, G. M. (1994) "Structure of Round, Fully Developed, Buoyant Turbulent Plumes," Journal of Heat Transfer, 116: 409 – 417
22. Deardoff , J.W., (1973) Journal of Fluids Engineering, 95, 429
23. DesJardin, P.E., O'Hern, T.J., Tiezen, S.R., Large eddy simulation and experimental measurements of the nar-field of a large turbulent helium plume, Physics of fluids, Vol. 16, pp. 1866-83, 2004
24. Dewan, A., Kalita, K., Dass, A.K., (2004) Comparison of three buoyancy extended version of the model in predictin turbulent plane plume, Applied Mathematical modeling, 28, 241-254
25. Eccardt, P.C., Landes, H., Lerch, R., Finite element Simulation of acoustic wave propagation within flowing media, IEEE untrasonics symposium, 1996. pp. 991-4
26. Erlebacher G, Hussein MY, Speziale CG, Zang TA. 1992. Toward the large-eddy simulation of compressible turbulent flows. J. Fluid Mech. 238:155–85
27. Favre A. 1965. Equations des gaz turbulents compressibles. J. Mec. 4:361–90
28. Fischer, H.B., List, E.J., Koh, R.C.Y., Imberger, J. and Brooks, N.H., 1979, "Mixing in Inland and Coastal Waters", Academic Press, New York
29. Gebhardt , B., Jaluria, Y., Mahajan, R.L., Sammakia B., (1988) Buoyancy-induced flows and Transportation, Hemisphere, New York.
30. George, W.K., Alpert R.L., Tamanini F., (1977) Turbulence measurements in an axisymmetric buoyant plume, Int. J. Heat Mass Tran. 20: 1145 – 1154.
31. Germano, M. 1992. Turbulence: the filtering approach. J. Fluid Mech. 238:325 – 36
32. Germano, M, Piomelli U, Moin P, Cabot WH. (1991) A dynamic subgrid-scale eddy viscosity model. Phys. Fluids A 3:1760 – 65
33. Ghosal, S., Lund, T.S., Moin, P., Akselvoll, K., (1995) A dynamic localization model for large-eddy simulation of turbulent flow, J. Fluid Mech., 286, 229-255
34. Ghosh, A., Young, G., Yu, K.H., Characterization of oscillatory heat release in unstable combustors, AIAA-2005-4325
35. Ghosh, A., Young, G., and Yu, K.H. Flame-Acoustic Interaction in GOX/GH2 Shear Coaxial Injector Flowfield, AIAA-2006-0762
36. Hara, T., Kato, S., (2004) Numerical simulation of thermal plumes in free space using the standard model, Fire Safety Journal 39: 105-129.
37. Heskestad, G., (2002) Fire plumes, flame height and air entrainments, SPFE Handbook, 3rd edition
38. Ho, C.M., Huerre, P., (1984) Perturbed Free Shear Layers, Annu. Rev. Fluid Mech. 16: 365-424

39. Hossain, M.S., Rodi, W., (1982) A turbulent model for buoyant flows and its application to vertical buoyant jets, pp 121-178
40. Hu, F.Q., (1996) On Absorbing Boundary Conditions for Linearized Euler Equations by a Perfectly Matched Layer, J. of Comp. Phy., 129, 201-219
41. Hulka, J., Huytt, J.J., Instability Phenomena in liquid oxygen/hydrogen propellant rocket engines, volume 169 of Progress in Astronautics and Aeronautics, pages 39 – 71. AIAA, 1995.
42. Im, H., (2002) Revised Formulation for S3D DNS code Compressible Reacting Flows, Notes on S3D
43. Jankiewicz, S. P. (2004) Prediction Smoke Detector Response Using A Quantitative Salt-Water Modeling Technique, MS Thesis, University of Maryland, College Park
44. Kelly, A. A. (2001) Examination Of Smoke Movement In A Two-Story Compartment Using Salt Water And Computational Fluid Dynamics Modeling, MS Thesis, University of Maryland, College Park
45. Karthik, B., Kumar, B.M., Sujith, R.I., Exact solutions to One-dimensional acoustic fields with temperature gradient and mean flow, Journal acoustic society of America, 108, pp.38-43
46. Kennedy, C.A., Carpenter, M.H., Comparison of several numerical methods for simulation of compressible shear layers, NASA Technical Paper 3483, 1997
47. Kennedy, C. A., Carpenter, M. H. and Lewis, R. H. (2000) Low-storage, explicit Runge-Kutta schemes for the compressible Navier-Stokes equations, Appl. Num. Math. 35,3:177-219.
48. Kinsler, L.E., Frey, A.R., Coppens, A.B., Sanders, J.V., Fundamentals of Acoustics. John Wiley and Sons, 1982; Chap 5, p.107, Sec.5.7
49. Kolmogorov, A.N., (1941) The local structure of turbulence in incompressible viscous fluid for very large Reynolds number. C.R. Acad.Sci. USSR 30:301
50. Kotsovinos, N.E., (1991). Turbulence spectra in free convection flow, Phys. Fluids A 3 (1) 163 – 167.
51. Kravchenko, A.G., Moin, P., On the effect of numerical errors in large eddy simulation of turbulent flows, Journal of computational physics, 131, 310-322 (1997)
52. Larsen, T., (1994) Numerical modeling of jet and plume – a civil engineering perspective, in Recent Research Advances in the Fluid Mechanics of Turbulent Jets and Plumes, ed. by Davies, P.A., Neves, M.J. V., NATO ASI Series, pp: 237-260
53. Launder, B.E., Spalding, D.B., (1972) Mathematical models on turbulence, Academic, London, England
54. Lele S.K. (1992) Compact finite difference schemes with spectral like resolution, J. Comput. Phys. 103 (1) (1992) 16-42
55. Lele S.K. (1992) A proposed modification of the Germano subgrid-scale closure method. Phys. Fluids A 4:633 – 35
56. Lilly DK. (1967) The representation of small-scale turbulence in numerical simulation experiments. In Proc. IBM Scientific Computing Symp. Environ. Sci., p. 195

57. Linden, P. F., Lane-Serff, G. F. and Smeed, D. A., (1990) Emptying filling boxes: the fluid mechanics of natural ventilation, Journal of Fluid Mechanics, 212: 309-335
58. List, E. J. (1982) Turbulent Jets and Plumes, Ann. Rev. Fluid Mech., 14:189-212.
59. List, E.J., Dugan R., (1994) Transition from jet plume dilution to ambient turbulent mixing, in Recent Research Advances in the Fluid Mechanics of Turbulent Jets and Plumes, ed. by Davies, P.A., Neves, M.J. V., NATO ASI Series, pp. 1-12
60. Marshall, W. Pal., S., Woodard, R., Santoro, R.J., Smith, R., Xia, G., Sankaran, V., Merkle, C.L., Experimental and combutational Investigation of combustor acoustics and instabilities, Part II: Transverse Modes, Reno, AIAA 2006-538
61. McGrattan K.B. (ed). (2004a). Fire Dynamics Simulator (Version 4), Technical Reference Guide. NIST Special Publication 1018, National Institute of Standards and Technology, Gaithersburg, Maryland, July 2004.
62. McGrattan K.B. (2004b). Private communication
63. McCaffrey, B. J., (1979) Purely Buoyant Diffusion Flames: Some Experimental Results, Center for Fire Research, National Engineering Laboratory, National Bureau of Standards, No. NBSIR 79-1910, 1979
64. Meinke, M., Schroeder, W., Krause, E., Rister, Th., A comparison of second- and sixth-order methods for large-eddy simulations, Computers and Fluids, (2002) 695-718
65. Meneveau, C. , Katz, J. (2000) Scale-Invariance and Turbulence Models for Large-Eddy Simulation, Annu. Rev. Fluid Mech., 32:1-32.
66. Meneveau C, Lund TS, Cabot WH. (1996) A Lagrangian dynamic subgrid-scale model of turbulence. J. Fluid Mech. 319:353–85
67. Mitler, H., Mathematical fire modeling, Progress in Aerospace Science, 1994
68. Moin, P., Squires, K., Cabot, W., Lee, S., (1991) A dynamic subgrid-scale model for compressible turbulence and scalar transport, Physics of Fluids, A 3(11), 2746-2757
69. Morton, B.R. , Taylor, G., Turns, J.S., (1956) Turbulent Gravitational Convection from Maintained and Instantaneous Sources, Proc. of the Royal Society of London, Vol. 234, Issue 1196:1–23.
70. Nam, S., Bill Jr. R.G., (1993). Numerical simulation of thermal plumes, Fire Safety Journal, 21, 231-256.
71. Novozhilov, V. (2001) Computational fluid dynamics modeling of compartment fires, Prog. Energy Combust. Sci., 27:611-666.
72. Panpanicolaou, P. N., and List, E. J. (1988) “ Investigation of Round Vertical Turbulent Buoyant Jets,” J. Fluid Mech., 195:341-391.
73. Panpanicolaou, D. List, E. J. (1989) “Large-Scale Structure In The Far Field Of Buoyant Jets”, J. Fluid Mech., 209:151-190.
74. Passot, T., Pouquet, A., (1986) Numerical simulation of compressible homogeneous flows in the turbulent regime, J. Fluid Mech., vol. 181: 441-466
75. Patankar, S.V., (1980) Numerical heat transfer and fluid flow, Hemisphere, Washington DC.

76. Petyt, M., Finite Element Techniques for Acoustics, in Theoretical Acoustics and Numerical Techniques, edited by Filippi, CISM courses and lectures No. 277, Italy, 1983
77. Pierce, C. D. & Moin, P. (1998) A dynamic model for subgrid-scale variance and dissipation rate of a conserved scalar, Phys. Fluids, 10:3041-3044.
78. Piomelli, U., Chasnov, J.R., (1996). Large-eddy simulation: theory and applications, M. Hallbaeck et al. (eds), Turbulence and transition modeling, Kluwer Academic Publishers, 269-336.
79. Poinsot, T., Lele, S.K., (1992) Boundary conditions for direct simulations of compressible viscous flows, Journal of computational physics, 101:104-129
80. Poinsot, T. , Veynante, D. (2001) Theoretical and numerical combustion, Edwards.
81. Pope SB. (2000) Turbulent Flows. Cambridge, Cambridge Univ. Press
82. Quintiere, J.G., Fundamentals of Fire Phenomena, John Wiley and Sons, 2006
83. Rajandram, V., Luo, K.H. (2002) Numerical simulation of buoyant fire plumes, Fire and Explosion Hazards, Proceedings of the third international seminar, pp. 251-261.
84. Ramshaw JD, O'Rourke, P.J., and Stein L.R., (1985) Pressure gradient scaling method for fluid flow with nearly uniform pressure, J. Comp. Phy., 58, 361-76
85. Rehm, R.G., Baum. H.R. (1978). The Equations of Motion for Thermally Driven, Buoyant Flows. NBS Journal of Research, 83:297 – 308
86. Rehm, R.G., Baum. H.R., Barnett, P.D., Buoyant convection computed in a vorticity, stream-function formulation, NBS Journal of Research, 87:165
87. Ribault, C.L., Stanley, S.A., Sarkar, S., (1999) Large eddy simulation of a plane jet, Phys. Fluids, vol. 11, No. 10
88. Ribault, C.L., Stanley, S.A., Sarkar, S., (2001) Large eddy simulation of Evolution of a passive Scalar in Plane Jet, AIAA Journal, Vol. 39, No. 8,
89. Rodi, W.,(ed), (1982). Turbulent buoyant jets and plumes, HMT, the science and applications of heat and mass transfer, 6, Pergamon Press
90. Rodi, W., (1984), Turbulence models and their application in hydraulics – a state of the art review, 2nd revised edition, University of Karlsruhe
91. Rodi W, Ferziger JH, Breuer M, Pourquie M., (1997) Status of large eddy simulation: results of a workshop. J. Fluids Eng.-T ASME, 119:248 – 62
92. Rogallo RS, Moin P. (1984) Numerical simulation of turbulent flows. Annu. Rev. Fluid Mech. 16:99 – 137
93. Rooney and linden, P.F., (1996) Similarity consideration for non-Boussinesq plumes in an unstratified environment, J. Fluid Mech. 318: 235-250
94. Rouse, H., Yih, C.S., and Humphreys, H.W., (1952) Gravitational convection from a boundary source, Tellus 4, 201
95. Rudy, D.H., Strikwerda, J.C., (1980) A Nonreflecting Outflow Boundary Condition for Subsonic Navier-Stokes Calculations, J. of Comp. Phy. 36, 55-70
96. Sagaut, (2002) Large eddy simulation of incompressible flows, page 1
97. Santoro, R.J., Combustion Instability Review, NASA Huntsville workshop, April.2006

98. Shabbir, A., and George, W. K. (1994) Experiments On a Round Turbulent Buoyant Plume, J. Fluid Mech., 275:1-32
99. Smagorinsky J. (1963) General circulation experiments with the primitive equations. I. The basic experiment. Mon. Weather Rev. 91:99
100. Stanley, S.A., Sarkar, S., (1999) Direct Numerical Simulation of the Developing Region of Turbulent Planar Jets, AIAA Journal, 99-0288
101. Stanley, S.A., Sarkar, S., (2002) A study of the flow-field evolution and mixing in a planar turbulent jet using direct numerical simulation, J. Fluid Mech., Vol. 450, pp. 377-407
102. Steckler, K. D., Baum, H. R. and Quintiere, J. G. (1986) "Salt Water Modeling Of Fire Induced Flows In Multi-compartment Enclosures", Twenty-first Symposium (international) on Combustion, The combustion Institute, 143-149.
103. Stokes, G.G., (1867) On the Communication of Vibration from a Vibrating Body to a Surrounding Gas, Proceedings of the Royal Society of London, pp. 470-471
104. Sutherland, J.C., Kennedy, C.A., (2003) Improved boundary conditions for viscous, reacting, compressible flows, J. of Comp. Physics, 191: 502-524
105. Tamanini, F., (1977) An improved version of the model of turbulence and its application to axisymmetric forced and buoyant jets, FMRC technical report, 22360-4
106. Taroudakis, M.I., Makrakis, G.N., Inverse problems in underwater acoustics, Springer, 2001
107. Trouvé, A., et al. Terascale High-Fidelity Simulations of Turbulent Combustion with Detailed Chemistry, DOE/Office of Science, Program Scientific Discovery through Advanced Computing (SciDAC): Computational Chemistry. http://scidac.psc.edu/, 2001
108. Vasilyev, O.V., Lund, T.S., Moin, P., (1998) A General Class of Commutative Filters for LES in Complex Geometries, Journal of Computational Physics, 146, 82-104
109. Vervisch, L., Poinsot, T. (1998). Direct Numerical Simulation of Non-premixed Turbulent Flames, Annual Review if Fluid Mechanics
110. Vreman B, Geurts B, Kuerten H. (1997) Large eddy simulation of the turbulent mixing layer. J. Fluid Mech. 339:357 – 90
111. Wang, Y., Trouvé, A., (2004) Artificial acoustic stiffness reduction in fully compressible, direct numerical simulation of combustion, Combustion Theory and Modeling, 8 633-660
112. Webb, A.T., Mansour, N.N., (2000), Towards LES models of jets and plumes, Center for Turbulence Research, Annual Research Briefs
113. Worthy, J., Rubini, P.A.., Large Eddy simulation of Buoyant Plumes, 4th international seminar on fire and explosion Hazards, Sept. 2003, London derry, UK
114. Worthy, J., Rubini, P.A.., A study of LES stress and Flux models applied to a buoyant jet, Numerical Heat Transfer, Part B., 48:235-256, 2005

115. Yang, V. and Anderson, W., editors. Liquid Rocket Engine Combustion Instability, volume 169 of Progress in Astronautics and Aeronautics. AIAA, Pennsylvania State University, 1995.
116. Yao, X., Ma, T., Marshall, A.W., Trouvé, A., Mixing and Turbulent Transport in Unconfined and Impinging Plume, Proceedings of the Interflame International Symposium, Edinburgh, England, July 2004
117. Yokoi, S. (1961) "Upward Convection Current From a Burning Wooden House. The Use of Models in Fire Research." Publication No. 786. National Academy of Science, National Research Council, Washington, D.C. See also: Building Research Institute, Ministry of Construction, Japan, Report No. 29.
118. Yoshizawa, A. (1986), Statistical theory for compressible turbulent shear flows, with the application to subgrid modeling, Physics of Fluids, 29, 2152-2164
119. Zang Y, Street RL, Koseff J. (1993) A dynamic mixed subgrid-scale model and its application to turbulent re-circulating flows. Phys. Fluids A 5:3186–96
120. Zhou, X., Luo, K.H., Williams, J.R., (2001a), Large-eddy simulation of a turbulent forced plume, Euro. J. Fluid Mech., 20, 233-254
121. Zhou, X., Luo, K.H., Williams, J.R., (2001b), Study of Density Effects in Turbulent Buoyant Jets using Large-eddy simulation, Theoretical Computation of Fluid Dynamics, 15, 95-120
122. Zukoski, E. E. (1995) Properties of Fire Plumes, in Combustion Fundamental of Fire, G. Cox, ed., New York, Academic Press.